MOLECULAR LEVEL INVESTIGATIONS OF SPECIFIC ION EFFECTS AT AIR/AQUEOUS INTERFACE

DOCTORAL THESIS

by

"Bhawna Rana" (2016PHZ0002)



DEPARTMENT OF PHYSICS INDIAN INSTITUTE OF TECHNOLOGY ROPAR April, 2023

MOLECULAR LEVEL INVESTIGATIONS OF SPECIFIC ION EFFECTS AT AIR/AQUEOUS INTERFACE

A Thesis Submitted
In Partial Fulfillment of the Requirements
for the Degree of

DOCTOR OF PHILOSOPHY

by

"Bhawna Rana" (2016PHZ0002)



DEPARTMENT OF PHYSICS INDIAN INSTITUTE OF TECHNOLOGY ROPAR April, 2023

Bhawna Rana: Molecular Level Investigations of Specific Ion Effects at Air/Aque Interface	eous
Copyright © "2023" by Indian Institute of Technology Ropar	
All Rights Reserved	

iv

DEDICATED TO My MAA PAPA and TEACHERS



Water has no taste, no color, no odor; it cannot be defined, art relished while ever mysterious. Not necessary to life, but rather life itself. It fills us with a gratification that exceeds the delight of the senses.

ANTOINE DE SAINT-EXUPERTY, 1939

God made the bulk; the surfaces were invented by the devil.

WOLFGANG ERNST PAULI, 1945

There is something in the air and while it may not be love, some says it's the next best things—negative ions.

DENISE MANN, 2002

Salt is so common, so easy to obtain, and so inexpensive that we have forgotten that from the beginning of civilization until about 100 years ago, salt was one of the most sought-after commodities in human history.

MARK KURLANSKY, 2002



DECLARATION OF ORIGINALITY

I hereby declare that the work which is being presented in the thesis entitled "MOLECULAR LEVEL

INVESTIGATIONS OF SPECIFIC ION EFFECTS AT AIR/AQUEOUS INTERFACE" has been solely

authored by me. It presents the result of my own independent investigation/research conducted during the time

period from July 2016 to April 2023 under the supervision of Dr. Kailash Chandra Jena, Associate Professor,

Department of Physics, IIT Ropar. To the best of my knowledge, it is an original work, both in terms of research

content and narrative, and has not been submitted or accepted elsewhere, in part or in full, for the award of any

degree, diploma, fellowship, associateship, or similar title of any university or institution. Further, due credit has

been attributed to our collaborators: Dr. David J. Fairhurst (Associate Professor, Department of Physics and Mathematics, Nottingham Trent University, Nottingham, United Kingdom) and Dr. Manoranjan Mishra

(Professor, Department of Mathematics, IIT Ropar). I also declare that any idea/data/fact/source stated in my

thesis has not been fabricated/ falsified/ misrepresented. All the principles of academic honesty and integrity

have been followed. I fully understand that if the thesis is found to be unoriginal, fabricated, or plagiarized, the

Institute reserves the right to withdraw the thesis from its archive and revoke the associated Degree conferred.

Additionally, the Institute also reserves the right to appraise all concerned sections of society of the matter for their information and necessary action (if any). If accepted, I hereby consent for my thesis to be available online

in the Institute's Open Access repository, inter-library loan, and the title & abstract to be made available to

outside organizations.

Signature

Bhawna Rana

2016PHZ0002

Ph.D.

Department of Physics

Indian Institute of Technology Ropar

Rupnagar, Punjab 140001

Date: 19.04,2023

ix



CERTIFICATE

This is to certify that the thesis entitled "Molecular Level Investigations of Specific Ion Effects at

Air/Aqueous Interface", submitted by Bhawna Rana (2016PHZ0002) for the award of the degree of Doctor

of Philosophy of Indian Institute of Technology Ropar, is a record of bonafide research work carried out under

my guidance and supervision. To the best of my knowledge and belief, the work presented in this thesis is

original and has not been submitted, either in part or full, for the award of any other degree, diploma, fellowship,

associateship or similar title of any university or institution.

In my opinion, the thesis has reached the standard fulfilling the requirements of the regulations relating to the

Ph.D. Degree.

Signature of the Supervisor

Dr. Kailash Chandra Jena

Associate Professor

Department of Physics

Indian Institute of Technology Ropar

Rupnagar, Punjab 140001

Date: 19/04/2023

χi



ACKNOWLEDGMENTS

I would like to take this opportunity to express my deep sense of gratitude and profound feeling of admiration to all those who helped me in the accomplishment of this thesis work.

First and foremost, I thank my thesis supervisor, Dr. Kailash Chandra Jena, for his trust in me. He introduced me to the fascinating field of nonlinear optics, biophotonics, and optofluidics. He provided me an opportunity to work on state-of-the-art laser technologies and cutting-edge research in Nonlinear Light Scattering and Biophotonics (NLSBP) lab at IIT Ropar. I am grateful for his unconditional support, insightful guidance, and consistent encouragement throughout this Ph.D. journey of six and a half years. With his passion for science, I could learn a lot about what it means to be a scientist.

I sincerely acknowledge our collaborators: Dr. David J. Fairhurst (Nottingham Trent University (NTU), United Kingdom), Dr. Manoranjan Mishra (IIT Ropar, India), Dr. Kamal P. Singh (IISER Mohali, India). I deeply admire Dr. David J. Fairhurst for all his support and encouragement. He gave me an opportunity to work in the scientific environment of SOFT group especially with Dr. Fouzia F. Ouali, Dr. Andrew M. J. Edwards, Dr. Akhshay Bhadwal, and Mr. Joey Kilbride, in the Department of Physics and Mathematics at NTU under the Newton-Bhabha Fellowship program 2019.

I would like to thank my doctoral committee: Dr. Shubhrangshu Dasgupta, Dr. Pushpendra Pal Singh, Dr. Manoranjan Mishra, and Dr. Asoka Biswas for their support and encouragement to work diligently throughout this time. I am thankful to the kind and supportive faculty members and staff at IIT Ropar. Special thanks to Mr. Anshu Vaid, Sr. Assistant, Department of Physics, for his support in the smooth processing of all the documentation work. I want to thank Mr. Damninder Singh for his help in carrying out UV-Visible absorbance studies. Thanks to Dr. Vishwajeet Mehandia for allowing us with viscosity studies.

I would like to take the occasion to thank all the former teachers and professors during my school, graduation, and post-graduation that paved my way and gave me lessons of life.

Funding for this research work includes a student fellowship from the Ministry of Human Resource Development, India, and the Newton Bhabha Fellowship from the British Council for a four-month research visit in Nottingham, United Kingdom. Additional financial support for the presentation of this work at national and international meetings is provided by Indian Institute of Technology Ropar.

I thank all the members of the NLSBP lab, Dr. Shilpi Chaudhary, Dr. Deepak Tomar, Dr. Harpreet Kaur, Dr. Monika Chaudhary, Dr. Harsharan Kaur, Ms. Sarabjeet Kaur, Mr. Rakshith, Mr. Sagar, Mr. Rakshit, Ms. Tuhina, Ms. Meenu, Ms. Sitara and Mr. Yagyaraj for creating a professional and intellectual working ambiance. I am happy to recall our best time together on trips during national conferences.

I am thankful to my roommates (Venus 107, IIT Ropar, India) and D-floor mates (Portland House, Nottingham, United Kingdom) for building a delightful living environment. Thanks to all the colleagues at IIT Ropar. Special Thanks to Dr. Aarti Tiwari and Dr. Vikram Singh for their care and support.

I am grateful to God for giving me this opportunity. I am indebted to my maa, papa, and little brother for their unconditional love and belief. They have been my sole source of motivation throughout. Thank you all!



ABSTRACT

Specific ion effects at air/aqueous interfaces are widely involved in physical, chemical, environmental, and biological processes imperative in modern surface science and technology. The kinetics and thermodynamics of these processes are determined by the ion speciation, and the influence of ions on the structure, conformation, and bonding environment of the molecular groups present at the air/aqueous interface. Several research groups have put a lot of effort into this research with various experimental and theoretical approaches. However, a detailed molecular level understanding of the specific ion phenomena is lacked to date. In the present thesis, the focus is positioned on providing the molecular level details into the intermolecular interactions as well as the structure and conformations of interfacial molecules to better comprehend the specific ion effects at the air/aqueous interface. In this direction, the present thesis investigates the water evaporation process, laserinduced liquid microjets, and ordering/disordering of macromolecule structure in the presence of ions at the air/aqueous interface in unprecedented detail. To achieve the targeted research objectives, in the experimental scheme, we have developed experimental setups: a) Time-resolved Newton's ring interferometry to investigate the evaporation dynamics of sessile aqueous droplets. b) Laser-induced microjets to study radiation-induced deformation of air/aqueous interface. We have utilized a state-of-the-art surface-specific sum frequency generation (SFG) vibrational spectroscopic tool to probe the molecular level structural details governing the specific ion effects at the air/aqueous interface.

The first research work of the thesis intends to investigate specific ion effects in the water evaporation process at the air/water interface. During evaporation, a water molecule breaks the intermolecular hydrogen (H-) bonds with its neighboring molecules at the air/water interface and enters the vapor phase. The phenomenon of water evaporation has been studied meticulously owing to its great importance in diverse fields of science and technology, specifically in Earth's water cycle. Most of the reported work primarily focuses on the macroscopic approach, which leads to a gap in the mechanistic interpretation of the process. This motivates the present research work to provide fundamental insights into the water evaporation process through molecular level details into the complex bonding environment of the surface water molecules evaporating from the air/water interface. For this, we have utilized Hofmeister ions (kosmotropes: HPO_4^{2-} , SO_4^{2-} , and CO_3^{2-} and chaotropes: NO_3^{-} , and I^{-}) purposefully to perturb the H-bonding environment at the air/water interface to excerpt their influence on the evaporation process. In our experimental scheme, we have developed in-house time-resolved interferometry to study the evaporation dynamics of sessile aqueous droplets. It is found that the kosmotropes reduce evaporation, whereas chaotropes accelerate the evaporation process of sessile salt droplets that follows the Hofmeister series: $HPO_4^{2-} < SO_4^{2-} < CO_3^{2-} < Cl^- \approx water < NO_3^- < I^-. To \ extract \ deeper \ molecular \ level \ insights \ into \ the$ observed Hofmeister trend in the evaporation rates, we have employed surface-specific SFG vibrational spectroscopy to investigate the air/water interface in the presence of Hofmeister ions. The SFG spectra reveal that the presence of ions significantly impacts the strength of the H-bonding environment and the orientation of free OH oscillators from ~ 36.2° to 48.4° at the air/water interface that follows the Hofmeister series, which in turn govern the evaporation process. It is established that the slow evaporating water molecules experience a strong H-bonding environment with free OH oscillators tilted away from the surface normal in the presence of kosmotropes. In contrast, the fast evaporating water molecules experience a weak H-bonding environment with free OH oscillators tilted towards the surface normal in the presence of chaotropes at the air/water interface. The present research work is this chapter demonstrates a comprehensive understanding of the role of hydrogen bonding environment and the orientation of the free OH moieties in governing the evaporation process at the air/water interface. The outcomes of this work would be helpful in designing interfacial water structures to manipulate the evaporation processes for future needs.

In the second research problem, we investigated specific ion effects in the generation of laser-induced liquid microjets at the air/rhodamine 6G (Rh6G) dye solution interface. Highly focused, fine diameter, and fast liquid microjets are generated when the air/aqueous interface is deformed upon absorbance of a laser beam in the aqueous media. They find potential applications as painless needle-free drug injection systems in the medical industry and especially in vaccination drives during Covid-endemic to mitigate the risk of disease spread owing to the contaminated needle waste worldwide. An efficient drug delivery system demands fine diameter, fast liquid jets with controlled speed and penetration depths. In the past ten years, exciting research works are reported employing the ideology of variation in laser energy, laser focusing inside the liquid and capillary diameters to produce liquid jets with desired characteristics. In the present research work, we have utilized sodium salts of Hofmeister series anions (SO₄²-, I⁻ and SCN⁻), which are the imperative constituents of drugs/vaccines, to showcase the contribution of ion-specific optical absorbance in determining the liquid jet characteristics, which has not been explored to date. In this direction, we have developed an in-house experimental setup using a picosecond laser to generate liquid microjets. We are able to generate liquid microjets of diameter ~ 40 µm, speed ~ 25±2 m/s with Rh6G at laser (532 nm) pulse energy of 400 µJ within a microcapillary of inner diameter ~ 400 µm. It is witnessed that the presence of ions do influence the velocity and power of liquid jets in Rh6G, which obeys the Hofmeister order as: $SO_4^{2-} \approx Rh6G > I^- > SCN^-$. The observed ion-specific liquid jet velocity is attributed to the ion-induced variation in the optical absorbance of Rh6G that also follows the Hofmeister series. This ion-specific optical absorbance is ascribed to the relative adsorption of ions toward the Rh6G molecule. It is suggested that the hydrophilic kosmotropic anion (SO₄²-) prefers to bind to the water molecules, whereas the hydrophobic chaotropic anions (I⁻, and SCN⁻) are prone to bind the NH- and hydrophobic CH-moieties of Rh6G. Therefore, this ion-specific interaction with the Rh6G in the solution determines the liquid jet velocities, which is then utilized to showcase the ion-specific penetration depths of liquid jets simulated for model soft tissues. The maximum penetration depth is observed with SO_4^{2-} , however, a three-fold reduction in penetration depth is reported for I⁻, and SCN⁻. It is evident from the results that the present research work demonstrates the contribution of ion-specific interactions in governing the jet velocity and jet power that is crucial in the development of needle-free drug delivery systems with controlled penetration depths.

The third research work of the thesis provides molecular level insights into the specific ion effect in ordering/disordering of macromolecule structure at the air/aqueous interface. Since 1888, when Franz Hofmeister first proposed the series of anions according to their efficacy to precipitate macromolecule in their aqueous solution, the series spans its horizons in various fields of science and technology like biophysics, chemistry, colloids, and environmental sciences. However, a detailed molecular level understanding of the Hofmeister phenomenon in a ternary system of ion, macromolecule, and water is still elusive. The current understanding involves the contribution of ion-water and ion-macromolecule interactions. However, some recent experimental reports have professed the undeniable contribution of ion-specific water-macromolecule interactions in the Hofmeister phenomenon, the exact molecular level mechanism of which has remained unknown to date. In this direction, we investigated the Hofmeister effect at the air/ polyvinylpyrrolidone (PVP)

aqueous interface using surface-specific SFG vibrational spectroscopy in different polarization schemes. The spectral signature observed from the ssp polarisation scheme reveals ion-specific ordering of water molecules following the Hofmeister series. However, it does not reflect any impact on the structure of the PVP macromolecule. Interestingly, the ppp-SFG spectra in the CH-stretch region reveal that ions significantly impact the structure of PVP macromolecule at the air/aqueous interface This is evidenced by the ion-induced changes in the orientation angle of vinyl chain CH_2 -groups from 62.5° to 33.6° that follows the Hofmeister series: SO_4^{2-} > $Cl^- > NO_3^- > Br^- > ClO_4^- > SCN^-$. The minimal orientation angle of CH_2 -groups in the presence of chaotropic anions ClO₄, and SCN⁻ indicates the ion-induced significant reordering in the PVP vinyl chains, which finds an intriguing correlation with the ion-specific water structure at the air/aqueous interface. From ppp-SFG spectra in OH-stretch region, it is compelling to observe that the presence of chaotropic anions brings significant spectral blue shift of ~ 40 cm⁻¹ in the OH-stretch band at 3540 cm⁻¹. The blue shift in the OH-feature has been attributed to the weaker interactions between the interfacial water molecules and the hydrophobic moieties of the PVP macromolecules at the air/aqueous interface. This enables us to comprehend the molecular level mechanism of the Hofmeister effect as follows. The weakly hydrated chaotropic anions (ClO₄, and SCN⁻), which are prone to adsorb towards the hydrophobic surface (-CH, -CH₂ of polymer backbone), offer binding sites to the surrounding water molecules to form weak interactions with the hydrophobic moieties of the macromolecule, that, in turn, reorders the macromolecule structure at the interface. The current research provides the first spectroscopic evidence of cooperative participation of ion-specific water-macromolecule interactions in the molecular level mechanism of the Hofmeister effect, along with the well-known ion-water and ionmacromolecule interactions.

The molecular level approach developed in this thesis could potentially motivate new experiments and theoretical studies to better comprehend the fundamentals of specific ion phenomena that widely prevail in various scientific and technological applications.

Keywords: Specific ion effects, Air/aqueous interface, Water, Kosmotropes, Chaotropes, Intermolecular interactions, Hydrogen (H-) bonding, Conformation, Orientation angle, Droplets, Evaporation, Laser-induced liquid microjets, Sum frequency generation (SFG) vibrational spectroscopy, Time-resolved Newton's ring interferometry.



LIST OF PUBLICATIONS

Journal papers

- [1]. Rana, B.; Fairhurst, D. J.; Jena, K. C. Ion-specific Water-Macromolecule Interactions at Air/Aqueous Interface: An Insight into the Hofmeister Effect. *J. Am. Chem. Soc.* 2023 (Accepted).
- [2]. Rana, B.; Fairhurst, D. J.; Jena, K. C. Investigation of water evaporation process at air/water interface using Hofmeister ions. *J. Am. Chem. Soc.* 2022, 144(39), 17832-17840.
- [3]. Kaur, H.; Verma, M.; Kaur, S.; **Rana, B.**; Singh, N.; Jena, K. C. Elucidating the Molecular Structure of Hydrophobically Modified Polyethylenimine Nanoparticles and Its Potential Implications for DNA Binding. *Langmuir* 2022, 38(44), 13456-13468.
- [4]. Chaudhary, S.; Kaur, H.; Kaur, H.; Rana, B.; Tomar, D.; Jena, K. C. Probing the Bovine Hemoglobin Adsorption Process and its Influence on Interfacial Water Structure at the Air–Water Interface. *Appl. Spectrosc.* 2021, 75(12), 1497-1509.
- [5]. Tomar, D.; **Rana, B.**; Jena, K. C. The structure of water–DMF binary mixtures probed by linear and nonlinear vibrational spectroscopy. *J. Chem. Phys.* 2020, 152(11), 114707.
- [6]. Rana, B.; Manoranjan, M.; Jena, K. C. Impact of Ion-Specific Interactions on Laser Induced Liquid Microjets. Submitted in *Appl. Phys. Lett.* 2023 (under review).

Conference papers

[1]. Rana, B.; Kaur, H.; and Jena, K. C. Probing the Influence of Polyvinylpyrrolidone Polymer on the Interfacial Water Structure at Air/Water Interface using Nonlinear Optical Vibrational Spectroscopy, *KIRAN: A Bulletin of the Indian Laser Association* 2019, 31, 1. (Featured on the Cover Page).

Book Chapters

- [1]. Kaur, H.; Rana, B.; Tomar, D.; Kaur, S.; Jena, K.C. Fundamentals of ATR-FTIR Spectroscopy and Its Role for Probing In-Situ Molecular level Interactions. *In Modern Techniques of Spectroscopy, Springer*, Singapore, 221; pp 3-37.
- [2]. Kaur, H.; Tomar, D.; Kaur, H.; Rana, B.; Chaudhary, S.; Jena, K. C. Sum-frequency generation vibrational spectroscopy: A nonlinear optical tool to probe the polymer interfaces. *In Advances in Spectroscopy: Molecules to Materials, Springer*, Singapore, 2019; pp. 39-55.
- [3]. Tomar, D.; Kaur, H.; Kaur, H.; Rana, B.; Talegaonkar, K.; Maharana, V.; Jena, K.C. ATR-FTIR Spectroscopy and Its Relevance to Probe the Molecular level Interactions Between Amino Acids and Metal-Oxide Nanoparticles at Solid/Aqueous Interface. In Advances in Spectroscopy: Molecules to Materials, Springer, Singapore, 2019; pp 3-21.

TABLE OF CONTENTS

Declaration	ix
Certificate	xi
Acknowledgements	xiii
Abstract	xv
List of Publications	xix
List of Figures	xxiv
List of Tables	xxxii
Notations and Abbreviations	xxxiii
1 Introduction	1
1.1 Specific Ion Effects: A Historical Background	1
1.2 Hofmeister Series and Its Characteristics	3
1.3 Applications of Specific Ion Effects	5
1.4 Intermolecular Interactions	12
1.5 Importance of Studying Specific Ion Effects at Air/Aqueous Interface	15
1.6 Challenges in the Investigation of Air/Aqueous Interface	16
1.7 Specific Ion Effects at Air/Water Interface	16
1.7.1 Conventional Textbook Picture of Depletion of Ions from the Air/Water Interface	16
1.7.2 SFG Investigations on Specific Ion Effects at the Air/Water Interface	18
1.8 Specific Ion Effects at Air/Aqueous Interface	22
1.9 Research Gaps and Motivation	26
1.10Aims and Objectives of the Thesis	27
1.11 Organization of the Thesis	28
2 Experimental Techniques and Methodology	31
2.1 Time-Resolved Newton's Ring Interferometry	31
2.1.1 Experimental Setup	31
2.1.2 Sample Preparation and Droplet Formation	32
2.1.1 Dynamic Newton's Ring Interference Pattern	32
2.1.2 Evaporation Rate of Sessile Aqueous Droplets	33
2.2 Laser-Induced Liquid Microjets	33
2.2.1 Time Evolution of Liqud Jets	34

2.2.2 Parameter Dependence of Jet Velocity	36
2.2.3 Experimental Setup	38
2.2.4 Calculation of Jet Velocity and Jet Power	39
2.2.5 Estimation of the Capillary Diameters	40
2.3 Sum Frequency Generation (SFG) Vibrational Spectroscopy	40
2.3.1 Nonlinear Optical Response of SFG from Surface/Interface	41
2.3.2 Surface Specificity of SFG Vibrational Spectroscopy	42
2.3.3 SFG is Both IR and Raman Active	42
2.3.4 Effective Nonlinear Susceptibility χ ^{(2), eff} and Fresnel's Factors	43
2.3.5 Molecular Orientation and Polarization Dependent SFG	44
2.3.6 Orientation Analysis for Molecular Groups with Different Symmetries	46
2.3.6.1 Orientation Angle Calculation for Free OH Oscillator	46
2.3.6.2 Orientation Angle Calculation for CH ₂ -Group	48
2.3.6.3 Significance of L-factor Correction in Orientation Angle Calculation	49
2.3.7 SFG Spectrometer	50
2.3.8 Piranha Cleaning and Sample Preparation	52
2.4 Surface Tension Measurements	53
2.5 UV-Visible Absorbance Studies	54
3 Water Evaporation Process at Air/Water Interface	55
3.1 Introduction	55
3.2 Experimental Section	57
3.2.1 Materials	57
3.2.2 Time-Resolved Newton's Ring Interferometry	57
3.2.3 Surface Tension Measurements	57
3.3 Sum Frequency Generation (SFG) Vibrational Spectroscopy	57
3.4 Results and Discussion	57
3.5 Conclusions	64
4 Laser-Induced Liquid Microjets at Air/Aqueous Interface	66
4.1 Introduction	66
4.2 Experimental Section	67
4.2.1 Materials and Sample Preparation	67
4.2.2 Laser-Induced Liquid Microjets	68

4.2.3 UV-Visible Absorbance Studies	69
4.3 Results and Discussion	69
4.4 Conclusions	75
5 Hofmeister Effect at Air/Polyvinylpyrrolidone Aqueous Interface	76
5.1 Introduction	76
5.2 Experimental Section	78
5.2.1 Materials	78
5.2.2 Sum Frequency Generation (SFG) Vibrational Spectroscopy	78
5.3 Results and Discussion	78
5.4 Conclusions	86
6 Summary and Conclusions	87
References	
Appendix A	111
Appendix B	
List of Research visits/Conferences/Workshops Attended	
Bio-Data of Author	121

LIST OF FIGURES

S. No.	Figure Caption	Page No.
1.1	A typical anionic Hofmeister series.	4
1.2	Schematic illustration of the mechanism of ion-specific optical properties of cationic	
	poly (3-alkoxy-4-methylthiopene) (PMNT). Reprinted from J. Phys. Chem. C 2013, 117,	
	42, 21870-21878. Copyright 2013 American Chemical Society. ⁴⁹	5
1.3	Schematic illustration of the working mechanism of organohydrogel-based cell based on	
	the themodiffusion effect, where replacement of water with glycerol in the hydrogel	
	improves the stability and temperature tolerance of the wearable device. Reprinted from	
	ACS Nano 2021, 15, 8, 13427-13435. Copyright 2021 American Chemical Society. 63	6
1.4	Schematic illustration of salt-in effect utilizing LiCl with Zwitterionic polymer for	
	improved atmospheric water harvesting (AWH). Reprinted from ACS Materials	
	Lett. 2022, 4, 3, 511-520. Copyright 2022 American Chemical Society. ⁸⁴	6
1.5	Schematic illustration of specific ion effects in the stability of hexadecane nanodroplets.	
	Reprinted from J. Phys. Chem. C 2019, 123, 27, 16621-16630. Copyright 2019	
	American Chemical Society. ⁹⁹	7
1.6	Schematic illustration of the influence of ions on the efficiency of bacterial ice	
	nucleators that follows the Hofmeister series. The different effects are due to specific	
	interactions of the ions with ice-nucleating proteins on the surface of the bacteria.	
	Reprinted from Chem. Eur. J. 2021, 27, 26, 7402-7407. Copyright 2021 The Authors.	
	Chemistry - A European Journal published by Wiley-VCH GmbH. 101	7
1.7	Side view of a water droplet on (a) PMTA-Ac, (b) PMTA-Cl, (c) PMTA-SCN, and (d)	<u> </u>
	PMTA-ClO ₄ . The averaged static contact angles are depicted in the images. Reprinted	
	from Ind. Eng. Chem. Res. 2018, 57, 15, 5268-5275. Copyright 2018 American	
	Chemical Society. 110	8
1.8	Schematic representation of the interaction between cationic octapeptide, lanreotide and	
	counterions that tune the diameter of self assembled NTs. Reprinted from J. Am. Chem.	
	Soc. 2012, 134, 1, 723-733. Copyright 2012 American Chemical Society. 112	9
1.9	Schematic representation of (a) solar desalination using the PVA-agar-MWCNT-100	
	hydrogel and (b) improvement in mechanical strength of hydrogel after soaking in	
	Hofmeister salt (NH ₄) ₂ SO ₄ owing to increased hydrogen bonding among polymers.	
	Reprinted from ACS Appl. Mater. Interfaces 2022, 14, 42, 47800-47809. Copyright	
	2022 American Chemical Society. 117	9
1.10	Pressure-dependent LLPS of the ATP/pLys system (schematically shown on the top (a))	
	in 30 mM Tris-buffer. Light microscopy snapshots of the LLPS of ATP and pLys	
	without (b) and with (c) 250 mM NaClO ₄ at selected pressures (1, 200, 500, 700, and	
	1000 bar). Sample: 40 mM ATP, 50 mM pLys (15-30 kDa), 30 mM Tris, pH 7.4, T =	
	25 °C. Scale bar: 30 μm. Pressure-dependent LLPS of the ATP/pLys system in 250 mM	
	NaClO4-Tris buffer. Reprinted from J. Am. Chem. Soc. 2021, 143, 13, 5247-5259.	
	Copyright 2021 American Chemical Society. 132	10

1.11	(a) Schematic Illustration of chemical reactions occurring in an electrolytic Zn-MnO ₂	
	battery. (b) Charge–discharge curves of MnO ₂ –Zn batteries in electrolyte of 1 M	
	$MnSO_4 + 1 M ZnSO_4 + 0/0.05/0.1 M H_2SO_4$. The battery is charged at 2.2 V to 0.5 mAh	
	and discharged at 0.5 mA to 0.8 V. Reprinted from Adv. Energy Mater. 2022, 12, 16,	
	2103705. Copyright 2022 Wiley-VCH GmbH. 133	11
1.12	Ion-specific effect on the parameters describing the nonequilibrium stability of GOX at	11
	2 M salt concentrations: activation energy, E_a , inactivation temperature T_k , and anion	
	polarizability, α. Color codes for anions: thiocyanate (red), iodide (orange), perchlorate	
	(green), bromide (light blue), nitrate (dark violet), and chloride (magenta). Reprinted	
	from J. Phys. Chem. B 2019, 123, 38, 7965-7973. Copyright 2019 American Chemical	
	Society. 136	11
1.13	Ion affects water diffusion near the unilamellar vesicle surface with the order of	11
	Hofmeister series. (a) Schematic diagram of spin-labeled phospholipid vesicles in	
	electrolyte solution. Spin-label, tempo, was drawn in skeletal formula. It is not drawn to	
	scale. Water diffusion activation energy for anions (b) and cations (c) follows	
	Hofmeister series. Activation energy error is $\pm 0.1k_BT$. Reprinted from J. Am. Chem.	
	Soc. 2014, 136, 6, 2642-2649. Copyright 2014 American Chemical Society. 40	12
1.14	Illustration of interactions between atoms, ions and molecules with distance R apart. μ ,	12
	and α correspond to electric dipole moment and electric polarizability respectively.	14
1.15	(a)-(d), Snapshots of the solution/air interfaces from the molecular dynamics	14
	simulations. Coloring scheme: water oxygen, blue; water hydrogen, gray; sodium ions,	
	green; chloride ions, yellow; bromide ions, orange; iodide ions, magenta. e-h, Number	
	densities, $\rho(z)$, of water oxygen atoms and ions plotted vs distance from the center of the	
	slabs in the direction normal to the interface (z), normalized by the bulk water	
	density, ρ_b . The ion densities have been scaled by the water/ion concentration ratio of 48	
	for ease of comparison. The colors of the curves correspond to the coloring of the atoms	
	in the snapshots. Reprinted from J. Phys. Chem. B 2001, 105, 43, 10468-10472.	
	Copyright 2001 American Chemical Society. 189	
		17
1.16	SSP polarized SFG spectra of (a) 0.015x and 0.036x NaCl, (b) 0.015x and 0.036x NaBr,	
	and (c) 0.015x and 0.036x NaI. The neat water SFG spectrum is plotted in each figure	
	for comparison. The open yellow and closed yellow triangles within (c) show the sum	
	frequency intensity of the 0.015x NaI in D ₂ O and pure D ₂ O, respectively. Insets: SFG	
	sodium halide aqueous solutions spectral fits. Component Lorentzian peaks are shown as	
	dashed pink lines, and the calculated fits from the component peaks are shown as black	
	lines that go through most of the data points. Reprinted from J. Phys. Chem. B 2004,	
	108, 7, 2252-2260. Copyright 2004 American Chemical Society. 190	18
1.17	(a) Vibrational sum frequency spectra of water and ~ 1 M potassium thiocyanate	
	solution. The presence of the ions at the interface decreases the 3200 cm ⁻¹ band. The	
	points and continuous lines represent the experimental data and fits, respectively. (b)	
	Conventional VSFG $ \chi_{eff}^{(2)} ^2$ spectra of the air/aqueous interfaces of neat water and 1.0 M	19

NaClO ₄ salt solution across the entire OH-stretching region (3000–3800 cm ⁻¹). ¹⁹⁵ (o	c)
VSF spectra of 0.03 mf NaI in H ₂ O (black). A neat vapor/water spectrum (grey)	is
shown for comparison. Reprinted from J. Phys. Chem. Lett. 2013, 4, 24, 4231-4236; ¹	94
J. Phys. Chem. C 2007, 111, 12, 4484-4486; J. Phys. Chem. B 2004, 108, 16, 505.	l-
5059. 191 Copyright 2013, 2007 and 2004 American Chemical Society.	
1.18 (a) SSP polarized SFG spectra of 0.015x NaF. Insets: SFG sodium halide aqueou	IS
solutions spectral fits. Component Lorentzian peaks are shown as dashed pink lines, an	d
the calculated fits from the component peaks are shown as black lines that go throug	h
most of the data points. 190 (b) VSF spectra of 0.03 mf NaI in H ₂ O (black). A near	at
vapor/water spectrum (grey) is shown for comparison. [91] (c) Calculated SFG spectra of	of
aqueous NaF solution and neat water. 200 Reprinted from J. Phys. Chem. B 2004, 108,	7,
2252-2260; ¹⁹⁰ J. Phys. Chem. B 2004, 108, 16, 5051-5059; ¹⁹¹ J. Phys. Chem. C 2012	2,
116, 20, 11082-11090. ²⁰⁰ Copyright 2004and 2012 American Chemical Society.	21
1.19 Conventional VSFG $ \chi^{(2)} ^2$ spectra of water molecules at vapor/aqueous solution	
interfaces of 1.1 M Na ₂ CO ₃ , 1.1 M Na ₂ SO ₄ , and 1.1 M (NH ₄) ₂ SO ₄ salt solutions. Nea	at
water spectra are shown as a reference (light gray line). Reprinted from J. Phys. Chem	n.
Lett. 2011, 2, 20, 2515-2520. Copyright 2011 American Chemical Society. ²⁰²	22
1.20 SFG spectra of ODA monolayers ($\Pi = 15 \text{ mN/m}$) spread on (a) D_2O subphases and (b)	
H ₂ O subphases at 20 °C. Each subphase contained 10 mM of a given salt as indicated it	n
the legend. All spectra were recorded with the ssp (s - signal, s - visible, p - infrared	d)
polarization combination. All the spectra in panel (a) are normalized to the signal from	a
piece of z-cut crystalline quartz. (c) Model representation of ODA monolayers spread of	n
aqueous subphases, where the disruption of alkyl chain ordering is ascribed to the	ie
relative propensity of anions to penetrate into the hydrophobic region of the monolaye	r.
Reprinted from J. Am. Chem. Soc. 2004, 126, 34, 10522-10523. Copyright 200	14
American Chemical Society. ⁶⁷	23
1.21 (a) Model representation of SFG studies on Poly-(N-isopropylacrylamide) adsorbed	at
the air/water interface. (b) SFG spectra show specific anion effects on PNIPAN	М
adsorbed at the air/water interface. Each subphase contained 1 M of a given salt a	ns
indicated in the legend except for NaF and Na ₂ SO ₄ , which are measured with saturate	d
solutions (\sim 0.8 M for both salts). (c) The same experiments repeated with D ₂ O. The	ne
spectra are offset for clarity. It was found that the relative propensity of ions to orien	nt
interfacial water molecules follows the Hofmeister series. Reprinted from J. Am. Chen	n.
Soc. 2007, 129, 40, 12272-12279. Copyright 2007 American Chemical Society. ⁶⁸	24
1.22 Schematic model of the CTA ⁺ /F ⁻ and CTA ⁺ /I ⁻ interfaces. Yellow line represents the	
hydrogen bond. Gray hydrogen inside the dashed circles is less $\chi^{(2)}$ active. Reprinte	ed
from J. Am. Chem. Soc. 2014, 136, 17, 6155-6158. Copyright 2014 American Chemica	al
Society. ²⁰⁵	24
1.23 Model Representation of ion-induced protonation of primary amine headgroups	
ODA/water interface. Reprinted from J. Phys. Chem. Lett. 2017, 8, 15, 3601-3600	6.
Copyright 2017 American Chemical Society. ²⁰⁶	25

1.24	OH stretching region of (a) NaNO ₃ solutions and (b) NaSCN solutions in contact with	
	DPTAP ⁺ monolayers in a SSP polarization combination. In part a, the SFG intensity	
	decreases uniformly with concentration, while in part b, the SCN ions apparently lead to	
	more substantive changes at the air/aqueous interface. Reprinted from J. Phys. Chem.	
	C 2020, 124, 1, 573-581. Copyright 2020 American Chemical Society. ²⁰⁷	26
1.25	Schematic model of Vibrational sum frequency generation spectroscopy of guanidinium	
	receptor anchored at the water-air interface. Study reveals that the guanidinium	
	receptor binds to an oxoanion series in the order $SO_4^{2-} > H_2PO_4^{-} > NO_3^{-} > NO_2^{-}$.	
	Reprinted from J. Phys. Chem. A 2020, 124, 49, 10171-10180. Copyright 2020	
	American Chemical Society. ⁴²	26
2.1	In-house developed experimental set up of time resolved Newton ring's interferometry	
	for the evaporation rate studies of sessile aqueous droplets.	31
2.2	(a) Schematic of time-resolved Newton's ring interferometry for the evaporation rate	
	studies of sessile aqueous droplets. (b) The snapshots with the variable intensity of the	
	central fringe of the dynamic Newton's ring pattern with the time sequence of one fringe	
	collapse (marked as A, B, and C, respectively). ⁶⁵	32
2.3	Schematic illustration of laser actuation scheme (a) side-view of a microcapillary filled	
	with a liquid showcasing air/liquid interface. (b) Laser pulse is focused inside the liquid	
	medium at a certain distance from the air/liquid interface. (c) Absorption of laser pulse	
	generates a bubble inside the microcapillary which further deforms the air/liquid	
	interface to produce a liquid microjet owing to the flow focusing effect. (d), (e) and (f)	
	correspond to the capillary snapshots during the liquid jet formation. The snapshots are	
	recorded at 10k fps. The diameter of the liquid jet is $\sim 40 \mu m$.	34
2.4	(a) Jet evolution when a laser pulse of energy 400 µJ is focused inside the liquid filled in	31
	a microcapillary of diameter ~ 400 μm. The capillary snapshots are recorded at 50k fps.	
	(b) Velocity of jet tip as a function of time showing a non-monotonic trend.	35
2.5	(a) Schematic optical layout of the experimental set up for the laser induced liquid	33
	microjets. (b) Side view of the glass capillary tube with control parameters of microjet	
	formation.	38
2.6	In-house developed experimental set up for the generation of liquid microjets using ps-	30
	pulsed lasers.	20
2.7	Camera snapshots for inner and outer diameter of the microcapillary utilized in the	39
	generation of laser induced liquid microjets.	40
2.8	Schematic representation of SFG in co-propagating geometry at the air/water interface.	40
	The vertical dotted line corresponds to the surface normal. Here xyz is the lab coordinate	
	system, where xz is the plane of incidence with y-axis perpendicular to it.	41
2.9	Energy level scheme for SFG. $ g\rangle$ is a ground state, $ v\rangle$ is the vibrational excited state	41
	and s\) is any other state. For SFG, the resonance is both IR and Raman active.	
2.10	Representation of Euler's angles (tilt θ , twist ψ and azimuthal φ) between lab	43
2.10	coordinates (xyz) and molecular coordinates (abc).	
2.11	(a) Representation of orientation angle θ formed by free OH oscillator with respect to	45
2.11	(a) Representation of orientation angle o formed by free Ori oscillator with respect to	46

	the surface normal. (b) Theoretical orientation curve plotted by using delta function,	
	showing variation of $\left \chi_{\rm ssp}^{(2),\rm eff}/\chi_{\rm ppp}^{(2),\rm eff}\right $ (equation 2.63) with angle θ for free OH oscillator	
	of $C_{\infty v}$ symmetry at the air/water interface.	
2.12	(a) Representation of orientation angle θ formed by CH ₂ -group with the surface normal.	
	(b) Theoretical orientation curve plotted by using delta function, showing variation of	
	$\left \chi_{ppp}^{(2),eff}(as)/\chi_{ppp}^{(2),eff}(ss)\right $ (equation 2.73) with θ for CH ₂ -group of C _{2v} symmetry at the	
	air/aqueous interface.	49
2.13	Theoretical orientation curves plotted by using delta function, showing variation of	77
	$\left \chi_{\rm ssp}^{(2),\rm eff}/\chi_{\rm ppp}^{(2),\rm eff}\right $ (grey curve) and $\left \chi_{\rm xxz}^{(2)}/\chi_{\rm zzz}^{(2)}\right $ (red curve) with angle θ for free OH	
	oscillator of $C_{\infty v}$ symmetry at the air/water interface. The horizontal dotted line	
	corresponds to the experimental amplitude ratio for free OH oscillator in ssp and ppp-	
	SFG spectra, the projection of which on the x-axis estimates the orientation angle	
	values.	50
2.14	(a) Schematic diagram of SFG set up with its essential components. M1-M7, Mirrors;	
	HWP1-HWP3, Half wave plates; L1-L4, Lenses; F1, Filter. (b) Lab SFG experimental	
	setup represents its constituent units namely, Nd:YAG Laser, SHG unit, OPA/DFG unit	
	and SFG spectrometer. (c) Inside of SFG spectrometer showing the optical layout where	
	two input pump laser beams (visible and tunable infrared) overlap at the sample surface	
	to generate sum frequency beam. (d) Molecular structure of a polymer,	
	polyvinylpyrrolidone (PVP) when present at the air/aqueous interface, the resultant SFG	
	spectrum is shown in the computer screen.	51
2.15	SFG spectra at air/aqueous interface carrying (a) Ethanol and (b) SDS, recorded in ssp-	31
	polarization scheme. The spectra are recorded with the motivation of optimization of the	
	SFG system alignment before conducting actual experimental series with the desired	
	samples.	52
2.16	(a) Schematic of Wilhelmy Plate method for the evaluation of surface tension of liquid	32
	samples and (b) Lab experimental set up of Langmuir Blodgett equipped with Wilhelmy	
	plate to perform surface tension studies of aqueous sample carried in the Teflon sample	
	cell.	53
2.17	Schematic ray diagram depicting the reflection, transmission and absorption of light	JJ
	beam incident on a sample cell carrying an aqueous solution.	54
3.1	(a) Change in droplet central thickness (Δd) vs. time for sessile aqueous droplets of	J 1
	pristine water and 1M sodium salt solutions. The slopes of these experimental plots	
	provide evaporation rates at the air/aqueous interface (panel (b)). 65	58
3.2	Surface tension values of 1M sodium salt solutions. ⁶⁵	59
3.3	(a) Sketch of SFG vibrational spectroscopic experiments on air/aqueous interface. (b)	JJ
	SFG spectrum collected from pristine air/water interface in ssp polarization scheme;	
	water species contributing into the shaded region of the spectrum are presented in panel	
	(a). Polarization scheme ssp designates s-SFG, s-visible, and p-polarization of IR beams.	
	Panel (c) and (d) SFG spectra at air/aqueous interface in the presence of 1M Hofmeister	60
		00

	series sodium salts. The curves are Lorentzian fitted profiles; the fitting parameters are	
	provided in table A1. Panel (e) and (f) represent the variation in relative oscillator	
	strength (amplitude ratio of SFG peaks at 3445 cm ⁻¹ and 3230 cm ⁻¹) and the integrated	
	area under the free OH peak (3660 cm ⁻¹ to 3750 cm ⁻¹) as a function of ions at the	
	air/aqueous interface. 65	
3.4	(a)-(g) SFG intensity spectra for free OH oscillator at air/aqueous interface in the	
	presence of various 1M Hofmeister series sodium salts in ssp and ppp-polarization	
	schemes. The points show experimental data, and the solid lines are the Lorentzian fit	
	curves. Fitting parameters are given in table A2 of Appendix A. The horizontal dotted	
	line reflects the apparent ion-specific variation in ppp-spectral intensity of free OH peak	
	compared to pristine air/water interface (a). ⁶⁵	61
3.5	(a) Representation of orientation angle (tilt angle) θ formed by free OH oscillator with	
	respect to surface normal at the air/water interface. (b) Theoretical orientation curve	
	showing variation of $ \chi_{ssp}^{(2),eff}/\chi_{ppp}^{(2),eff} $ with angle θ of free OH oscillator of surface water	
	molecules with $C_{\scriptscriptstyle \infty \scriptscriptstyle V}$ symmetry; The horizontal solid lines are the experimental ratio of	
	free OH amplitudes evaluated from the Lorenzian fitted ssp, ppp spectra recorded at	
	air/salt-water interface (figure 3.4). The intersection points of horizontal lines with the	
	theoretical curve (black solid line) facilitates the values of free OH tilt angle with respect	
	to the surface normal in presence of variety of ions, values given in table A3.65	62
3.6	(a) Ion-specific variation in tilt angle values of free OH oscillator (left axis) in inverse	02
	correlation with the evaporation rates (right axis) studied at the air/aqueous interface. (b)	
	Evaporation rates of the sessile droplets obtained from interferometry experiment	
	(Figure 3.1b) plotted as a function of relative OH oscillator strength observed from SFG	
	spectra (Figure 3.3c-d). ⁶⁵	63
3.7	Variation in free energy of water molecule as a function of number of H-bonds it makes	03
	with the surrounding water molecules. The data has been extracted from Musolino et al. ⁸	64
3.8	Ion-specific H-bonding environment and orientation of free OH oscillator control the	04
	water evaporation at the air/water interface. ⁶⁵	65
4.1	Molecular structure of Rh6G.	68
4.2	(a) UV-Visible absorbance spectra of water (reference) and Rh6G dye (0.1mM)	- 55
	solution. (b) The observed jet velocity (v_j) and jet power (P_j) for both the aqueous	
	samples of neat water and Rh6G (0.1 mM) with various input excitation energies of the	
	laser pulse at 532 nm.	69
4.3	(a) Concentration dependent UV-Visible absorbance spectra of Rh6G dye solution. (b)	
	Variation in jet speed as a linear function of laser pulse energy, as studied for different	
	concentration of Rh6G. An increment in jet velocity with increase in Rh6G	
	concentration is yellow highlighted for laser pulse energy of 400 µJ.	70
4.4	Snapshots of laser-induced liquid microjets for the pristine Rh6G dye solution (0.1 mM)	70
	and in the presence of 50 mM sodium salts; Na ₂ SO ₄ , NaI, and NaSCN. Ion-specific	
	variation in Jet length is recorded for three different pulse energies of 200 µJ, 300 µJ,	71
L		71

	and 400 μJ . The camera snapshots of liquid microjets are captured at 100 μs after the	
	laser pulse of known energy is made to impinge on the capillary.	
4.5	(a) UV-visible absorbance spectra of Rh6G dye solution (0.1 mM) in the presence of 50	
	mM sodium salts: Na ₂ SO ₄ , NaI, and NaSCN. (b) Schematic illustration of the proposed	
	interactions between Hofmeister anions and Rh6G in aqueous solution governing the	
	ion-specific optical absorbance (figure 4.5a).	72
4.6	Ion-specific variation of (a) jet velocity and (b) jet power as a function of absorbance,	
	studied for different pulse energies of 532 nm at 200 μ J, 300 μ J, and 400 μ J. The data	
	points for the calculation of velocity and power are taken from ion-specific jet lengths	
	(figure 4.4). The ion-specific absorbance values at λ_{exc} 532 nm are extracted from UV-	
	Visible spectra of Rh6G (0.1 mM) in presence of Hofmeister sodium salts (figure 4.5a).	72
4.7	(a) Snapshots of laser induced liquid microjets in Rh6G dye solution (0.1 mM) and that	12
	in presence of NaSCN (1.0 mM, 2.5 mM, 5.0 mM). Concentration dependent variation	
	in Jet length is recorded for three different pulse energies of 200 μJ , 300 μJ , and 400 μJ .	
	The jet snapshots are captured from an ultrafast camera at 100 µs after a laser pulse of	
	known energy is made to impinge on the capillary. (b) UV-visible absorbance spectra of	
	Rh6G dye solution (0.1 mM) and that in presence of NaSCN (1.0 mM, 2.5 mM, 5.0	
	mM), showing concentration (NaSCN) dependent variation in optical absorbance of	
	Rh6G. (c) Jet velocity is a linear function of concentration of NaSCN in the solution,	
	which is verified for three different pulse energies (200 μJ, 300 μJ, and 400 μJ).	73
4.8	Ion-specific penetration depths of liquid jets of Rh6G (0.1 mM) solution for the model	/3
	soft tissue materials. The data points are simulated by cube root dependence of	
	penetration depth on jet power, i.e., $\sqrt[3]{P_J}$. The values of jet powers for different salt	
	solutions have been evaluated from the measured jet lengths and jet velocity in Rh6G for	
	the laser pulse energy of 400 µJ (figure 3c).	74
4.9	Ion-specific interactions with Rh6G govern the characteristics of laser induced liquid	/4
	microjets at the air/Rh6G dye solution interface.	75
5.1	(a) Molecular structure of PVP polymer. (b) Schematic illustration of air/PVP-water	13
	interface probed by SFG spectroscopy with the scope to perform polarization-dependent	
	studies such as in ssp and ppp, polarization configuration. Here, the three letters indicate	
	the states of polarization of the fields in the sequence of SFG, visible and infrared	
	beams, respectively. The letters "s" and "p" stand for the beam polarization	
	perpendicular and parallel to the plane of incidence. SFG spectra at the air/PVP-water	
	interface in the CH-stretch region (panel c in ssp and d in ppp) and OH-stretch region	
	(panel e in ssp and f in ppp). The scattered points in the plots (panel c-f) represent	
	experimental data, while the solid line is the Lorentzian fit to the spectra. The details of	
	fitting parameters are given in tables B1 and B2 of Appendix B.	79
5.2	(a) ssp- SFG spectra at air/PVP-water interface with 1M sodium salts in the aqueous	
	subphase, showing anion-specific variation in the OH-region intensity. (b) Anion-	
	specific variation in 3440 cm ⁻¹ OH-oscillator's strength shows a monotonic increment	80

	and follows the Hofmeister series. The data points are Lorentzian fit amplitudes at 3440	
	cm ⁻¹ peak of SFG spectra as provided in panel (a). See table B3 of Appendix B for	
	fitting parameters.	
5.3	ssp-SFG spectra in CH-stretch region at (a) air/PVP-water interface and (b) air/PVP-	
	D ₂ O interface in the presence of 1 M sodium salts (Na ₂ SO ₄ , NaCl, NaNO ₃ , NaBr,	
	NaClO ₄ , and NaSCN). All the spectra are normalized with respect to the max intense t-	
	CH peak (2862 cm ⁻¹). The details of fitting parameters are given in tables B4 and B5 of	
	Appendix B.	81
5.4	(a) ppp-SFG spectra in the CH-stretch region at air/PVP-D ₂ O interface in the presence	
	of various sodium salts at 1 M concentration. All the SFG spectra are normalized with	
	respect to the max intense CH ₂ (ss) peak (2924 cm ⁻¹). The scattered points represent	
	experimental data, while the solid line is the Lorentzian fit to the spectra. The details of	
	fitting parameters are given in table B6 of Appendix B. (b) Representation of orientation	
	angle θ formed by $\text{CH}_2\text{-group}$ with the surface normal. (c) Theoretical orientation curve	
	plotted by using delta function, showing variation of $ \chi_{ppp}^{(2),eff}(as)/\chi_{ppp}^{(2),eff}(ss) $ (equation	
	5.3) with θ for CH_2 -group of $C_{2\nu}$ symmetry at the air/PVP-D ₂ O interface. The horizontal	
	dashed lines are the experimental values of $ \chi_{ppp}^{(2),eff}(as)/\chi_{ppp}^{(2),eff}(ss) $ and the respective	
	projection on x-axis gives the tilt angle values. The observed trend in the tilt angle	
	values as a function of anions is shown in (panel d), which follows the Hofmeister	
	series. Lower CH2-tilt angle values indicate towards the onset of disorderness in the	
	vinyl chain of PVP in presence of weakly hydrated anions (ClO ₄ -, and SCN-).	82
5.5	(a) ppp-SFG spectra in OH-stretch region at air/PVP-water interface in presence of 1 M	-
	Na ₂ SO ₄ , NaCl, NaNO ₃ , NaBr, NaClO ₄ , and NaSCN. The scattered points represent	
	experimental data, while the solid line is the Lorentzian fit to the spectra. The details of	
	fitting parameters are given in table B8 of Appendix B. (b) Illustration of intermolecular	
	interactions of PVP with surrounding water molecules. H-bonding interaction (yellow	
	line) between C=O group of PVP and water, vibrational signature appear at 3540 cm ⁻¹ ;	
	Weak interactions between hydrophobic methylene moieties of PVP and water (red	
	dotted line) appear at 3580 cm ⁻¹ .	
5.6	ppp-SFG spectra in OH-stretch region at air/water interface in presence of 1 M NaClO ₄ ,	84
	and NaSCN. The scattered points represent experimental data, while the solid line is the	
	Lorentzian fit to the spectra. The details of fitting parameters are given in table B9 of	
	Appendix B.	0.5
5.7	Ion-specific water-macromolecule interactions cooperatively participate with the ion-	85
	water and ion-macromolecule interactions to govern the order/disorder in the	
	macromolecule structure at the air/aqueous interface.	96
	-	86

LIST OF TABLES

2.1 Calculated L-factors characteristic of free OH (3704 cm ⁻¹ , 2.7 μm) at the air/water interface. 2.2 Calculated L-factors characteristic of vinyl methylene symmetric stretch (2923 cm ⁻¹ , 3.4 μm) and asymmetric stretch modes at (2986 cm ⁻¹ , 3.3 μm) at the air/PVP-D ₂ O interface. 3.1 Binding Energy values for aqueous ionic clusters. ^{15±155} A1 Fitting parameters of SFG spectra at air/aqueous interface carrying IM salt solutions as recorded in OH-stretch region (3000 cm ⁻¹ -3800 cm ⁻¹) in ssp-polarization scheme (figure 3.3 b-d). A2 Fitting parameters of SFG spectra at air/aqueous interface carrying IM sodium salt solutions as recorded in Free OH-region (3660-3750) cm ⁻¹ in ssp-and ppp-polarization scheme (figure 3.4). A3 Free OH peak (3704 cm ⁻¹) ratio, χ _{ssp} ⁽²⁾ /χ _{ppp} ^(f) /χ _{ppp} ⁽²⁾ as estimated from fitted A _v /Γ _v , table A2 for ssp and ppp SFG spectra for IM sodium salt solutions at the air/aqueous interface (figure 3.4) and the resultant ion-specific orientation angle (θ). B1 Fitting parameters of CH-region SFG spectra at the air/PVP-water interface as probed in ssp and ppp-polarization schemes (figure 5.1 c and d). B2 Fitting parameters of OH-region SFG spectra at the air/PVP-water interface in presence of series of IM sodium salts (figure 5.2a). B3 Fitting parameters of OH-region ssp-SFG spectra at the air/PVP-water interface in presence of series of IM sodium salts (figure 5.3a). B4 Fitting parameters of CH-region sp-SFG spectra at the air/PVP-D ₂ O interface in the presence of series of IM sodium salts (figure 5.3b). B5 Fitting parameters of CH-region ppp-SFG spectra at the air/PVP-D ₂ O interface in the presence of series of IM sodium salts (figure 5.4a). B7 Variation in orientation angle of vinyl chain CH ₂ groups at the air/PVP-D ₂ O interface in the presence of series of IM sodium salts (figure 5.4a and d) χ _{ppp} ⁽²⁾ (2) (2) (2) (2) (2) (2) (2) (2) (2) (2)	S. No.	Table Caption	Page No.
2.2 Calculated L-factors characteristic of vinyl methylene symmetric stretch (2923 cm ⁻¹ , 3.4 μm) and asymmetric stretch modes at (2986 cm ⁻¹ , 3.3 μm) at the air/PVP-D ₂ O interface. 3.1 Binding Energy values for aqueous ionic clusters. 48 Fitting parameters of SFG spectra at air/aqueous interface carrying 1M salt solutions as recorded in OH-stretch region (3000 cm ⁻¹ -3800 cm ⁻¹) in ssp-polarization scheme (figure 3.3 b-d). A2 Fitting parameters of SFG spectra at air/aqueous interface carrying 1M sodium salt solutions as recorded in Free OH-region (3660-3750) cm ⁻¹ in ssp-and ppp-polarization scheme (figure 3.4). A3 Free OH peak (3704 cm ⁻¹) ratio, \(\chi_{\chi_{\text{SpP}}}^{(2)\text{,eff}} \(\chi_{\text{ppp}}^{(2)\text{,eff}} \) as estimated from fitted \(\lambda_{\text{v}}/\Gamma_{\text{v}}\) [11: \(\text{data})\text{,eff} \) [12: \(\text{data})\text{,eff} \) [13: \(\text{asy}\) and the resultant ion-specific orientation angle (0). B1 Fitting parameters of CH-region SFG spectra at the air/PVP-water interface as probed in ssp and ppp-polarization schemes (figure 5.1 c and d). B2 Fitting parameters of OH-region SFG spectra at the air/PVP-H ₂ O interface in presence of series of 1M sodium salts (figure 5.2a). B3 Fitting parameters of CH-region ssp-SFG spectra at the air/PVP-water interface in presence of series of 1M sodium salts (figure 5.3a). B4 Fitting parameters of CH-region ssp-SFG spectra at the air/PVP-D ₂ O interface in presence of series of 1M sodium salts (figure 5.3a). B5 Fitting parameters of CH-region ppp-SFG spectra at the air/PVP-D ₂ O interface in the presence of series of 1M sodium salts (figure 5.4c and d) \(\text{\chi_{\text{v}}}\) \(\text	2.1	Calculated L-factors characteristic of free OH (3704 cm ⁻¹ , 2.7 μm) at the air/water	
3.4 µm) and asymmetric stretch modes at (2986 cm ⁻¹ , 3.3 µm) at the air/PVP-D ₂ O interface. 3.1 Binding Energy values for aqueous ionic clusters. ¹⁵⁴⁻¹³⁵ 64 A1 Fitting parameters of SFG spectra at air/aqueous interface carrying 1M salt solutions as recorded in OH-stretch region (3000 cm ⁻¹ -3800 cm ⁻¹) in ssp-polarization scheme (figure 3.3 b-d). A2 Fitting parameters of SFG spectra at air/aqueous interface carrying 1M sodium salt solutions as recorded in Free OH-region (3660-3750) cm ⁻¹ in ssp-and ppp-polarization scheme (figure 3.4). A3 Free OH peak (3704 cm ⁻¹) ratio, \(\chi_{\text{33p}}^{\text{23peff}}/\chi_{\text{2ppff}}\) as estimated from fitted \(\lambda_{\text{v}}/\text{V}_{\text{v}}\), table A2 for ssp and ppp SFG spectra for 1M sodium salt solutions at the air/aqueous interface (figure 3.4) and the resultant ion-specific orientation angle (0). B1 Fitting parameters of CH-region SFG spectra at the air/PVP-water interface as probed in ssp and ppp-polarization schemes (figure 5.1 c and d). B2 Fitting parameters of OH-region SFG spectra at the air/PVP-H ₂ O interface in presence of series of 1M sodium salts (figure 5.2a). B3 Fitting parameters of CH-region ssp-SFG spectra at the air/PVP-D ₂ O interface in presence of series of 1M sodium salts (figure 5.3a). B4 Fitting parameters of CH-region ssp-SFG spectra at the air/PVP-D ₂ O interface in the presence of series of 1M sodium salts (figure 5.3b). B5 Fitting parameters of CH-region ppp-SFG spectra at the air/PVP-D ₂ O interface in the presence of series of 1M sodium salts (figure 5.4a). B7 Variation in orientation angle of vinyl chain CH ₂ groups at the air/PVP-D ₂ O interface in the presence of series of 1M sodium salts (figure 5.4c and d) \(\frac{\chi_{\text{22}\text{eff}}{\text{(as)}}/\chi_{\text{22}\text{ppp}}(\text{(ss)}) is estimated by \(\lambda_{\text{v}}\) and solium salts (figure 5.4c and d) \(\frac{\chi_{\text{22}\text{eff}}{\text{(as)}}/\chi_{\text{22}\text{ppp}}(\text{(ss)}) is estimated by \(\lambda_{\text{v}}\)		interface.	46
interface. 3.1 Binding Energy values for aqueous ionic clusters, 154-155 A1 Fitting parameters of SFG spectra at air/aqueous interface carrying 1M salt solutions as recorded in OH-stretch region (3000 cm ⁻¹ -3800 cm ⁻¹) in ssp-polarization scheme (figure 3.3 b-d). A2 Fitting parameters of SFG spectra at air/aqueous interface carrying 1M sodium salt solutions as recorded in Free OH-region (3660-3750) cm ⁻¹ in ssp-and ppp-polarization scheme (figure 3.4). A3 Free OH peak (3704 cm ⁻¹) ratio, \(\frac{\chi_{23pff}}{\chi_{2pff}}\rho_{ppp}\rhoff \) as estimated from fitted \(\frac{I_{v}}{V_{v}}\right \), table A2 for ssp and ppp SFG spectra for 1M sodium salt solutions at the air/aqueous interface (figure 3.4) and the resultant ion-specific orientation angle (0). B1 Fitting parameters of CH-region SFG spectra at the air/PVP-water interface as probed in ssp and ppp-polarization schemes (figure 5.1 c and d). B2 Fitting parameters of OH-region SFG spectra at the air/PVP-H ₂ O interface in presence of series of 1M sodium salts (figure 5.2a). B3 Fitting parameters of CH-region ssp-SFG spectra at the air/PVP-water interface in presence of series of 1M sodium salts (figure 5.3a). B4 Fitting parameters of CH-region ssp-SFG spectra at the air/PVP-D ₂ O interface in the presence of series of 1M sodium salts (figure 5.3a). B5 Fitting parameters of CH-region spp-SFG spectra at the air/PVP-D ₂ O interface in the presence of series of 1M sodium salts (figure 5.4a). B7 Variation in orientation angle of vinyl chain CH ₂ groups at the air/PVP-D ₂ O interface in the presence of series of 1M sodium salts (figure 5.4c and d) \(\frac{\chi_{20}(\chi	2.2	Calculated L-factors characteristic of vinyl methylene symmetric stretch (2923 cm ⁻¹ ,	
3.1 Binding Energy values for aqueous ionic clusters. NA-185 A1 Fitting parameters of SFG spectra at air/aqueous interface carrying 1M salt solutions as recorded in OH-stretch region (3000 cm ⁻¹ -3800 cm ⁻¹) in ssp-polarization scheme (figure 3.3 b-d). A2 Fitting parameters of SFG spectra at air/aqueous interface carrying 1M sodium salt solutions as recorded in Free OH-region (3660-3750) cm ⁻¹ in ssp-and ppp-polarization scheme (figure 3.4). A3 Free OH peak (3704 cm ⁻¹) ratio, \(\frac{\chi_{ssp}^{(2)}}{\chi_{ssp}^{(2)}}\) \(\frac{\chi_{ssp}^{(2)}}{\chi_{ppp}^{(2)}}\) as estimated from fitted \(\frac{A_v}{V_v}\) \(\frac{A_v}{V_v}\) \(\text{,table A2 for ssp and ppp SFG spectra for 1M sodium salt solutions at the air/aqueous interface (figure 3.4) and the resultant ion-specific orientation angle (θ). B1 Fitting parameters of CH-region SFG spectra at the air/PVP-water interface as probed in ssp and ppp-polarization schemes (figure 5.1 c and d). B2 Fitting parameters of OH-region SFG spectra at the air/PVP-H ₂ O interface in presence of series of 1M sodium salts (figure 5.2a). B3 Fitting parameters of CH-region ssp-SFG spectra at the air/PVP-D ₂ O interface in presence of series of 1M sodium salts (figure 5.3a). B4 Fitting parameters of CH-region ssp-SFG spectra at the air/PVP-D ₂ O interface in the presence of series of 1M sodium salts (figure 5.3b). B5 Fitting parameters of CH-region ppp-SFG spectra at the air/PVP-D ₂ O interface in the presence of series of 1M sodium salts (figure 5.4a). B7 Variation in orientation angle of vinyl chain CH ₂ groups at the air/PVP-D ₂ O interface in the presence of series of 1M sodium salts (figure 5.4c and d) \(\frac{\chi_{2}(2),eff}{\chi_{ppp}}(as)/\(\chi_{ppp}(ss)) \) \(\frac{\chi_{2}(2),eff}{\chi_{2}(ps)}(ss) \) is estimated by A _v values provided in table B6. B8 Fitting parameters of OH-region ppp-SFG spectra at the air/PVP-water interface in the presence of series of 1M sodium salts (figure 5.5). B9 Fitting parameters of OH-region ppp-SFG spectra		3.4 μm) and asymmetric stretch modes at (2986 cm ⁻¹ , 3.3 μm) at the air/PVP-D ₂ O	
A1 Fitting parameters of SFG spectra at air/aqueous interface carrying 1M salt solutions as recorded in OH-stretch region (3000 cm ⁻¹ -3800 cm ⁻¹) in ssp-polarization scheme (figure 3.3 b-d). A2 Fitting parameters of SFG spectra at air/aqueous interface carrying 1M sodium salt solutions as recorded in Free OH-region (3660-3750) cm ⁻¹ in ssp-and ppp-polarization scheme (figure 3.4). A3 Free OH peak (3704 cm ⁻¹) ratio, \(\frac{\chi_{esp}}{\chi_{sp}}\frac{\chi_{opp}}{\chi_{ppp}}\right \) as estimated from fitted \(\frac{I}{\chi_{v}}\Gamma_{v}\right \) table A2 for ssp and ppp SFG spectra for 1M sodium salt solutions at the air/aqueous interface (figure 3.4) and the resultant ion-specific orientation angle (θ). B1 Fitting parameters of CH-region SFG spectra at the air/PVP-water interface as probed in ssp and ppp-polarization schemes (figure 5.1 c and d). B2 Fitting parameters of OH-region SFG spectra at the air/PVP-H ₂ O interface in presence of series of 1M sodium salts (figure 5.2a). B3 Fitting parameters of CH-region ssp-SFG spectra at the air/PVP-water interface in presence of series of 1M sodium salts (figure 5.3a). B4 Fitting parameters of CH-region ssp-SFG spectra at the air/PVP-D ₂ O interface in the presence of series of 1M sodium salts (figure 5.3a). B5 Fitting parameters of CH-region ppp-SFG spectra at the air/PVP-D ₂ O interface in the presence of series of 1M sodium salts (figure 5.4a). B6 Fitting parameters of CH-region ppp-SFG spectra at the air/PVP-D ₂ O interface in the presence of series of 1M sodium salts (figure 5.4c and d) \(\frac{\chi_{opp}(\chi_{opp}(as))}{\chi_{opp}(\chi_{opp}(as))}\) \(\frac{\chi_{opp}(\chi_{opp}(as))}{\chi_{opp}(\chi_{opp}(as))}\) is estimated by \(\hat{A}_v\) values provided in table B6. B7 Fitting parameters of OH-region ppp-SFG spectra at the air/PVP-water interface in the presence of series of 1M sodium salts (figure 5.5c).		interface.	48
A1 Fitting parameters of SFG spectra at air/aqueous interface carrying 1M salt solutions as recorded in OH-stretch region (3000 cm ⁻¹ -3800 cm ⁻¹) in ssp-polarization scheme (figure 3.3 b-d). A2 Fitting parameters of SFG spectra at air/aqueous interface carrying 1M sodium salt solutions as recorded in Free OH-region (3660-3750) cm ⁻¹ in ssp-and ppp-polarization scheme (figure 3.4). A3 Free OH peak (3704 cm ⁻¹) ratio, \(\frac{\chi_{csp}}{\chi_{ssp}} \frac{\chi_{csp}}{\chi_{ppp}} \frac{\chi_{csp}}{\chi_{ppp}} \frac{\chi_{csp}}{\chi_{ppp}} \frac{\chi_{csp}}{\chi_{ppp}} \frac{\chi_{csp}}{\chi_{csp}} \frac{\chi_{csp}}{\chi_{ppp}} \frac{\chi_{csp}}{\chi_{csp}} \frac{\chi_{csp}}{\chi_{ppp}} \frac{\chi_{csp}}{\chi_{csp}} \frac{\chi_{csp}}{\chi_{c	3.1	Binding Energy values for aqueous ionic clusters. 154-155	64
3.3 b-d). A2 Fitting parameters of SFG spectra at air/aqueous interface carrying 1M sodium salt solutions as recorded in Free OH-region (3660-3750) cm ⁻¹ in ssp-and ppp-polarization scheme (figure 3.4). A3 Free OH peak (3704 cm ⁻¹) ratio, \(\frac{\chi_{ssp}^{(2),eff}}{\chi_{ssp}^{(2),eff}}\) \(\chi_{psp}^{(2),eff}\) as estimated from fitted \(\lambda_{V}/\Gamma_{V}\) , table A2 for ssp and ppp SFG spectra for 1M sodium salt solutions at the air/aqueous interface (figure 3.4) and the resultant ion-specific orientation angle (0). B1 Fitting parameters of CH-region SFG spectra at the air/PVP-water interface as probed in ssp and ppp-polarization schemes (figure 5.1 c and d). B2 Fitting parameters of OH-region SFG spectra at the air/water and air/PVP-water interface as probed in ssp and ppp-polarization schemes (figure 5.1 e and f). B3 Fitting parameters of OH-region ssp-SFG spectra at the air/PVP-H ₂ O interface in presence of series of 1M sodium salts (figure 5.3a). B4 Fitting parameters of CH-region ssp-SFG spectra at the air/PVP-water interface in presence of series of 1M sodium salts (figure 5.3b). B5 Fitting parameters of CH-region ppp-SFG spectra at the air/PVP-D ₂ O interface in the presence of series of 1M sodium salts (figure 5.4a). B6 Fitting parameters of CH-region ppp-SFG spectra at the air/PVP-D ₂ O interface in the presence of series of 1M sodium salts (figure 5.4c and d) \(\frac{\chi_{csp}}{\chi_{ppp}}\)(\frac{\chi_{csp}}{\chi_{ppp}}\)(\frac{\chi_{csp}}{\chi_{ppp}}\)(\frac{\chi_{csp}}{\chi_{ppp}}\)(\frac{\chi_{csp}}{\chi_{ppp}}\)(\frac{\chi_{csp}}{\chi_{ppp}}\)(\frac{\chi_{csp}}{\chi_{ppp}}\)(\frac{\chi_{csp}}{\chi_{psp}}\)(\frac{\chi_{csp}}{\chi_{psp}}\)(\frac{\chi_{csp}}{\chi_{psp}}\)(\frac{\chi_{csp}}{\chi_{psp}}\)(\frac{\chi_{csp}}{\chi_{psp}}\)(\frac{\chi_{csp}}{\chi_{psp}}\)(\frac{\chi_{csp}}{\chi_{psp}}\)(\frac{\chi_{csp}}{\chi_{psp}}\)(\frac{\chi_{csp}}{\chi_{psp}}\)(\frac{\chi_{csp}}{\chi_{csp}}\)(\frac{\chi_{csp}}{\chi_{csp}}\)(\frac{\chi_{csp}}{\chi_{csp}}\)(\frac{\chi_{csp}}{	A1	Fitting parameters of SFG spectra at air/aqueous interface carrying 1M salt solutions as	
A2 Fitting parameters of SFG spectra at air/aqueous interface carrying 1M sodium salt solutions as recorded in Free OH-region (3660-3750) cm ⁻¹ in ssp-and ppp-polarization scheme (figure 3.4). A3 Free OH peak (3704 cm ⁻¹) ratio, χ _{csp} ^{(2),eff} /χ _{ppp} ^{(2),eff} as estimated from fitted A _v /Γ _v , table A2 for ssp and ppp SFG spectra for 1M sodium salt solutions at the air/aqueous interface (figure 3.4) and the resultant ion-specific orientation angle (θ). B1 Fitting parameters of CH-region SFG spectra at the air/PVP-water interface as probed in ssp and ppp-polarization schemes (figure 5.1 c and d). B2 Fitting parameters of OH-region SFG spectra at the air/water and air/PVP-water interface as probed in ssp and ppp-polarization schemes (figure 5.1 e and f). B3 Fitting parameters of OH-region ssp-SFG spectra at the air/PVP-H ₂ O interface in presence of series of 1M sodium salts (figure 5.2a). B4 Fitting parameters of CH-region ssp-SFG spectra at the air/PVP-water interface in presence of series of 1M sodium salts (figure 5.3a). B5 Fitting parameters of CH-region ppp-SFG spectra at the air/PVP-D ₂ O interface in the presence of series of 1M sodium salts (figure 5.4a). B6 Fitting parameters of CH-region ppp-SFG spectra at the air/PVP-D ₂ O interface in the presence of series of 1M sodium salts (figure 5.4c and d) χ _{ppp} ^{(2),eff} (as)/χ _{ppp} ^{(2),eff} (ss) is estimated by A _V values provided in table B6. B7 Fitting parameters of OH-region ppp-SFG spectra at the air/PVP-water interface in the presence of series of 1M sodium salts (figure 5.5). B9 Fitting parameters of OH-region ppp-SFG spectra at the air/PVP-water interface in the presence of series of 1M sodium salts (figure 5.5).		recorded in OH-stretch region (3000 cm ⁻¹ -3800 cm ⁻¹) in ssp-polarization scheme (figure	
A2 Fitting parameters of SFG spectra at air/aqueous interface carrying 1M sodium salt solutions as recorded in Free OH-region (3660-3750) cm ⁻¹ in ssp-and ppp-polarization scheme (figure 3.4). A3 Free OH peak (3704 cm ⁻¹) ratio, χ _{ssp} ^{(2),eff} /χ _{ssp} ^{(2),eff} as estimated from fitted A _V /Γ _V , table A2 for ssp and ppp SFG spectra for 1M sodium salt solutions at the air/aqueous interface (figure 3.4) and the resultant ion-specific orientation angle (θ). B1 Fitting parameters of CH-region SFG spectra at the air/PVP-water interface as probed in ssp and ppp-polarization schemes (figure 5.1 c and d). B2 Fitting parameters of OH-region SFG spectra at the air/water and air/PVP-water interface as probed in ssp and ppp-polarization schemes (figure 5.1 e and f). B3 Fitting parameters of OH-region ssp-SFG spectra at the air/PVP-H ₂ O interface in presence of series of 1M sodium salts (figure 5.2a). B4 Fitting parameters of CH-region ssp-SFG spectra at the air/PVP-water interface in presence of series of 1M sodium salts (figure 5.3a). B5 Fitting parameters of CH-region ppp-SFG spectra at the air/PVP-D ₂ O interface in the presence of series of 1M sodium salts (figure 5.4a). B6 Fitting parameters of CH-region ppp-SFG spectra at the air/PVP-D ₂ O interface in the presence of series of 1M sodium salts (figure 5.4c and d) χ _{ppp} ^{(2),eff} (as)/χ _{ppp} ^{(2),eff} (ss) is estimated by A _V values provided in table B6. B7 Fitting parameters of OH-region ppp-SFG spectra at the air/PVP-water interface in the presence of series of 1M sodium salts (figure 5.5). B8 Fitting parameters of OH-region ppp-SFG spectra at the air/PVP-water interface in the presence of series of 1M sodium salts (figure 5.5).		3.3 b-d).	112
scheme (figure 3.4). A3 Free OH peak (3704 cm ⁻¹) ratio, χ ^{(2),eff} / _{xssp} / _{xppp} as estimated from fitted	A2	Fitting parameters of SFG spectra at air/aqueous interface carrying 1M sodium salt	
Free OH peak (3704 cm ⁻¹) ratio, χ ^{(2),eff} / _{Ssp} / χ ^{(2),eff} / _{ppp} as estimated from fitted		solutions as recorded in Free OH-region (3660-3750) cm ⁻¹ in ssp-and ppp-polarization	
A3 Free OH peak (3704 cm²) ratio, χ _{ssp} ²/(χ _{ssp} ²/(χ _{ppp} ²) as estimated from fitted A _v /Γ _v , table A2 for ssp and ppp SFG spectra for 1M sodium salt solutions at the air/aqueous interface (figure 3.4) and the resultant ion-specific orientation angle (θ). B1 Fitting parameters of CH-region SFG spectra at the air/PVP-water interface as probed in ssp and ppp-polarization schemes (figure 5.1 c and d). B2 Fitting parameters of OH-region SFG spectra at the air/water and air/PVP-water interface as probed in ssp and ppp-polarization schemes (figure 5.1 e and f). B3 Fitting parameters of OH-region ssp-SFG spectra at the air/PVP-H ₂ O interface in presence of series of 1M sodium salts (figure 5.2a). B4 Fitting parameters of CH-region ssp-SFG spectra at the air/PVP-water interface in presence of series of 1M sodium salts (figure 5.3a). B5 Fitting parameters of CH-region ssp-SFG spectra at the air/PVP-D ₂ O interface in the presence of series of 1M sodium salts (figure 5.3b). B6 Fitting parameters of CH-region ppp-SFG spectra at the air/PVP-D ₂ O interface in the presence of series of 1M sodium salts (figure 5.4a). B7 Variation in orientation angle of vinyl chain CH ₂ groups at the air/PVP-D ₂ O interface in the presence of series of 1M sodium salts (figure 5.4c and d) χ ⁽²⁾ _{ppp} ((as)/χ ⁽²⁾ _{ppp} (f(ss)) is estimated by A _V values provided in table B6. B8 Fitting parameters of OH-region ppp-SFG spectra at the air/PVP-water interface in the presence of series of 1M sodium salts (figure 5.5). B9 Fitting parameters of OH-region ppp-SFG spectra at the air/PVP-water interface in the presence of series of 1M sodium salts (figure 5.5).		scheme (figure 3.4).	113
air/aqueous interface (figure 3.4) and the resultant ion-specific orientation angle (θ). B1 Fitting parameters of CH-region SFG spectra at the air/PVP-water interface as probed in ssp and ppp-polarization schemes (figure 5.1 c and d). B2 Fitting parameters of OH-region SFG spectra at the air/water and air/PVP-water interface as probed in ssp and ppp-polarization schemes (figure 5.1 e and f). B3 Fitting parameters of OH-region ssp-SFG spectra at the air/PVP-H ₂ O interface in presence of series of 1M sodium salts (figure 5.2a). B4 Fitting parameters of CH-region ssp-SFG spectra at the air/PVP-water interface in presence of series of 1M sodium salts (figure 5.3a). B5 Fitting parameters of CH-region ssp-SFG spectra at the air/PVP-D ₂ O interface in the presence of series of 1M sodium salts (figure 5.3b). B6 Fitting parameters of CH-region ppp-SFG spectra at the air/PVP-D ₂ O interface in the presence of series of 1M sodium salts (figure 5.4a). B7 Variation in orientation angle of vinyl chain CH ₂ groups at the air/PVP-D ₂ O interface in the presence of series of 1M sodium salts (figure 5.4c and d) \(\chi_{ppp}^{(2),eff}(as) / \(\chi_{ppp}^{(2),eff}(ss) \) is estimated by A _V values provided in table B6. B8 Fitting parameters of OH-region ppp-SFG spectra at the air/PVP-water interface in the presence of series of 1M sodium salts (figure 5.5). B9 Fitting parameters of OH-region ppp-SFG spectra at the air/water interface in the presence of series of 1M sodium salts (figure 5.5).	A3	Free OH peak (3704 cm ⁻¹) ratio, $\left \chi_{\rm ssp}^{(2),\rm eff}/\chi_{\rm ppp}^{(2),\rm eff}\right $ as estimated from fitted	
B1 Fitting parameters of CH-region SFG spectra at the air/PVP-water interface as probed in ssp and ppp-polarization schemes (figure 5.1 c and d). B2 Fitting parameters of OH-region SFG spectra at the air/water and air/PVP-water interface as probed in ssp and ppp-polarization schemes (figure 5.1 e and f). B3 Fitting parameters of OH-region ssp-SFG spectra at the air/PVP-H ₂ O interface in presence of series of 1M sodium salts (figure 5.2a). B4 Fitting parameters of CH-region ssp-SFG spectra at the air/PVP-water interface in presence of series of 1M sodium salts (figure 5.3a). B5 Fitting parameters of CH-region ssp-SFG spectra at the air/PVP-D ₂ O interface in the presence of series of 1M sodium salts (figure 5.3b). B6 Fitting parameters of CH-region ppp-SFG spectra at the air/PVP-D ₂ O interface in the presence of series of 1M sodium salts (figure 5.4a). B7 Variation in orientation angle of vinyl chain CH ₂ groups at the air/PVP-D ₂ O interface in the presence of series of 1M sodium salts (figure 5.4c and d) \(\chi_{\text{ppp}}^{(2),\text{eff}}(as)/\chi_{\text{ppp}}^{(2),\text{eff}}(ss)\) is estimated by A _V values provided in table B6. B8 Fitting parameters of OH-region ppp-SFG spectra at the air/PVP-water interface in the presence of series of 1M sodium salts (figure 5.5). B9 Fitting parameters of OH-region ppp-SFG spectra at the air/water interface in the presence of series of 1M sodium salts (figure 5.6)		$ A_v/\Gamma_v $, table A2 for ssp and ppp SFG spectra for 1M sodium salt solutions at the	
B1 Fitting parameters of CH-region SFG spectra at the air/PVP-water interface as probed in ssp and ppp-polarization schemes (figure 5.1 c and d). B2 Fitting parameters of OH-region SFG spectra at the air/water and air/PVP-water interface as probed in ssp and ppp-polarization schemes (figure 5.1 e and f). B3 Fitting parameters of OH-region ssp-SFG spectra at the air/PVP-H ₂ O interface in presence of series of 1M sodium salts (figure 5.2a). B4 Fitting parameters of CH-region ssp-SFG spectra at the air/PVP-water interface in presence of series of 1M sodium salts (figure 5.3a). B5 Fitting parameters of CH-region ssp-SFG spectra at the air/PVP-D ₂ O interface in the presence of series of 1M sodium salts (figure 5.3b). B6 Fitting parameters of CH-region ppp-SFG spectra at the air/PVP-D ₂ O interface in the presence of series of 1M sodium salts (figure 5.4a). B7 Variation in orientation angle of vinyl chain CH ₂ groups at the air/PVP-D ₂ O interface in the presence of series of 1M sodium salts (figure 5.4c and d) χ ^{(2),eff} _{ppp} (as)/χ ^{(2),eff} _{ppp} (ss) is estimated by A _V values provided in table B6. B8 Fitting parameters of OH-region ppp-SFG spectra at the air/PVP-water interface in the presence of series of 1M sodium salts (figure 5.5). B9 Fitting parameters of OH-region ppp-SFG spectra at the air/water interface in the presence of series of 1M sodium salts (figure 5.6).		air/aqueous interface (figure 3.4) and the resultant ion-specific orientation angle (θ).	114
Fitting parameters of OH-region SFG spectra at the air/water and air/PVP-water interface as probed in ssp and ppp-polarization schemes (figure 5.1 e and f). B3 Fitting parameters of OH-region ssp-SFG spectra at the air/PVP-H ₂ O interface in presence of series of 1M sodium salts (figure 5.2a). B4 Fitting parameters of CH-region ssp-SFG spectra at the air/PVP-water interface in presence of series of 1M sodium salts (figure 5.3a). B5 Fitting parameters of CH-region ssp-SFG spectra at the air/PVP-D ₂ O interface in the presence of series of 1M sodium salts (figure 5.3b). B6 Fitting parameters of CH-region ppp-SFG spectra at the air/PVP-D ₂ O interface in the presence of series of 1M sodium salts (figure 5.4a). B7 Variation in orientation angle of vinyl chain CH ₂ groups at the air/PVP-D ₂ O interface in the presence of series of 1M sodium salts (figure 5.4c and d) \(\chi_{ppp}^{(2),eff}(as) \) /\(\chi_{ppp}^{(2),eff}(ss) \) is estimated by A _V values provided in table B6. B8 Fitting parameters of OH-region ppp-SFG spectra at the air/PVP-water interface in the presence of series of 1M sodium salts (figure 5.5). B9 Fitting parameters of OH-region ppp-SFG spectra at the air/water interface in the presence of series of 1M sodium salts (figure 5.6).	B1	Fitting parameters of CH-region SFG spectra at the air/PVP-water interface as probed in	
B2 Fitting parameters of OH-region SFG spectra at the air/water and air/PVP-water interface as probed in ssp and ppp-polarization schemes (figure 5.1 e and f). B3 Fitting parameters of OH-region ssp-SFG spectra at the air/PVP-H ₂ O interface in presence of series of 1M sodium salts (figure 5.2a). B4 Fitting parameters of CH-region ssp-SFG spectra at the air/PVP-water interface in presence of series of 1M sodium salts (figure 5.3a). B5 Fitting parameters of CH-region ssp-SFG spectra at the air/PVP-D ₂ O interface in the presence of series of 1M sodium salts (figure 5.3b). B6 Fitting parameters of CH-region ppp-SFG spectra at the air/PVP-D ₂ O interface in the presence of series of 1M sodium salts (figure 5.4a). B7 Variation in orientation angle of vinyl chain CH ₂ groups at the air/PVP-D ₂ O interface in the presence of series of 1M sodium salts (figure 5.4c and d) χ(2),eff(as)/χ(2),eff(ss) is estimated by A _V values provided in table B6. B8 Fitting parameters of OH-region ppp-SFG spectra at the air/PVP-water interface in the presence of series of 1M sodium salts (figure 5.5). B9 Fitting parameters of OH-region ppp-SFG spectra at the air/water interface in the presence of series of 1M sodium salts (figure 5.6).		ssp and ppp-polarization schemes (figure 5.1 c and d).	115
Fitting parameters of OH-region ssp-SFG spectra at the air/PVP-H ₂ O interface in presence of series of 1M sodium salts (figure 5.2a). B4 Fitting parameters of CH-region ssp-SFG spectra at the air/PVP-water interface in presence of series of 1M sodium salts (figure 5.3a). B5 Fitting parameters of CH-region ssp-SFG spectra at the air/PVP-D ₂ O interface in the presence of series of 1M sodium salts (figure 5.3b). B6 Fitting parameters of CH-region ppp-SFG spectra at the air/PVP-D ₂ O interface in the presence of series of 1M sodium salts (figure 5.4a). B7 Variation in orientation angle of vinyl chain CH ₂ groups at the air/PVP-D ₂ O interface in the presence of series of 1M sodium salts (figure 5.4c and d) \(\frac{\chi_{Q}}{\chi_{ppp}} (as) \rangle \chi_{ppp} (ss) \rangle is estimated by A_V values provided in table B6. B8 Fitting parameters of OH-region ppp-SFG spectra at the air/PVP-water interface in the presence of series of 1M sodium salts (figure 5.5). B9 Fitting parameters of OH-region ppp-SFG spectra at the air/water interface in the presence of series of 1M sodium salts (figure 5.6).	B2	Fitting parameters of OH-region SFG spectra at the air/water and air/PVP-water	110
B3 Fitting parameters of OH-region ssp-SFG spectra at the air/PVP-H ₂ O interface in presence of series of 1M sodium salts (figure 5.2a). B4 Fitting parameters of CH-region ssp-SFG spectra at the air/PVP-water interface in presence of series of 1M sodium salts (figure 5.3a). B5 Fitting parameters of CH-region ssp-SFG spectra at the air/PVP-D ₂ O interface in the presence of series of 1M sodium salts (figure 5.3b). B6 Fitting parameters of CH-region ppp-SFG spectra at the air/PVP-D ₂ O interface in the presence of series of 1M sodium salts (figure 5.4a). B7 Variation in orientation angle of vinyl chain CH ₂ groups at the air/PVP-D ₂ O interface in the presence of series of 1M sodium salts (figure 5.4c and d) χ(2),eff(as)/χ(2),eff(ss) is estimated by A _V values provided in table B6. B8 Fitting parameters of OH-region ppp-SFG spectra at the air/PVP-water interface in the presence of series of 1M sodium salts (figure 5.5). B9 Fitting parameters of OH-region ppp-SFG spectra at the air/water interface in the presence of series of 1M sodium salts (figure 5.6).		interface as probed in ssp and ppp-polarization schemes (figure 5.1 e and f).	115
B4 Fitting parameters of CH-region ssp-SFG spectra at the air/PVP-water interface in presence of series of 1M sodium salts (figure 5.3a). B5 Fitting parameters of CH-region ssp-SFG spectra at the air/PVP-D ₂ O interface in the presence of series of 1M sodium salts (figure 5.3b). B6 Fitting parameters of CH-region ppp-SFG spectra at the air/PVP-D ₂ O interface in the presence of series of 1M sodium salts (figure 5.4a). B7 Variation in orientation angle of vinyl chain CH ₂ groups at the air/PVP-D ₂ O interface in the presence of series of 1M sodium salts (figure 5.4c and d) χ _{ppp} ^{(2),eff} (as)/χ _{ppp} ^{(2),eff} (ss) is estimated by A _V values provided in table B6. B8 Fitting parameters of OH-region ppp-SFG spectra at the air/PVP-water interface in the presence of series of 1M sodium salts (figure 5.5). B9 Fitting parameters of OH-region ppp-SFG spectra at the air/water interface in the presence of series of 1M sodium salts (figure 5.6).	В3	Fitting parameters of OH-region ssp-SFG spectra at the air/PVP-H ₂ O interface in	-
B4 Fitting parameters of CH-region ssp-SFG spectra at the air/PVP-water interface in presence of series of 1M sodium salts (figure 5.3a). B5 Fitting parameters of CH-region ssp-SFG spectra at the air/PVP-D ₂ O interface in the presence of series of 1M sodium salts (figure 5.3b). B6 Fitting parameters of CH-region ppp-SFG spectra at the air/PVP-D ₂ O interface in the presence of series of 1M sodium salts (figure 5.4a). B7 Variation in orientation angle of vinyl chain CH ₂ groups at the air/PVP-D ₂ O interface in the presence of series of 1M sodium salts (figure 5.4c and d) χ ^{(2),eff} _{ppp} (as)/χ ^{(2),eff} _{ppp} (ss) is estimated by A _V values provided in table B6. B8 Fitting parameters of OH-region ppp-SFG spectra at the air/PVP-water interface in the presence of series of 1M sodium salts (figure 5.5). B9 Fitting parameters of OH-region ppp-SFG spectra at the air/water interface in the presence of series of 1M sodium salts (figure 5.6).		presence of series of 1M sodium salts (figure 5.2a).	115
B5 Fitting parameters of CH-region ssp-SFG spectra at the air/PVP-D ₂ O interface in the presence of series of 1M sodium salts (figure 5.3b). B6 Fitting parameters of CH-region ppp-SFG spectra at the air/PVP-D ₂ O interface in the presence of series of 1M sodium salts (figure 5.4a). B7 Variation in orientation angle of vinyl chain CH ₂ groups at the air/PVP-D ₂ O interface in the presence of series of 1M sodium salts (figure 5.4c and d) χ ^{(2),eff} _{ppp} (as) / χ ^{(2),eff} _{ppp} (ss) is estimated by A _V values provided in table B6. B8 Fitting parameters of OH-region ppp-SFG spectra at the air/PVP-water interface in the presence of series of 1M sodium salts (figure 5.5). B9 Fitting parameters of OH-region ppp-SFG spectra at the air/water interface in the presence of series of 1M sodium salts (figure 5.6).	B4	Fitting parameters of CH-region ssp-SFG spectra at the air/PVP-water interface in	
B5 Fitting parameters of CH-region ssp-SFG spectra at the air/PVP-D ₂ O interface in the presence of series of 1M sodium salts (figure 5.3b). B6 Fitting parameters of CH-region ppp-SFG spectra at the air/PVP-D ₂ O interface in the presence of series of 1M sodium salts (figure 5.4a). B7 Variation in orientation angle of vinyl chain CH ₂ groups at the air/PVP-D ₂ O interface in the presence of series of 1M sodium salts (figure 5.4c and d) χ ^{(2),eff} _{ppp} (as)/χ ^{(2),eff} _{ppp} (ss) is estimated by A _V values provided in table B6. B8 Fitting parameters of OH-region ppp-SFG spectra at the air/PVP-water interface in the presence of series of 1M sodium salts (figure 5.5). B9 Fitting parameters of OH-region ppp-SFG spectra at the air/water interface in the presence of series of 1M sodium salts (figure 5.6).		presence of series of 1M sodium salts (figure 5.3a).	116
B6 Fitting parameters of CH-region ppp-SFG spectra at the air/PVP-D ₂ O interface in the presence of series of 1M sodium salts (figure 5.4a). B7 Variation in orientation angle of vinyl chain CH ₂ groups at the air/PVP-D ₂ O interface in the presence of series of 1M sodium salts (figure 5.4c and d) χ(2),eff(as)/χ(2),eff(ss) is estimated by A _V values provided in table B6. B8 Fitting parameters of OH-region ppp-SFG spectra at the air/PVP-water interface in the presence of series of 1M sodium salts (figure 5.5). B9 Fitting parameters of OH-region ppp-SFG spectra at the air/water interface in the presence of series of 1M sodium salts (figure 5.6).	В5	Fitting parameters of CH-region ssp-SFG spectra at the air/PVP-D ₂ O interface in the	
B6 Fitting parameters of CH-region ppp-SFG spectra at the air/PVP-D ₂ O interface in the presence of series of 1M sodium salts (figure 5.4a). B7 Variation in orientation angle of vinyl chain CH ₂ groups at the air/PVP-D ₂ O interface in the presence of series of 1M sodium salts (figure 5.4c and d) χ(2),eff(as)/χ(2),eff(ss) is estimated by A _V values provided in table B6. B8 Fitting parameters of OH-region ppp-SFG spectra at the air/PVP-water interface in the presence of series of 1M sodium salts (figure 5.5). B9 Fitting parameters of OH-region ppp-SFG spectra at the air/water interface in the presence of series of 1M sodium salts (figure 5.6).		presence of series of 1M sodium salts (figure 5.3b).	116
B7 Variation in orientation angle of vinyl chain CH ₂ groups at the air/PVP-D ₂ O interface in the presence of series of 1M sodium salts (figure 5.4c and d) χ ^{(2),eff} _{ppp} (as)/χ ^{(2),eff} _{ppp} (ss) is estimated by A _V values provided in table B6. B8 Fitting parameters of OH-region ppp-SFG spectra at the air/PVP-water interface in the presence of series of 1M sodium salts (figure 5.5). B9 Fitting parameters of OH-region ppp-SFG spectra at the air/water interface in the presence of series of 1M sodium salts (figure 5.6).	В6	Fitting parameters of CH-region ppp-SFG spectra at the air/PVP-D ₂ O interface in the	
 Variation in orientation angle of vinyl chain CH₂ groups at the air/PVP-D₂O interface in the presence of series of 1M sodium salts (figure 5.4c and d) χ^{(2),eff}_{ppp} (as)/χ^{(2),eff}_{ppp} (ss) is estimated by A_V values provided in table B6. B8 Fitting parameters of OH-region ppp-SFG spectra at the air/PVP-water interface in the presence of series of 1M sodium salts (figure 5.5). B9 Fitting parameters of OH-region ppp-SFG spectra at the air/water interface in the presence of series of 1M sodium salts (figure 5.6). 		presence of series of 1M sodium salts (figure 5.4a).	117
estimated by A _V values provided in table B6. B8 Fitting parameters of OH-region ppp-SFG spectra at the air/PVP-water interface in the presence of series of 1M sodium salts (figure 5.5). B9 Fitting parameters of OH-region ppp-SFG spectra at the air/water interface in the presence of series of 1M sodium salts (figure 5.6).	В7	Variation in orientation angle of vinyl chain CH ₂ groups at the air/PVP-D ₂ O interface in	
B8 Fitting parameters of OH-region ppp-SFG spectra at the air/PVP-water interface in the presence of series of 1M sodium salts (figure 5.5). B9 Fitting parameters of OH-region ppp-SFG spectra at the air/water interface in the presence of series of 1M sodium salts (figure 5.6).		the presence of series of 1M sodium salts (figure 5.4c and d) $\left \chi_{ppp}^{(2),eff}(as)/\chi_{ppp}^{(2),eff}(ss)\right $ is	
B8 Fitting parameters of OH-region ppp-SFG spectra at the air/PVP-water interface in the presence of series of 1M sodium salts (figure 5.5). B9 Fitting parameters of OH-region ppp-SFG spectra at the air/water interface in the presence of series of 1M sodium salts (figure 5.6).		estimated by A _V values provided in table B6.	117
B9 Fitting parameters of OH-region ppp-SFG spectra at the air/water interface in the	B8	Fitting parameters of OH-region ppp-SFG spectra at the air/PVP-water interface in the	111
B9 Fitting parameters of OH-region ppp-SFG spectra at the air/water interface in the		presence of series of 1M sodium salts (figure 5.5).	118
presence of series of 1M sodium salts (figure 5.6).	В9	Fitting parameters of OH-region ppp-SFG spectra at the air/water interface in the	110
119		presence of series of 1M sodium salts (figure 5.6).	118

NOTATIONS AND ABBREVIATIONS

Sr. No.	Symbols/Abbreviations	Description
1.	С	speed of light
2.	ê	Unit polarization vector
3.	L	Fresnel's Factor
4.	φ	Azimuthal angle
5.	Ψ	Twist angle
6.	i	Iota (imaginary factor)
7.	<>	Ensemble average
8.	σ	Variance
9.	M	Molar
10.	V	volt
11.	mA	milliampere
12.	°C	Degree Celsius
13.	ω	Wavenumber
14.	mM	millimolar
15.	Ea	Activation energy
16.	T_k	Inactivation temperature
17.	k _B	Boltzmann's Constant
18.	T	Temperature
19.	$\Phi_{ m el}$	Electrostatic potential
20.	Z	Atomic number
21.	e	Electronic charge
22.	ϵ_0	Dielectric constant of vacuum
23.	$\epsilon_{ m r}$	Dielectric constants of medium
24.	R	Distance
25.	nm	nanometer
26.	θ	Angle
27.	π	pi
28.	U	Ionic potential
29.	$\sigma_{ m st}$	Surface tension

30.	$a_{ m el}$	Electrolyte activity
31.	$R_{\rm g}$	Gas constant
32.	ρ	Density
33.	λ	Wavelength
34.	MΩ	Megaohm
35.	μΙ	Microliter
36.	n	Refractive index
37.	d	Central thickness of droplet
38.	ΔΛ	Path difference
39.	Δφ	Phase difference
40.	I	Intensity
41.	μm	Micrometer
42.	μЈ	Microjoule
43.	V	Speed
44.	p	Pressure
45.	t	Time
46.	R _c	Radius of curvature
47.	D	Tube Diameter
48.	Н	Distance between Laser focus and free surface
49.	E	Energy
50.	ps	Picosecond
51.	nm	Nanometer
52.	mJ	Milijoule
53.	Hz	hertz
54.	W	watt
55.	cm	Centimeter
56.	mm	Millimeter
57.	Pj	Jet power
58.	D _j	Jet diameter
59.	k	Wave vector
60.	μ	Dipole moment
61.	Р	Polarization

	T	
62.	α	Polarizability
63.	χ ⁽¹⁾	Linear susceptibility
64.	$\chi^{(2)}$	Second-order susceptibility
65.	$\chi^{(3)}$	Third-order susceptibility
66.	β	First-order hyperpolarizability
67.	γ	Second-order hyperpolarizability
68.	E'	Electric field
69.	P ⁽²⁾	Second-order non-linear polarization
70.	P ⁽³⁾	Third-order non-linear polarization
71.	Γ	Damping constant
72.	$A_{\rm v}$	Resonance Amplitude of vth vibration mode
73.	SS	Symmetric stretching
74.	as	Asymmetric stretching
75.	W	Width
76.	F	Force
77.	ď′	Thickness
78.	A	Absorbance
79.	1	Wetting parameter
80.	Ľ'	Optical path length
81.	ε	Molar extinction coefficient
82.	χ ^{(2),eff}	Effective second-order nonlinear susceptibility
83.	L	Fresnel's factor
84.	С	Concentration
85.	g>	ground state
86.	v>	vibrational excited state
87.	s>	Any other state
88.	ATGEE	Acetyltetraglycine ether ester
89.	LMWA	Law of matching water affinities
90.	ODNP	Overhauser dynamic nuclear polarization
91.	PDEA	poly(N, N-diethylacrylamide)
92.	NMR	Nuclear magnetic resonance
93.	ATR-FTIR	Attenuated total reflection Fourier transform infrared

94.	SFG	Sum frequency generation
95.	IRRAS	Infrared reflection absorption spectroscopy
96.	CCN	Cloud condensation nuclei
97.	ERHs	Efflorescence relative humidities
98.	DRHs	Deliquescence relative humidities
99.	OHS-TENG	Organohydrogel-based single electrode triboelectric nanogenerator
100.	LEDs	Light emitting diodes
101.	AWH	Atmospheric water harvesting
102.	PDMAPS	poly-[2-(methacryloyloxy)ethyl]dimethyl-(3-sulphopropyl)ammonium hydroxide
103.	DFT	Density functional theory
104.	PBS	Proton barrier separator
105.	PVA	poly(vinyl alcohol)
106.	XRD	X-ray diffraction
107.	XPS	X-ray photoelectron spectroscopy
108.	NDs	Nanodiamonds
109.	DNA	Deoxyribonucleic acid
110.	DOXH ⁺	Doxorubicin
111.	KCl	Potassium chloride
112.	CaCl ₂	Calcium chloride
113.	$(NH_4)_2SO_4$	Ammonium sulphate
114.	SNDs	Small nanodiamonds
115.	LNDs	Large nanodiamonds
116.	LLPS	Liquid-liquid phase separation
117.	ATP	Adenosine Triphosphate
118.	CCPs	Cationic conjugated polymers
119.	PMNT	poly (3-alkoxy-4-methylthiopene)
120.	MD	Molecular dynamics
121.	DTAB	Dodecyltrimethylammonium bromide
122.	Na ₂ HPO ₄	Sodium hydrogen phosphate
123.	Na ₂ SO ₄	Sodium sulphate
124.	Na ₂ CO ₃	Sodium carbonate
125.	NaBr	Sodium bromide

126.	NaCl	Sodium chloride
127.	NaNO ₃	Sodium nitrate
128.	NaI	Sodium iodide
129.	NaSCN	Sodium thiocyanate
130.	NaClO ₄	Sodium perchlorate
131.	Rh6G	Rhodamine 6G
132.	PVP	Polyvinylpyrrolidone
133.	Pt	Platinum
134.	DLVO	Derjaguin-Landau-Verwey-Overbeek
135.	IN	Ice nucleators
136.	INP	Ice nucleation protein
137.	PMTA	poly[2- (methacryloyloxy)ethyltrimethylammonium]
138.	Cs ⁺	Cesium cation
139.	Rb ⁺	Rubidium cation
140.	Li ⁺	Lithium cation
141.	QA ⁺	Quaternary ammonium cation
142.	NT	Nanotube
143.	NaF	Sodium fluoride
144.	SAXS	Small-angle X-ray scattering
145.	TEM	Transmission electron microscopy
146.	ISSG	Interfacial solar steam generation
147.	PVA	poly (vinyl alcohol)
148.	MWCNT	Multi-walled carbon nanotubes
149.	GOX	Glucose oxidase
150.	NEXAFS	Near-edge X-ray absorption fine structure spectroscopy
151.	SERS	Surface-enhanced Raman scattering
152.	WOS	Wagner and Onsager and Samaras
153.	D_2O	Deuterated water (heavy water)
154.	H_2O	Water
155.	ОН	Oscillator of H ₂ O
156.	OD	Oscillator of D ₂ O
157.	ODA	Octadecylamine

158.	CH_3	Methyl
159.	CH_2	Methylene
160.	PNIPAM	Poly-(N isopropylacrylamide)
161.	LCST	Lower critical solution temperature
162.	BSA	Bovine serum albumin
163.	DPTAP	1,2-dipalmitoyl-3-trimethylammonium-propane
164.	DS	Sodium 1-dodecanesulfonate
165.	DLPC	1,2-dilauroyl-sn-glycero-3-phosphocholine
166.	ELP	Elastin-like polypeptide
167.	CTA^{+}	Positively charged cetyltrimethylammonium
168.	TOMA ⁺	Quaternary amine methyltrioctyl ammonium
169.	UV	Ultraviolet
170.	Vis	Visible
171.	He-Ne	Helium-Neon
172.	CCD	Charge-coupled device
173.	Nd:YAG	Neodymium doped yattrium alluminium garnate
174.	DPSS	Diode pumped solid state
175.	DC	Direct current
176.	NR	Non resonant
177.	IR	Infrared
178.	DKDP	Potassium dideuterium phosphate
179.	BBO	beta-barium borate
180.	PG	Parametric generation
181.	OPO	Optical parametric oscillation
182.	OPA	Optical parametric amplification
183.	OPG	Optical parametric generation
184.	AgGaS_2	Silver Gallium Sulphide
185.	GaSe	Gallium Selenide
186.	PMT	Photomultiplier tube
187.	SDS	Sodiumdodecylsulphate
188.	H_2O_2	Hydrogen peroxide
189.	H_2SO_4	Sulphuric acid

CHAPTER 1

INTRODUCTION

In the present chapter, we briefly introduce specific ion effects and discuss selected latest literature highlighting its vast applicability with a basic outlook on the fundamental intermolecular interactions contributing to the said phenomenon. This chapter also highlights the need to investigate specific ion effects at the air/aqueous interface and discusses the capability of present techniques in probing the interfacial region. Later, this chapter contains a critical literature review on exploring specific ion effects at the air/water and air/aqueous interface using surface-specific sum frequency generation (SFG) vibrational spectroscopy. Based on the understanding developed through the literature survey, we have identified the research gaps and the associated questions that have remained unanswered. The last section of this chapter presents the research objectives we designed and intended to work in the present thesis and briefly showcases the overall organization of the following chapters.

1.1 Specific Ion Effects: A Historical Background

In 1847 Poiseuille reported the first pioneering studies on the viscosities of electrolyte solutions. He found that some salts increase water viscosity, whereas others decrease it. Later in 1876, Kohlrausch measured the conductivity of electrolyte solutions.² He quantified the electrochemical mobility of ions, migrating through the solution in the presence of an applied electric field. It is found that the ion-specific mobility for halide anions is $Br^- > I^- > Cl^- > F^-$. The observation came opposite to the expectation that the mobility would have been high for small ions like F⁻ and low for the big ions like Br⁻. The accepted explanation is that the actual effective size of ions in water i.e., the hydrodynamic radius is quite different from the crystallographic radius. Small ions (F⁻) owing to their high charge density, are strongly hydrated, which makes their motion slow enough in comparison to the bigger, poorly hydrated ions (Br⁻). During the 1880s and 1890s, Franz Hofmeister and his coworkers reported a series of seven papers in German literature entitled "Zur Lehre von der Wirkung der Salze," which in English means "About the science of the effect of salts". The second paper of the series entitled "About regularities in the protein precipitating effects of salts and the relation of these effects with the physiological behavior of salts," and the third⁵ paper of the series entitled "About the water withdrawing effect of the salts" are the most important ones and constituted a breakthrough in the electrolyte chemistry. These were the first extended, systematic studies on specific ion effects beyond the effect of different charges. Hofmeister studied specific ion effects on the precipitation of proteins, colloidal ferric oxide, sodium oleate, and collagen (insisglass) with several series of salts carrying a common cation (or anion). His ingenious conclusion drawn from these studies allowed him to order the salts according to their "water withdrawing effect" in link to their precipitation ability, known as the Hofmeister series (figure 1). His approach to rationalizing specific ion effects in terms of interactions between salt ions and water molecules is adopted by proponents later to introduce the terminology of kosmotropes (water structure-makers) and chaotropes (water structure-breakers). Similar post-Hofmeister studies were also reported by Robertson (1911), Loeb (1920), Gustavson (1926), and Green (1932)⁹. Jones and Dole¹⁰ (1929), and Cox and Wolfenden¹¹ (1934) refined the specific ion effects in water viscosity and introduced Jones-Dole viscosity B coefficients. In 1945 Frank and Evans presented the first correlation between ion-specific viscosity and the structural entropy of the solution. It is accepted that the ions with positive value of B increased the viscosity of aqueous solutions, actually 'make the order' in the water structure and are called 'kosmotropes'. Those with a negative value of B decreased viscosity of aqueous solutions, 'break the order' in the water structure and are called 'chaotropes'. The strong electrostatic field around the small and strongly hydrated kosmotropes interacts with the permanent dipole moments of the surrounding water molecules and imparts a higher order on local water molecules via charge-dipole interactions. Instead, the big and scarcely hydrated chaotropes, which produce a weaker electrostatic field, perturb the dynamic quasi-ordered (hydrogen-bonded) array in bulk water and make the surrounding water molecules more disordered. In 1936 Voet introduced a quantitative approach to explain the order of salting effects as seen in viscosity, precipitation, and mobility in terms of lyotropic numbers. He believed that the lyotropicity of ions is related to the electrostatic field of the ions. Later in 1948, Eckfedlt stated that the lyotropicity of ions is a combination of i) the electrostatic effect ii) the compound formation from the chemical species present in the ternary system, and iii) the ionic polarization effect. In 1963, Pearson classified the series of ions in terms of soft (polarizable) ions and hard (non-polarizable) ions. The appellations "structure making" and "structure breaking", ascribed to Gurney (1953) have been applied to various ions. In the structure in the structure breaking, ascribed to Gurney (1953) have been applied to various ions.

However, there exists paralleled literature reports which highlight that the specific ion effects cannot be solely explained by the ion-water interactions only, the existence of protein or the macromolecule (the third entity of the aqueous salt solution) should be taken into consideration. Indirect information on this can be seen in the experimental studies where Pauli (1898-1899) showcased that the salting out efficacy of salts for electronegative protein follows the Hofmeister series, whereas an opposite trend is observed for the electropositive proteins, as reported by Posternak (1901).⁶ Meyer and Klemm (1940) studied the impact of salts on the solubility of diketopiperazine and suggested the increment in solubility in the presence of alkali bromide and iodide solutions is a result of the direct amide-ion interactions.¹⁷ Bello, Riese, and Vinogard (1962) studied the impact of lowconcentration electrolyte NaCl on the melting point of gels of gelatin. 18 The authors suggested that the effect of salt in tuning the melting points of gelatin can be attributed to the interactions of ions with the peptide backbone. It was Robinson (1965) who investigated the activity coefficients of uncharged model peptide acetyltetraglycine ether ester (ATGEE) in the presence of concentrated salt solutions and demonstrated that the interactions of ions with the protein surfaces play a significant role in determining the Hofmeister effect alongside the hydration properties of the salt ions. ¹⁹ The idea is further supported by Schrier and Schrier (1967), ²⁰ Nandi (1972), ²¹ Von Hippel (1973)²², and Arakawa (1982)²³. Von Happel (1973) utilized the recycling chromatography on polyacrylamide columns to study the binding of ions to amide and nonpolar groups of the macromolecule.²² It is reported that the relative binding affinity of salts towards the polyacrylamide gels follows the Hofmeister series and, in turn, governs the stabilization/destabilization of the macromolecule. Arakawa (1982), through thermodynamic considerations, showcased that the weakly hydrated thiocyanate anions are favorably bind to the bovine serum albumin compared to the strongly hydrated sulphate anions.²³ This implies increased solubility (salt-in effect) and destabilization of the protein in the presence of weakly hydrated anions. In contrast, the presence of the strongly hydrated anions brings precipitation of the macromolecule from the aqueous solution. The picture that emerges from these studies demonstrates that the Hofmeister effect can be explained by ionwater interactions and ion-macromolecule interactions (interaction of ions with the amide group of protein backbone or macromolecule surface). Whenever the water structural effects of the ions are discussed, effects beyond their hydration shells are generally meant.²⁴⁻²⁷ In view of this, Marcus (1992-2009) introduced different parameters to quantify the modifications in water structure owing to ion effects beyond its hydration shell like a) work necessary to create a cavity in the liquid, which can be expressed in terms of the difference between the cohesive energy density and the internal pressure, b) deficit of its molar entropy as Trouton's constant, c) Kirkwood dipole orientation correlation parameter d) heat capacity density. ²⁴⁻²⁷ Whether and how much influence an ion has beyond the hydration shell(s) is still an open question. The pragmatical explanation of the specific ion effects can be given by Collin's (2004) law of matching water affinities (LMWA). ²⁸⁻²⁹ It states that oppositely charged ions in free solution form inner sphere ion pairs spontaneously only when they have equal water affinities. The rule turns out to be quite general and applicable to many ion-specific phenomena, and the concept is confirmed by Jungwirth and group ³⁰ through molecular dynamics simulation studies. The specific ion effects have been investigated rigorously on different molecular systems with a variety of experimental techniques/molecular dynamics simulation approaches and are reviewed in the literature. ²⁷⁻³⁹

Recent advancements in spectroscopic techniques have revealed new outcomes in specific ion phenomena. Song (2014) utilized Overhauser dynamic nuclear polarization (ODNP) relaxometry technique to study water diffusion dynamics near lipid surfaces. ⁴⁰ They suggested that the ion-specific changes in activation energies of diffusion originated from the ion-specific water-macromolecule interactions, the molecular level mechanism of which is unknown. Cremer and coworkers (2015) reported that an NH-moiety is not necessary for ion-macromolecule interactions. ⁴¹ The authors showcased that the weakly hydrated anions (SCN⁻, ClO₄⁻, I⁻, NO₃⁻, and Br⁻) prone to bind with hydrophobic CH- and CH₂- groups of the poly(N, N-diethylacrylamide) (PDEA) polymer backbone and results in a salting-in effect. They utilized nuclear magnetic resonance (NMR) and attenuated total reflection Fourier transform infrared (ATR-FTIR) spectroscopy to elucidate the mechanism of anion binding to PDEA even in the absence of NH-moiety. Interestingly in a recent report, Allen and group (2020) utilized sum frequency generation (SFG) vibrational spectroscopy and infrared reflection absorption spectroscopy (IRRAS) to investigate the selectivity of the anion binding. They showcased that the weakly hydrated guanidinium receptor has a significant affinity to bind with the strongly hydrated sulphate anion in comparison to the weakly hydrated iodide, which is in stark contrast to Collin's rule. ⁴²

The literature discussion elucidates that more than one type of interaction (apart from the conventional ion-water interactions) needs to be considered while the explanation of the Hofmeister series/Specific ion effects, the exact molecular level mechanism is still under investigation.

1.2 Hofmeister Series and Its Characteristics

Figure 1.1 represents a typical ordering of the anionic Hofmeister series, where ions are ordered according to their precipitation effects. In the series, the ions to the left of chloride are called kosmotropes, strongly hydrated, hard (non-polarizable) ions and precipitate protein out of the solution. In contrast, ions to the right are called chaotropes, weakly hydrated, soft (polarizable) ions, and salt protein in the solution. Some of the characteristics of the Hofmeister series are mentioned as follows:^{28, 36}

- a) Different measures of the Hofmeister series typically give a similar, characteristic rank ordering with slight alterations.
- b) Dominated by anion effects.
- c) Since the pioneering work of Goggenheim, ⁴³⁻⁴⁴ the idea that specific ion effects are approximately additive over all species in the solution has prevailed and is consistent to date. However, recently, some nonadditive specific ion effects have also been reported. ⁴⁵⁻⁴⁷

d) Concentration range: Earlier, it was assumed that the Hofmeister phenomenon occurs only at high salt concentrations (i.e., 0.5–3 M). Recently, ion specificity is found to occur at physiological concentrations (~0.1 to 0.15 M and below) reflecting its vast applications in biology.⁴⁷⁻⁴⁹

Hofmeister Series

CO₃² SO₄² HPO₄² OAc cit F Cl Br NO₃ ClO₃ I ClO₄ SCN PF₆

Kosmotropic Chaotropic Structure breakers Structure makers ↑Surface tension ↓Surface tension Harder to make cavity Easier to make cavity ↑ Solubility of hydrocarbons ↓ Solubility of hydrocarbons Salt in (solubilize) Salt out (aggregate) ↓ Protein denaturation ↑ Protein denaturation ↑ Protein stability ↓ Protein stability Strongly hydrated Weakly hydrated Hard anions of high charge density Soft anions of low charge density Low surface propensity High surface propensity Low adsorption on High adsorption on Hydrophobic surface Hydrophobic surface

Figure 1.1 A typical anionic Hofmeister series.

Ubiquitous: Specificity is a rule rather than an exception and prevails everywhere. ²⁷⁻³⁹ Examples of these include diffusion coefficients, ⁴⁰ electrolyte activities, ⁵⁰⁻⁵² buffers, ⁵³⁻⁵⁴ viscosities, ^{1,10-11} osmotic pressure, ⁵⁵ pH, ⁵⁶ optical rotation of amino acids, ⁵⁷⁻⁵⁸ hygroscopic properties of amino acids, ⁵⁹ colloidal stability, ⁶⁰ voltage stability of energy storage devices, ⁶¹ conductivity of organohydrogels, ⁶²⁻⁶³ surface tension, ⁶⁴⁻⁶⁶ surface potential, ⁶⁶⁻⁶⁸ heat capacity, ³⁶ refractive index, ³⁶ water evaporation, ⁶⁵ozone depletion, ⁶⁹⁻⁷⁰ aerosol chemistry, ^{62, 71} bubble coalescence, ⁷²⁻⁷⁴ surfactant and microemulsion phases, ⁷⁵⁻⁷⁶ ionic liquids, ⁷⁷⁻⁸⁰ upper critical/lower critical temperature of thermoresponsive polymer, ⁸¹⁻⁸² zeta potential, ⁸³ sorption efficiency of hydrogels, ⁸⁴⁻⁸⁵ enzyme activities, ⁸⁶⁻⁹² protein adsorption at silica surfaces, ⁹³ protein cloud points, ⁹⁴⁻⁹⁶ protein surface charges, ⁹⁷ optical properties of polymers for chemo/biosensors, ^{49, 98} stability of nanodroplets, ⁹⁹⁻¹⁰⁰ ice nucleation, ¹⁰¹⁻¹⁰² electrophoretic mobilities, ¹⁰³⁻¹⁰⁵ growth rates of microorganisms, ¹⁰⁶⁻¹⁰⁷ wetting and/or antifouling, ¹⁰⁸⁻¹¹⁰ self-assembly, ¹¹¹⁻¹¹⁵ solar desalination, ¹¹⁶⁻¹¹⁷ waste water treatment, ¹¹⁸⁻¹¹⁹ stability of nanomaterials for drug delivery, ¹²⁰⁻¹²³ bioavailability of drugs/vaccines, ¹²⁴⁻¹³⁰ liquid-liquid phase separation, ¹³¹⁻¹³² order/disorder in macromolecule structure at air/aqueous interface, ⁶⁷ orientation of free OH oscillators at air/water interface, ⁶⁵ metal-ion batteries, ¹³³ surface adsorption of proteins ¹³⁴⁻¹³⁵ and many others ¹³⁶⁻¹³⁹.

1.3 Applications of Specific Ion Effects

Here we have discussed some of the selected literature reports showcasing the vast applications of the specific ion phenomenon.

Water-soluble cationic conjugated polymers (CCPs) have been widely utilized as chemo-or biosensors, as detection tools for biomolecules, toxic ions, and surfactants. CCPs generate rapid and collective optical responses (absorption/emission) upon complexation with different targets. Qiu et al. investigated the impact of Hofmeister salts on the optical properties of poly (3-alkoxy-4-methylthiopene) (PMNT) (figure 1.2). It is found that the presence of I⁻ and SCN⁻ bring red-shift in the absorption spectrum, whereas no change is observed with SO_4^{2-} and F⁻. The authors provided molecular level insights into the observed Hofmeister effect in ionochromism of PMNT using molecular dynamics (MD) simulations. It is suggested that the weakly hydrated anions I⁻ and SCN⁻ have high affinity towards the apolar backbone, thus avoid hydrophobic collapse of PMNT backbone, leading to extended conformations with red shift absorption. However, strongly hydrated SO_4^{2-} and F⁻ avoid hydrophobic PMNT backbone keeping the coiled conformation intact without any changes in the absorption profile.

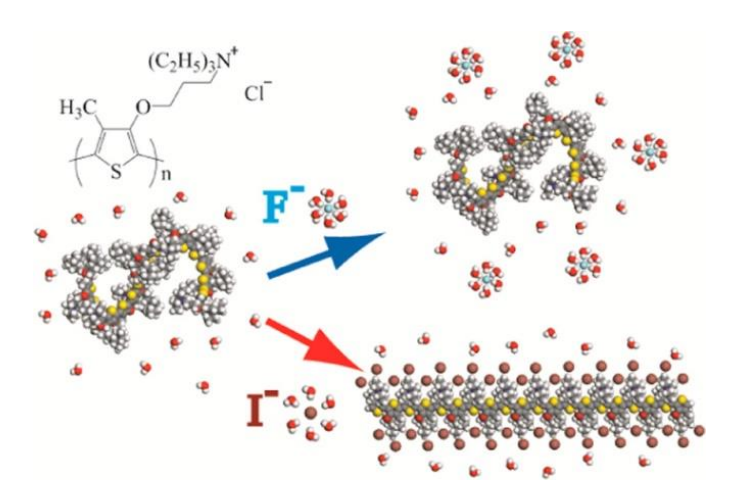


Figure 1.2 Schematic illustration of the mechanism of ion-specific optical properties of cationic poly (3-alkoxy-4-methylthiopene) (PMNT). Reprinted from J. Phys. Chem. C 2013, 117, 42, 21870-21878. Copyright 2013 American Chemical Society.⁴⁹

Hygroscopicity is crucial in determining the physicochemical properties of atmospheric aerosols and their activity as cloud condensation nuclei (CCN).⁵⁹ This, in turn, affects cloud formation and controls the Earth's water cycle. Ashraf et al. studied specific ion effects/Hofmeister effect on the hygroscopicity of aerosols.⁵⁹ The authors prepared micrometer sized particles of glycine amino acid and salt mixtures and examined their efflorescence relative humidities (ERHs) and deliquescence relative humidities (DRHs). It is found that the presence of kosmotropic anion (SO_4^{2-}) and chaotropic anion (NO_3^{-}) significantly perturb the hygroscopic properties of glycine while no change is observed for Cl^{-} . Later, the ion-specific hygroscopic properties of glycine are attributed to the water mediated glycine-ion interactions as probed by FTIR vibrational spectroscopy.

The demand of flexible and sustainable power sources for the next generation wearable electronics has led to increased research interest in biomechanical energy harvesters, i.e., nanogenerators. ⁶²⁻⁶³ Wu et al. utilized the Hofmeister effect and electrostatic interaction to raise the ionic conductivity and power efficiency of

organohydrogel-based single-electrode triboelectric nanogenerator (OHS-TENG) (figure 1.3).⁶³ The contribution of ion-specific H-bonding and electrostatic interactions towards the improvement of organohydrogel properties is showcased by FTIR studies. The authors demonstrated the wearable applications, i.e., when the OHS-TENG device is in contact with skin or clothes, it harvests biomechanical energy, and the generated electricity can be used to light up LEDs or monitor human's motion. They reported that replacing water with glycerol in the hydrogel helps in excellent long terms stability (four months) and temperature tolerance (-50-100°C) of the wearable device.

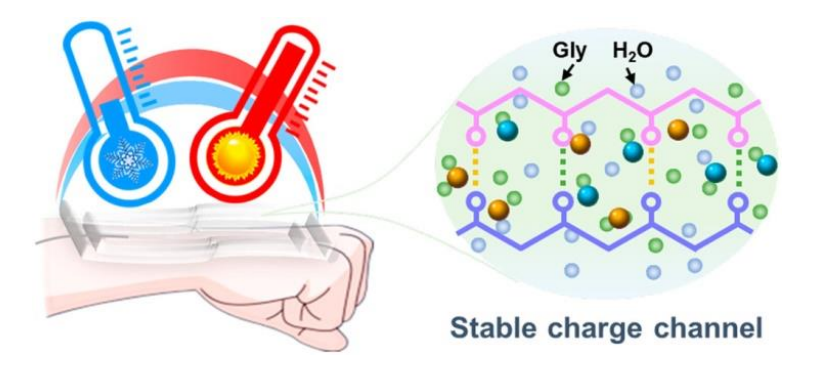


Figure 1.3 Schematic illustration of the working mechanism of organohydrogel-based cell based on the themodiffusion effect, where replacing water with glycerol in the hydrogel improves the stability and temperature tolerance of the wearable device. Reprinted from ACS Nano 2021, 15, 8, 13427-13435. Copyright 2021 American Chemical Society.⁶³

Earth's atmosphere stores billion tons of water in the form of droplets and vapor. In recent years, atmospheric water harvesting (AWH) has attracted research interest in producing fresh water as an alternate option to the regions suffering from fresh water scarcity, especially in landlocked and (semi) arid areas. Aleid et al. utilized the salting-in effect in Zwitterionic polymer to facilitate atmospheric water harvesting (figure 1.4). They prepared salt-hydrogel composite with zwitterionic hydrogel poly-[2-(methacryloyloxy)ethyl]dimethyl-(3-sulphopropyl)ammonium hydroxide (PDMAPS) and hygroscopic salt of LiCl. The authors demonstrated a fully solar energy-driven AWH process where the salting-in effect results in high water sorption capacity,

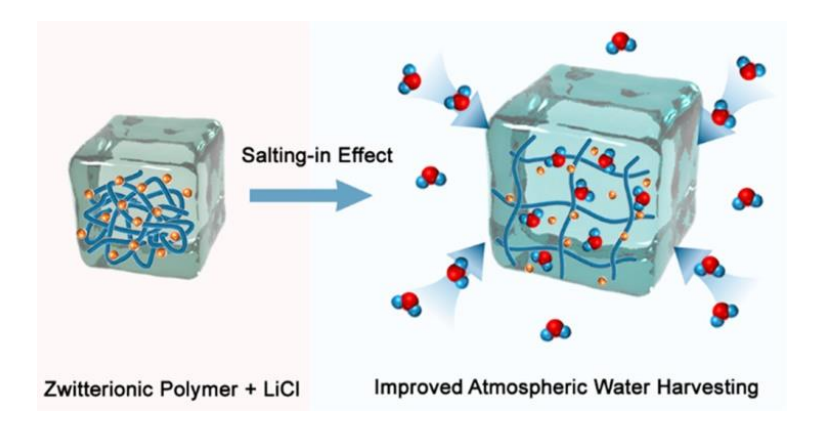


Figure 1.4 Schematic illustration of salt-in effect utilizing LiCl with Zwitterionic polymer for improved atmospheric water harvesting (AWH). Reprinted from ACS Materials Lett. 2022, 4, 3, 511-520. Copyright 2022 American Chemical Society.⁸⁴

robust water storage capacity, and high stability of salt-hydrogel composite sorbent. The improved characteristics are attributed to the ion-mediated breaking of electrostatic interactions between the cationic and anionic groups of the zwitterionic hydrogel, as studied by ATR-FTIR spectroscopy, further confirmed by DFT calculations. The work proposed hydrogel-based AWH sorbent for improved water vapor sorption performances.

Zdrali et al. investigated specific ion effects in the stability of nanometer-sized droplets (figure 1.5). The authors produced nanodroplets of hexadecane stabilized with surfactant dodecyltrimethylammonium bromide (DTAB). It is reported that nanodroplets remain stable in NaSCN, NaNO₃, and NaCl electrolyte solutions with a concentration range from 0-600 mM. However, the nanometer droplets remain stable with Na₂SO₄ up to a maximum concentration of 300 mM, above which destabilization of the emulsion is observed. The authors attempted to provide molecular level insights into the observed specific ion effects by utilizing DLVO theory, which could not quantify the observed droplet stability. They speculated that the reasoning behind the observed discrepancy could be attributed to diverse conformations of the complex interfacial structure involving different types of interactions.

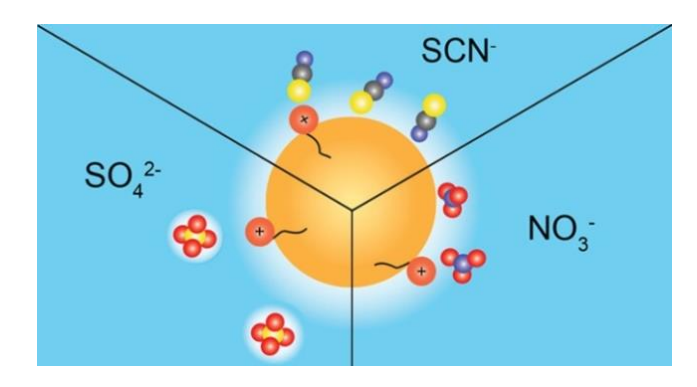


Figure 1.5 Schematic illustration of specific ion effects in the stability of hexadecane nanodroplets. Reprinted from J. Phys. Chem. C 2019, 123, 27, 16621-16630. Copyright 2019 American Chemical Society.⁹⁹

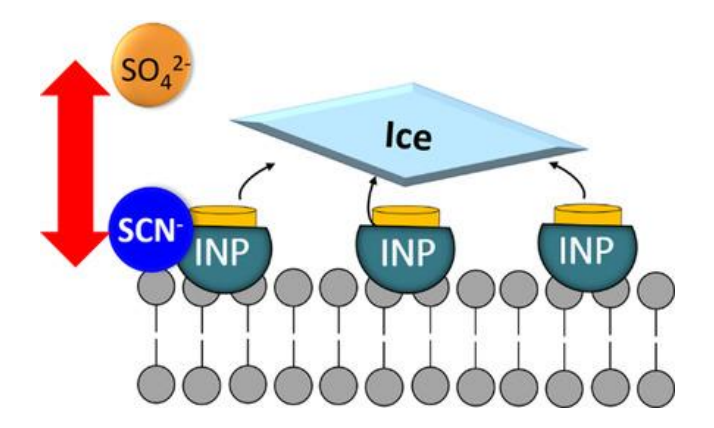


Figure 1.6 Schematic illustration of the influence of ions on the efficiency of bacterial ice nucleators that follows the Hofmeister series. The different effects are due to specific interactions of the ions with ice-nucleating proteins on the surface of the bacteria. Reprinted from Chem. Eur. J. 2021, 27, 26, 7402-7407. Copyright 2021 The Authors. Chemistry - A European Journal published by Wiley-VCH GmbH.¹⁰¹

Bacterial ice nucleation has found applications in agriculture, microbial ecology, geology, cloud formation, and precipitation in the atmosphere. ¹⁰¹ Schwidetzky et al. investigated specific ion effects in the efficiency of the

proteinaceous ice nucleators (IN) from Pseudomonas syringae (figure 1.6). ¹⁰¹ It is reported that the ions significantly affect the ice nucleation protein (INP)-mediated freezing temperatures that follow the Hofmeister series. Weakly hydrated SCN⁻ ion lowers the INP-mediated freezing temperature, whereas strongly hydrated SO₄² facilitate the freezing by enhancement in INP-mediated freezing temperature. Presence of chloride showed negligible effect on freezing temperatures. They reported that the presence of specific ion-protein interactions governs the ice nucleation process by bacteria characterized by surface-specific sum frequency generation (SFG) spectroscopy and MD simulations.

Higaki al. reported the water droplet contact angle cationic poly[2-(methacryloyloxy)ethyltrimethylammonium] (PMTA) brushes is specific to the presence of counteranions that follows Hofmeister series as well (figure 1.7). 110 It is shown that the presence of strongly hydrated counteranions (Ac⁻ and Cl⁻) promote wetting, whereas weakly hydrated anions (SCN⁻and ClO₄) made PMTA brushes hydrophobic, as evidenced by an increment in the contact angle. The authors explained the observation in terms of variation in the hydration state of cationic polyelectrolyte PMTA brushes in the presence of different anions, which was estimated through neutron reflectivity (NR) and FTIR (Fourier transform infrared) spectroscopy experiments. It is suggested that the presence of weakly hydrated anions which have a strong affinity towards weakly hydrated quaternary ammonium (QA+) cations in the PMTA that induce dehydration of brush chains and a resultant hydrophobic surface. The research provides essential insights in designing innovative surfaces with desired interfacial properties like wetting and antifouling.

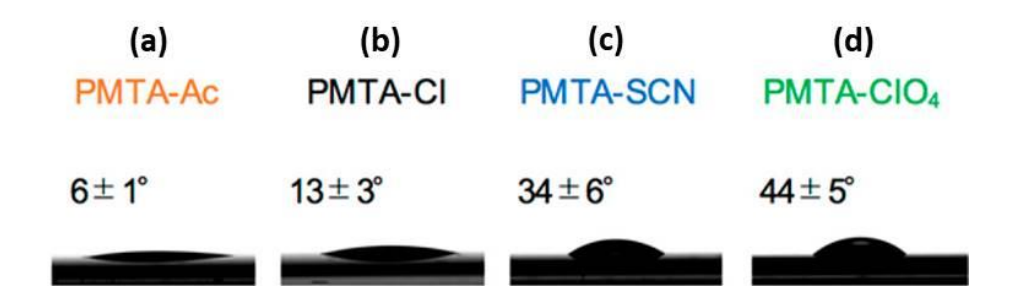


Figure 1.7 Side view of a water droplet on (a) PMTA-Ac, (b) PMTA-Cl, (c) PMTA-SCN, and (d) PMTA-ClO₄. The averaged static contact angles are depicted in the images. Reprinted from Ind. Eng. Chem. Res. 2018, 57, 15, 5268-5275. Copyright 2018 American Chemical Society. ¹¹⁰

Nanotube (NT) assemblies have shown immense potential in biological and non-biological domains like electronics, drug delivery, medical imaging, magnetic devices, sensors, and ion channels owing to their physical and chemical properties tunable via control of their size. Gobeaux et al. reported the contribution of ions in governing the diameter of self assembled NTs of a cationic octapeptide, lanreotide in water (figure 1.8). They characterize the structure and morphology of NTs in the presence of monovalent ions like F, Cl⁻, NO₃⁻, Br⁻, I⁻, ClO₄⁻, and carboxylate anions. Using small-angle X-ray scattering (SAXS) and Transmission electron microscopy (TEM) the authors reported that the ionic radii of the small counterions are proportional to the inverse of the diameter of NTs and follow a trend as well. However, no such trend was observed with bigger carboxylate anions. It is demonstrated that the anion-specific adsorption sites on the inner sides of the NT walls control the diameters of self-assemblies.

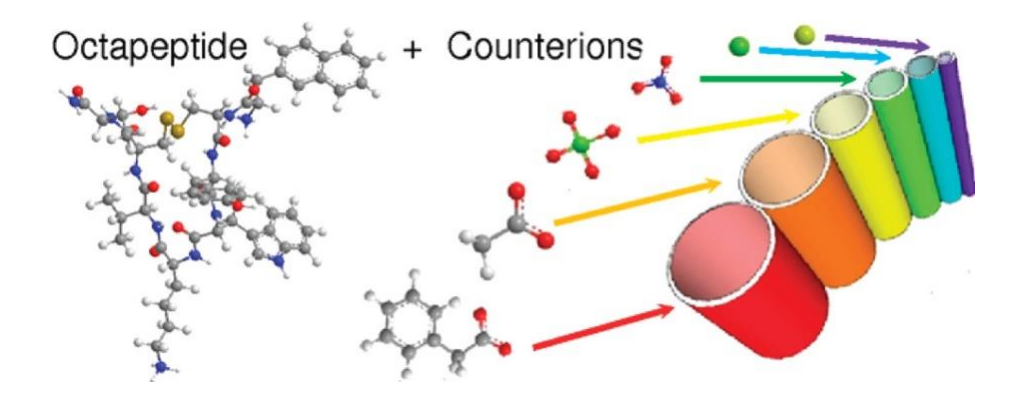


Figure 1.8 Schematic representation of the interaction between cationic octapeptide, lanreotide and counterions that tune the diameter of self assembled NTs. Reprinted from J. Am. Chem. Soc. 2012, 134, 1, 723-733. Copyright 2012 American Chemical Society. 112

Interfacial solar steam generation (ISSG)-based solar desalination carries great potential in mitigating the scarcity of fresh water. Wilson et al. reported poly (vinyl alcohol) (PVA) based hydrogel PVA-agar incorporated with multi-walled carbon nanotubes (MWCNT) with improved efficiency to desalinate the seawater (figure 1.9). They utilized kosmotropic ammonium sulphate to improve the mechanical strength of the hydrogel, which is crucial in governing the sustainability of the hydrogel based solar desalination. It is suggested that the presence of kosmotropic ions reduces the water-polymer interactions and improves the intermolecular hydrogen bonds between the polymers, thus enhancing the mechanical strength of the hydrogel.

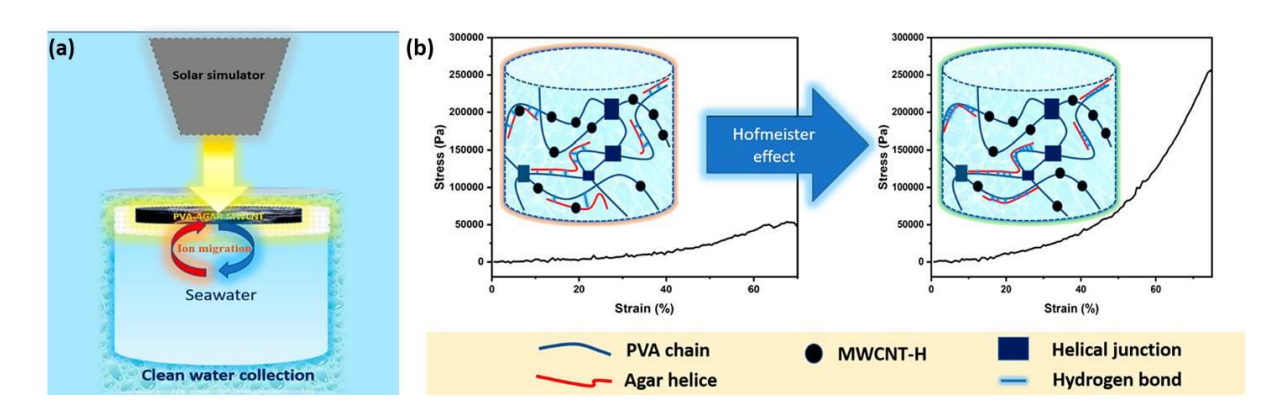


Figure 1.9 Schematic representation of (a) solar desalination using the PVA–agar–MWCNT-100 hydrogel and (b) improvement in mechanical strength of hydrogel after soaking in Hofmeister salt (NH₄)₂SO₄ owing to increased hydrogen bonding among polymers. Reprinted from ACS Appl. Mater. Interfaces 2022, 14, 42, 47800-47809. Copyright 2022 American Chemical Society. ¹¹⁷

Recycling oily wastewater is essential to mitigate the risk of environmental pollution during petroleum extraction. ¹¹⁹ Zuo et al. presented the application of the Hofmeister effect in the treatment of oily wastewater. ¹¹⁹ They reported that the gelatin-tannic acid-coated stainless steel mesh has shown a high water flux of over 1.74x 10⁵ Lm⁻²h⁻¹ and separation efficiency of 99% for oil/water separation. The authors utilized the Hofmeister effect to enhance the separation water flux of the mesh. It is said that immersing the mesh in NaCl solution led to improve gelatin swelling properties owing to enhanced hydrophobic interactions and chain binding within the gelatin that, in turn, resulted in good separation efficiency and wetting performance.

Colloidal nanodiamonds (NDs) have attracted considerable attention owing to their potential applications in the controlled delivery of therapeutics, proteins, DNA, and other biological agents. ¹²¹⁻¹²³ Guo et al. has investigated the impact of Hofmeister effect of salts and amino acids on doxorubicin (DOXH⁺) drug loading capacity of NDs of different sizes. ¹²² The performed experiments with inorganic salts: NaCl, Na₂SO₄, KCl, CaCl₂, (NH₄)₂SO₄ and amino acids: serine, glycine, alanine, arginine, and lysine. It has been reported that these inorganic salts and amino acids like arginine and lysine (isoelectric point above 7) increase the drug loading capacity of small nanodiamonds (SNDs, 5-10 nm). However, amino acids with isoelectric points below 7, like serine, glycine, and alanine, increase DOXH⁺ loading capacity of large nanodiamonds (LNDs, 80-100 nm). The loading efficiency is explained in terms of electrostatic interactions between H⁺ of doxorubicin (DOXH⁺) drug and negative, positive facets of SNDs and LNDs, respectively.

Biomolecular liquid-liquid phase separation (LLPS), which plays a vital role in developing protocells, has attracted significant research on the origin of life on other planets and synthetic biology. ¹³²Fetahaj et al. investigated the impact of Hofmeister salts (ClO_4^- and SO_4^{2-}) and high pressures encountered in the subsurface of Martian salt lakes on the formation of liquid-like biomolecular condensates of a variety of proteins (figure 1.10). ¹³² The authors studied the LLPS of coacervate ATP/polylysin, globular γ d-crystallin, partially disordered P-granule protein LAF1, and fully disordered peptide α -elastin. It is reported that the chaotropic (ClO_4^-) salts and kosmotropic (SO_4^{2-}) salts of the Hofmeister series carry different impacts not only on the stability of the proteins but also on the phase separation and formation of biomolecular condensates of various proteins under high pressures. It is proposed that the attractive short-range interactions, ion-correlation effects, hydrophobic and π -driven interactions enable LLPS and sustain habitability in extreme environments.

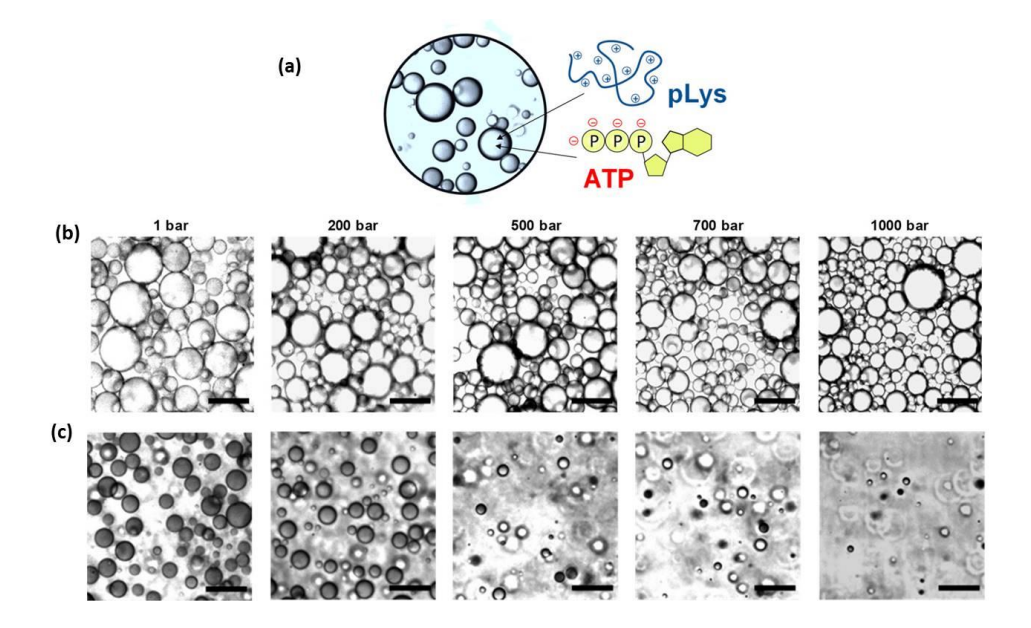


Figure 1.10 Pressure-dependent LLPS of the ATP/pLys system (schematically shown on the top (a)) in 30 mM Tris-buffer. Light microscopy snapshots of the LLPS of ATP and pLys without (b) and with (c) 250 mM NaClO₄ at selected pressures (1, 200, 500, 700, and 1000 bar). Sample: 40 mM ATP, 50 mM pLys (15–30 kDa), 30 mM Tris, pH 7.4, T = 25 °C. Scale bar: 30 μ m. Pressure-dependent LLPS of the ATP/pLys system in 250 mM NaClO4–Tris buffer. Reprinted from J. Am. Chem. Soc. 2021, 143, 13, 5247-5259. Copyright 2021 American Chemical Society. 132

Electrolyte MnO₂-Zn batteries are a potential alternative for Li-ion batteries with high cost and safety concerns. However, the production of protons during the battery charging process deteriorates Zn-metal and liberates H₂ gas. To mitigate this concern, Yuan et al. reported a proton barrier separator (PBS) based on poly(vinyl alcohol) (PVA) via the Hofmeister effect of SO₄²⁻ ions (figure 1.11). The presence of sulphate ions renders PVA to form a discontinuous hydrogen bond network with hydrophilic cages, which improve Zn²⁺ transfer but prevent proton migration to Zn anode and impede H₂-evolution. The cost-effective PBS deployed in electrolytic MnO₂- Zn batteries results in high energy retention (91.2% after 200 cycles) and enhanced rate performance (20 C) in a high areal capacity of 6.67 mAh cm⁻², which is better than the commercial aqueous metal-ion batteries. The contribution of the Hofmeister effect in the excellent electrochemical performance of Electrolyte MnO₂-Zn batteries is characterized by XRD, FTIR, XPS, and DFT calculations.

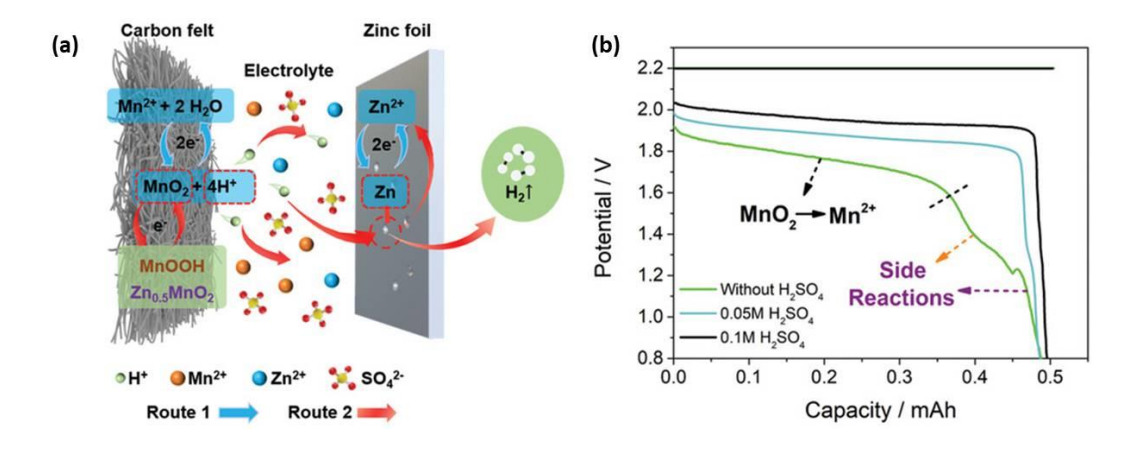


Figure 1.11 (a) Schematic Illustration of chemical reactions occurring in an electrolytic Zn-MnO₂ battery. (b) Charge–discharge curves of MnO₂–Zn batteries in electrolyte of 1 M MnSO₄ + 1 M ZnSO₄ + 0/0.05/0.1 M H₂SO₄. The battery is charged at 2.2 V to 0.5 mAh and discharged at 0.5 mA to 0.8 V. Reprinted from Adv. Energy Mater. 2022, 12, 16, 2103705. Copyright 2022 Wiley-VCH GmbH. ¹³³

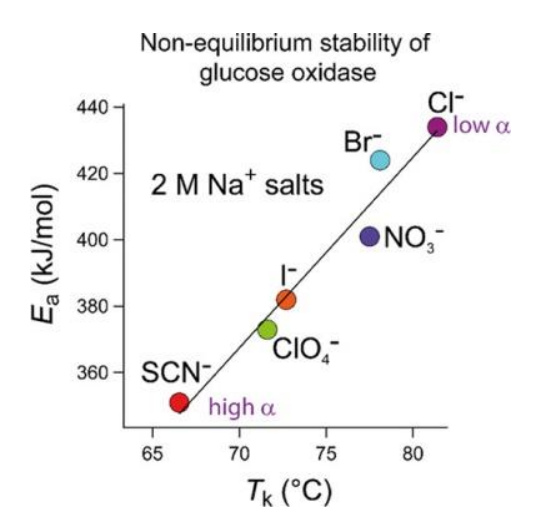


Figure 1.12 Ion-specific effect on the parameters describing the nonequilibrium stability of GOX at 2 M salt concentrations: activation energy, E_a , inactivation temperature T_k , and anion polarizability, α . Color codes for anions: thiocyanate (red), iodide (orange), perchlorate (green), bromide (light blue), nitrate (dark violet), and chloride (magenta). Reprinted from J. Phys. Chem. B 2019, 123, 38, 7965-7973. Copyright 2019 American Chemical Society.¹³⁶

Long-term stability of enzymes and proteins impacts their applications in biotechnology, the food industry, and clinical diagnostics. Sedlak et al. investigated the Hofmeister effect in unfolding kinetics of homodimeric glucose oxidase (GOX) from *Aspergillus niger* (figure 1.12). Using microcalorimetry, they showcased that for high salt concentration (> 1 M) the inactivation temperatures obey the Hofmeister effect at the protein/water interface. The authors pointed out that the surface tension of the protein/water interface is critical in determining the kinetic stability of the enzyme.

Till now, we have seen that the specific ion effects are explained in terms of ion-water and ion-macromolecule interactions. In an exciting study, Song et al. professed that the ion-specific water-macromolecule interactions also contribute in the origin of the Hofmeister effect.⁴⁰ The authors reported that the presence of ions significantly modulates the diffusion dynamics of water near hydrophilic POPC (1-palmitoyl-2-oleyl-sn-glycero-3-phosphocholine) lipid surfaces (figure 1.13).⁴⁰ They utilized Overhauser dynamic nuclear polarization (ODNP) relaxometry technique to quantify the translational dynamics of water near lipid vesicles and showcased that ion-specific changes in activation energies of diffusion follow the Hofmeister series (figure 1.13). This indicates that the strength of hydration water near hydrophilic lipid surfaces is perturbed in the presence of ions; the molecular level insights into the underlying mechanism require further investigation.

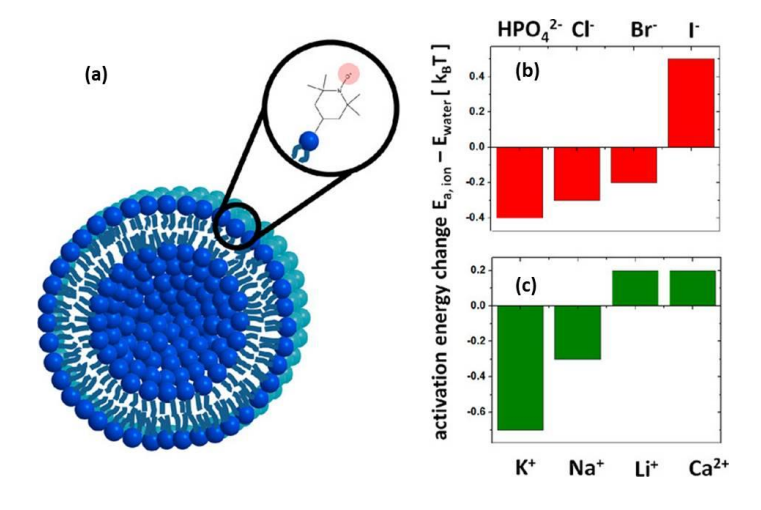


Figure 1.13 Ion affects water diffusion near the unilamellar vesicle surface with the order of the Hofmeister series. (a) Schematic diagram of spin-labeled phospholipid vesicles in an electrolyte solution. Spin-label, tempo, was drawn in the skeletal formula. It is not drawn to scale. Water diffusion activation energy for anions (b) and cations (c) follows the Hofmeister series. Activation energy error is $\pm 0.1 k_B T$. Reprinted from J. Am. Chem. Soc. 2014, 136, 6, 2642-2649. Copyright 2014 American Chemical Society.⁴⁰

1.4 Intermolecular Interactions

The presence and the nature of the dissolved electrolytes strongly influence the specific ion effects as discussed in the previous sections. The analysis of these phenomena leads to the Hofmeister sequence of ions. Its widespread applicability implies that the ion-specific phenomenon can be considered an interplay between different electrostatic, dipolar, and dispersion forces experienced by ions and molecules in different environments. Here, we provide a brief outlook on the intermolecular interactions (figure 1.14). 35-38, 140-141

The electrostatic potential Φ_{el} working between ions of charges (z_1e and z_2e) following Coulomb's law, is given by:

$$\Phi_{\rm el}(R) = \pm \frac{z_1 z_2 e^2}{4\pi \varepsilon_0 \varepsilon_r R} \tag{1.1}$$

Here, the z_1e and z_2e are considered point charges; the interionic distance R is assumed to be larger than their actual physical size. ε_0 and ε_r are the dielectric constants of the vacuum and the solvent, respectively. In an electrolyte solution, neighboring ions tend to screen the electrostatic interactions. Thus, the effective potential is approximated as:

$$\Phi(R)_{eff} \propto \Phi_{el}(R) \exp(-\kappa_D R)$$
 (1.2)

Here κ_D is the inverse of the Debye screening length. The Debye length measures the range of the electrostatic interactions that is ~ 0.8 nm or about three water molecules in the physiological media.

The interaction potential generated by ion-dipole interactions is given by:

$$\Phi_{\text{ion-dipole}}(R) = -\frac{ze\mu cos\theta}{4\pi\epsilon_0\epsilon_r R^2}$$
(1.3)

Here R is the distance between the ion and the center of the dipole (assuming R is much larger than the charge displacement in the dipolar molecule). θ is the angle made by the dipole vector with the ion-dipole axis. The average value, as obtained after integration over all possible orientations and using the Boltzmann distribution, is given by:

$$\langle \Phi_{\rm ion-dipole}(R) \rangle = -\frac{1}{6k_BT} \left(\frac{ze\mu}{4\pi\epsilon_0 \epsilon_r R^2} \right)^2 \eqno(1.4)$$

This formula implies that the distance at which the hydrating water molecules are strongly oriented in the presence of the ion electric field is approximated as:

$$R^* \approx \left(\frac{ze\mu}{4\pi\epsilon_0\epsilon_r k_B T}\right)^{1/2} \tag{1.5}$$

and for a generic ion in water, R^* is ~ 0.2 nm. The observed result suggests that the influence of ions on water structure is restricted up to approximately the first hydration shell only. The intuition drawn from this is quite debatable as supported ¹⁴²⁻¹⁴⁵ and opposed ¹⁴⁶⁻¹⁴⁷ by many studies.

Keesom or orientation potential for the interaction between two permanent dipoles μ_A and μ_B , as approximated by the thermal average over all angles of rotation, is given by:

$$\langle \Phi_{\text{orient}}(R) \rangle = -\frac{2}{3k_B T} \left(\frac{\mu_A \mu_B}{4\pi \epsilon_0}\right)^2 R^{-6}$$
 (1.6)

Here R is the distance between the dipoles, much larger than the charge displacements in the molecules A and B.

Induction or Debye term corresponds to the mutual polarization between two dipoles, A and B, due to the induction effect of a permanent dipole of one molecule on the electronic cloud of the other carrying a static polarizability $\alpha(0)$:

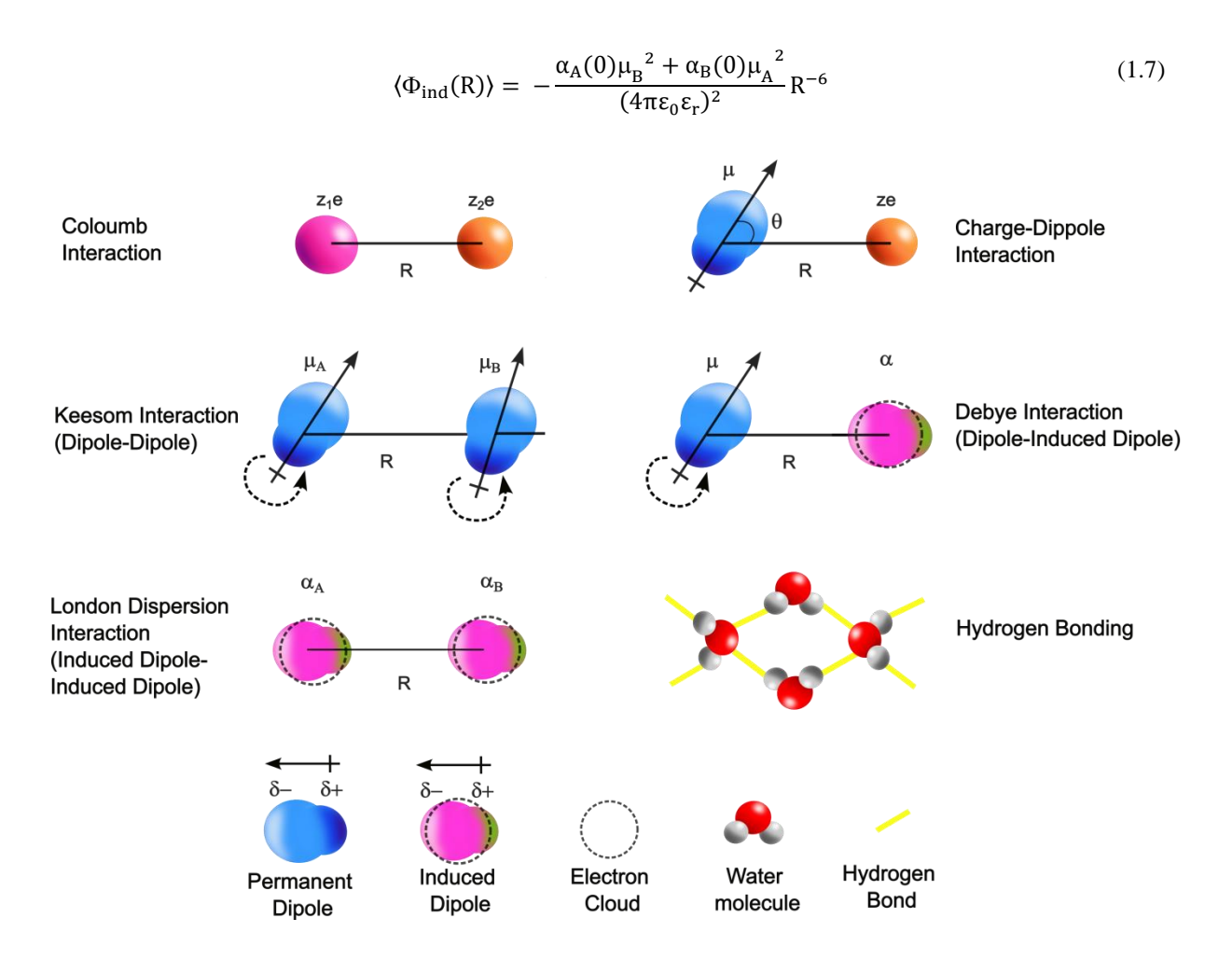


Figure 1.14 Illustration of interactions between atoms, ions, and molecules with distance R apart. μ , and α correspond to electric dipole moment and electric polarizability, respectively.

Another net attractive potential that exists in all polar and apolar species is London or dispersion interaction. It derives from the formation of instantaneous dipoles in the two interacting species and depends on the polarizabilities α and ionic potentials U of the participating molecules as:

$$\Phi_{\rm dis}(R) = -\frac{3\alpha_{\rm A}\alpha_{\rm B}U_{\rm A}U_{\rm B}}{2(4\pi\epsilon_0\epsilon_{\rm r})^4(U_{\rm A} + U_{\rm B})}R^{-6}$$
(1.8)

The expressions of interaction potential showcased here might differ by factors of two or more when ab initio calculations of polarizabilities and many-body effects are taken into consideration.³⁶

It is evident that Φ_{el} depends only on the net charges and stoichiometric coefficients. This implies that NaCl, NaBr, NaI, NaNO₃, NaSCN, and NaClO₄ should behave in the same manner, which is not the case (as seen in sections 1.2 and 1.3). However, the non-electrostatic potentials, which depend on μ , α , and U, carry the information on the distribution and properties of the electronic clouds surrounding the nuclei. Along with this,

Hydrogen bonding among water molecules, ions, and macromolecules determines specific ion effects in numerous observations. 35-39, 137-139,146-149 This special type of attractive interaction takes place between two neighboring moieties carrying an H-atom and an electronegative atom with lone pairs of electrons. 140-141, 146-152 The complicated short change interaction potential is inversely proportional to the distance R between the participating neighboring moieties. The term complex is attributed to the partial electrostatic and covalent nature of the H-bond as proposed by Pauling (1935) 150 and later confirmed by Isaacs (1999) through their Compton-scattering experiments. H-bonding tremendously prevails in determining the unique characteristics of liquid water and the stability of various biological systems. 140-141, 150-152 Shape is another crucial parameter participating in specific ion effects. Ions, like halides and chalcogenides, are spherical, whereas ions, such as nitrate, thiocyanate, perchlorate, dihydrogen phosphate, acetate, and hydroxide, possess a non-spherical structure. Consequently, they produce isotropic and/or anisotropic interactions since the polarizability in non-spherical ions during their interactions with another molecule or interface will depend on the direction of approach. 35-39, 140-141

Other interactions, such as π -ion interactions, acceptor-donor coupling, van der Waals forces, and steric and hydration interactions, also contribute to the specific ion effects. This motivates the development of a consistent and exhaustive theory that considers the impact of electrostatic, non-electrostatic, many-body interactions, and structural features to explain specific ion effects. In this regard, encouraging research work is in progress and reviewed in the literature. $^{35-39, 137-139, 153-156}$

1.5 Importance of Studying Specific Ion Effects at Air/Aqueous Interface

Specific ion effects at air/aqueous interfaces are widely involved in physical, chemical, environmental, and biological processes. 35-36, 39, 42, 67-68, 76, 134-135 The air/aqueous interface is defined as a boundary separating air and the liquid medium. This boundary region comprises the thickness of one to several molecular layers and possesses distinct properties compared to that of the bulk. This is decided by the orientation and structure of interfacial molecules, originating from the asymmetry of the electric field and forces experienced by the molecules present at the interface. 157-163 Ions at the air/water interface play a substantial role in numerous atmospheric and environmental chemistry processes, e.g., rain, evaporation of droplets across aerosol particles, cloud formation, ice nucleation, ozone depletion, etc. 64-65,69-70,164-166 The kinetics and thermodynamics of these processes are determined by the ion concentration, the ion speciation, and the influence of ions on the interfacial water structure. 35,64-65,164,167-171 Along with this, the interfacial water structure and intermolecular interactions in the presence of relative adsorption of ions at the air/aqueous interface control the thermodynamics of macromolecules and biomacromolecules in the aqueous solution that plays an imperative role in the modern surface science and technology. 35,39,42,67-68,76,101,134-135,172 To the special interest, it is considered that the widely applicable Hofmeister series microscopically pertains to the interface between a macromolecule and the ion solution. Investigating air/aqueous interface provides an ideal platform to selectively probe molecular level insights into various intermolecular interactions participating in the specific ion effects, like a) the adsorption of ions at the air/water interface, b) the adsorption of ions towards the macromolecule surface in light of Collin's Law of matching water affinities, c) the conventional interpretation of the impact of ions on the water structure in terms of water structure breaking/making, and d) the impact of ions on the water structure near the macromolecule surface. Therefore, it is essential to study the conformation of the macromolecule and the interfacial water structure at the air/aqueous interface to elucidate the mechanism that gives rise to the Hofmeister series.

1.6 Challenges in the Investigation of Air/Aqueous Interface

The investigation of the adsorption of ions at the air/aqueous interface and the consequent impact on the conformation and bonding environment of interfacial molecular groups encounters a couple of inherent challenges, discussed as follows. 35,173-174 First, the interfacial investigations comprise probing the molecular structure from the topmost few molecular layers of the system. However, the signals from conventional techniques such as Infrared, Raman, or UV-spectroscopy are often dominated by the bulk contributions and, consequently, lack surface specificity. Second, the interfacial region is prone to get contaminated from even a small impurity present in bulk or in the surrounding environment. Third, many robust surface-specific techniques such as electron loss spectroscopy, near-edge X-ray absorption fine structure spectroscopy (NEXAFS), X-ray photoelectron spectroscopy (XPS), and surface-enhanced Raman scattering (SERS) have special requirements to the sample preparation, environment conditions (e.g., UHV conditions) and huge equipments (e.g., synchrotron) that limit their applicability to the air/aqueous interface. An elegant alternative is sum frequency generation (SFG) vibrational spectroscopy, which is a second order nonlinear optical reflection technique that provides an intrinsic surface sensitivity up to ~1nm. The inherent surface specificity of SFG vibrational spectroscopy has been discussed in detail in the experimental section in chapter 2. Bloembergen and Pershan laid the theoretical background of nonlinear spectroscopy. 175 Du et al. were the first who recognize the potential as a surfacespecific probe in the mid-1990s. 176-177 Since then, SFG vibrational spectroscopy has emerged as a powerful noninvasive technique that contributed significantly to our current understanding of various air/aqueous interfaces. 35,39,42,159, 170-171,173-174,176-182 In the coming sections, we will discuss some fundamental insights on specific ion effects at air/water and air/aqueous interfaces as derived from the SFG vibrational spectroscopy.

1.7 Specific Ion Effects at Air/Water Interface

1.7.1 Conventional Textbook Picture of Depletion of Ions from the Air/Water Interface

The surface tension measurements derive the conventional picture of the air/water interface carrying simple salt solutions. First reported by Heydweiller et al.¹⁸³ there has been many literatures reporting the surface tension studies on various salt solutions.^{35,64-66,170,184-186} In general, the surface tension of water is increased in the presence of ions. For anions, the excess surface tension follows the Hofmeister series as well.^{35,64-66,170,183-186} However, it is worth mentioning that certain combinations of ions decrease the surface tension or have a negligible effect.^{35,66,184-186} The thermodynamic analysis of the surface isotherm implies that the interfacial zone is depleted of ions. ^{35,184-186} The surface deficiency is calculated by using the Gibbs equation: ^{35,184-186}

$$\Pi_{\rm el}^{\rm H_2O} = -\frac{1}{\rm R_g T} \left(\frac{\rm d\sigma_{\rm st}}{\rm dlna_{\rm el}} \right) \tag{1.9}$$

Here, σ , a_{el} , R_g and T designate the equilibrium surface tension, electrolyte activity, gas constant, and temperature. Since the slope of the isotherm comes out to be positive, it is concluded that the interfacial region is depleted of ions. Wagner and Onsager and Samaras (WOS) provided an explanation of this behavior. 35,66,187 They suggest that an ion is repelled from the interface between two media of different dielectric constants as an image charge of the same size and polarity is located on the other side of the interface. These observations and interpretations of the deficiency of ions at the air/water interface define the textbook picture.

This point of view was initially challenged by Frumkin when he reported that all the halogen salts (except fluoride) make the potential difference across the air/water interface more negative compared to the pristine

air/water interface. This indicates that in comparison to cations, halogen anions (except fluoride) are prone to get adsorbed towards the interface. The conventional interpretation of ions at the air/water interface as provided by WOS theory, has been further challenged by the progress in understanding atmospheric reactions, which motivated molecular dynamics (MD) simulations. MD simulations using polarizable force fields predict that soft ions such as halides are enriched at the interface and possess non-monotonic ion profiles (figure 1.15). Evidently, direct experimental evidence of the ion profiles is highly necessitated. In this direction, some critical SFG results are discussed in the coming section.

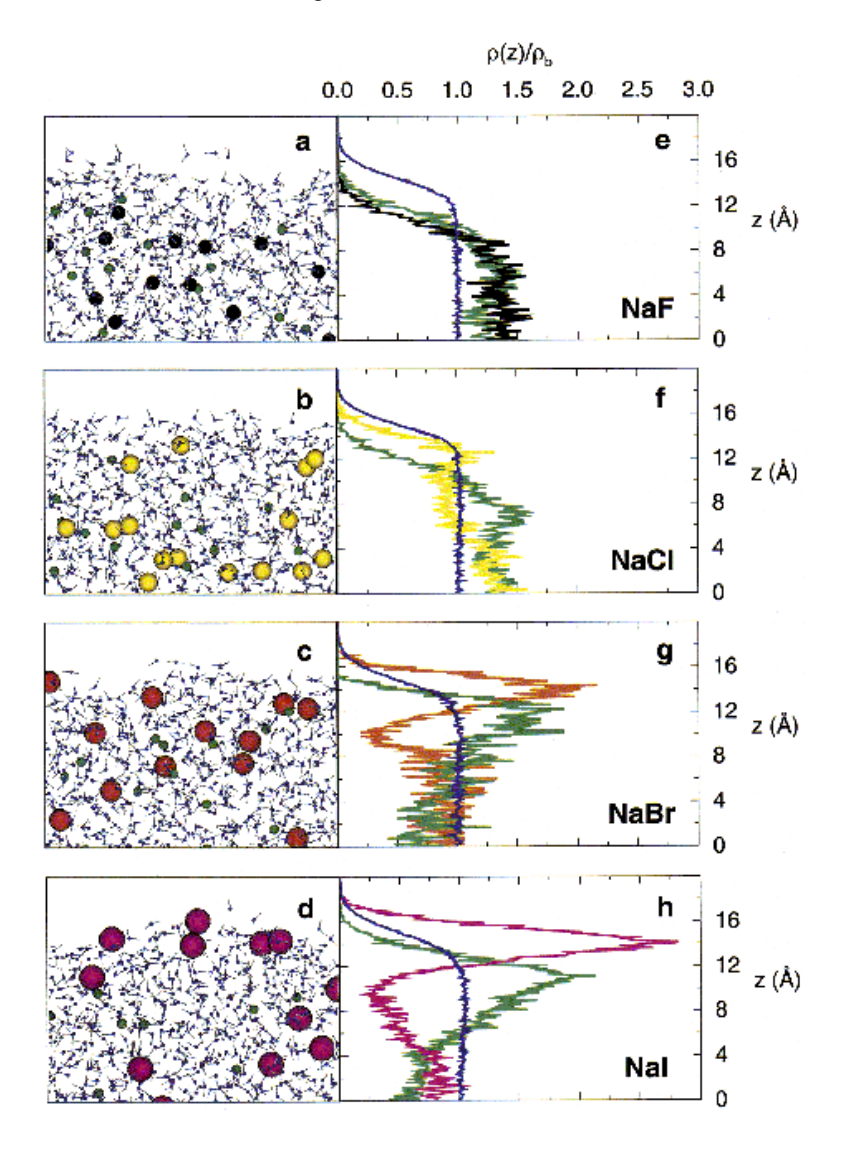


Figure 1.15 (a)–(d), Snapshots of the solution/air interfaces from the molecular dynamics simulations. Coloring scheme: water oxygen, blue; water hydrogen, gray; sodium ions, green; chloride ions, yellow; bromide ions, orange; iodide ions, magenta. e–h, Number densities, $\rho(z)$, of water oxygen atoms and ions plotted vs distance from the center of the slabs in the direction normal to the interface (z), normalized by the bulk water density, ρ_b . The ion densities have been scaled by the water/ion concentration ratio of 48 for ease of comparison. The colors of the curves correspond to the coloring of the atoms in the snapshots. Reprinted from J. Phys. Chem. B 2001, 105, 43, 10468-10472. Copyright 2001 American Chemical Society. 189

1.7.2 SFG Investigations on Specific Ion Effects at the Air/Water Interface

Various research groups have investigated the distribution of ions in the interfacial region and their impact on the water structure at the air/water interface. This section presents some of the significant results and the understanding developed in this field supported by a thorough discussion of appropriate literature based on SFG vibrational spectroscopy.

Liu et al. performed SFG vibrational spectroscopy experiments to probe the surface structure of aqueous halide solutions. ¹⁹⁰ It is evident from the spectra in figure 1.16 that the presence of anions significantly perturbs the H-bonding network of water at the air/water interface. The SFG spectrum at the neat air/water interface consists of a broad H-bonded region from 3000-3600 cm⁻¹ and a sharp peak at 3700 cm⁻¹ attributed to the free OH oscillator protruding from the interface. The enhancement in SFG intensity around 3400 cm⁻¹ band (weakly H-bonded band) follows the order I⁻ > Br⁻ > Cl⁻. However, there is some decrement in SFG intensity around 3250 cm⁻¹ (Strongly H-bonded band) in a similar order compared to the pristine water interface. The SFG results, when compared to the bulk water structure profiles of aqueous halide solutions using ATR-FTIR spectroscopy, indicate the higher adsorption of iodide and bromide towards the air/water interface. Based on this data set, the authors confirmed the prediction of the MD simulation results regarding the enhanced adsorption of the more polarizable anions within the interfacial region. ¹⁸⁹

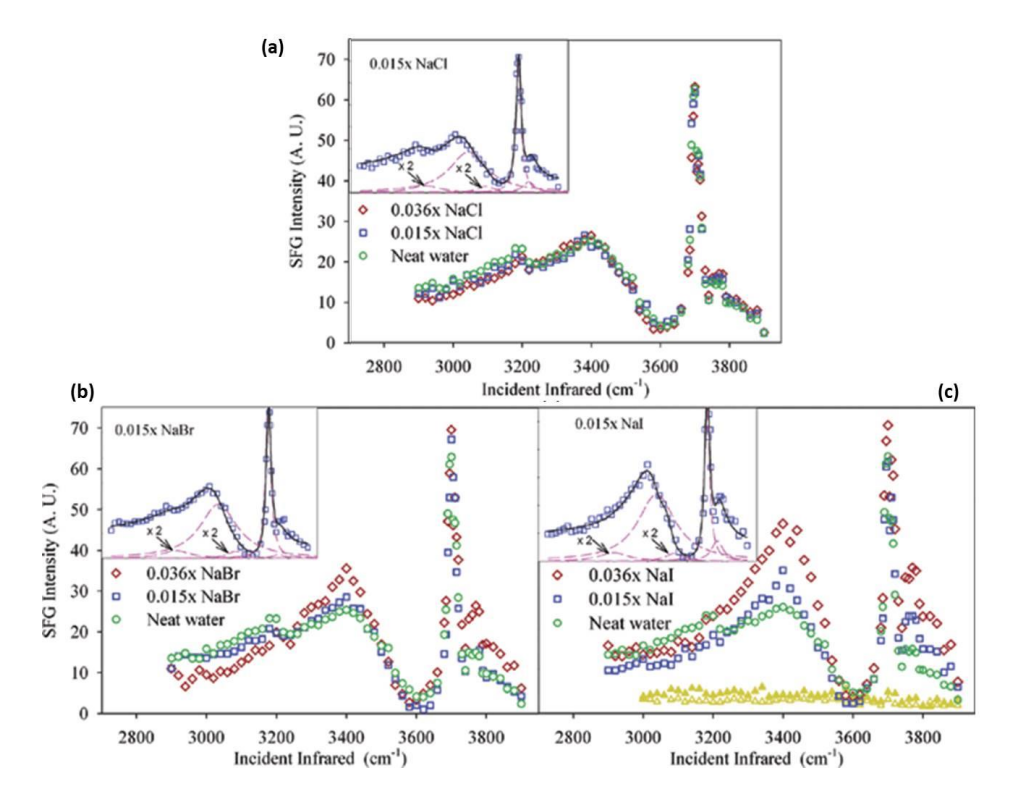


Figure 1.16 SSP polarized SFG spectra of (a) 0.015x and 0.036x NaCl, (b) 0.015x and 0.036x NaBr, and (c) 0.015x and 0.036x NaI. The neat water SFG spectrum is plotted in each figure for comparison. The open yellow and closed yellow triangles within (c) show the sum frequency intensity of the 0.015x NaI in D_2O and pure D_2O , respectively. Insets: SFG sodium halide aqueous solutions spectral fits. Component Lorentzian peaks are shown as dashed pink lines, and the calculated fits from the component peaks are shown as black lines that go through most of the data points. Reprinted from J. Phys. Chem. B 2004, 108, 7, 2252-2260. Copyright 2004 American Chemical Society. 190

Later, similar SFG intensity profiles for NaI, NaBr, and NaCl were reported by Raymond et al. ¹⁹¹ The surface propensity of iodide anion near the air/water interface and their influence on the interfacial water hydrogen bonding structure was further supported by phase-sensitive SFG studies by Tian et al. ¹⁹² Piatkowski et al. utilized the static and time-dynamic SFG spectroscopy to study the energy transfer rates between interfacial water molecules at air/solution interface carrying NaCl and NaI in heavy water. ¹⁹³ The authors reported that the presence of anions affects the interfacial water structure and brings a blue shift in the hydrogen-bonded OD feature (between 2350 cm⁻¹ and 2600 cm⁻¹). It is reported that the blue shift for NaI is more significant than NaCl implies that the strength of H-bonded interfacial water decreases as follows: Cl⁻>I⁻, which points towards the surface propensity of anions. This, in turn, results in a weaker vibrational energy transfer between surface water molecules.

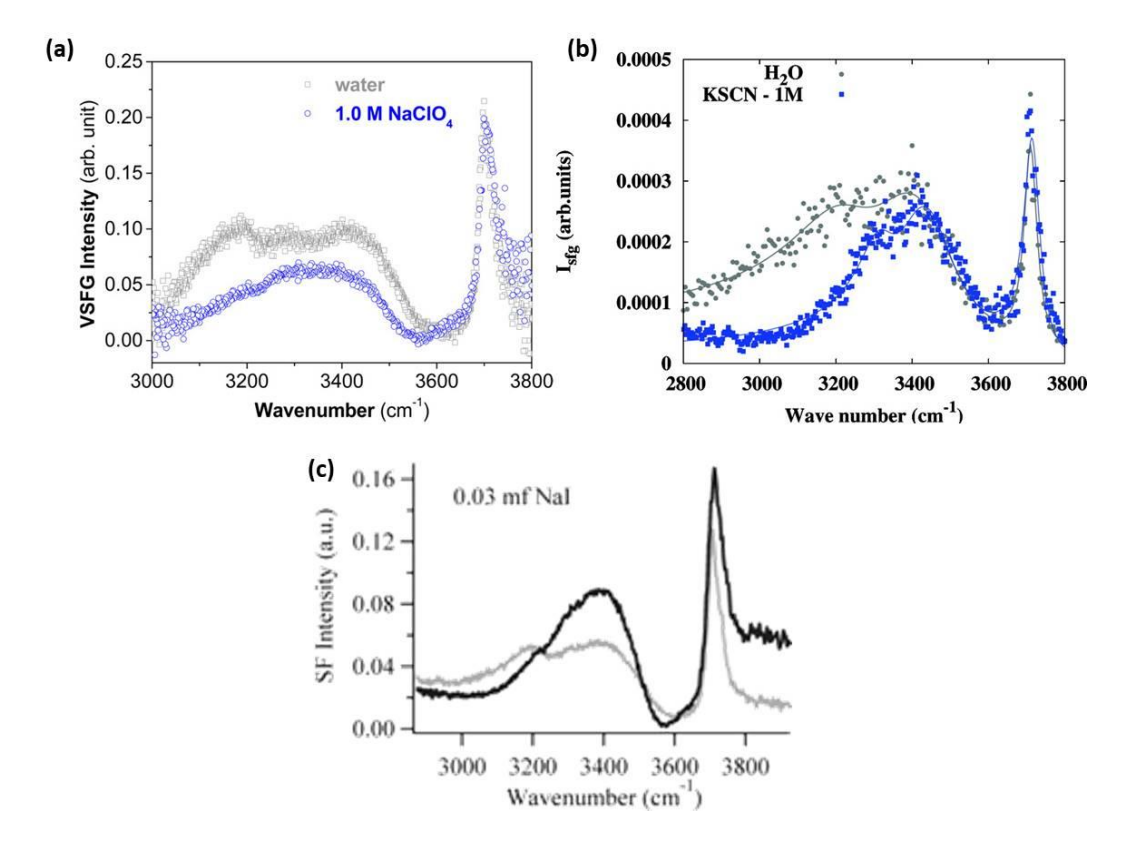


Figure 1.17 (a) Vibrational sum frequency spectra of water and ~ 1 M potassium thiocyanate solution. The presence of the ions at the interface decreases the 3200 cm⁻¹ band. The points and continuous lines represent the experimental data and fits, respectively.¹⁹⁴ (b) Conventional VSFG $|\chi_{\rm eff}^{(2)}|^2$ spectra of the air/aqueous interfaces of neat water and 1.0 M NaClO₄ salt solution across the entire OH-stretching region (3000–3800 cm⁻¹).¹⁹⁵ (c) VSF spectra of 0.03 mf NaI in H₂O (black).¹⁹¹ A neat vapor/water spectrum (grey) is shown for comparison. Reprinted from J. Phys. Chem. Lett. 2013, 4, 24, 4231-4236;¹⁹⁴ J. Phys. Chem. C 2007, 111, 12, 4484-4486;¹⁹⁵ J. Phys. Chem. B 2004, 108, 16, 5051-5059.¹⁹¹ Copyright 2013, 2007 and 2004 American Chemical Society.

Moving towards other chaotropic anions of the Hofmeister series, Hua et al. studied the water structure organization and propensity of perchlorate anion at the air-water interface. Figure 1.17a presents SFG spectra of air/NaClO₄ solution, where we have observed a significant decrement in the intensity of broad OH-region in comparison to the neat air/water interface. The spectral profile in OH-region indicates that the water structure is disordered in the presence of perchlorate anions in comparison to the pristine air/water interface. This points towards a significant surface propensity of the perchlorate anion for the air/water interface. Viswanath and

Motschmann studied the most chaotropic anion, thiocyanate at the air/water interface in an interesting way. ¹⁹⁵⁻¹⁹⁶ Till now, we have seen that the ions were monitored indirectly through SFG measurements, where the presence of ions is realized through the impact of the ions on the water structure. Figure 1.17b shows the interfacial water structure in the presence of thiocyanate anion at the air/water interface. ¹⁹⁵ Evidently, a significant decrement is observed around 3200 cm⁻¹. Interestingly, along with probing the impact of ions on the interfacial water structure, the authors also monitored the CN-stretching vibration (2064 cm⁻¹) of the SCN⁻ anion in different polarization combinations. It is reported that the rod-like SCN⁻ anion adopts **a** preferential orientation of 45° with respect to the surface normal. ¹⁹⁶ The combined data confirms the surface enrichment of the anion at the interface.

In figure 1.17, we have showcased the SFG spectra of the air/water interface carrying different monovalent chaotropic anions ClO_4^- , SCN^- , and I^- . The distinct OH-region spectral features provide an interesting comparison of the influence of different anions (despite carrying similar charges) on the water bonding network at the air/water interface. The observed ion-specific disordering effect on the interfacial water structure could be attributed to the shape anisotropy of the anions involved, i.e., the tetrahedral structure of ClO_4^- , linear SCN^- , and spherical I^- . I^{194}

In order to detect the relative distributions of ions at the charged interfaces, Tian et al. employed phase-sensitive SFG vibrational spectroscopy at the air/water interface for a set of different salt solutions containing a variety of ions: I^- , NO_3^- , Cl^- , SO_4^{2-} . ¹⁹² The authors measured the imaginary second-order nonlinear susceptibility of the air/aqueous interface. The measurement characterizes the vibrational response from the surface water molecules and informs about the strength and direction of the surface field owing to the presence of ions. It is reported that the relative surface propensities of ions at the air-water interface follow the order: $I^- > NO_3^- > Cl^- > SO_4^{2-}$. I^- and NO_3^- have shown a significant propensity of adsorption towards the surface, whereas sulphate (SO_4^{2-}) is repelled from the surface and lying closer to the bulk water. The observations agree with the predictions of MD simulations. ^{164, 179, 189, 197-198} Based on the relative tendency of anions toward the interface; they are also known as hydrophobic/hydrophilic ions. The chaotropic ions like I^- , and NO_3^- which are prone towards the hydrophobic air/water interface are termed hydrophobic ions, whereas the kosmotropic anion like SO_4^{2-} which tend toward the bulk water are known as hydrophilic ions.

In contrast to the chaotropic ions, which we have discussed in the preceding sections, the kosmotropic anions like sulphate (SO_4^{2-}) , fluoride (F^-) and carbonate (CO_3^{2-}) are found to be repelled from the topmost surface layers. The ions are reported to be lying closer towards the bulk water and are known as buried ions. It would be interesting to visualize how the presence of these buried ions affects the interfacial water structure. In the coming section, we will discuss the influence of SO_4^{2-} , F^- and CO_3^{2-} ions on the water structure at the air/water interface.

Different research groups have recorded the SFG spectra at the air/water in the presence of NaF, but there exists an inconsistency in the reported spectra, as shown in figure 1.18. Liu et al. reported that the presence of NaF does not bring significant changes in the bonded OH region (3000-3600 cm⁻¹), and the SFG spectrum is consistent with that of the neat air/water interface, as shown in figure 1.18a. However, Raymond et al. reported a significant decrement in SFG intensity in the bonded OH region in the presence of NaF compared to the neat air/water interface (figure 1.18b). He SFG spectrum at the air/water interface in the presence of NaF as measured by Feng et al. Significant to that reported by Raymond et al. In contrast, Imamura et al. calculated

the SFG spectrum of NaF solution using MD simulation (figure 1.18c), which appears to be analogous to the neat air/water interface. Recently, Roy et al. reported SFG spectra at the air/NaF-water interface, and the results are consistent with those reported by Richmond and coworkers. Imamura et al. pointed out that the observed discrepancy among the reported experimental SFG spectra of NaF could be attributed to some uncontrollable surface impurities in their experimental conditions. The authors speculated that the intrinsically generated species like HF and OH during the hydrolysis of F ions in the NaF solution could act as impurities at the air/aqueous interface that might result in inconsistent spectra of NaF from different research groups.

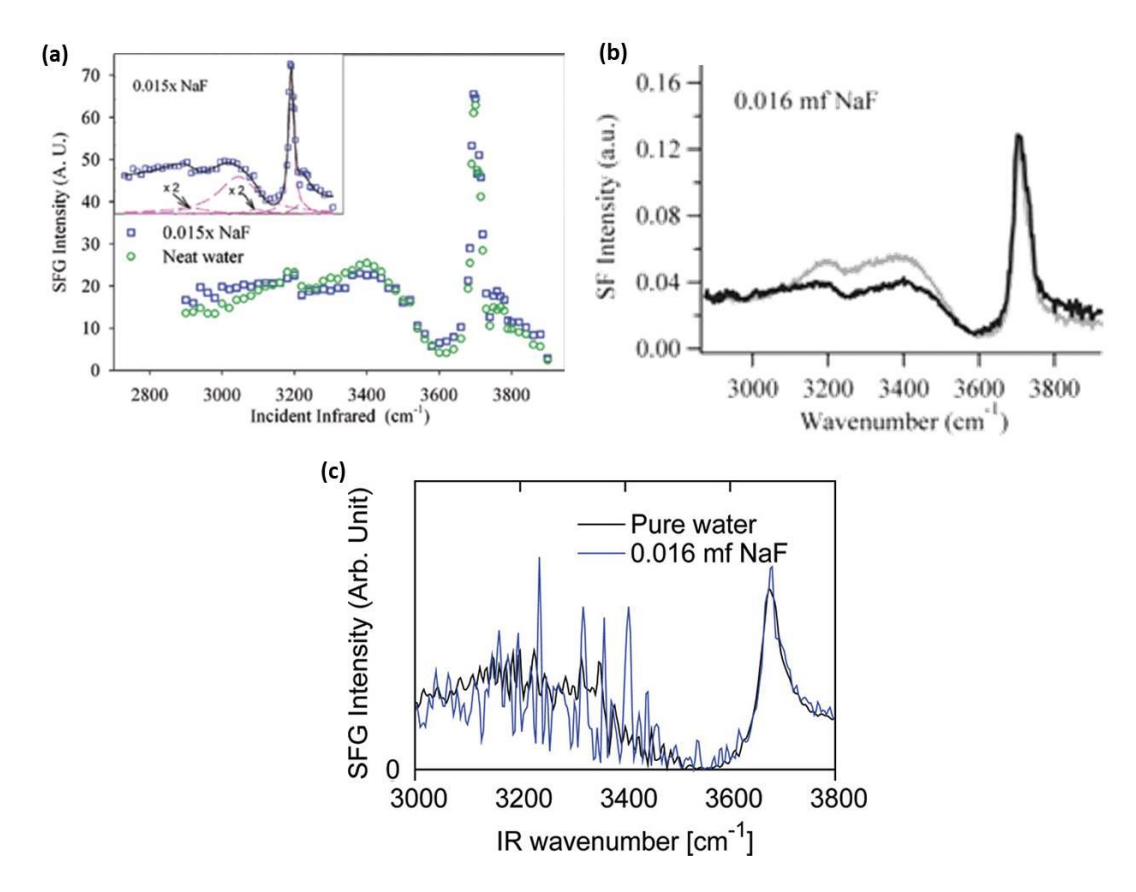


Figure 1.18 (a) SSP polarized SFG spectra of 0.015x NaF. Insets: SFG sodium halide aqueous solutions spectral fits. Components of Lorentzian peaks are shown as dashed pink lines, and the calculated fits from the component peaks are shown as black lines that go through most of the data points. ¹⁹⁰ (b) VSF spectra of 0.016 mf NaF in H₂O (black). A neat vapor/water spectrum (grey) is shown for comparison. ¹⁹¹ (c) Calculated SFG spectra of aqueous NaF solution and neat water. ²⁰⁰ Reprinted from J. Phys. Chem. B 2004, 108, 7, 2252-2260; ¹⁹⁰ J. Phys. Chem. B 2004, 108, 16, 5051-5059; ¹⁹¹ J. Phys. Chem. C 2012, 116, 20, 11082-11090. ²⁰⁰ Copyright 2004 and 2012 American Chemical Society.

In contrast to F^- ion, the presence of other kosmotropic anions like SO_4^{2-} , and CO_3^{2-} bring significant perturbations in the interfacial water structure (figure 1.19). The SFG spectra show significant intensity enhancement in the lower frequency region around 3200 cm⁻¹ for the presence of Na_2SO_4 and Na_2CO_3 at the air/water interface. Similar spectral profiles have been reported by Tarbuck et al. and recently by Deiseroth et al. at the air/D₂O interface. The substantial increase in SFG intensity for the vibrational feature of tetrahedrally coordinated water around 3200 cm⁻¹ is explained as the convolution of strong ion-dipole interactions and orientation of water molecules in the presence of the surface field of ions buried deeper in the interface. The interpretation is supported by various groups. Interestingly, Deiseroth et al. pointed out that in comparison to the

SFG spectrum for carbonate, there is an enhancement around 3400 cm⁻¹ as well for the presence of sulphate at the interface. The authors speculate that in comparison to sulphate, carbonate is effectively involved in strengthening the H-bonded water structure at the interface. The water structure making capacity of kosmotropic anions is further examined by Roy et al. The authors performed the isotopic dilution studies at the air/water interface in the presence of F⁻and CO_3^{2-} anions. By combining phase-sensitive SFG spectroscopy and Raman spectra, they reported the existence of strongly hydrogen-bonded water molecules in the hydration shell of the kosmotropic anions CO_3^{2-} and F⁻. The degree of structure making capacity of the anions follows the order: $CO_3^{2-} > F^-$.

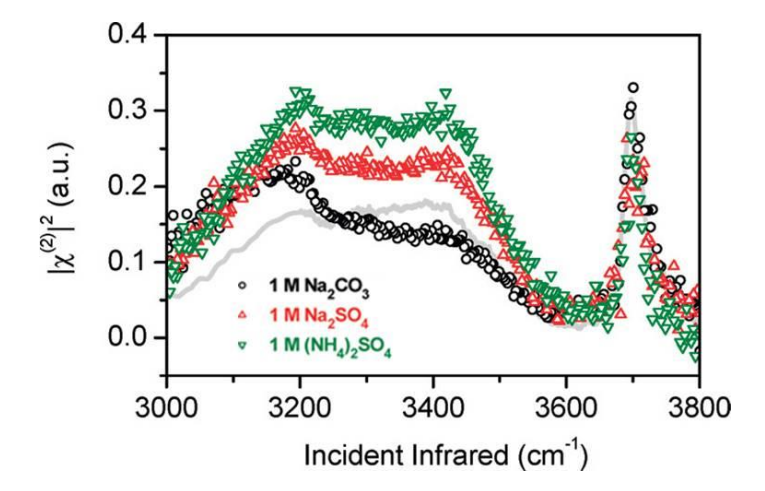


Figure 1.19 Conventional VSFG $|\chi^{(2)}|^2$ spectra of water molecules at vapor/aqueous solution interfaces of 1.1 M Na₂CO₃, 1.1 M Na₂SO₄, and 1.1 M (NH₄)₂SO₄ salt solutions. Neat water spectra are shown as a reference (light gray line). Reprinted from J. Phys. Chem. Lett. 2011, 2, 20, 2515-2520. Copyright 2011 American Chemical Society.²⁰²

1.8 Specific Ion Effects at Air/Aqueous Interface

The previous section discussed a critical literature review on SFG studies at the air/water interface carrying inorganic ions. In this section, we have targeted a more complex system. Here, we present SFG spectroscopic studies on the air/aqueous interface, where the aqueous solution is a ternary mixture consisting of ions, water, and a macromolecule.

Gurau et al. investigated specific ion effects on fatty amine monolayer of octadecylamine (ODA) spread at the air/water interface. The authors probed the impact of ions on the ordering/disordering of the monolayer at the air/aqueous interface and the interfacial water structure. Significant variation in SFG intensities for methyl symmetric stretch, v_s (CH₃) at 2891 cm⁻¹ and the methylene symmetric stretch, v_s (CH₂) near 2863 cm⁻¹ is observed as a function of anion in the aqueous subphase (figure 1.20a). The resultant ion-specific ordering in the ODA monolayer follows the anionic Hofmeister series. The ion-specific changes in the monolayer structure are attributed to the portioning of ions at the air/aqueous interface. The chaotropes iodide, perchlorate and thiocyanate are prone toward the hydrophobic groups at the interface and disrupt the monolayer ordering. In contrast, the kosmotropic sulphate anion resides more towards bulk and has little tendency to disrupt the structure. The sum frequency spectra in the OH-stretch region (figure 1.20b) show significant variation in intensity, which is attributed to the orientation of water molecules in the presence of the surface field of ions at the air/aqueous interface. However, no correlation between the Hofmeister series and the ion-specific orientation

of interfacial water could be observed. The authors conclude that the dispersion forces (ion-macromolecule interactions) play a large role in the order of the Hofmeister series compared to mere changes in interfacial water structure (figure 1.20).

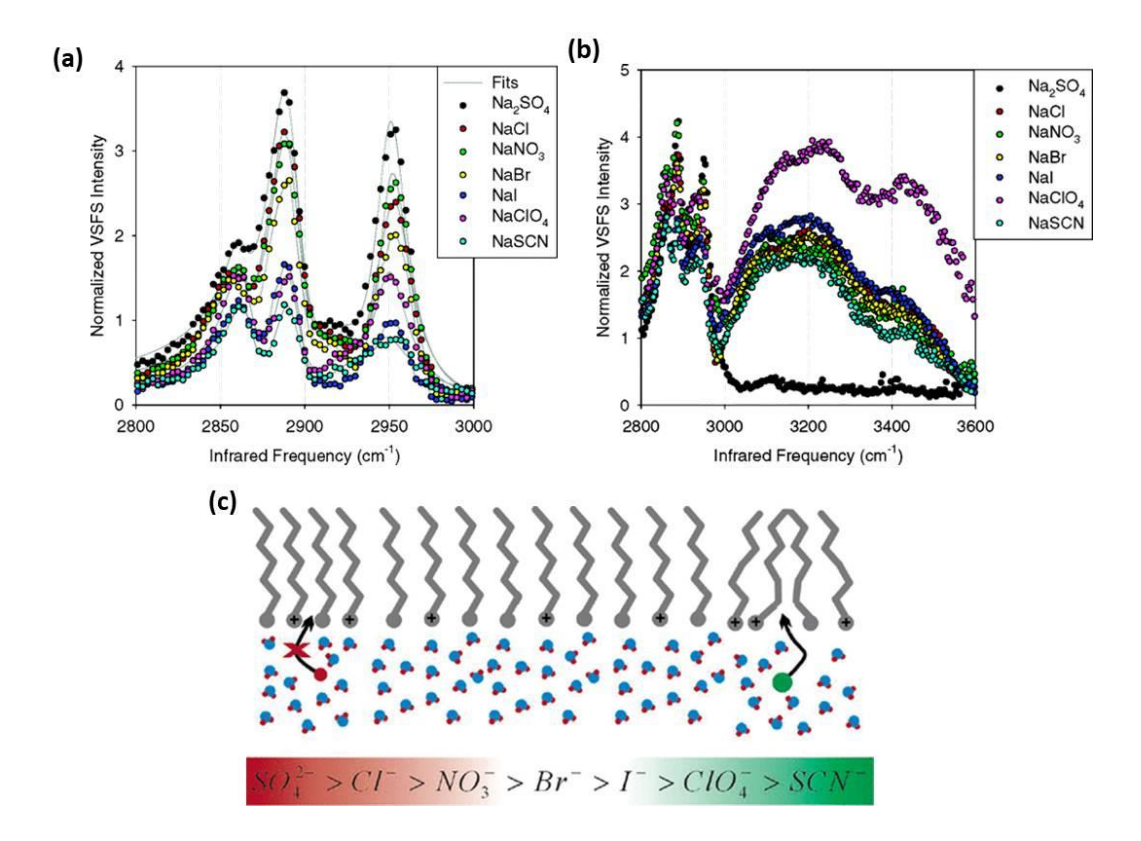


Figure 1.20 SFG spectra of ODA monolayers ($\Pi = 15 \text{ mN/m}$) spread on (a) D₂O subphases and (b) H₂O subphases at 20 °C. Each subphase contained 10 mM of a given salt as indicated in the legend. All spectra were recorded with the ssp (s - signal, s - visible, p - infrared) polarization combination. All the spectra in panel (a) are normalized to the signal from a piece of z-cut crystalline quartz. (c) Model representation of ODA monolayers spread on aqueous subphases, where the disruption of alkyl chain ordering is ascribed to the relative propensity of anions to penetrate into the hydrophobic region of the monolayer. Reprinted from J. Am. Chem. Soc. 2004, 126, 34, 10522-10523. Copyright 2004 American Chemical Society.⁶⁷

Poly-(N isopropylacrylamide), i.e., PNIPAM is a thermoresponsive polymer whose lower critical solution temperature (LCST) is found to follow the Hofmeister series.⁶⁸ In order to investigate the underlying intermolecular interactions participating in the Hofmeister effect, Chen et al. studied specific ion effects on the interfacial water structure at the air/ PNIPAM aqueous interface using SFG vibrational spectroscopy (figure 1.21a).⁶⁸ They found that anion-induced orientation of water dipoles and variation in OH-region SFG intensity obeys the Hofmeister order (figure 1.21b). In contrast, ions did not significantly perturb the structural alignment of PNIPAM at the air/aqueous interface, as evidenced by the nearly similar SFG intensities in the CH-stretch region (Figure 1.21c). The alignment of interfacial water structure is ascribed to the anion induced variation in surface charge density as a consequence of ion-macromolecule interactions at the air/aqueous interface.

In another work, Chen et al. investigated the impact of ions on the interfacial water structure adjacent to bovine serum albumin (BSA), surfactant monolayers (positively charged 1,2-dipalmitoyl-3-trimethylammonium-propane (chloride salt) (DPTAP), negatively charged sodium 1-dodecanesulfonate (DS), and zwitterionic 1,2-dilauroyl-sn-glycero-3-phosphocholine (DLPC)) and neutral elastin-like polypeptide (ELP) monolayer at the

air/water interface.⁷⁶ The authors observed different degrees of enhancement/attenuation in the OH-region SFG intensity in the presence of ions for various systems at the air/aqueous interface. The results are explained in terms of net surface charge density owing to the adsorption of ions at the air/aqueous interface that governs the specific ion effects.

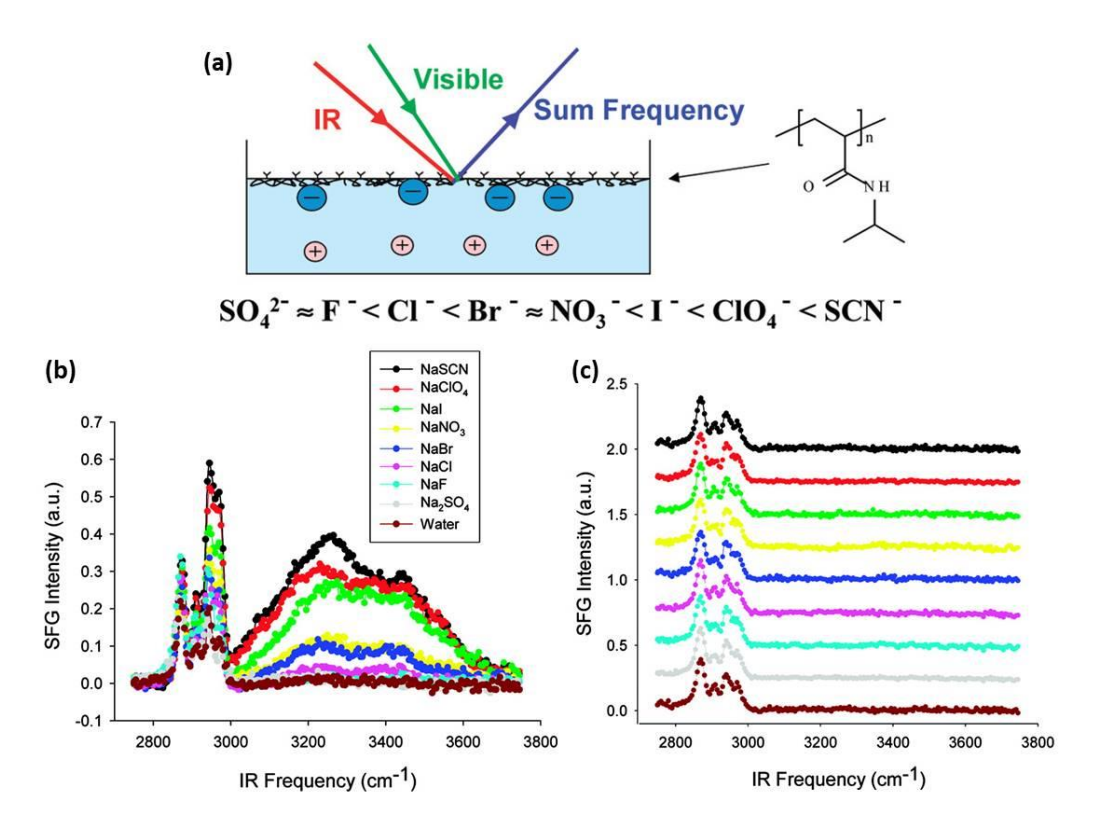


Figure 1.21 (a) Model representation of SFG studies on Poly-(N-isopropylacrylamide) adsorbed at the air/water interface. (b) SFG spectra show specific anion effects on PNIPAM adsorbed at the air/water interface. Each subphase contained 1 M of a given salt, as indicated in the legend, except for NaF and Na₂SO₄, which are measured with saturated solutions (~0.8 M for both salts). (c) The same experiments were repeated with D₂O. The spectra are offset for clarity. It was found that the relative propensity of ions to orient interfacial water molecules follows the Hofmeister series. Reprinted from J. Am. Chem. Soc. 2007, 129, 40, 12272-12279. Copyright 2007 American Chemical Society.⁶⁸

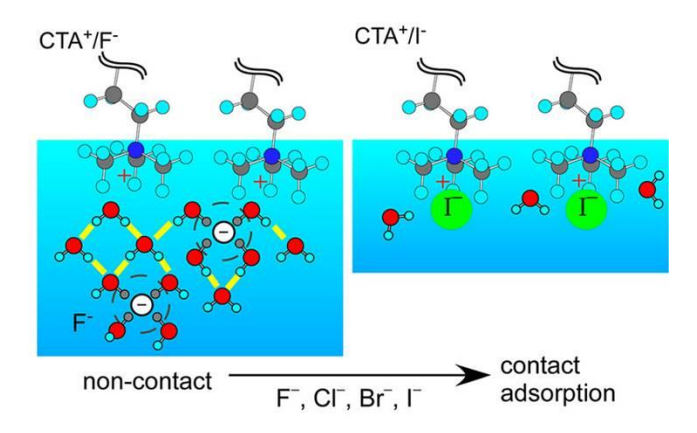


Figure 1.22 Schematic model of the CTA⁺/F⁻ and CTA⁺/I⁻ interfaces. Yellow line represents the hydrogen bond. Gray hydrogen inside the dashed circles is less $\chi^{(2)}$ active. Reprinted from J. Am. Chem. Soc. 2014, 136, 17, 6155-6158. Copyright 2014 American Chemical Society.²⁰⁵

Nihonyanagi et al. applied heterodyne-detected vibrational sum frequency generation spectroscopy to study the anion effect on the interfacial water structure at the positively charged cetyltrimethylammonium (CTA⁺) monolayer/electrolyte solution interface (figure 1.22).²⁰⁵ The intensity of the OH band of the interfacial water decreases in the order of the Hofmeister series. This is reported that the adsorption of halide anions onto the interface governs the Hofmeister order, similar to the previous reports by Chen et al.^{68,76}

The charge state of amine groups plays a crucial role in many biological functions. ²⁰⁶ Using SFG spectroscopy, Sung et al. demonstrated that the presence of salts facilitates the protonation of primary amine headgroups at the air/aqueous interface (figure 1.23). ²⁰⁶ For this, they investigated the interfacial water structure at the air/aqueous interface consisting of primary fatty amine (ODA) with different salt concentrations (NaCl, NaI). By increasing the ionic strength, an enhancement in SFG intensity of the water OH band was observed up to ~1 mM, followed by a decrement thereafter. The authors suggested that the primary amine headgroups are initially nearly chargeneutral even at pH much lower than its pKa due to the effect of nearby amine groups in the compact monolayer. The addition of salt in the solution promotes protonation of these amine groups to reorient water molecules giving rise to strong SF signal; subsequently, counter ion adsorption screens the electric field.

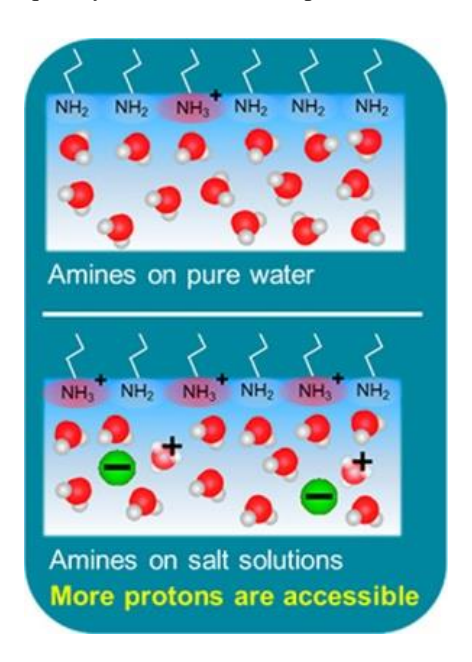


Figure 1.23 Model Representation of ion-induced protonation of primary amine headgroups at ODA/water interface. Reprinted from J. Phys. Chem. Lett. 2017, 8, 15, 3601-3606. Copyright 2017 American Chemical Society.²⁰⁶

Lovering et al. investigated specific ion effects in the solvent extraction process of lanthanides. 207 It is known that with quaternary amine methyltrioctyl ammonium (TOMA⁺) salt as an extractant, lighter lanthanides are better extracted in the presence of NO $_3^-$ ions, whereas heavy lanthanides are better extracted in the presence of SCN $^-$. In order to provide molecular level insights into the extraction selectivity of anions, the authors performed SFG spectroscopy at the air/aqueous interface. It is reported that the anion-specific dramatic variation in the OH-region solvation water structure of the monolayer could be responsible for the ion selectivity towards the lanthanides in the solvent extraction systems (figure 1.24).

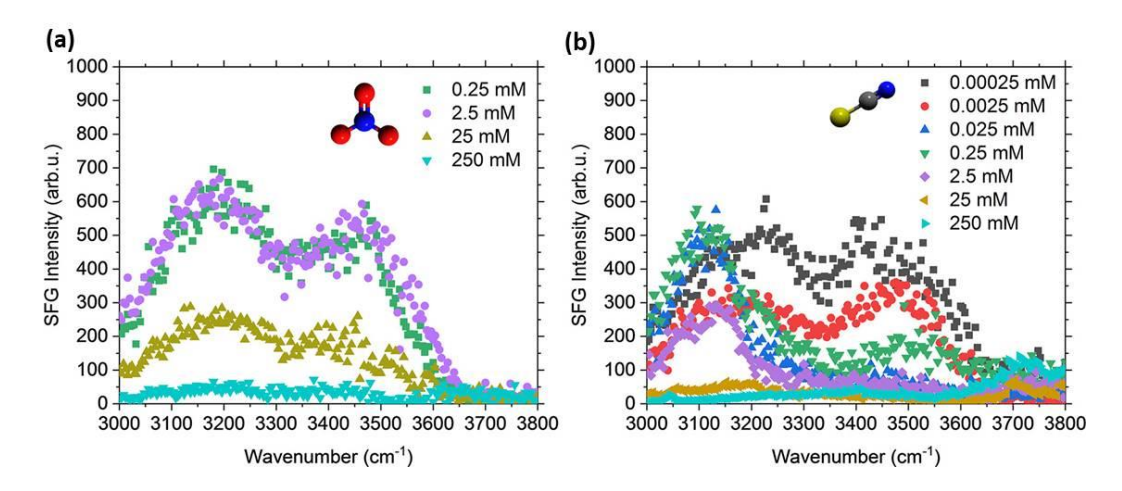


Figure 1.24 OH stretching region of (a) NaNO₃ solutions and (b) NaSCN solutions in contact with DPTAP⁺ monolayers in an SSP polarization combination. In part a, the SFG intensity decreases uniformly with concentration, while in part b, the SCN ions apparently lead to more substantive changes at the air/aqueous interface. Reprinted from J. Phys. Chem. C 2020, 124, 1, 573-581. Copyright 2020 American Chemical Society.²⁰⁷

Interestingly, Neil et al. studied the anion binding selectivity of cationic surfactant guanidinium receptor anchored at air/aqueous interface (figure 1.25).⁴² A dramatic variation in SFG strength in OH-region is observed owing to the screening of surface charge due to electrostatic interactions between the surfactant head group and the anions at the air/aqueous interface. Surprisingly, in contrast to Collin's rule, it is observed that the weakly hydrated guanidinium receptor has a large affinity to bind with the strongly hydrated sulphate anion in comparison to the weakly hydrated iodide. Evidently, the work emphasized the consideration of ion recognition and ion partitioning towards the specific ion effects.

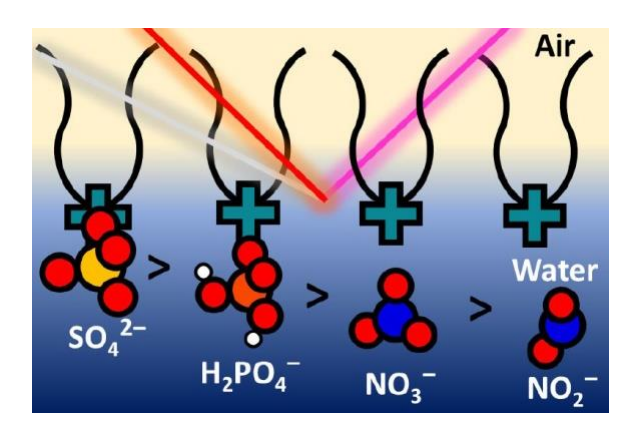


Figure 1.25 Schematic model of Vibrational sum frequency generation spectroscopy of guanidinium receptor anchored at the water–air interface. The study reveals that the guanidinium receptor binds to an oxoanion series in the order $SO_4^{2-} > H_2PO_4^{-} > NO_3^{-} > NO_2^{-}$. Reprinted from J. Phys. Chem. A 2020, 124, 49, 10171-10180. Copyright 2020 American Chemical Society.⁴²

1.9 Research Gaps and Motivation

In the previous sections, we reviewed versatile applications of specific ion effects in various fields, where researchers have utilized different techniques to provide unique insights into the intermolecular interactions contributing to the phenomenon mentioned above. We have presented a critical literature review to showcase

how the surface-specific SFG vibrational spectroscopy has contributed to our present understanding of the relative propensity of ions, ion-specific conformational changes in the macromolecule structure, and the bonding environment of water molecules at the air/aqueous interface. Still, some fundamental aspects of the specific ion phenomenon and its applicability in certain fields remain unexplored. In the following section, we have listed some research gaps, the molecular level investigations of which are crucial and remain unaddressed to date.

- Free OH oscillators in the topmost layer at the air/aqueous interface play a vital role in governing the
 interfacial properties. A detailed investigation of specific ion effects on the orientation of free OH
 oscillators has remained unaddressed. The information could be crucial in designing surfaces/interfaces
 with desired characteristics.
- Ion-specific impact on the hydrogen bonding environment of water molecules at the air/water interface
 is primarily studied. However, their contribution to determining the water evaporation process is still
 lacking. The information could be helpful in the development of surfaces/interfaces with controlled
 evaporation.
- The specificity of ions in perturbing the optical properties of aqueous media is extensively known, but their impact on the characteristics of laser-induced liquid microjets has remained unrevealed. Laserinduced liquid microjets generated at the air/aqueous interface are the potential candidates for needlefree drug delivery systems in the medical healthcare industry.
- Specific ion effects are primarily understood as a combined effect of ion-water and ion-macromolecule
 interactions. In contrast, recent reports have also professed the contribution of ion-specific watermacromolecule interactions. The experimental findings and the exact molecular level mechanism have
 remained unidentified.
- A correlation between ion-specific ordering/disordering of the macromolecule at the air/aqueous interface and the ion-specific water structure is missing. The molecular level insights into specific ion effects developed in this direction could help better understand this widely prevailed phenomenon.

1.10 Aims and Objectives of the Thesis

The present thesis aims to provide fundamental insights into the specific ion effects at the air/aqueous interface. As highlighted in the previous section on research gaps and motivation, the present thesis investigates molecular level insights into the water evaporation process, laser-induced liquid microjets, and the Hofmeister effect at the air/aqueous interface in unprecedented detail. The research work herein provides the molecular level details into the intermolecular interactions and the conformations of surface molecules that govern the ion-specific phenomenon at the air/aqueous interface. To achieve this, we have designed the objectives of the present thesis as follows:

- 1) Water Evaporation Process at Air/Water Interface: This research aims to investigate ion-specific H-bonding environment and the Orientation of Free OH-oscillators in the topmost layer of water molecules of the air/water interface and their contribution in governing the water evaporation process.
- 2) Laser-Induced Liquid Microjets at Air/Aqueous Interface: This research intends to probe the impact of ions in the generation of laser-induced liquid microjets at the air/rhodamine 6G (Rh6G) dye solution interface. The work showcases ion-specific control in the jet's velocity and penetration depths for developing needle-free drug injection systems.

3) Hofmeister Effect at Air/Polyvinylpyrrolidone Aqueous Interface: This research work aims to provide molecular level insights into the contribution of ion-specific water-macromolecule interactions in the mechanism of the Hofmeister effect along with the well-accepted ion-water and ion-macromolecule interactions. The macromolecule targeted in the present study is polyvinylpyrrolidone (PVP) polymer.

1.11 Organization of the Thesis

The current thesis contributes in developing the molecular scale understanding of the specific ion phenomena at the air/aqueous interface in terms of intermolecular interactions and the conformations of molecules prevailed in the interfacial region. For this, the thesis is organized into six chapters, outlined as follows:

Chapter 1. Introduction

This chapter includes a historical background of specific ion effects combined with an overview of the latest literature highlighting its vast applicability in various fields of science and technology. A molecular level insight into the intermolecular interactions participating in the underlying mechanism is also provided. The chapter highlights the importance of studying specific ion effects at air/aqueous interface and the limitations of experimental techniques in probing the interfacial region. This chapter intends to present a careful literature review on investigations of specific ion effects at the air/water interface and air/aqueous interface highlighting the molecular level insights provided by the surface-specific SFG vibrational spectroscopy. The last section of the chapter presents the research gaps and the aims/objectives of the present thesis work. The chapter also provides a structural organization of the following chapters of the thesis.

Chapter 2. Theory and Experimental Methods

This chapter briefly introduce the experimental setups and the associated theoretical aspects utilized in the data analysis as presented in the current thesis work. In order to achieve the targeted research objectives of the present thesis, we have developed the following experimental setups in our lab: 1) Time-resolved Newton's ring interferometry to investigate the evaporation dynamics of sessile aqueous droplets. 2) Laser-induced microjets to study radiation-induced deformation of air/aqueous interface. Along with this, we have utilized surface-specific SFG vibrational spectroscopy to investigate the intermolecular interactions, bonding environment, and conformations of molecules at the air/aqueous interface. The present research work also employed other conventional techniques like surface tensiometry and UV-visible absorbance spectroscopy, which have been discussed briefly in this chapter.

Chapter 3. Water Evaporation Process at Air/Water Interface

This chapter investigates specific ion effects in the water evaporation process at the air/water interface. The intention of the present research work is to provide fundamental insights into water evaporation through molecular level details of hydrogen bonding environment and orientation of surface water molecules evaporating from the air/water interface. The water evaporation process is of primary interest to our Earth's natural water cycle. It has been studied meticulously, considering its important role in atmospheric processes and various industrial and analytical applications. Most of the work reported in the literature on evaporation is primarily focused on the macroscopic approach, which leads to a gap in the mechanistic interpretation of the process. Along with this, the role of free OH (dangling) groups which constitute around more than 20 % of the population at the topmost water layer of the air/water interface, in the water evaporation is still unclear. The research

provides a detailed molecular level insight into the water evaporation process at the air/aqueous interface. In our experimental scheme, we have employed SFG vibrational spectroscopy to harness the structural information of molecules at the air/aqueous interface in the presence of Hofmeister ions. We witness the significant impact of ions on the strength of the H-bonding environment and the orientation of free OH oscillators at the air/aqueous interface, which in turn govern the water evaporation process that follows the Hofmeister series. We have also developed in-house time-resolved interferometry to study the evaporation dynamics of sessile aqueous droplets to estimate the evaporation rate for various Hofmeister ions to correlate with our findings from SFG spectroscopy. The present research work is the first experimental report demonstrating a comprehensive understanding of the role of the hydrogen bonding environment and the orientation of the free OH (dangling) moieties at the interface in determining the water evaporation process.

Chapter 4. Laser-Induced Liquid Microjets at Air/Aqueous Interface

This chapter presents an exciting research work investigating specific ion effects in laser-induced liquid microjets. Highly focused, fine diameter, and fast liquid microjets are generated when the air/aqueous interface is deformed upon absorbance of a laser beam in the aqueous media. Laser-induced liquid microjets find potential applications in the medical industry as needle-free drug injection systems. To mitigate the risk of disease spread and pain associated with needles, and the challenges faced during the Covid-pandemic, the research on needle-free injection systems has grabbed the attention in the direction of safe and better delivery tools for drugs and vaccination. In this direction, we have highlighted a critical observation of ion-specific variation in velocity and power of liquid microjets generated from an optical dye solution of rhodamine 6G (Rh6G) that governs the ion-specific penetration depth of liquid jets simulated for skin models. The ion-specific liquid jet phenomenon is explained based on variation in optical absorbance in Rh6G dye solution owing to ion-specific interactions with the macromolecule Rh6G. We have developed an experimental setup comprising picosecond 1064 nm and 532 nm laser beams to actuate laser-induced liquid microjets for the current studies. The importance of the present work lies in the generation of liquid microjets to achieve desired penetration depths crucial in the development of needle-free injection systems as well as scalpels for medical surgeries.

Chapter 5. Hofmeister Effect at Air/Polyvinylpyrrolidone Aqueous Interface

This chapter intends to provide molecular level insights into the Hofmeister effect at air/polyvinylpyrrolidone aqueous interface. The research presents the first experimental report demonstrating the existence and important contribution of ion-specific water-macromolecule interactions towards the hundred year's old standing mystery of the Hofmeister effect. Since 1888, the Specific ion effect and/or Hofmeister effect spans its horizons in various fields of science and technology, e.g., biophysics, chemistry, colloids, and environmental sciences. In a ternary system of ion, macromolecule, and water, the current understanding involves the contribution of ion-water and ion-macromolecule interactions. Still, it lacks the inherent role of water-macromolecule interactions towards the Hofmeister effect. Some experimental reports have professed the impact of ions on the bonding strength of water-macromolecule interactions, but the exact molecular level mechanism has remained unknown to date. In the present work, we have investigated the Hofmeister effect at the air/aqueous interface carrying Polyvinylpyrrolidone (PVP). PVP is a neutral macromolecule and serves as a model protein. We have performed experiments at the air/PVP-water interface in the presence of various 1M sodium salts in different polarization combinations of SFG vibrational spectroscopy. Utilizing SFG spectroscopy in different polarization schemes has enabled us to probe the ion-induced structural/conformational changes in the PVP macromolecule, which

correlates well with the concomitantly appearing changes in the strength of interfacial water bonding environment, and explains the Hofmeister effect. The molecular level insights presented in this chapter will be helpful in developing a better understanding of the mechanism of the Hofmeister effect/specific ion effects.

Chapter 6. Summary and Conclusions

This chapter summarizes the conclusions derived from the research works carried out in the present thesis. It also highlights the future aspects and further investigations which can be carried forward by being motivated by the research outcomes of the current thesis work.

CHAPTER 2

EXPERIMENTAL TECHNIQUES AND METHODOLOGY

This chapter briefly introduces the experimental setups and the associated theoretical aspects utilized in the data collection and their analysis as presented in the current thesis work. We have developed the following experimental setups in our lab as a part of the current thesis: 1) Time-resolved Newton's ring interferometry to investigate the evaporation dynamics of sessile aqueous droplets. 2) Laser-induced liquid microjets to study radiation-induced deformation of air/aqueous interface. Along with this, we have utilized surface-specific SFG vibrational spectroscopy to investigate the intermolecular interactions, bonding environment and conformations of molecules at the air/aqueous interface. Later in this chapter, we briefly introduced other conventional techniques like the Wilhelmy plate method for surface tension studies and UV-visible absorbance spectroscopy, which we have employed to carry out the research works.

2.1 Time-Resolved Newton's Ring Interferometry

We have utilized a time-resolved Newton's ring interferometry to estimate the evaporation rate of sessile aqueous droplets. 65,208-209 The experimental setup of the interferometry, developed as a part of the present thesis work, is showcased in figure 2.1.

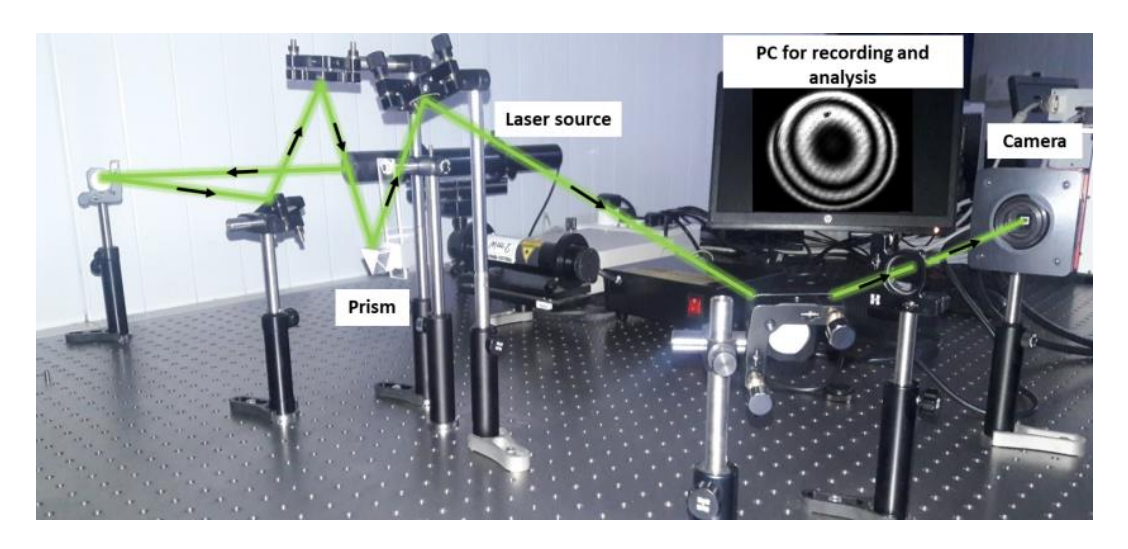


Figure 2.1 In-house developed experimental setup of time-resolved Newton ring's interferometry for the evaporation rate studies of sessile aqueous droplets.

2.1.1 Experimental Setup

In this setup, a low-power INNOLAS He-Ne laser beam of wavelength $\lambda = 543$ nm is directed onto the surface of an aqueous droplet sitting on a glass prism of refractive index 1.5. The Fresnel reflections generated from the air/water interface and the water/glass interface (shown in the optical layout figure 2.2a) spatially overlap to form a dynamic Newton's ring interference pattern, recorded by a CCD camera (ThorCam 340M) at 57 fps (frames per second) and is further analyzed with an associated computer.

2.1.2 Sample Preparation and Droplet Formation

All the aqueous samples are prepared in deionized water (Merck Millipore direct-Q3, 18 M Ω .cm). We have utilized a micropipette to place the aqueous droplets on the prism surface. The droplets of 20 μ l have been employed in our whole evaporation rate experiments. All the experiments are performed at a lab temperature of 21.5 ± 0.5 °C.

2.1.3 Dynamic Newton's Ring Interference Pattern

Consider a sessile droplet of central thickness, d of a liquid having a refractive index n_l placed on a prism with a refractive index 1.5. A laser beam of wavelength λ is incident from air (n_i = 1) on the droplet with an angle of incidence θ_i with respect to the surface normal, as shown in the optical layout (figure 2.2a). The beam is partially reflected from the air/water surface, with an angle of reflection equal to the angle of incidence (law of reflection). The angle of refraction (θ_r) of the beam transmitting into the droplet is given by Snell's law as follows:

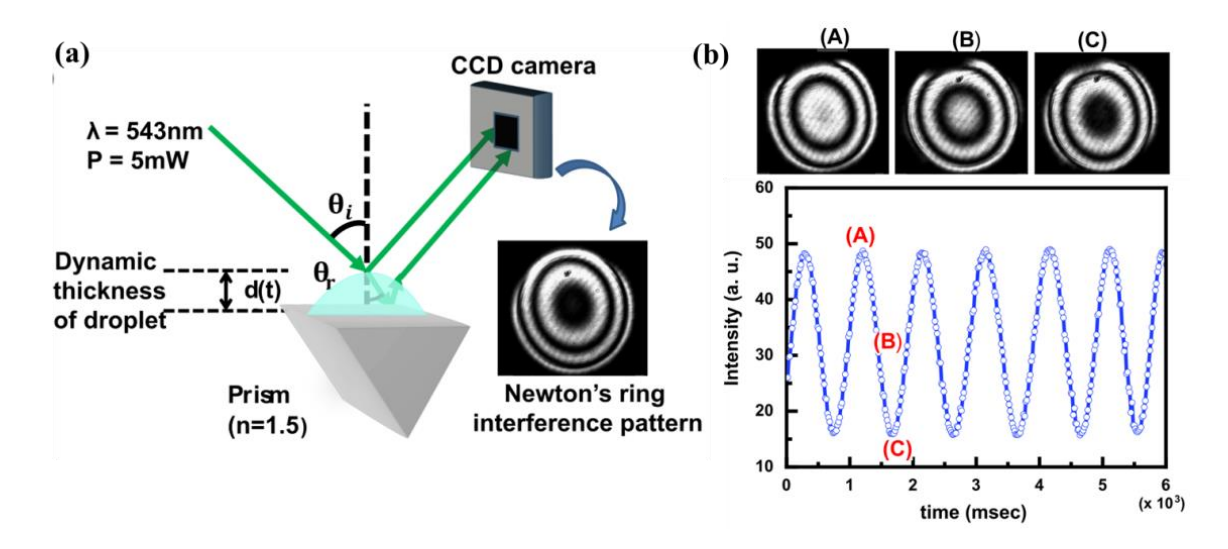


Figure 2.2 (a) Schematic of time-resolved Newton's ring interferometry for the evaporation rate studies of sessile aqueous droplets. (b) The snapshots with the variable intensity of the central fringe of the dynamic Newton's ring pattern with the time sequence of one fringe collapse (marked as A, B, and C, respectively). 65

$$n_{i}\sin\theta_{i} = n_{l}\sin\theta_{r} \tag{2.2}$$

The Fresnel reflections generated from the droplet's top (air/water interface) and bottom (water/glass interface) overlap and result in Newton's ring interference pattern, as depicted in figure 2.2. The path difference between the two interfering beams is given by:^{65,208}

$$\Delta \Lambda = \left(\frac{2n_1 d}{\cos \theta_n}\right) \tag{2.2}$$

The phase difference between the two interfering Fresnel reflections, which results in Newton's ring pattern, is given by: 65,208-209

$$\Delta \phi = \frac{2\pi}{\lambda} \left(\frac{2n_1 d}{\cos \theta_r} \right) \tag{2.3}$$

As the droplet is continuously evaporating, the droplet's moving surface of height (d) leads to a dynamic optical path and consequently a varying phase difference between the interfering beams, which is given by: 65,208-209

$$\Delta \phi(t) = \frac{2\pi}{\lambda} \left(\frac{2n_{l}d(t)}{\cos \theta_{r}} \right) \tag{2.4}$$

Consequently, the intensity at the central fringe of the dynamic Newton's ring interference pattern is a function of time (figure 2.2b) as follows: 65,208-209

$$I(t) \propto \cos^2(\Delta \phi(t))$$
 (2.5)

The variable intensity profile of the central fringe of the dynamic Newton's ring interference pattern is shown in figure 2.2b, with snapshots at various stages of one fringe collapse designated by A, B, and C, respectively.

2.1.4 Evaporation Rate of Sessile Aqueous Droplets

The variable intensity profile of the dynamic Newton's ring interference pattern (figure 2.2b) is then utilized to calculate the change in droplet height $\Delta d(t)$ as follows. The intensity of the central fringe alternates between bright and dark provided the conditions for central maxima and minima are given as:^{65,208}

$$\Delta \phi(t) = 2k\pi \tag{2.6}$$

$$\Delta \phi(t) = (2k+1)\pi \tag{2.7}$$

Here, k is an integer having values 0, 1, 2, 3, etc. The variation in the central fringe intensity from one maximum (or minimum) to the next results in a phase change of $\Delta \phi = 2\pi$. Substituting this value of phase change in equation 2.4 corresponds to a thickness change of:⁶⁵

$$\Delta d'^{(t)} = \frac{\lambda \cos \theta_{\rm r}}{2n_{\rm l}} \approx 200 \, nm \tag{2.8}$$

Here $\theta_r \sim 8^\circ$, thus moving over (k+1) consecutive maxima gives a change in droplet thickness as given by:⁶⁵

$$\Delta d(t) = k \left(\frac{\lambda \cos \theta_r}{2n_l} \right) \tag{2.9}$$

Here, k is an integer having values 0, 1, 2, 3, etc. Plotting $\Delta d(t)$ with time gives a straight line plot, the slope of which measures the evaporation rate of the sessile aqueous droplet.⁶⁵

2.2 Laser-Induced Liquid Microjets

When a liquid surface concaves towards the gas and is impulsively accelerated, the liquid is focused and converges towards the center of the curvature, generating high-speed liquid jets. ²¹⁰⁻²²² Liquid jets find potential application in developing needle-free drug injectors, liquid scalpels for soft tissue dissection, or devices for gene delivery. ²¹⁰⁻²²⁶ The conventional methods based on pressurized gases, string actuation, or piezo crystal actuation are associated with generating liquid jets with uncontrolled characteristics. ²²³⁻²²⁶ In the present thesis, we have discussed the generation of highly focused, fine-diameter liquid microjets using lasers. The absorption of the laser pulse inside the liquid medium generates a vapor bubble owing to the abrupt vaporization of the liquid. The

resultant pressure gradient between the bubble and the liquid surface creates a flow focussed liquid microjet (figure 2.3). 212,216-219

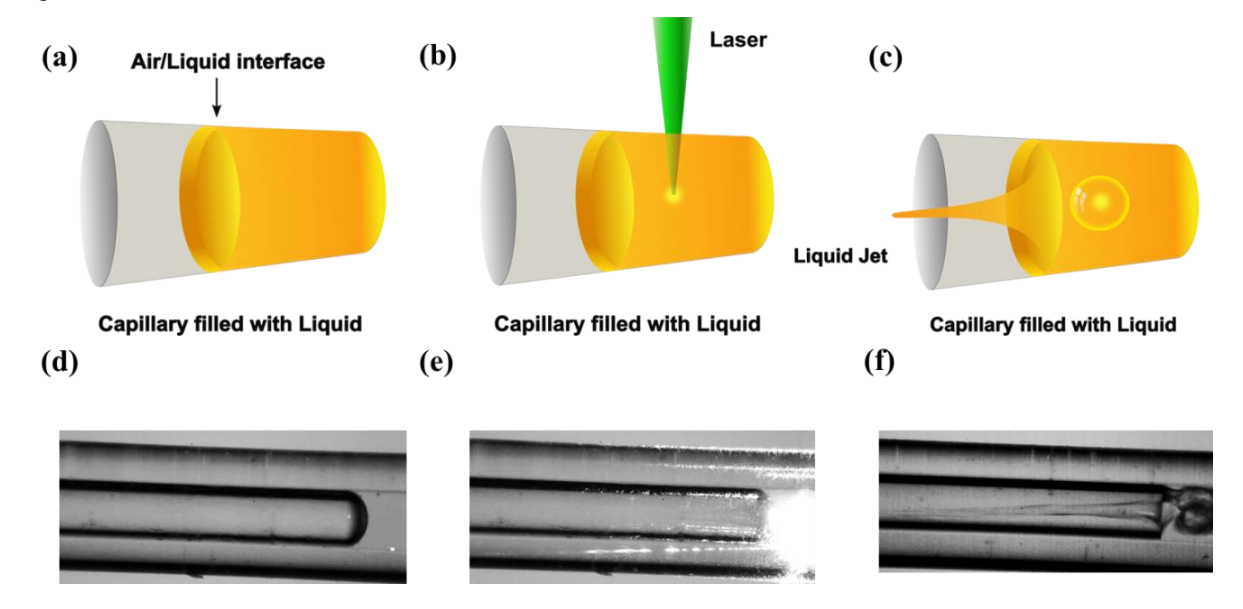


Figure 2.3 Schematic illustration of laser actuation scheme (a) side-view of a microcapillary filled with a liquid showcasing air/liquid interface. (b) A laser pulse is focused inside the liquid medium at a certain distance from the air/liquid interface. (c) Absorption of the laser pulse generates a bubble inside the microcapillary which further deforms the air/liquid interface to produce a liquid microjet owing to the flow-focusing effect. (d), (e) and (f) correspond to the capillary snapshots during the liquid jet formation. The snapshots are recorded at 10k fps. The diameter of the liquid jet is $\sim 40 \mu m$.

2.2.1 Time Evolution of Liquid Jets

Figure 2.4a presents capillary snapshots which showcase a typical sequence of evolution of the liquid jet when a laser is focused inside the liquid. The corresponding estimated velocity of the jet tip is shown in figure 2.4b, which is seen to be non-monotonic with time. The plot consists of three regions: (i) acceleration in jet velocity, where the jet attains the maximum velocity, (ii) deceleration in jet velocity; and (iii) the jet attains a nearly constant asymptotic velocity value. This non-monotonic variation in jet velocity with time is understood as follows. $^{216-217}$ The interface is set into motion immediately after the laser pulse has impinged on the capillary. Due to the initial concave shape of the meniscus, a kinematic focusing leads to a fine diameter, well shaped and maximum velocity (v_{max}) jet that appears along the capillary axis (stage (i) in figure 2.4b). Since by this time, the meniscus loses its initial concave shape, and a subsequent deceleration in jet-tip velocity is evident. It is known to occur due to the surface tension effect (stage (ii) in figure 2.4b). Later, as the jet becomes thinner, the surface tension becomes less critical, and the jet tip reaches an asymptotic value v_j (stage (iii) in figure 2.4b). We have achieved an asymptotic speed of $\sim 25\pm 2$ m/s comparable to the one reported by Tagawa et al. 216 with 500 μ m diameter capillary at 400 μ J laser pulse energy.

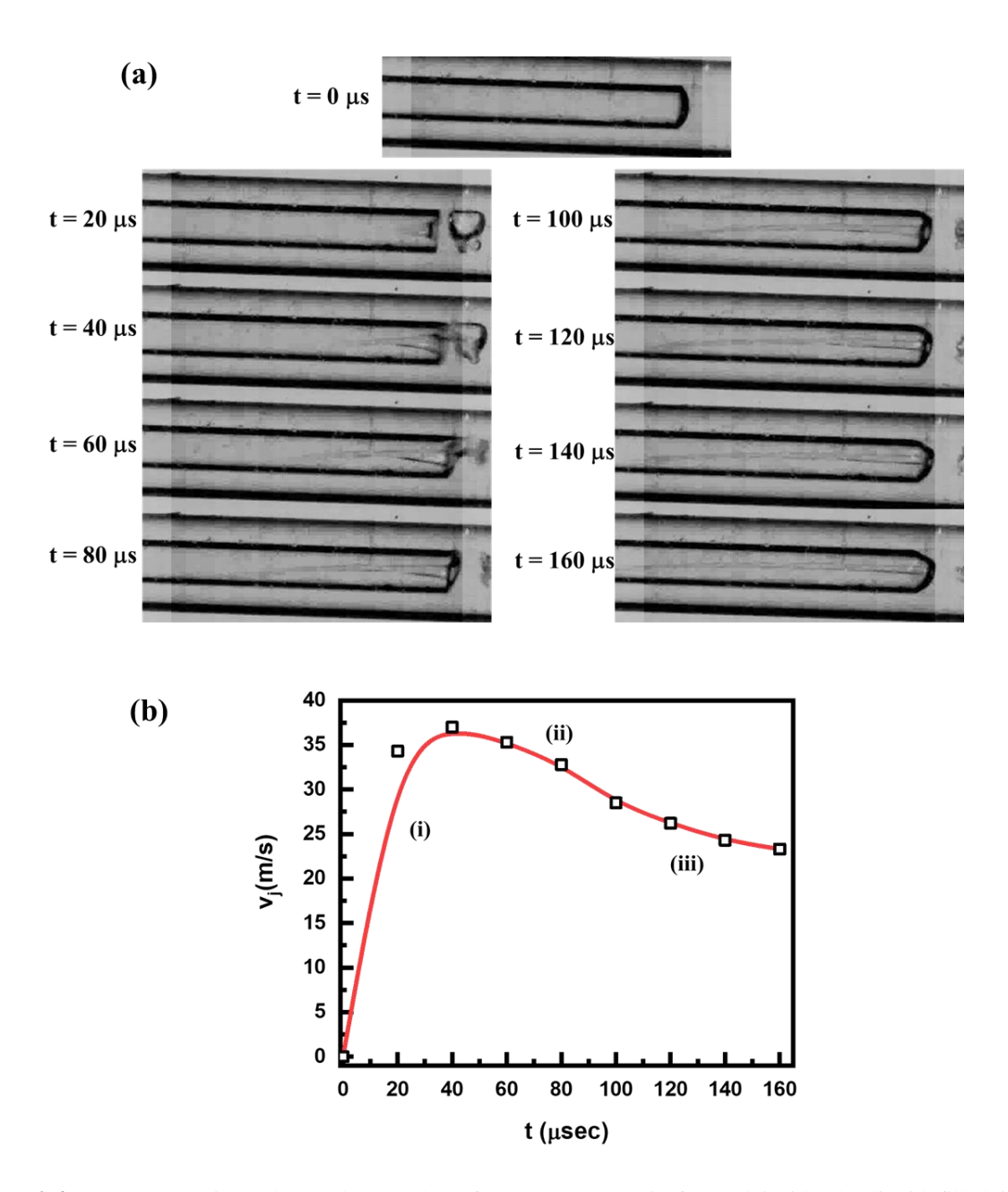


Figure 2.4 (a) Jet evolution when a laser pulse of energy 400 μ J is focused inside the liquid filled in a microcapillary of diameter \sim 400 μ m. The capillary snapshots are recorded at 50k fps. (b) jet tip velocity as a function of time showing a non-monotonic trend.

constant asymptotic velocity value. This non-monotonic variation in jet velocity with time is understood as follows. $^{216-217}$ The interface is set into motion immediately after the laser pulse has impinged on the capillary. Due to the initial concave shape of the meniscus, a kinematic focusing leads to a fine diameter, well shaped and maximum velocity (v_{max}) jet that appears along the capillary axis (stage (i) in figure 2.4b). Since by this time, the meniscus loses its initial concave shape, and a subsequent deceleration in jet-tip velocity is evident. It is known to occur due to the surface tension effect (stage (ii) in figure 2.4b). Later, as the jet becomes thinner, the surface tension becomes less critical, and the jet tip reaches an asymptotic value v_j (stage (iii) in figure 2.4b). We have achieved an asymptotic speed of $\sim 25\pm 2$ m/s comparable to the one reported by Tagawa et al. 216 with 500 μ m diameter capillary at 400 μ J laser pulse energy.

2.2.2 Parameter Dependence of Jet Velocity

The generation of laser jet and the associated jet velocity is dependent on various parameters inside the microcapillary, as presented in figure 2.5, and are discussed as follows:²¹⁶⁻²¹⁷

The laser pulse absorption causes abrupt vaporization of a small volume of the capillary liquid that generates a pressure wave inside the capillary. The pressure wave travels through the tube and reflects on the free surface and the tube boundaries, resulting in a pressure gradient between the vapor bubble and the free surface. This pressure pulse determines the initial velocity of the liquid, which is estimated by a one-dimensional Euler equation (after neglecting viscosity and compressibility) as follows:²¹⁷

$$\frac{\partial \mathbf{u}}{\partial \mathbf{t}} = -\frac{1}{\rho} \frac{\partial \mathbf{p}}{\partial \mathbf{z}} \tag{2.10}$$

Where u is the axial velocity of the liquid and t is the time. The axial pressure gradient is given by the pressure in the bubble Δp and the distance λ' between the bubble and the free surface:²¹⁷

$$\frac{\partial \rho}{\partial z} = \frac{\Delta p}{\lambda'} \tag{2.11}$$

The velocity v_0 of the free surface after the pressure pulse is obtained by integrating over the duration Δt of the pressure pulse as follows:²¹⁷

$$v_0 = \frac{\Delta p \, \Delta t}{\rho \lambda'} \tag{2.12}$$

Here λ' is assumed to be constant for small values of Δt .

The pressure pulse governs the initial jet speed, whereas focussing of the flow accounts for a further acceleration of the jet, discussed as follows:

Let us consider a spherical surface with a radius of curvature R_c and velocity v_o is directed normal to it due to the initial acceleration by pressure pulse. The principle of mass conservation estimates the new velocity acquired due to the geometric focusing as follows: $^{216-217}$

$$(v_0 + \Delta v)(R_c - \Delta R)^2 = v_0 R_c^2$$
 (2.13)

Here, $\Delta R = v_o \Delta t$ and Δv are the decrements in curvature radius and increment in velocity after time Δt , respectively. The acceleration in jet velocity is given by: $^{216-217}$

$$a = \frac{\Delta v}{\Delta t} = \frac{2v_o^2}{R_c} \tag{2.14}$$

$$a = \frac{\Delta v}{\Delta t} = 2v_o^2 \frac{\cos \theta_c}{R_t} \tag{2.15}$$

$$R_{t} = R_{c} \cos \theta_{c} \tag{2.16}$$

Here, R_t is the tube radius and θ_c is the contact angle of the liquid with the tube boundary wall. Considering: ²¹⁶-217

$$\Delta t = \frac{R_t}{v_0} \tag{2.17}$$

The increment in jet velocity due to flow focusing is given by:²¹⁷

$$\Delta v \sim a\Delta t = 2v_0 \cos\theta_c \tag{2.18}$$

Thus the maximum jet velocity owing to the pressure pulse and flow focusing is given by: 216-217

$$v_{\text{max}} = v_0 + \Delta v = v_0 (1 + b \cos \theta_c) \tag{2.19}$$

$$v_{\text{max}} = \frac{\Delta p \, \Delta t}{\rho \lambda'} (1 + b \cos \theta_{\text{c}}) \tag{2.20}$$

Here, b is a proportionality factor of the order of unity. Thus, the pressure impulse and the flow focusing accounts for the two acceleration mechanisms. The surface tension account for a further slowdown.

The surface tension of the liquid associated with the capillary walls governs the concept of threshold energy for jet formation. It is defined as the minimum amount of laser energy required to generate a liquid jet, i.e., below which jet formation is impossible. This is because a large amount of laser energy is lost in heating up the liquid before a bubble is created, thus, surface tension prevents the jet formation. Once the kinetic energy is much larger than the surface energy related to the formation of the jet and the potential energy associated with the size of the bubble, a jet can be formed. Further, the decrease in jet velocity (v_s) due to the surface tension can be estimated by balancing the kinetic energy per unit length of the jet (E_k) with the surface energy of the jet per unit length (E_s) as follows:²¹⁷

$$E_k = E_s \tag{2.21}$$

$$\frac{\pi \rho R_j^2 v_s^2}{2} = 2\pi \sigma_{st} R_j \tag{2.22}$$

$$v_{s} \sim \sqrt[2]{\frac{4\sigma_{st}}{\rho R_{j}}} \tag{2.23}$$

As shown in figure 2.4, after the deceleration stage, owing to surface tension, the jet velocity attains an asymptotic value, v_i .

Laser Energy (E): The pressure impulse ($\Delta p \Delta t$) between the bubble and the free liquid surface is directly related to the experimental parameter of laser energy absorbed in the liquid medium contained in the microcapillary. ^{212,216-218}

$$\Delta p \propto E$$
 (2.24)

This implies that the greater the amount of absorbed laser energy, the greater the pressure impulse at the air/liquid interface, and in turn, the higher the jet velocity.

Tube diameter (D): The pressure impulse necessary for the generation of liquid jets strongly depends on the capillary tube's radius. For a fixed absorbance of laser energy (E), the produced pressure is related to the volume (V_e) of the liquid that is exposed to the laser energy as: $^{212,216-218}$

$$\Delta p \propto \frac{E}{V_o}$$
 (2.25)

A smaller capillary tube results in a smaller volume of the liquid exposed to laser energy and thus generates huge pressure impulse. This is why high-speed jets are possible even with low laser energies for smaller-diameter capillary tubes, as reported in the literature.

Distance between Laser focus and free surface (H): In the laser-induced liquid jet experiments, let us consider H is the distance between the laser focus position inside the capillary and the free liquid surface. Using equation 2.20, the jet velocity v_i can be expressed via an inverse relation with H, as:²¹⁶

$$v_j \propto \frac{1}{H}$$
 (2.26)

The reasoning could be related to the pressure wave amplitude on the free liquid surface, which will decrease with the increment in H.

Combining all the parameters discussed here, the dependency of v_j is expressed as: $^{212,216-218,220}$

$$v_j \approx f(D) \frac{E(1 + b\cos\theta_c)}{H}$$
 (2.27)

Here, the prefactor f(D) incorporates the dependence on capillary diameter.

2.2.3 Experimental Setup

Figure 2.5a represents the schematical layout of the experimental setup, which is developed as a part of the present thesis work for the generation of laser-induced liquid microjets. Figure 2.5b shows the side view of the microcapillary together with control parameters in the generation of laser-induced liquid microjets. The experimental lab setup is showcased in figure 2.6. Here, we have used a mode-locked Nd:YAG diode pumped solid state (DPSS) laser system (PL2231-50) from EKSPLA, which delivers an infrared beam of 1064 nm with a pulse width of 28 ps and maximum energy of 40 mJ at a repetition rate of 50 Hz. This seed laser of 1064 nm is then utilized in the second harmonic generation unit to give 532 nm in the output. The second harmonic laser beam (532 nm) is then guided through the optics and made to focus on a microcapillary via a 10x microspot objective (Thorlabs, LMH-10X-532) to actuate the liquid jets. The diffraction-limited laser beam waist after focusing is estimated to be $\sim 6.5 \, \mu m$, which leads to a peak intensity of $\sim 10^{13} \, \text{W/cm}^2$ at the focal point.

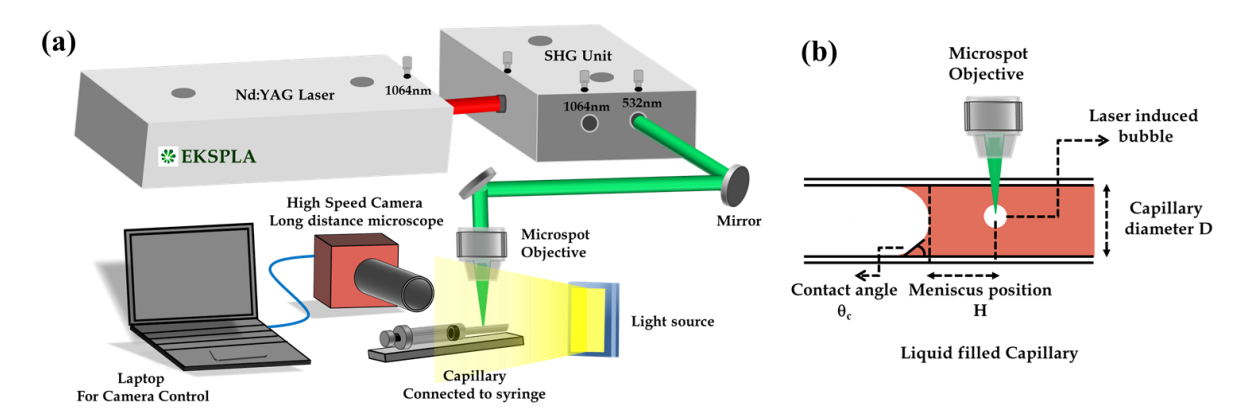


Figure 2.5 (a) Schematic optical layout of the experimental setup for the laser-induced liquid microjets. (b) Side view of the capillary glass tube with control parameters of microjet formation.

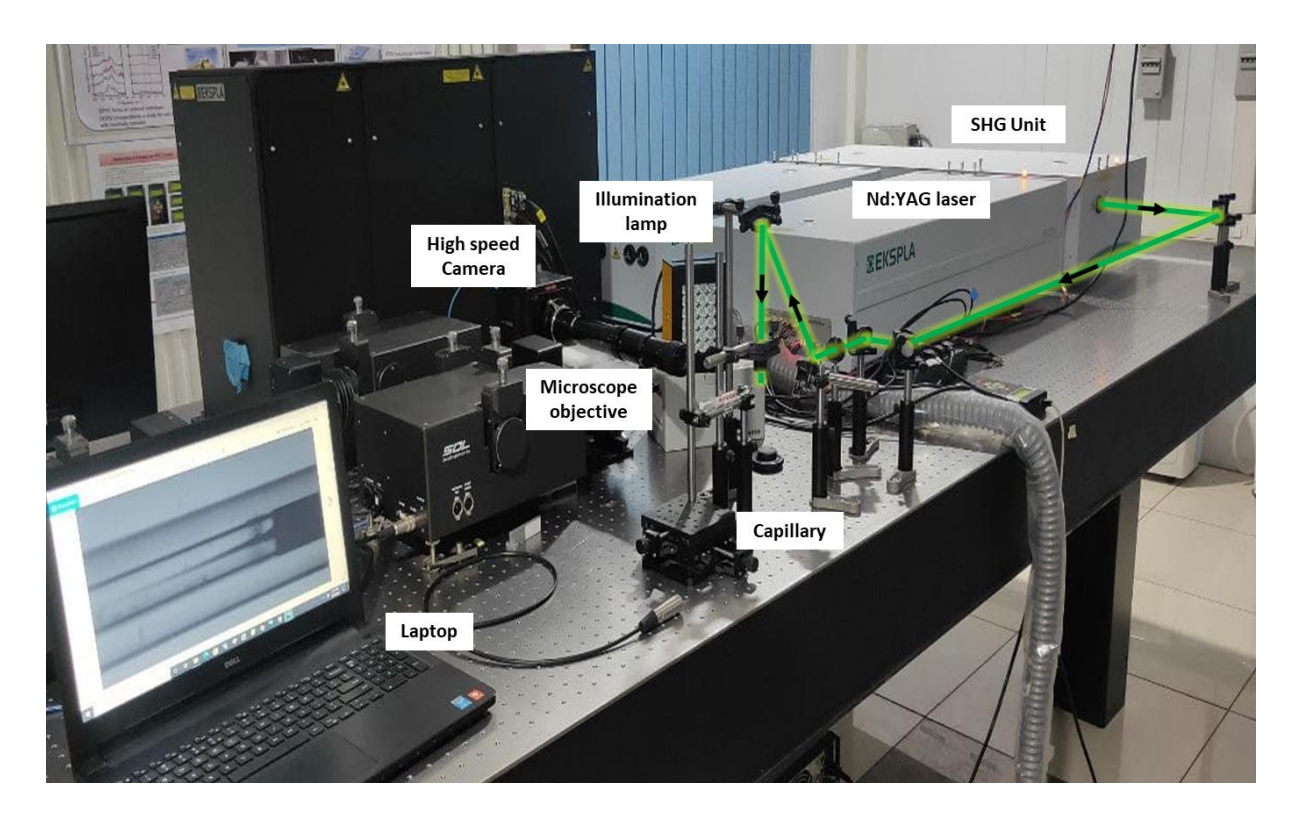


Figure 2.6 In-house developed experimental setup for the generation of liquid microjets using ps-pulsed lasers.

The energy of laser pulses used to generate the liquid jets is monitored by a power meter Nova II from Ophir. Borosilicate glass capillary tubes with an inner diameter of 400 µm and an outer diameter of 1200 µm are used in the experiments. One end of the microcapillary is connected to a syringe containing a water-based dye solution, and the other end is open to the air. The jet formation is recorded by using a high-speed camera FastCAM MINI AX from Photron with a maximum frame rate of up to 10⁵fps. A long-distance microscope with a maximum magnification of 12x (Navitar) is connected to the camera in order to capture the side view of the jet formation. The field of view can be adjusted by varying the magnification of the Navitar lens. A light source (GSVITEC MultiLED) provides illumination to capture good contrast images. The Images are analyzed in a laptop equipped with the Photron software (PFV4).

2.2.4 Calculation of Jet Velocity and Jet Power

The velocity of liquid microjets is calculated by using formula:

$$v_{i} = \Delta l_{i} / \Delta t \tag{2.28}$$

Where, v_j is the jet velocity, Δl_j is change in jet length in time interval Δt , and Δt is the time interval between the consecutive camera frames.

Jet power (P_i) is calculated as: ^{212,219}

$$P_{j} = \frac{1}{8} \rho \pi D_{j}^{2} v_{j}^{3}$$
 (2.29)

Here, ρ , D_i are the density of the liquid solution filled in the microcapillary and the jet diameter, respectively.

2.2.5 Estimation of the Capillary Diameters

It is essential to figure out the inner and outer diameters of the microcapillary we have utilized in the present thesis work. We estimated the capillary diameter values using the camera FastCAM MINI AX from Photron equipped with a long-distance microscope with a maximum magnification of 12x (Navitar). In figure 2.7, we have presented the camera snapshots to analyze capillary diameters using Photron software. The inner and outer diameter of the cylindrical microcapillary comes out to be 120 and 360 pixels. For the present camera adjustments, the calibration constant is $3.25 \mu m/pixel$. Utilizing the camera calibration constant, the inner and outer diameters are estimated as $400 \mu m$ and $\sim 1200 \mu m$, respectively.

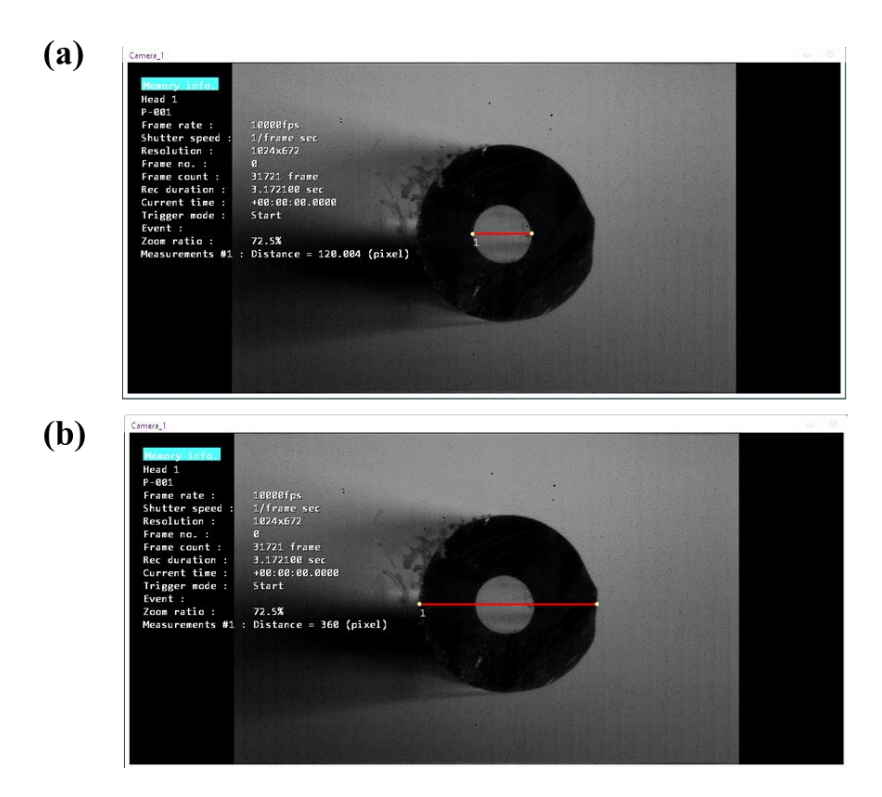


Figure 2.7 Camera snapshots for the inner and outer diameter of the microcapillary utilized in the generation of laser-induced liquid microjets.

2.3 Sum Frequency Generation (SFG) Vibrational Spectroscopy

We have employed SFG vibrational spectroscopy to probe the orientation and vibrational characteristics of molecules involved in various bonding environments at the air/aqueous interface. SFG is an ideal vibrational spectroscopic tool to selectively probe the conformation and structure of the moieties present at surfaces/interfaces. $^{35,65,170-171,173-182,227-250}$ It is based on a second-order nonlinear optical process where SFG signal (ω) occurs when a fixed frequency visible (ω_1) and tunable infrared, IR (ω_2) pulsed laser beams are temporally and spatially overlapped at the interface (figure 2.8). Since energy and momentum of laser fields parallel to the surface/interface are conserved during the SFG process, the frequency of the resultant SFG signal is given by: 65,173,227,229,231,233,238,242

$$\omega = \omega_1 + \omega_2 \tag{2.30}$$

and the direction of the SFG signal is given by: 229,238

$$\vec{k}^{\parallel} = \overrightarrow{\mathbf{k}_{1}}^{\parallel} + \overrightarrow{\mathbf{k}_{2}}^{\parallel}$$

$$k. \sin \xi = \mathbf{k}_{1}. \sin \xi_{1} + \mathbf{k}_{2}. \sin \xi_{2}$$
(2.31)

Here \vec{k} , $\vec{k_1}$, and $\vec{k_2}$ are the wave vectors and angles ξ , ξ_1 , and ξ_2 of SFG, visible, and IR laser beams, respectively. That are measured with respect to the surface normal (figure 2.8). To obtain such nonlinear optical response from a material, large incident fields are required compared to the internal field maintaining the electronic structure in an atom. The intensity of this magnitude are obtained from pulsed laser sources.

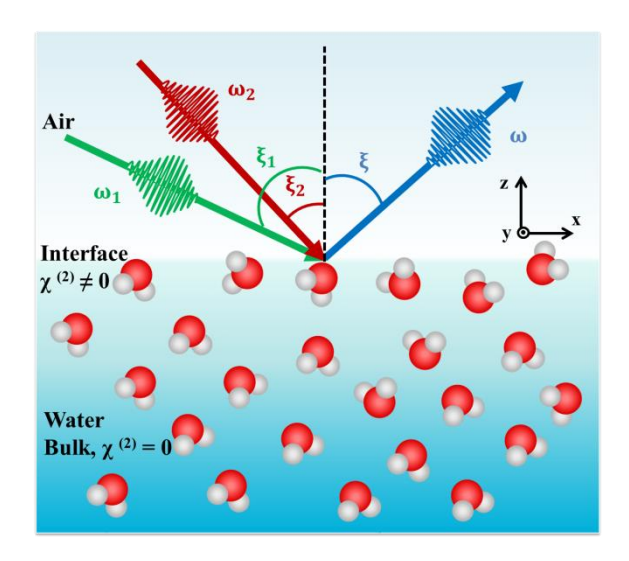


Figure 2.8 Schematic representation of SFG in co-propagating geometry at the air/water interface. The vertical dotted line corresponds to the surface normal. Here xyz is the lab coordinate system, where xz is the plane of incidence with y-axis perpendicular to it.

2.3.1 Nonlinear Optical Response of SFG from Surface/Interface

When a low-intensity and non-coherent light carrying the electric field (E') is impinged on a material, the induced electric dipole (μ) in the isotropic medium is given by:^{229,231}

$$\mu = \mu_0 + \alpha E' \tag{2.32}$$

Here μ_0 is the permanent (static) dipole of the material, and α is the polarizability of molecular electrons comprising the medium. The net dipole moment per unit volume, i.e., polarization (P) induced by an oscillating electric field, is given by (assuming zero static polarization): 227,229,231

$$P = \varepsilon_0 \chi^{(1)} E' \tag{2.33}$$

Here ε_0 is the vacuum permittivity and $\chi^{(1)}$ is the macroscopic average of α and is known as linear susceptibility. Consequently, the induced dipole oscillates and emits light at the same frequency as the incident field. In the presence of pulsed laser sources, the amplitude of the incident electric field is comparable to the internal field experienced by electrons of the atoms comprising the medium; the resultant dipole moment incorporates additional terms as expressed in Taylor's series expression: 229,231

$$\mu = \mu_0 + \alpha E' + \beta E'^2 + \gamma E'^3 + \cdots$$
 (2.34)

Here β and γ are first-and second-order hyperpolarizabilities, respectively. The polarization becomes: 227,229,231

$$P = \varepsilon_0 \left(\chi^{(1)} E' + \chi^{(2)} E'^2 + \chi^{(3)} E'^3 + \cdots \right)$$

$$= P^{(1)} + P^{(2)} + P^{(3)} + \cdots$$
(2.35)

Here $\chi^{(2)}$ and $\chi^{(3)}$ are second-and third-order susceptibilities, respectively. $P^{(2)}$ and $P^{(3)}$ are the second-and third-order nonlinear polarization terms, where $P^{(2)}$ is responsible for the SFG signal, explained as follows:

For two laser beams of frequency ω_1 and ω_2 , the electric field E' is given by: ^{227,229}

$$E' = E'_1 \cos \omega_1 t + E'_2 \cos \omega_2 t \tag{2.36}$$

$$P^{(2)} = \varepsilon_0 \chi^{(2)} E'^2 = \varepsilon_0 \chi^{(2)} [(E'_1 \cos \omega_1 t)^2 + (E'_2 \cos \omega_2 t)^2 + 2E'_1 E'_2 \cos \omega_1 t \cos \omega_2 t]$$
 (2.37)

$$P^{(2)} = \frac{1}{2} \epsilon_0 \chi^{(2)} \begin{bmatrix} E_1'^2 (1 + \cos 2\omega_1 t) + E_2'^2 (1 + \cos 2\omega_2 t) \\ +2E_1' E_2' \{\cos(\omega_1 + \omega_2) t + \cos(\omega_1 - \omega_2) t\} \end{bmatrix}$$
(2.38)

$$P^{(2)} = \frac{1}{2} \epsilon_0 \chi^{(2)} \left[\frac{\left(E_1'^2 + E_2'^2 \right) + \left(E_1'^2 \cos 2\omega_1 t + E_2'^2 \cos 2\omega_2 t \right)}{+2E_1' E_2' \cos (\omega_1 + \omega_2) t + 2E_1' E_2' \cos (\omega_1 - \omega_2) t} \right]$$
(2.39)

Here, the terms on the right-hand side of equation 2.39 represent the DC field (zero frequency dependence), second Harmonic generation (SHG), i.e., $2\omega_1$, $2\omega_2$, SFG ($\omega_1+\omega_2$), and difference frequency generation (DFG) ($\omega_1-\omega_2$) respectively.

2.3.2 Surface Specificity of SFG Vibrational Spectroscopy

From equation 2.39, the intensity of the SFG signal is given by:

$$I \propto \left| \chi^{(2)} \right|^2 I_1 I_2 \tag{2.40}$$

Here the second-order susceptibility $\chi^{(2)}$ is a tensor of rank 3 with 27 elements that relates the electric fields of incident beams to the induced polarization at the interface. The number of independent and non-zero elements of $\chi^{(2)}$ are defined by symmetry constraints. In a centrosymmetric environment, $\chi^{(2)}_{ijk}$ should be identical in two opposite directions:^{227,229,238}

$$\chi_{ijk}^{(2)} = \chi_{-i-j-k}^{(2)} \tag{2.41}$$

Since, $\chi_{ijk}^{(2)}$ is a third rank tensor, reversing the axis system will change the sign of physical quantity as well: 227,229,238

$$\chi_{ijk}^{(2)} = -\chi_{-i-j-k}^{(2)} \tag{2.42}$$

The two equations can be valid only for $\chi_{ijk}^{(2)} = 0$, implies that SFG is forbidden in the centrosymmetric environment. Most bulk media are centrosymmetric, and the surfaces/interfaces are inherently non-centrosymmetric, therefore, are SFG active.

2.3.3 SFG is Both IR and Raman Active

The second-order nonlinear susceptibility $\chi_{ijk}^{(2)}$ is expressed as the macroscopic average of molecular hyperpolarizability $\beta_{pqr}^{(2)}$ as follows: $^{173,229,233,237-239,242}$

$$\chi_{ijk}^{(2)} \propto \frac{N}{\varepsilon_0} \sum_{\text{pqr}} \langle \beta_{\text{pqr}}^{(2)} \rangle$$
 (2.43)

Here N is the number density of molecules at the interface contributing to the SFG signal. The angle brackets represent the orientational average of $\beta_{pqr}^{(2)}$. Under the assumption of a two-level system consisting of a ground state $|g\rangle$ and a vibrationally excited state $|v\rangle$, $\beta_{pqr}^{(2)}$ can be expressed as a product of the IR transition moment μ_r and Raman tensor elements α_{pq} : ${}^{173,229,233,238-239,242}$

$$\beta_{pqr}^{(2)} = \frac{\alpha_{pq}\mu_r}{\omega_v - \omega_2 - i\Gamma_v}$$
 (2.44)

Here ω_2 , ω_v are the frequency of the incident tunable IR beam and vibrational frequency of vth resonant mode, i is the imaginary unit and Γ_v is the damping constant. When ω_2 resonates with ω_v , $\beta^{(2)}$, and correspondingly $\chi^{(2)}$ is resonantly enhanced, and the vibrational spectrum characteristic of molecules at surfaces/interfaces is obtained. This highlights a vital selection rule for SFG: for a vibrational mode to be SFG active, it must be both IR and Raman active.

Vibrational Resonance

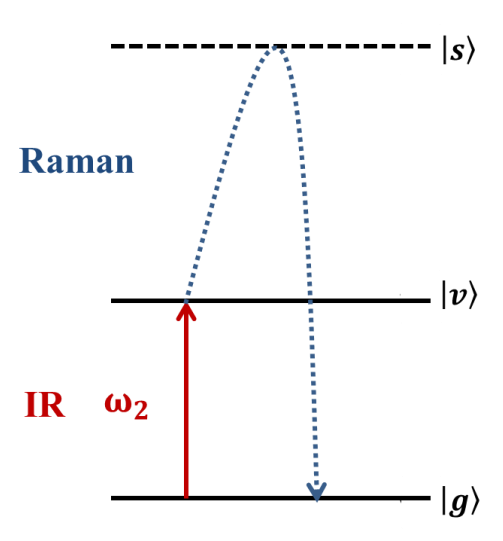


Figure 2.9 Energy level scheme for SFG. $|g\rangle$ is a ground state, $|v\rangle$ is the vibrationally excited state and $|s\rangle$ is any other state. For SFG, the resonance is both IR and Raman active.

2.3.4 Effective Nonlinear Susceptibility $\chi^{(2), \text{ eff}}$ and Fresnel's Factors

The detailed expression for SFG intensity is presented as: 173,233,238,242

$$I = \frac{8\pi^{3} sec^{2} \xi}{c^{3} n_{I}(\omega) n_{I}(\omega_{1}) n_{I}(\omega_{2})} |\chi^{(2),eff}|^{2} I_{1} I_{2}$$
(2.45)

Here c is the speed of light, $n_I(\omega_i)$ is the refractive index of medium I at a frequency ω_i . Here $\chi^{(2),eff}$ is the second-order effective nonlinear susceptibility tensor and comprised of the following two components: $^{173,233,238-239,242}$

$$\chi^{(2),\text{eff}} = \chi_{NR}^{(2)} + \sum_{\nu} \frac{A_{\nu}}{(\omega_{\nu} - \omega_2 - i\Gamma_{\nu})}$$
 (2.46)

 $\chi_{NR}^{(2)}$ is the non-resonant component of the susceptibility. The resonant term is represented by a Lorentzian profile, used to fit all the SFG spectra. Resonance occurs when the frequency of the incident tunable infrared beam (ω_2) coincides with vibrational characteristic frequency mode (ω_v) of the interfacial molecules. Here, A_v is the amplitude and Γ^{-1} is the relaxation time of the vibrationally excited state involved in resonance. The second-order effective nonlinear susceptibility $\chi^{(2),eff}$ is related to the actual molecular response $\chi^{(2)}$ by Fresnel Factors as follows:

$$\chi^{(2),\text{eff}} = [\hat{\mathbf{e}}(\omega) \cdot \mathbf{L}(\omega)] \cdot \chi^{(2)} : [\mathbf{L}(\omega_1) \cdot \hat{\mathbf{e}}(\omega_1)] [\mathbf{L}(\omega_2) \cdot \hat{\mathbf{e}}(\omega_2)]$$
(2.47)

Here, $\hat{e}(\omega_i)$ and $L(\omega_i)$ are the unit polarization vector and Fresnel's Factors (or L-Factors) associated with the interfering laser fields impinged at the interface to generate the sum frequency signal. In the co-propagation reflection geometry of SFG (figure 2.8), the unit polarization vectors are given by: 229,237,238

$$\hat{\mathbf{e}}_{x} = \pm \cos \xi_{i}$$

$$\hat{\mathbf{e}}_{y} = 1$$

$$\hat{\mathbf{e}}_{z} = \sin \xi_{i}$$
(2.48)

Here, \hat{e}_x is positive for the visible and IR laser beams and negative for the SFG signal. The diagonal elements of Fresnel's factors that measure the field present in the interfacial region are given as: 173,233,238,242

$$L_{xx}(\omega_i) = \frac{2n_I(\omega_i)\cos\zeta_i}{n_I(\omega_i)\cos\zeta_i + n_{II}(\omega_i)\cos\xi_i}$$
(2.49)

$$L_{yy}(\omega_i) = \frac{2n_I(\omega_i)cos\xi_i}{n_I(\omega_i)cos\xi_i + n_{II}(\omega_i)cos\zeta_i}$$
(2.50)

$$L_{zz}(\omega_i) = \frac{2n_{II}(\omega_i)cos\xi_i}{n_I(\omega_i)cos\xi_i + n_{II}(\omega_i)cos\xi_i} \left(\frac{n_I(\omega_i)}{n'(\omega_i)}\right)^2$$
(2.51)

$$n_{I}(\omega_{i})\sin\xi_{i} = n_{II}(\omega_{i})\sin\zeta_{i}$$
 (2.52)

$$\left(\frac{n_{\rm I}(\omega_{\rm i})}{n'(\omega_{\rm i})}\right)^2 = \frac{4 n_{\rm II}^2(\omega_{\rm i}) + 2}{n_{\rm II}^2(\omega_{\rm i})(n_{\rm II}^2(\omega_{\rm i}) + 5)}$$
(2.53)

Here x,y, z are the laboratory coordinates. ζ_i is the angle of refraction and ξ_i is the angle of incidence of the ω_i SFG signal and input laser beams (visible and infrared) with respect to the interface normal. ζ_i can be calculated by using Snell's law (2.52). n_I , n_{II} , n' are the refractive indices of mediums I, II and that of the interfacial layer.

2.3.5 Molecular Orientation and Polarization Dependent SFG

To obtain molecular and orientational information about the molecular groups present at the surfaces/interfaces, it is necessary to relate the macroscopic $\chi^{(2)}_{ijk}$ elements of laboratory coordinate system (xyz) with the molecular hyperpolarizability tensor $\beta^{(2)}_{pqr}$ in the molecular frame (abc). The detailed expression of $\chi^{(2)}_{ijk}$ is given as: 173,229,233,238,242

$$\chi_{ijk}^{(2)} = \frac{N}{\epsilon_0} \sum \langle R_{ip}(\psi) R_{jq}(\theta) R_{kr}(\phi) \rangle \langle \beta_n^{(2)} \rangle$$
 (2.54)

The angular brackets represent the orientational average over all possible molecular orientations. This is achieved by applying Euler angle transformations using Euler angles (θ, ϕ, ψ) : define the rotation of molecular

axes (abc) with respect to laboratory coordinate axes (xyz). θ represents the tilt from the surface normal, φ , and ψ represent the azimuthal and twist angles (figure 2.10). Here $R_{ip}(\psi)$, $R_{jq}(\theta)$, and $R_{kr}(\varphi)$ are the Euler's rotation matrices that perform transformation between laboratory frame and molecular coordinate frames.

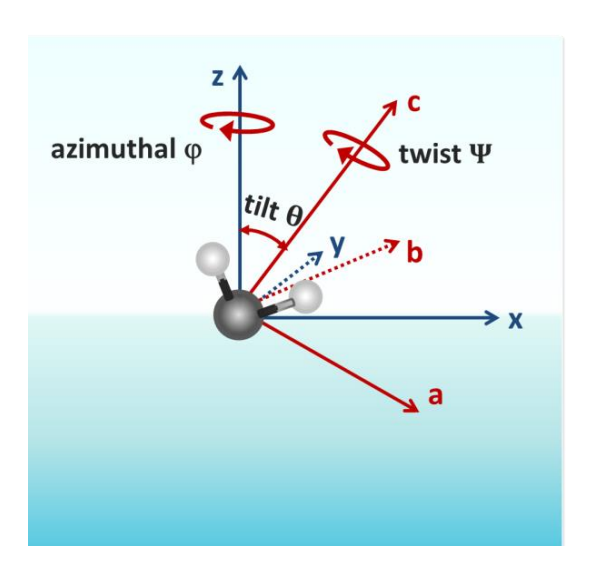


Figure 2.10 Representation of Euler's angles (tilt θ , twist ψ and azimuthal ϕ) between lab coordinates (xyz) and molecular coordinates (abc).

For an azimuthally isotropic surface or interface, there exist four independent nonvanishing components of $\chi^{(2)}$ i.e., $\chi^{(2)}_{yyz} = \chi^{(2)}_{xxz}$, $\chi^{(2)}_{yzy} = \chi^{(2)}_{xzx}$, $\chi^{(2)}_{zyy} = \chi^{(2)}_{zxx}$, and $\chi^{(2)}_{zzz}$. These independent components of $\chi^{(2)}$ contains information about molecular orientation at the interface. This can be probed by different polarization schemes of input (visible, IR) and SFG beams, namely ssp, ppp, and sps. Here, the letter "s" and "p" designate the polarization of laser beams perpendicular and parallel to the plane of incidence. $\chi^{(2),eff}$ in different polarization schemes is given as follows: 173,233,239,242

$$\chi_{ssp}^{(2),eff} = L_{yy}(\omega)L_{yy}(\omega_1)L_{zz}(\omega_2)\sin\xi_2\chi_{yyz}^{(2)}$$
 (2.55)

$$\chi_{sps}^{(2),eff} = L_{yy}(\omega)L_{zz}(\omega_1)L_{yy}(\omega_2)\sin\xi_1\chi_{yzy}^{(2)}$$
 (2.56)

$$\chi_{ppp}^{(2),eff} = -L_{xx}(\omega)L_{xx}(\omega_1)L_{zz}(\omega_2)\cos\xi\cos\xi_1\sin\xi_2\chi_{xxz}^{(2)}$$

$$- L_{xx}(\omega)L_{zz}(\omega_{1})L_{xx}(\omega_{2})\cos\xi\sin\xi_{1}\cos\xi_{2}\chi_{xzx}^{(2)} + L_{zz}(\omega)L_{xx}(\omega_{1})L_{xx}(\omega_{2})\sin\xi\cos\xi_{1}\cos\xi_{2}\chi_{zxx}^{(2)} + L_{zz}(\omega)L_{zz}(\omega_{1})L_{zz}(\omega_{2})\sin\xi\sin\xi_{1}\sin\xi_{2}\chi_{zzz}^{(2)}$$
(2.57)

Sometimes, the expression for ppp-polarization is considered as contributions from two terms instead of four, assuming nearly comparable amplitudes of $\chi^{(2)}_{xzx}$ and $\chi^{(2)}_{zxx}$ terms. Thus, $\chi^{(2),eff}_{ppp}$ can be rewritten as follows: 239,243,251

$$\begin{split} \chi_{ppp}^{(2),eff} &= -L_{xx}(\omega) L_{xx}(\omega_1) L_{zz}(\omega_2) \cos \xi \cos \xi_1 \sin \xi_2 \, \chi_{xxz}^{(2)} \\ &+ \, L_{zz}(\omega) L_{zz}(\omega_1) L_{zz}(\omega_2) \sin \xi \sin \xi_1 \sin \xi_2 \, \chi_{zzz}^{(2)} \end{split} \tag{2.58}$$

It is clear that the different non-zero susceptibility elements of the interfacial layer can be experimentally determined by measuring the intensity of SFG signal in various polarization schemes as mentioned above, provided the optical constants (Fresnel factors) of the other media are known.

2.3.6 Orientation Analysis for Molecular Groups with Different Symmetries

Performing SFG experiments in different polarization schemes enable us to evaluate the orientation of molecular oscillators or molecular groups at the interface. Here we have demonstrated the procedure to calculate the orientation angle of molecular groups carrying two different symmetries, for example, a) free OH oscillator of the water molecule with $C_{\infty v}$ symmetry present in the topmost layer at the air/water interface, and b) methylene group (CH₂-) having C_{2v} symmetry.

2.3.6.1 Orientation Angle Calculation for Free OH Oscillator

The free OH oscillator corresponds to the OH-bond of water molecules present at the topmost layer of the air/water interface, which does not involve in making H-bonds with the neighboring molecules. Its vibrational feature appears at 3704 cm^{-1} and is discussed in detail in chapter 3. To calculate the orientation angle θ formed by the free OH oscillator at the air/water interface (figure 2.11a), we utilized the expressions of $\chi^{(2),eff}$ in ssp and ppp polarization schemes, as shown in equations 2.55 and 2.58. For this, we first calculated the L-factors for the free OH oscillator (3704 cm⁻¹, 2.7 μ m) at the air/water interface, as shown in table 2.1. To generate this table, we have utilized the formulae as provided in equations 2.49-2.53. Here, $n_I(\omega_i)$ is taken unity for air and $n_{II}(\omega_i)$ from references.

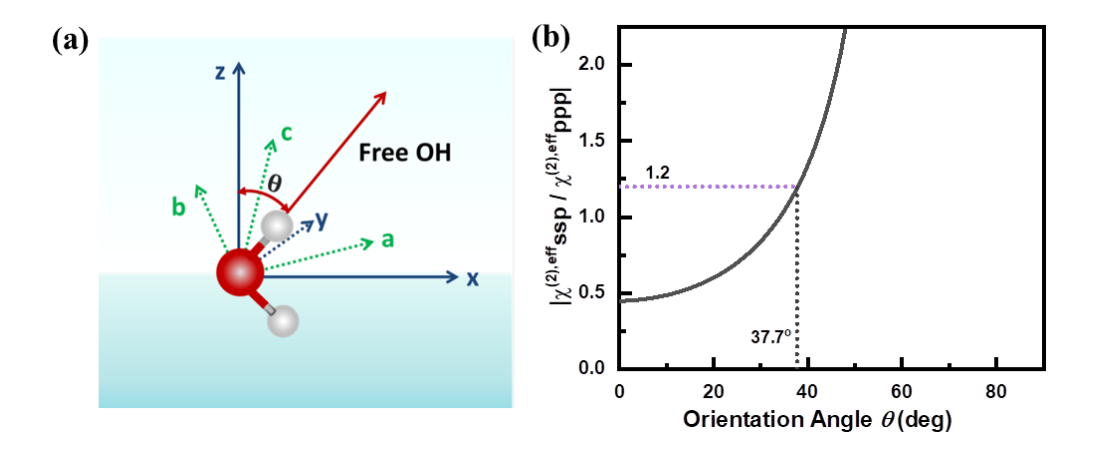


Figure 2.11 (a) Representation of orientation angle θ formed by free OH oscillator with respect to the surface normal. (b) Theoretical orientation curve plotted by using the delta function, showing the variation of $\left|\chi_{\text{ssp}}^{(2),\text{eff}}/\chi_{\text{ppp}}^{(2),\text{eff}}\right|$ (Equation 2.63) with angle θ for free OH oscillator of $C_{\infty v}$ symmetry at the air/water interface.

Table 2.1 Calculated L-factors characteristic of free OH (3704 cm⁻¹, 2.7 μm) at the air/water interface. 65

	n	ξ	L_{xx} . $cos \xi$	L_{yy}	L_{zz} . $sin \xi$
ω(444 nm)	1.34	61.7	0.51	0.64	0.61
$\omega_1(532 \text{ nm})$	1.34	63	0.50	0.62	0.60
$\omega_2(2.7~\mu m)$	1.18	56	0.58	0.80	0.68

We have also checked that considering the imaginary part of the refractive index in $n_{II} = 1.18 + 0.012i$ does not affect the L-factors values. In the present calculations, we have taken n_{II} from reference. Incorporating L-factor values in equations 2.55 and 2.58, we find that the effective second-order nonlinear susceptibility is related to molecular $\chi^{(2)}$ as follows:⁶⁵

$$\chi_{\rm ssp}^{(2),\rm eff} = 0.27 \, \chi_{\rm yyz}^{(2)}$$
 (2.59)

$$\chi_{\rm ppp}^{(2),\rm eff} \approx -0.27\chi_{\rm xxz}^{(2)} + 0.25\chi_{\rm zzz}^{(2)}$$
(2.60)

The free OH bond of water molecules at the air/aqueous interface is known to possess $C_{\infty v}$ symmetry as showcased in the molecular axis system in figure 2.11a. ^{176,199,251,253-255} The corresponding macroscopic susceptibility ($\chi^{(2)}$) is related to the microscopic hyperpolarizability ($\beta^{(2)}$) as follows: ^{65,173,251,254}

$$\chi_{yyz}^{(2)} = \chi_{xxz}^{(2)} = \frac{1}{2} N \beta_{ccc}^{(2)} ((1+r)\langle \cos \theta \rangle - (1-r)\langle \cos^3 \theta \rangle)$$
 (2.61)

$$\chi_{\rm zzz}^{(2)} = N\beta_{\rm ccc}^{(2)}(r\langle\cos\theta\rangle + (1-r)\langle\cos^3\theta\rangle)$$
 (2.62)

Here, N is the number density, and θ is the orientation angle of the free OH oscillator (Figure 2.11a). r is the Raman hyperpolarizability ratio and had been assumed here with value 0.32. ^{65,173,176,253-255} Combining equations 2.59-2.62, we get $\chi^{(2),eff}$ is related to the molecular orientation angle θ as follows: ⁶⁵

$$\left| \frac{\chi_{\text{ssp}}^{(2),\text{eff}}}{\chi_{\text{ppp}}^{(2),\text{eff}}} \right| = \left| \frac{0.18 \langle \cos\theta \rangle - 0.09 \langle \cos^3\theta \rangle}{(-0.04) \langle \cos\theta \rangle + 0.23 \langle \cos^3\theta \rangle} \right|$$
(2.63)

The right-hand side of the equation represents the theoretical orientation curve as depicted in figure 2.11b. The ensemble average $\langle \cos \theta \rangle$ and $\langle \cos^3 \theta \rangle$ can be evaluated by using Gaussian distribution function $f(\theta)$ or by delta function with variance $\sigma = 0$ as follows: $^{65,233,238-239,254}$

$$f(\theta) = \frac{1}{\sigma\sqrt{2\pi}} e^{-(\theta - \theta_0)^2/2\sigma^2}$$
 (2.64)

$$\langle \cos \theta \rangle = \int_0^{\pi} f(\theta) \sin \theta \cos \theta d\theta \qquad (2.65)$$

$$\langle \cos^3 \theta \rangle = \int_0^{\pi} f(\theta) \sin\theta \cos^3 \theta d\theta \tag{2.66}$$

The orientation curve in figure 2.11b is produced by using the delta distribution function. The orientation angle of the molecular group (free OH oscillator) is estimated by the experimental value of $|\chi_{\rm ssp}^{(2),\rm eff}/\chi_{\rm ppp}^{(2),\rm eff}|$, which is estimated by the fitted amplitude ratio of the respective peaks in ssp and ppp-SFG spectra. The ssp and ppp-SFG spectra for the free OH oscillator are given in chapter 3. As depicted in figure 2.11b, the horizontal line corresponds to the experimental value of $|\chi_{\rm ssp}^{(2),\rm eff}/\chi_{\rm ppp}^{(2),\rm eff}|$, and the projection of its intersection with the theoretical curve provides the estimation for the orientation angle value. The angle of the free OH oscillator at the air/water interface comes out to be 37.7(in close agreement with the literature-reported values). $^{176,199,254-255}$

Here, we have showcased the procedure to evaluate the orientation angle by using $\chi^{(2),eff}$ ratio for different polarization schemes, i.e., ssp and ppp of SFG spectroscopy. In the coming section, we are presenting the procedure to estimate the orientation angle of a methylene group at the surface/interface using $\chi^{(2),eff}$ ratio for symmetric and asymmetric vibrational modes in the same polarization, i.e., ppp-SFG scheme.

2.3.6.2 Orientation Angle Calculation for CH2- Group

In the molecular frame (a, b, c), for C_{2v} symmetry methylene groups, the c-axis is defined along the bisector of the two C-H bonds, the a-axis in the H-C-H plane with b-axis out of the plane as depicted in figure 2.12a. For C_{2v} symmetry methylene groups present at an azimuthally isotropic surface/interface, the second-order nonlinear macroscopic susceptibility is related to second-order nonlinear microscopic hyperpolarizability as follows: 173,230,233,242,256

For symmetric stretching (ss) modes:

$$\chi_{yyz}^{(2)} = \chi_{xxz}^{(2)} = \frac{1}{4} N \left(\beta_{aac}^{(2)} + \beta_{bbc}^{(2)} + 2\beta_{ccc}^{(2)} \right) \langle \cos \theta \rangle + \frac{1}{4} N \left(\beta_{aac}^{(2)} + \beta_{bbc}^{(2)} - 2\beta_{ccc}^{(2)} \right) \langle \cos^3 \theta \rangle$$
 (2.67)

$$\chi_{zzz}^{(2)} = \frac{1}{2} N \left(\beta_{aac}^{(2)} + \beta_{bbc}^{(2)} \right) \langle \cos \theta \rangle - \frac{1}{2} N \left(\beta_{aac}^{(2)} + \beta_{bbc}^{(2)} - 2 \beta_{ccc}^{(2)} \right) \langle \cos^3 \theta \rangle$$
 (2.68)

For asymmetric stretching (as) modes:

$$\chi_{yyz}^{(2)} = \chi_{xxz}^{(2)} = -\frac{1}{2} N(\beta_{aca}^{(2)}) (\langle \cos \theta \rangle - \langle \cos^3 \theta \rangle)$$
 (2.69)

$$\chi_{\rm zzz}^{(2)} = N(\beta_{\rm aca}^{(2)})(\langle \cos \theta \rangle - \langle \cos^3 \theta \rangle) \tag{2.70}$$

With $\beta_{aac}^{(2)}+\beta_{bbc}^{(2)}=2\beta_{ccc}^{(2)}\approx 0.98\beta_o^{(2)}$ and $\beta_{aca}^{(2)}=\beta_{caa}^{(2)}\approx 0.66\beta_o^{(2)}$ where β_o is a hyperpolarizability constant for C-H bond. Thus, $\beta_{aac}^{(2)}+\beta_{bbc}^{(2)}-2\beta_{ccc}^{(2)}\approx 0.$

Table 2.2 Calculated L-factors characteristic of vinyl methylene symmetric stretch (2924 cm⁻¹, 3.4 μm) and asymmetric stretch modes at (2984 cm⁻¹, 3.3 μm) at the air/PVP-D₂O interface.

		n	ξ	L_{xx} . $cos\xi$	L_{yy}	L_{zz} . $sin \xi$
	ω(459.1 nm)	1.33	61.95	0.51	0.64	0.61
D_2O	ω(460.6 nm)	1.33	61.97	0.51	0.64	0.61
	$\omega_1(532\text{nm})$	1.33	63	0.50	0.63	0.61
	$\omega_2(3.4~\mu m)$	1.24	56	0.58	0.76	0.65
	$\omega_2(3.3~\mu m)$	1.25	56	0.58	0.75	0.64

The symmetric and asymmetric vibrational modes of methylene groups present in the vinyl chain of polyvinylpyrrolidone (PVP) polymer appear at 2923 cm⁻¹ and 2986 cm⁻¹ respectively.²⁵⁷ The CH-region SFG vibrational spectra characteristic of PVP at the air/PVP-D₂O interface are discussed in chapter 5. The molecular structure of the polymer is provided in figure 2.14d. We have calculated the L-factors of the air/ PVP-D₂O interface as shown in table 2.2. Here, $n_I(\omega_i)$ is taken unity for air and $n_{II}(\omega_i)$ is taken similarly to that of D₂O from Bertie et al.²⁵⁸

Utilizing L-factors values from table 2.2 in equation 2.58, we obtained the relation between the $\chi^{(2),eff}$ and the actual molecular response $\chi^{(2)}$ as given below:

$$\chi_{\text{DDD}}^{(2),\text{eff}}(\text{ss}) \approx -0.17\chi_{\text{XXZ}}^{(2)}(\text{ss}) + 0.24\chi_{\text{ZZZ}}^{(2)}(\text{ss})$$
(2.71)

$$\chi_{ppp}^{(2),eff}(as) \approx -0.17 \chi_{xxz}^{(2)}(as) + 0.24 \chi_{zzz}^{(2)}(as)$$
 (2.72)

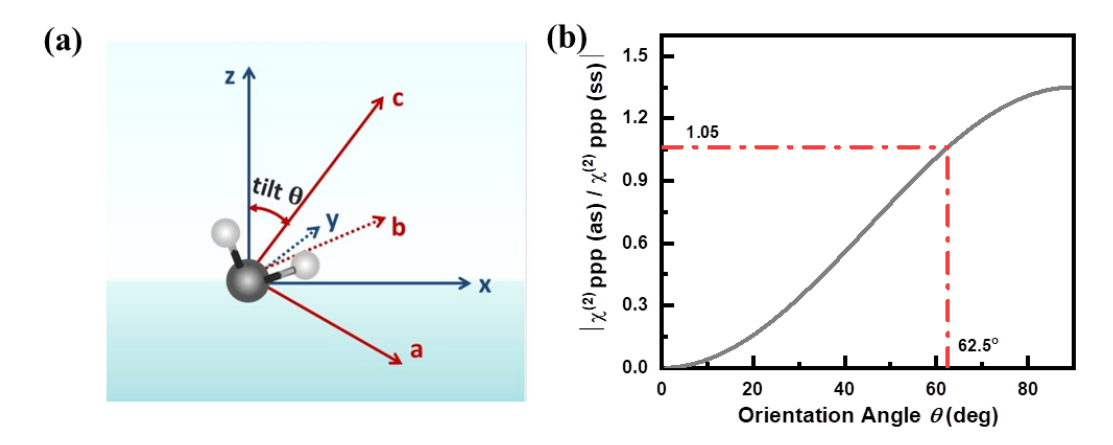


Figure 2.12 (a) Representation of orientation angle θ formed by CH₂-group with the surface normal. (b) Theoretical orientation curve plotted by using delta function, showing the variation of $\left|\chi_{ppp}^{(2),eff}(as)/\chi_{ppp}^{(2),eff}(ss)\right|$ (Equation 2.73) with θ for CH₂-group of C_{2v} symmetry at the air/aqueous interface.

Combining the information from equations 2.67-2.72, we will get:

$$\frac{\chi_{\text{ppp}}^{(2),\text{eff}}(\text{as})}{\chi_{\text{ppp}}^{(2),\text{eff}}(\text{ss})} = \frac{5.89(\langle \cos\theta \rangle - \langle \cos^3\theta \rangle)}{\langle \cos\theta \rangle}$$
(2.73)

We have utilized the right-hand side of the equation to plot the theoretical orientation curve, as depicted in figure 2.12b. The orientation curve is produced by using the delta distribution function. The orientation angle of the methylene group is estimated by the experimental value of $|\chi_{ppp}^{(2),eff}(as)/\chi_{ppp}^{(2),eff}(ss)|$, which is estimated by the fitted amplitude ratio of the asymmetric and symmetric vibrational peaks of CH₂-groups in ppp-SFG spectra (see chapter 5 for spectral details). As depicted in figure 2.12b, the horizontal line corresponds to the experimental value of $|\chi_{ppp}^{(2),eff}(as)/\chi_{ppp}^{(2),eff}(ss)|$, and the projection of its intersection with the theoretical curve provides the estimation for the orientation angle value. For the methylene groups, the angle comes out to be ~ 62° at the air/aqueous interface.

A similar procedure can be adopted to evaluate the orientation angle of molecular groups at surfaces/interfaces utilizing different combinations of ssp, ppp, and sps polarization schemes of SFG vibrational spectroscopy, i.e., ssp (ss)/ssp (as), ssp (ss)/ppp (as), ssp (ss)/ppp (as), ppp (as), ppp (ss)/ppp (ss), ppp (ss)/sps (as) etc.

2.3.6.3 Significance of L-factor correction in Orientation angle Calculation

In this section, we intend to emphasize the importance of incorporating L-factors during the calculation of the orientation angle of a molecular group at surfaces/interfaces. For this, we have presented a comparison of orientation angle analysis for the free OH oscillator of water molecules present at the pristine air/water interface. In the previous section, we plotted the theoretical curve for the L-factor corrected $|\chi_{\rm ssp}^{(2),\rm eff}/\chi_{\rm ppp}^{(2),\rm eff}|$ and the resultant orientation angle for the free OH oscillator comes out to be 37.7° (figure 2.11), which agrees with those reported in the literature. However, if we do not take into consideration of L-factors and directly incorporate $|\chi_{xxz}^{(2)}/\chi_{zzz}^{(2)}|$, this would result in an inaccurate estimation of orientation angles, as showcased below.

In figure 2.13, we have plotted the L-factor corrected $|\chi_{\rm ssp}^{(2),\rm eff}/\chi_{\rm ppp}^{(2),\rm eff}|$ and $|\chi_{xxz}^{(2)}/\chi_{zzz}^{(2)}|$ to highlight the comparative orientation analysis. The expression for the theoretical curve $|\chi_{\rm xxz}^{(2)}/\chi_{zzz}^{(2)}|$ is estimated from equations 2.61-2.62 after incorporation of Raman hyperpolarizability ratio 'r' equal to 0.32. ^{65,173,176,253-255} The resulting equation is as follows:

$$\left| \frac{\chi_{xxz}^{(2)}}{\chi_{zzz}^{(2)}} \right| = \left| \frac{0.66 \langle \cos\theta \rangle - 0.34 \langle \cos^3\theta \rangle}{(0.32) \langle \cos\theta \rangle + 0.68 \langle \cos^3\theta \rangle} \right|$$
(2.74)

If we estimate the ratio $|\chi_{xxz}^{(2)}/\chi_{zzz}^{(2)}|$ with the experimentally obtained amplitude ratio of ssp and ppp-SFG spectra, it estimates an orientation angle of ~ 60° for the free OH oscillator, which is far from the well-accepted angle value of ~ 38°. This error in orientation angle calculation appeared when we ignored the Fresnel's factors (L-factors) in the procedure, which considers the effective electric fields interacting with the molecules present at the surfaces/interfaces.

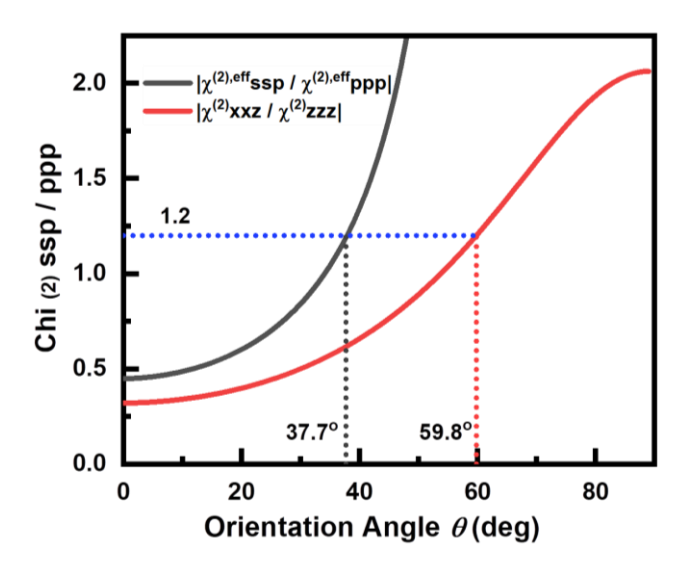


Figure 2.13 Theoretical orientation curves plotted by using the delta function, showing the variation of $|\chi_{\text{ssp}}^{(2),\text{eff}}/\chi_{\text{ppp}}^{(2),\text{eff}}|$ (grey curve) and $|\chi_{xxz}^{(2)}/\chi_{zzz}^{(2)}|$ (red curve) with angle θ for free OH oscillator of $C_{\infty v}$ symmetry at the air/water interface. The horizontal dotted line corresponds to the experimental amplitude ratio for the free OH oscillator in ssp and ppp-SFG spectra, the projection of which on the x-axis estimates the orientation angle values.

2.3.7 SFG Spectrometer

The schematic layout of the SFG spectrometer we have employed in the present thesis curve is shown in figure 2.14. The SFG spectrometer (EKSPLA, Lithuania, SFG061) consists of a picosecond Nd:YAG laser system (PL2231-50). It is a mode-locked, diode-pumped solid-state laser that provides a 28 ps infrared (IR) beam at 1064 nm with an output energy of 40 mJ at a repetition rate of 50 Hz. The schematic diagram of the SFG spectrometer is provided in figure 2.14. The fundamental 1064 nm beam is then used in the second harmonic generation (SHG) unit (SFGH500-2H) to generate a visible beam at 532 nm. Potassium dideuterium phosphate (DKDP) nonlinear crystals are being utilized in the SHG unit to double the frequency of the incident fundamental one. The harmonic unit consists of three DKDP crystals, which result in three 532 nm beams in the

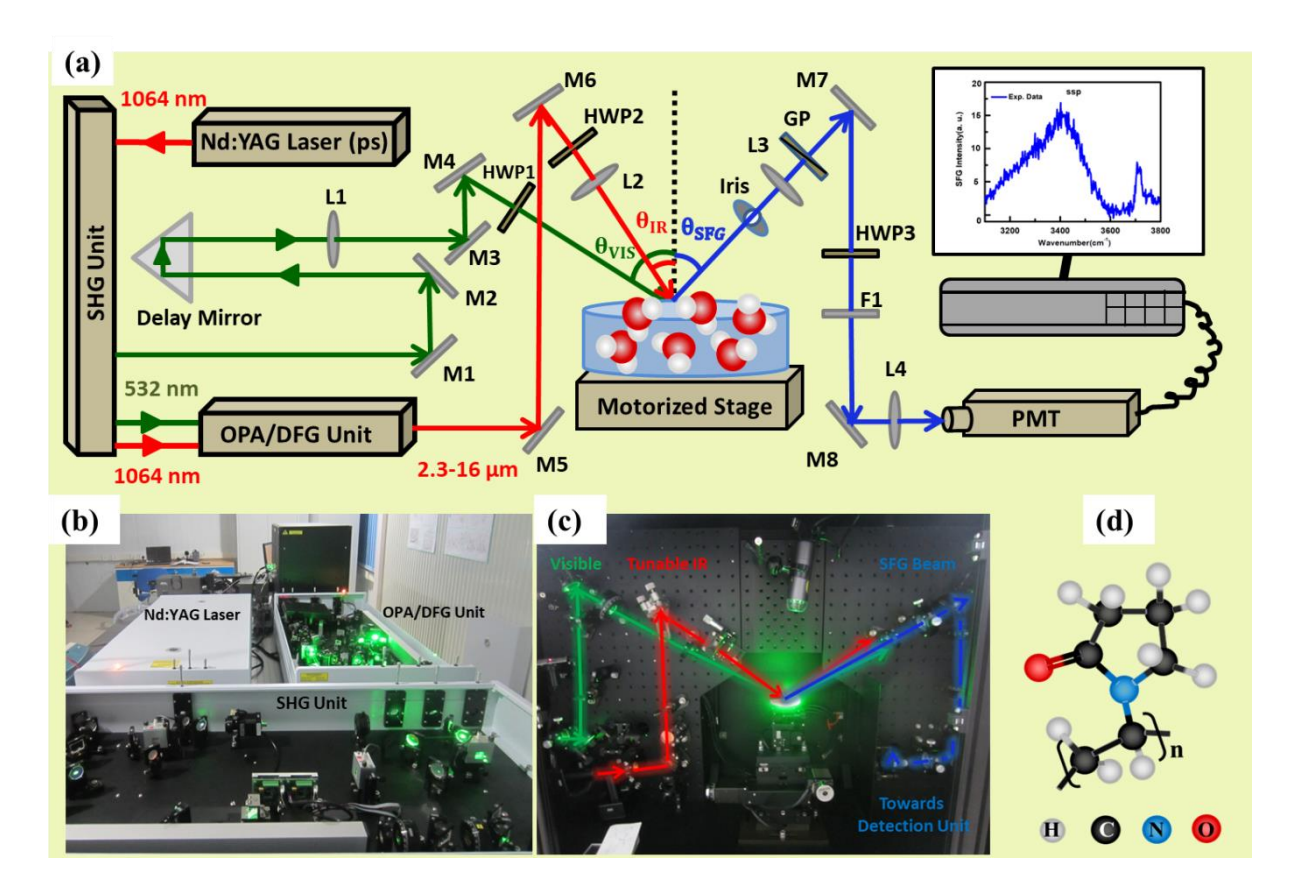


Figure 2.14 (a) Schematic diagram of SFG setup with its essential components. M1-M7, Mirrors; HWP1-HWP3, Half wave plates; L1-L4, Lenses; F1, Filter. (b) Lab SFG experimental setup represents its constituent units: Nd:YAG Laser, SHG unit, OPA/DFG unit, and SFG spectrometer. (c) Inside the SFG spectrometer showing the optical layout where two input pump laser beams (visible and tunable infrared) overlap at the sample surface to generate a sum frequency beam. (d) The molecular structure of the polymer, polyvinylpyrrolidone (PVP), when present at the air/aqueous interface, the resultant SFG spectrum is shown on the computer screen.

output. One of them is utilized at the auxiliary output. The second 532 nm beam is made to pass through the prism-based delay line, which allows synchronization in the SFG spectrometer for the generation of the SFG beam. The third 532 nm beam and the infrared 1064 nm are then fed to the parametric generation unit (PG501-DFG2). Here, 532 nm is utilized in the optical pumping of BBO crystals (beta-barium borate) for optical parametric oscillation (OPO) and optical parametric amplification (OPA) processes of the optical parametric generation (OPG) section of the PG unit. The resultant idler signal (1190-1900 nm) and the fundamental 1064 nm are then fed to the difference frequency generation (DFG) section of the PG unit to produce the tunable IR output from 2300 to 16000 nm. Two BBO crystals are used in the OPG/OPA units, whereas AgGaS₂ (2300 nm -12000 nm) and GaSe (8000 nm -16000 nm) are used in the DFG unit. The fixed frequency visible 532 nm and tunable IR beams are made to impinge on the sample surface at angles ~63° and ~56° with respect to the surface normal to produce the SFG signal. The resultant sum frequency signal reflected at an angle of ~61° is then guided with steering optics to the detection unit. The detection unit consists of a monochromator (MS2001i, SOL instruments Ltd. Belarus) having a wavelength resolution of 0.06 nm and a UV-Visible sensitive photomultiplier tube (Hamamatsu R7899). All the units are automated, and their functioning is controlled by a computer equipped with LabVIEW software. The SFG spectrometer can be operated in different polarization schemes (ssp, ppp, and sps) of input and output laser beams. The polarization scheme ssp designates s-SFG, s-visible, and

p-polarization of incident IR beams. The spatial overlapping of visible and tunable IR beams incident on the sample surface is achieved by manually adjusting guiding mirrors. A guiding red laser diode is utilized for the tunable IR beam to attain the visual overlapping. The temporal overlap of visible and tunable IR pulse beams is ensured by a prism-based motorized delay line placed in the SHG unit. The temporal and spatial overlapping is optimized with the observance of maximum SFG signal intensity at a resonant vibrational frequency of the aqueous sample. To optimize the SFG signal, we work with reference samples of ethanol and/or sodium dodecyl sulphate (SDS). We used to optimize the system alignment at 2930 cm⁻¹ and 3220 cm⁻¹, as these are the maximum intense peaks in the SFG spectra of Ethanol and SDS, respectively, at the air/aqueous interface (figure 2.15). After optimizing the system alignment, we record the SFG spectra on the desired sample interfaces. All the spectra are collected at a step size of 2 cm⁻¹ with an acquisition per step of 200 and are fitted with Lorentzian line shape function (Equation 2.46).

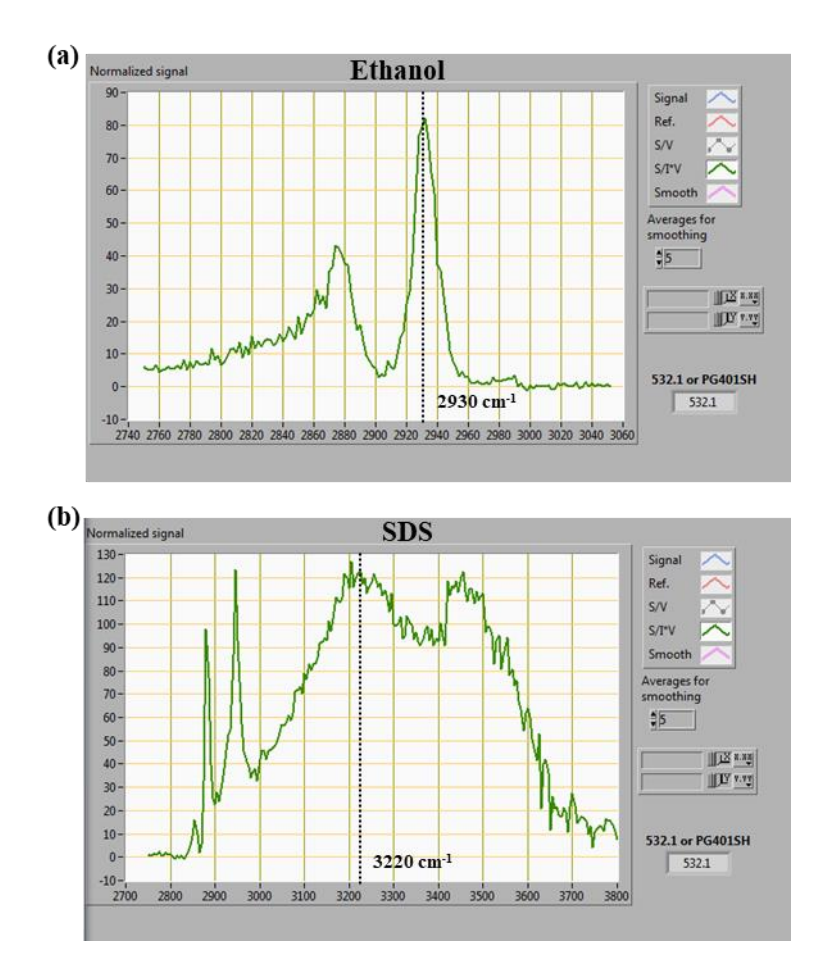


Figure 2.15 SFG spectra at air/aqueous interface carrying (a) Ethanol and (b) SDS, recorded in the ssp-polarization scheme. The spectra are recorded to optimize the SFG system alignment before conducting actual experimental series with the desired samples.

2.3.8 Piranha Cleaning and Sample Preparation

We have utilized a Teflon sample cell (diameter ~5cm) to carry aqueous sample solutions to perform SFG measurements. Cleanliness of the sample cell carries great importance as any minute contaminants might spoil the liquid surface under investigation. Therefore, to achieve the contaminant-free SFG spectra for the pristine air/water interface as reported in the present thesis, we used to perform rigorous piranha cleaning of the sample cell discussed as follows.

Piranha solution is prepared by 3:1 v/v of concentrated sulphuric acid and 30% hydrogen peroxide solution. Since adding hydrogen peroxide (H_2O_2) to sulphuric acid (H_2SO_4) is a highly exothermic reaction; therefore, one should handle the glass container carrying the hot piranha solution with utmost care and safety measures. We used to keep the sample cell in the hot piranha solution for 3-5 hours and then rinse it thoroughly with deionized water. A similar procedure is adopted to clean all the glass wares used during the SFG experiments.

All the samples under SFG investigations are purchased from Sigma Aldrich. The aqueous solution of the samples is prepared by directly dissolving the desired amount of the sample in the deionized water (Millipore ultrapure, type-1, resistivity 18.2 M Ω .cm, pH 5.8) at the lab temperature of 21.5 \pm 0.5°C.

2.4 Surface Tension Measurements

Surface tension measurements of the aqueous samples are carried out by employing the Wilhelmy plate method (figure 2.16a), using Biolin Scientific KSV NIMA Langmuir-Blodgett apparatus (figure 2.16b). Surface tension measures the force acting on the Wilhelmy plate when it comes in contact with the liquid surface. The equation below can be utilized to calculate surface tension with an accuracy of 0.1% under complete wetting conditions.²⁵⁹

$$\sigma_{\rm st} = \frac{F}{I} \tag{2.75}$$

Here, F is the force acting on the plate due to wetting. I is the wetting parameter given by 2 (d'+w). d' and w are the thickness and width of the plate (figure 2.16a).

The experimental lab system consists of a platinum (Pt) plate, which is dipped into the aqueous samples carried in a Teflon sample cell (~ 5 cm diameter and 7 ml capacity). The sample cell is cleaned every time before the experiment using a piranha solution (3:1 v/v of concentrated sulphuric acid to 30% hydrogen peroxide solution) and then rinsed thoroughly with deionized water. The Pt plate is also cleaned by rinsing thoroughly with ethanol and deionized water before use. All the samples are prepared in deionized water, and the measurements are conducted at the lab temperature of $21.5\pm 0.5^{\circ}$ C.

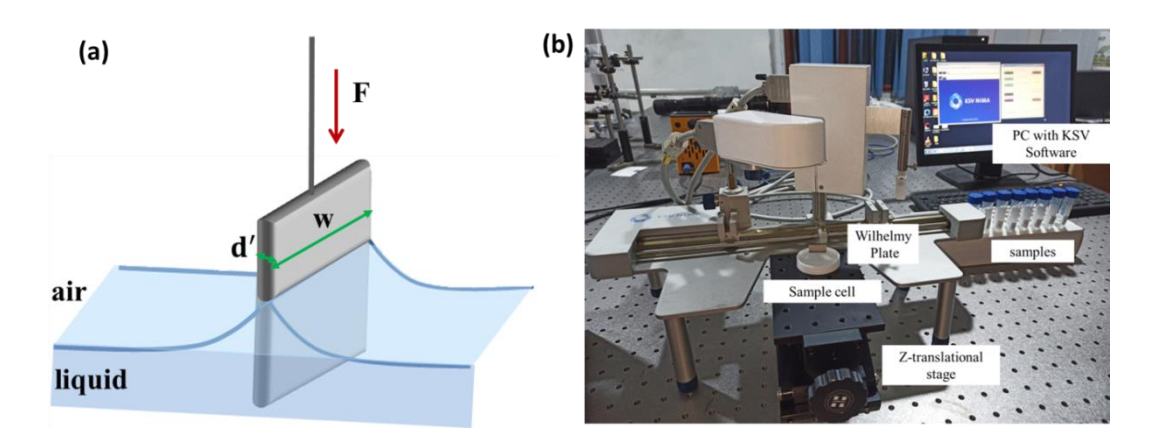


Figure 2.16 (a) Schematic of Wilhelmy Plate method for evaluating the surface tension of liquid samples and (b) Lab experimental set up of Langmuir Blodgett equipped with Wilhelmy plate to perform surface tension studies of the aqueous sample carried in the Teflon sample cell.

2.5 UV-Visible Absorbance Studies

The absorbance studies of aqueous sample solutions are performed with a UV-Visible spectrometer Lamda 950 (from Perkin Elmer). The aqueous samples are carried in quartz cuvettes (path length of 1mm). The absorbance of light passing through the sample cell obeys Beer's Lambert Law as follows: 260-262

$$A = \varepsilon CL' = -\log\left(\frac{I_T}{I_0}\right) \tag{2.76}$$

Here, ϵ and C are the molar extinction coefficient and concentration of the aqueous sample, respectively. L' represents the optical path length i.e., the distance traveled by the light through the sample. I_0 is the intensity of light incident on the sample and I_T is the intensity of light transmitted through the sample, represented in figure 2.17. The sample cells of quartz cuvettes are adequately rinsed with deionized water during the experimental sequence. The studies are conducted at the lab temperature of 21.5 ± 0.5 °C.

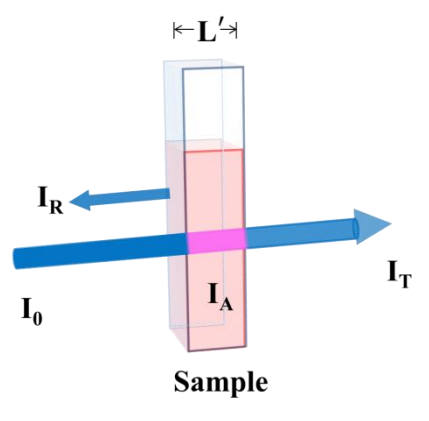


Figure 2.17 Schematic ray diagram depicting the reflection, transmission, and absorption of the light beam incident on a sample cell carrying an aqueous solution.

CHAPTER 3

WATER EVAPORATION PROCESS AT AIR/WATER INTERFACE

In this chapter, we have discussed our work published in the Journal of The American Chemical Society as: Bhawna Rana, David J. Fairhurst, and Kailash C. Jena. Investigation of Water Evaporation Process at Air/Water Interface using Hofmeister Ions. *J. Am. Chem. Soc.* 2022, 144(39), 17832-17840.⁶⁵

Evaporation is an interfacial phenomenon in which a water molecule breaks the intermolecular hydrogen (H-) bonds and enters the vapor phase. However, a detailed demonstration of the role of interfacial water structure in the evaporation process is still lacking. Here, we purposefully perturb the H-bonding environment at the air/water interface by introducing kosmotropic (HPO $_4^2$, SO $_4^2$, and CO $_3^2$) and chaotropic ions (NO $_3$ and I $^-$) to excerpt their influence on the evaporation process. Using time-resolved interferometry on aqueous salt droplets, we found that the kosmotropes reduce evaporation, whereas chaotropes accelerate the evaporation process, following the Hofmeister series: $HPO_4^{2-} < SO_4^{2-} < CO_3^{2-} < Cl^- < NO_3^- < I^-$. To extract deeper molecular level insights into the observed Hofmeister trend in the evaporation rates, we investigated the air/water interface in the presence of ions using surface-specific sum frequency generation (SFG) vibrational spectroscopy. The SFG vibrational spectra reveal the significant impact of ions on the strength of the H-bonding environment and the orientation of free OH oscillators from ~ 36.2° to 48.4° at the air/water interface, where both the effects follow the Hofmeister series. It is established that the slow evaporating water molecules experience a strong Hbonding environment with free OH oscillators tilted away from the surface normal in the presence of kosmotropes. In contrast, the fast evaporating water molecules experience a weak H-bonding environment with free OH oscillators tilted towards the surface normal in the presence of chaotropes at the air/water interface. Our experimental outcomes showcase the complex bonding environment of interfacial water molecules and their decisive role in the evaporation process.

3.1 Introduction

Understanding and controlling water evaporation is of great importance in diverse fields of science and technology, including surface patterning, optical mapping of DNA molecules, biological activity on Mars, separating crude oil from water, water harvesting, and disease diagnosis in pharmaceutical industries, etc. 263-268 In the domain of environmental sciences, the rate of evaporation of water molecules from the surface of aqueous aerosols decides the formation or growth of cloud droplets, which plays an indispensable role in maintaining the earth's water cycle and global temperature. 269-271 Thus, understanding water evaporation is of general interest. Despite the prevailing importance of evaporation in our daily lives, the molecular level understanding of this phenomenon is still speculative. The water molecule breaks its hydrogen bonds (H-bonds) with neighboring molecules and leaves the interface to enter the air during the evaporation process. It is worth emphasizing that the interfacial molecular structure of water is quite different from the bulk, displaying a constellation of mono-, di-, tri-, and tetra-coordinated water species, with dangling/free OH, weakly H-bonded, and strongly H-bonded water molecules. 176,178,272 Therefore, the H-bonding environment of the interfacial water molecules inherently carries the potential to play a vital role in the evaporation process. Previous studies of the evaporation of water droplets have shown the influence of co-solvents, gravity, and magnetic fields on evaporation dynamics. 273-276 Recently, Li et al.²⁷⁴ and Edwards et al.²⁷⁶ observed that gravity reverses the convective flows within the evaporating binary micro-droplets. Furthermore, it is also demonstrated that the presence of a magnetic field

affects the thermo-solutal advection and enhances the evaporation rates of paramagnetic aqueous droplets.²⁷⁵ These studies present an understanding of the evaporation phenomenon through macroscopic diffusion, thermal convection, and solutal advection. Molecular dynamics (MD) simulation studies have attempted to develop a molecular level understanding of the process. ²⁷⁷⁻²⁸⁰ For example, Varillay et al. have shown that evaporation can be considered as a ballistic escape from the liquid surface where molecules in the higher energy tail of the Boltzmann's distribution are more susceptible to breaking free. 277 According to Mason, the water species having H-bond coordination numbers one and two possess sufficient energy to escape from the liquid surface.²⁷⁸ Recently, Nagata et al. reported that exactly 44fs after an H-bond formation, two oscillating water molecules are at the closest approach and provide a sufficiently strong energetic kick to a third molecule to get it ejected from the surface.²⁷⁹ In addition, Musolino et al. proposed that the orientation of surface water molecules can also influence the evaporation kinetics. 280 The prevailing literature highlights the importance of how the detailed Hbonding environment and orientation of water molecules is required for a complete mechanistic depiction of the evaporation process. The contribution of free OH (dangling) groups that constitute more than 20% of the population at the topmost water layer of the air/water interface; 176 towards the evaporation process is not explored yet. This prompted us to offer a detailed experimental demonstration with quantitative analysis to reveal the role of interfacial water molecules and their bonding environment in the evaporation process.

In the present study, we build a comprehensive understanding of the evaporation phenomenon by probing the conformation and H-bonding environment of water molecules at the air/aqueous interface. The H-bonded network can be easily perturbed in the presence of guest moieties. 171,178,181,234,239-240,272,281-282 We have used this fact and purposefully employed a series of Hofmeister sodium salts; the selected anions are as follows:

$$HPO_4^{2-} > SO_4^{2-} > CO_3^{2-} > Cl^- > NO_3^- > I^-$$
 (3.1)

Franz Hofmeister reported this series in 1888, in which ions are placed as per their capacity to precipitate proteins from their aqueous solution.⁵ The ions to the left of chloride ion are known as kosmotropes (structure-makers) while those to the right as chaotropes (structure-breakers).³⁵⁻³⁹ The ions have a significant structuring effect on the bonding environment of water molecules at the air/aqueous interface. Therefore, we have selectively utilized the influence of Hofmeister ions to tune the interfacial structure of water molecules to extract new molecular level insights about the evaporation process.

Here, we first studied the impact of Hofmeister ions on the evaporation dynamics of sessile water droplets using an in-house time-resolved interferometry setup. It is observed that the kosmotropes impede evaporation, whereas chaotropes accelerate the evaporation rate compared to the pristine air/water interface. The observed ion-specific variation in the evaporation rates is ascribed to the variation in interfacial water structure at the air/aqueous interface as investigated by Sum frequency generation (SFG) vibrational spectroscopy. We have performed orientation angle calculation for the free OH oscillator at the air/aqueous interface in the presence of ions to see their influence on evaporation. It is found that the kosmotropes promote strongly H-bonded water species at the interface with free OH oscillators tilted away from the surface normal, reflecting the signature of slowing down the evaporation process. In contrast, the presence of chaotropes brings weakly bonded water species with the free OH oscillator tilted more towards the surface normal, accelerating the evaporation.

3.2 Experimental Section

3.2.1 Materials

In the present work, we have performed experiments with six inorganic sodium salts (Na₂HPO₄, Na₂SO₄, Na₂CO₃, NaCl, NaNO₃, and NaI), purchased from Sigma Aldrich and used without any further purification.

3.2.2 Time-Resolved Newton's Ring Interferometry

We have utilized time-resolved Newton's ring interferometry to estimate the evaporation rate of sessile aqueous droplets. The details of the experimental setup and theory behind calculating evaporation rates are discussed in section 2.1 of chapter 2. In the present experiments, we have performed evaporation rate studies with 20 μ l aqueous sessile droplets of pristine water and 1M sodium salt solutions. All the aqueous samples are prepared in deionized water (Merck, Millipore direct-Q3, electrical resistivity of 18 M Ω .cm).

3.2.3 Surface Tension Measurements

We have performed the surface tension measurements of the aqueous samples using the Wilhelmy plate method, using Biolin Scientific KSV NIMA Langmuir-Blodgett apparatus. The system consists of a platinum (Pt) plate, which is dipped into the aqueous samples carried in a Teflon sample cell (~ 5 cm diameter and 7 ml capacity). The sample cell is cleaned every time before the experiment using a piranha solution (3:1 v/v of concentrated sulphuric acid to 30% hydrogen peroxide solution) and then rinsed thoroughly with deionized water. The Pt plate is also cleaned by rinsing thoroughly with ethanol and deionized water before use. All the samples are prepared in deionized water, and the measurements are conducted at the lab temperature of 21.5 ± 0.5 °C.

3.2.4 Sum Frequency Generation (SFG) Vibrational Spectroscopy

We have used surface-specific SFG vibrational spectroscopy to investigate the bonding environment and orientation of water molecules present at the air/aqueous interface. The theory and instrumental setup are discussed in section 2.3 of chapter 2. All the SFG spectra are collected in different polarization schemes (ssp and ppp) in the OH stretching region from 3000 to 3800 cm⁻¹ at a step size of 2 cm⁻¹ and acquisition per step of 200 and are fitted with Lorentzian line shape function (equation 3.2). The fitting parameters are provided in appendix A.

$$\chi^{(2),\text{eff}} = \chi_{NR}^{(2)} + \sum_{\nu} \frac{A_{\nu}}{(\omega_{\nu} - \omega_{2} - i\Gamma_{\nu})}$$
 (3.2)

All the aqueous samples for SFG measurements are prepared in deionized water. We used a Teflon sample cell (diameter \sim 5cm) to carry the aqueous sample for SFG measurements. The sample cell is cleaned every time before the experiment using a piranha solution (3:1 v/v of concentrated sulphuric acid to 30% hydrogen peroxide solution) and then rinsed thoroughly with deionized water. All the experiments are conducted in the lab temperature of 21.5 \pm 0.5°C.

3.3 Results and Discussion

Figure 3.1a shows evaporation rate plots for aqueous droplets of pristine water and that of different sodium salt solutions with an initial concentration of 1M. The slopes of these plots are utilized to quantify the evaporation

rate values. The ion-specific evaporation rates of sessile droplets (Figure 3.1b) follow the Hofmeister series as follows:

$$HPO_4^{2-} < SO_4^{2-} < CO_3^{2-} < Cl^- < NO_3^- < I^-$$
(3.3)

with a minimum evaporation rate for Na_2HPO_4 (83 nm/sec) and a maximum evaporation rate for NaI (333 nm/sec). Evidently, the presence of kosmotropes (HPO_4^{2-} , SO_4^{2-} , and CO_3^{2-}) impedes the evaporation, whereas the presence of chaotropes (NO_3^{--} , and I^{--}) accelerate the evaporation rate at the air/water interface compared to the pristine water droplet (147 nm/sec). The findings from the time-resolved interferometry experiment confirm the significant impact of ions on the evaporation process.

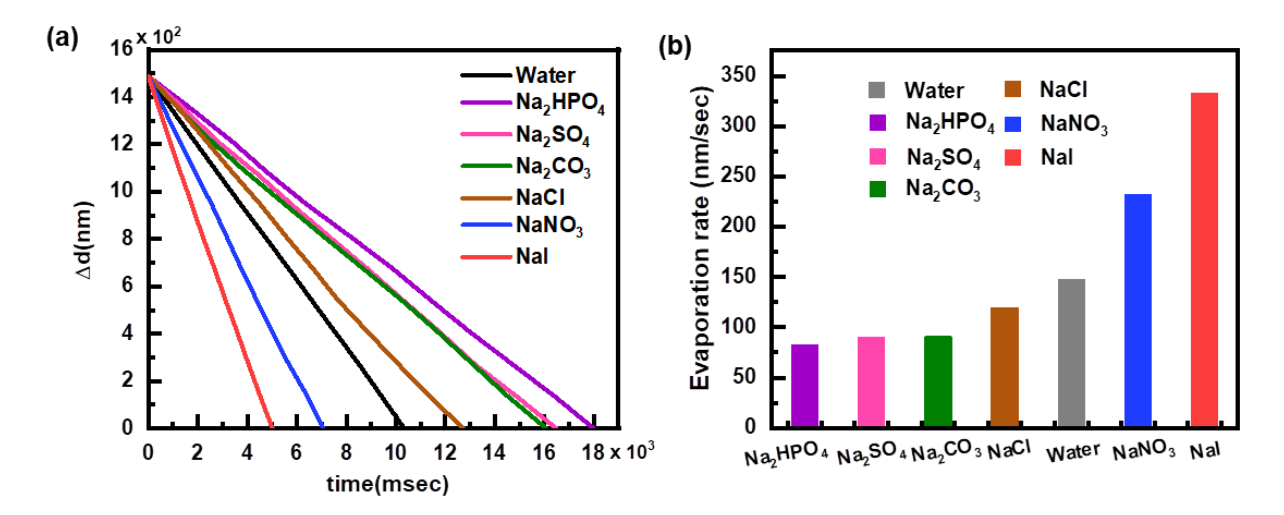


Figure 3.1 (a) Change in droplet's central thickness (Δd) vs. time for sessile aqueous droplets of pristine water and 1M sodium salt solutions. The slopes of these experimental plots provide evaporation rates at the air/aqueous interface (panel (b)).⁶⁵

Ions significantly affect the surface tension of water, which could be responsible for the observed variation in the evaporation rate studies. In order to investigate the same, we have carried out the surface tension measurements of 1M sodium salt solutions (Figure 3.2). It has been noticed that the surface tension values of the salt solutions are higher than the pristine water and follow the Hofmeister trend:

$$CO_3^{2-} > HPO_4^{2-} > SO_4^{2-} > Cl^- > NO_3^- > I^-$$
 (3.4)

This implies that the net effective force on the surface water molecules from the molecules present at the subsurface is enhanced by introducing sodium salt solutions compared to the neat water. Therefore, the water molecules anticipating to evaporate with the presence of Hofmeister ions would require more energy to overcome the high surface tension and, thereby, based on Gibb's energy theorem, is not a thermodynamically favorable event. The observed high surface tension values justify slower evaporation rates in the presence of kosmotropes. However, it fails to explain the high evaporation rates in the presence of chaotropes compared to the pristine water. The surface tension measurements lack a detailed molecular level understanding of the molecules residing at the interfacial region. This suggests that the surface tension measurements cannot solely explain the observed evaporation rate studies. Therefore, a detailed molecular level probing scheme needs to be implemented to extract the microscopic details about the H-bonding environment of the water molecules at the air/aqueous interface.

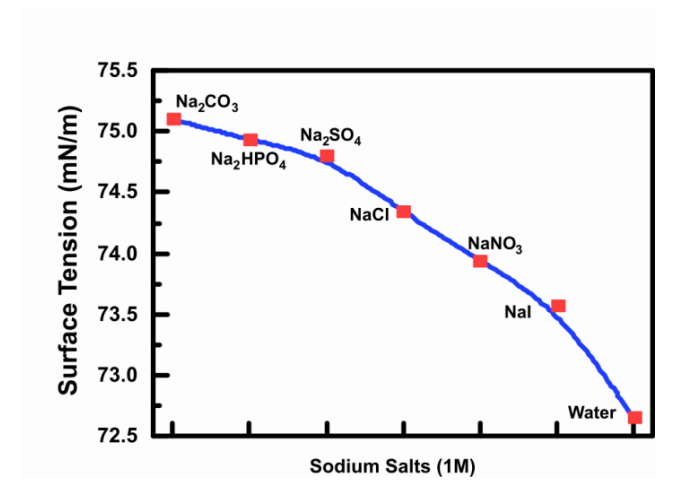


Figure 3.2 Surface tension values of 1M sodium salt solutions. 65

To extract a detailed molecular level understanding of the observed Hofmeister trend in the evaporation rate, we have employed SFG vibrational spectroscopy to probe the influence of ions on interfacial water structure at the air/aqueous interface. The schematic layout of the SFG experiments is presented in figure 3.3a. SFG vibrational spectroscopy is based on a second-order nonlinear optical process. It is an ideal spectroscopic tool to probe the conformation and structure of the moieties selectively lying in the interfacial region. 35,65,170-171,173-182,227-251,253-254 We consider the SFG spectrum at the pristine air/water interface as the reference spectrum to observe the comparative impact of various salts (Figure 3.3b). The spectra (Figure 3.3b-d) consist of a broad region from 3000 to 3650 cm⁻¹ is assigned with three peak positions at around 3230, 3445, and 3550 cm⁻¹. The lowest frequency ensemble is attributed to strongly H-bonded (tetrahedral coordinated) water molecules, and the higher frequency peaks correspond to weakly H-bonded water molecules; however, still the exact assignment of these peaks continues to be ambiguous. 160,171,176,178,181,193,272,283-290 The sharp peak at 3704 cm⁻¹ corresponds to the stretching mode of the non-hydrogen bonded free OH oscillator (dangling bond) of water molecules protruding out of the interface. The SFG intensity plots shown in figure 3.3 (c and d) reflect the water spectra in the presence of ions at the air/aqueous interface. 171,190,202 For our analysis, we considered the peak amplitude ratio of 3445 cm-1 to 3230 cm-1 to estimate the strength of the H-bonding environment of water molecules at the interface. 160,289 It is quite evident from the SFG plots that the presence of ions significantly perturbs the Hbonding environment of the water molecules. The relative enhancement in SFG intensity around 3230 cm⁻¹ in the presence of kosmotropes (HPO $_4^{2-}$, SO $_4^{2-}$, and CO $_3^{2-}$) and at 3445 cm⁻¹ for chaotropes (NO $_3^{-}$ and I $_2^{-}$) has been attributed to the size, charge, polarizability, and surface propensity of respective ions at the air/aqueous interface. 171,191-192,201,203 We have plotted the variation in relative oscillator strength as a function of ions present at the interface (Figure 3.3e). The relative oscillator strength follows the Hofmeister series (equation 3.3), where the minimum value is observed for HPO₄²⁻, and maximum in the presence of I⁻. It indicates the ability of kosmotropes to make more strongly H-bonded water species at the interface compared to the neat air/water interface. In contrast, we have witnessed an increase in the weakly H-bonded molecules in the presence of chaotropes.

The ability of kosmotropes and chaotropes to make strong/weak H-bonded water structure can be understood as follows: It is known that due to the small size and low polarizability, the kosmotrope anions are repelled from the interface and are strongly hydrolyzed. 35-39,64,66,167,292 Owing to the high charge density of kosmotropes, the water molecules in their surroundings are closely packed and thus use the configuration to make a strongly H-

bonded network.^{155,292} However, with the large size and high polarizability, the chaotropes are known to get adsorbed at the interface where the ions lose part of their hydration sheath, resulting in weakly H-bonded water molecules.^{64,154,167,292}

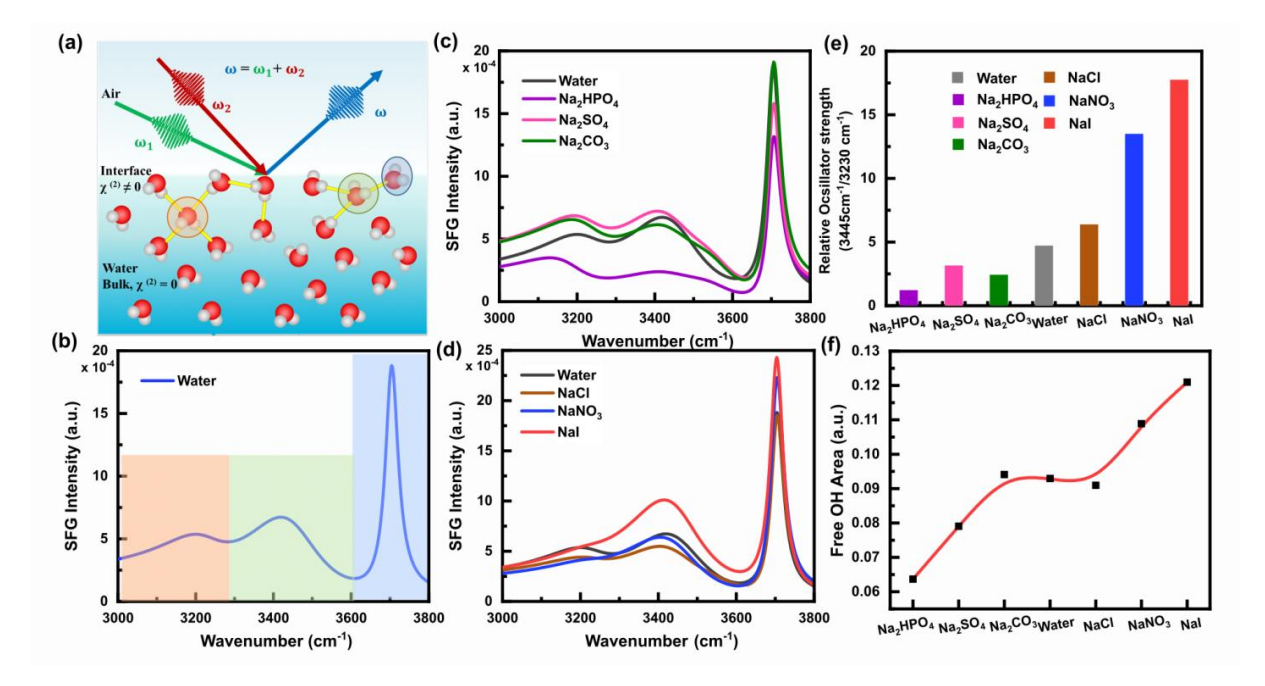


Figure 3.3 (a) Sketch of SFG vibrational spectroscopic experiments on air/aqueous interface. (b) SFG spectrum collected from the pristine air/water interface in ssp polarization scheme; water species contributing to the shaded spectrum region are presented in panel (a). Polarization scheme ssp designates s-SFG, s-visible, and p-polarization of IR beams. Panel (c) and (d) SFG spectra at air/aqueous interface in the presence of 1M Hofmeister series sodium salts. The curves are Lorentzian fitted profiles; the fitting parameters are provided in table A1. Panel (e) and (f) represent the variation in relative oscillator strength (amplitude ratio of SFG peaks at 3445 cm⁻¹ and 3230 cm⁻¹) and the integrated area under the free OH peak (3660 cm⁻¹ to 3750 cm⁻¹) as a function of ions at the air/aqueous interface.⁶⁵

Figure 3.3f demonstrates the variation in free OH peak area as a function of various ions. An increasing trend is observed moving from kosmotropes towards chaotropes, with a minimum free OH area for Na_2HPO_4 and a maximum value for NaI. This observation can be attributed to the possible enhanced population of free OH water molecules in the presence of chaotropes compared to kosmotropes at the interfacial region. This is because the SFG signal intensity is proportional to $N(\cos\theta)$. Here, N represents the number of molecules participating in the SFG process at the interface while θ is the orientation angle. Therefore, the contribution from θ cannot be ignored; for which, we must consider the contribution of the orientation of free OH oscillators towards the observed variation in the SFG intensity or integrated area.

We performed a quantitative analysis to determine the impact of Hofmeister ions on the orientation of free OH groups at the air/aqueous interface. Du et al. ¹⁷⁶ first studied the orientation of free OH groups at the air/aqueous interface and was subsequently investigated by various groups. ^{251,253-255,293-294} Figure 3.4 shows the recorded SFG spectra in ssp and ppp-polarization schemes at the air/aqueous interface in the presence of 1M sodium salts from 3660 cm⁻¹ to 3750 cm⁻¹. For our analysis, we have normalized the ssp-SFG spectra and accordingly scaled the

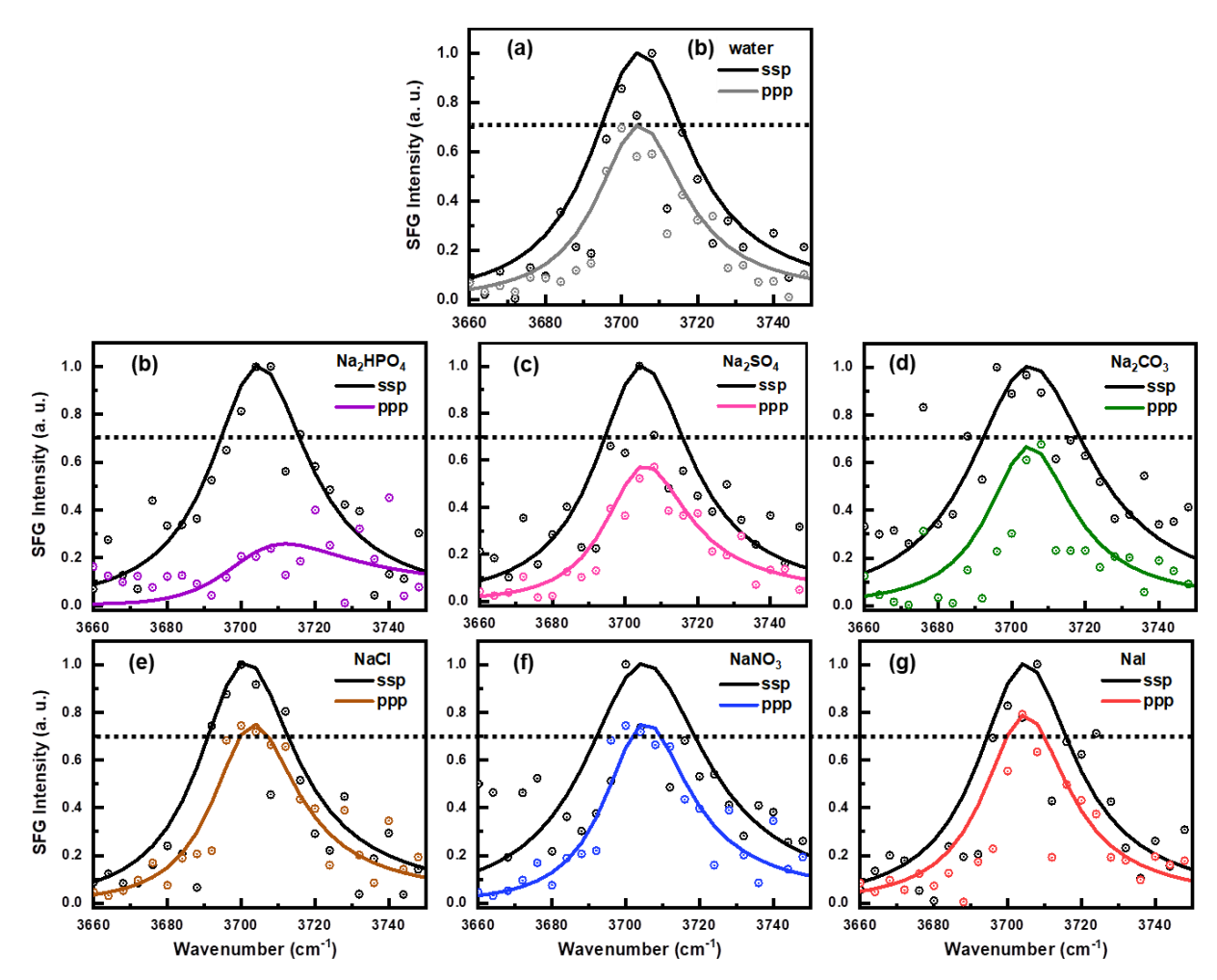


Figure 3.4 (a)-(g) SFG intensity spectra for free OH oscillator at air/aqueous interface in the presence of various 1M Hofmeister series sodium salts in ssp and ppp-polarization schemes. The points show experimental data, and the solid lines are the Lorentzian fit curves. Fitting parameters are given in table A2 of Appendix A. The horizontal dotted line reflects the apparent ion-specific variation in ppp-spectral intensity of free OH peak compared to pristine air/water interface (a).⁶⁵

ppp-SFG spectra; which demonstrate the ion-specific perturbations in the free OH peak intensity. The free OH spectral profiles recorded in ssp and ppp-schemes are then utilized for the calculation of the orientation angle of the free OH oscillator with respect to the surface normal (Figure 3.5). The detailed theory and calculation of the orientation angle of the free OH oscillator are discussed in sections 2.3.4-2.3.6 of chapter 2. Figure 3.5b represents the theoretical orientation curve, as generated from the right-hand side of equation 3.5.

$$\left| \frac{\chi_{\text{ssp}}^{(2),\text{eff}}}{\chi_{\text{npp}}^{(2),\text{eff}}} \right| = \left| \frac{0.18 \left\langle \cos\theta \right\rangle - 0.09 \left\langle \cos^3\theta \right\rangle}{\left(-0.04 \right) \left\langle \cos\theta \right\rangle + 0.23 \left\langle \cos^3\theta \right\rangle} \right| \tag{3.5}$$

where the ensemble average $\langle\cos\theta\rangle$ and $\langle\cos^3\theta\rangle$ are evaluated by using delta distribution function $f(\theta)$ with $\sigma=0$ as follows: $^{65,233,238-239,254}$

$$f(\theta) = \frac{1}{\sigma\sqrt{2\pi}} e^{-(\theta - \theta_0)^2/2\sigma^2}$$
(3.6)

$$\langle \cos \theta \rangle = \int_0^{\pi} f(\theta) \sin \theta \cos \theta d\theta$$
 (3.7)

$$\langle \cos^3 \theta \rangle = \int_0^{\pi} f(\theta) \sin\theta \cos^3 \theta d\theta \tag{3.8}$$

The left-hand side of equation 3.5 corresponds to the horizontal lines in figure 3.5b, which are estimated by the amplitude ratio of the free OH oscillator obtained from Lorentzian fitting of ssp and ppp-SFG spectra (figure 3.4). The intersection points of horizontal lines with the theoretical curve facilitate the values of free OH tilt angle with respect to the surface normal. The values of free OH tilt angles in the presence of a variety of ions at the air/water interface are given in table A3 and plotted in figure 3.6a.

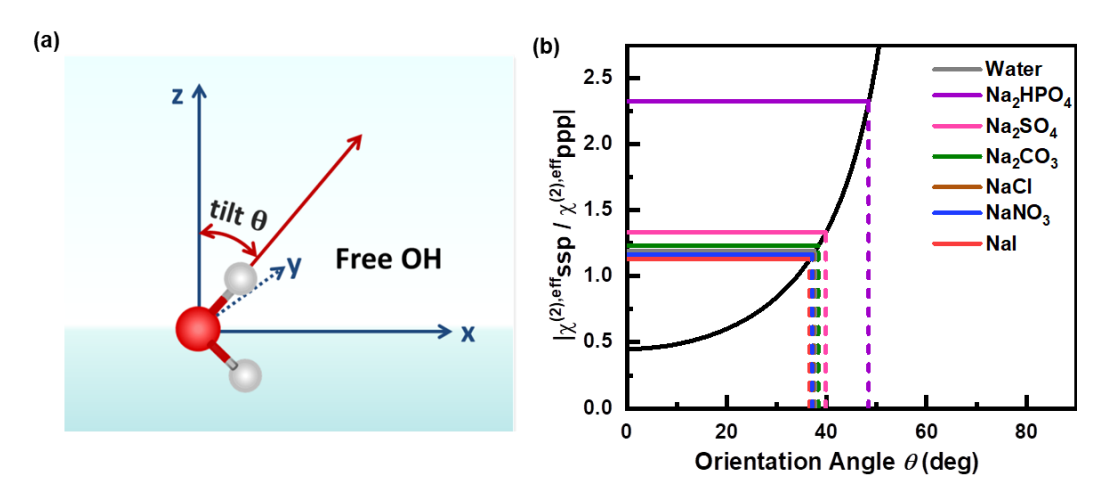


Figure 3.5 (a) Representation of orientation angle (tilt angle) θ formed by free OH oscillator with respect to surface normal at the air/water interface. (b) Theoretical orientation curve showing the variation of $\left|\chi_{ssp}^{(2),eff}/\chi_{ppp}^{(2),eff}\right|$ with angle θ of free OH oscillator of surface water molecules with $C_{\infty v}$ symmetry; The horizontal solid lines are the experimental ratio of free OH amplitudes evaluated from the Lorentzian fitted ssp, ppp spectra recorded at air/salt-water interface (figure 3.4). The intersection points of horizontal lines with the theoretical curve (black solid line) facilitate the values of free OH tilt angle with respect to the surface normal in the presence of a variety of ions, values given in table A3.⁶⁵

For the pristine air/water interface, we determine the free OH angle to be 37.7° which is in close agreement with the values reported in the literature. ^{176,199,254-255} In comparison to the pristine air/water interface, we have observed an enhancement in free OH tilt angle in the presence of kosmotropes, whereas a minute decrement is observed for chaotropes. Figure 3.6a (left axis) shows the variation in the orientation angle of free OH as a function of ions present at the air/aqueous interface, which follows the Hofmeister series (Equation 3.1). The free OH orientation angle is maximum ~ 48.4° in the presence of Na₂HPO₄, and decreases as we move from kosmotropes to chaotropes (left to right, Figure 3.6a) with a minimum value of 36.2° in the presence of NaI. In the past, ion-specific orientation studies of free OH groups have not been explored in detail. A recent report by Feng et al. showed that the presence of NaF (kosmotrope) rotates the free OH group away from the surface normal. ¹⁹⁹ This finding agrees with our experimental observations of the reorientation of the free OH oscillator

towards the air/aqueous interface in the presence of kosmotropic ions. The significant increase in free OH tilt angle in the presence of HPO_4^{2-} and SO_4^{2-} correlates well with the previously observed decrease in free OH peak

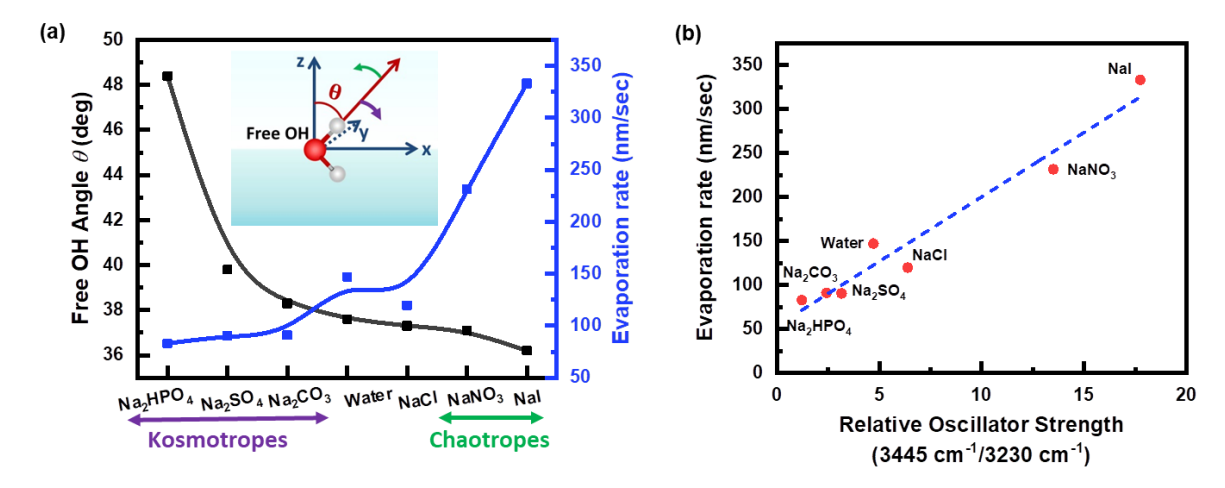


Figure 3.6 (a) Ion-specific variation in tilt angle values of free OH oscillator (left axis) in inverse correlation with the evaporation rates (right axis) studied at the air/aqueous interface. (b) Evaporation rates of the sessile droplets obtained from interferometry experiment (Figure 3.1b) plotted as a function of relative OH oscillator strength observed from SFG spectra (Figure 3.3c-d).⁶⁵

area (Figure 3.4f). However, for the case of chaotropes, the relative change in the orientation of the free OH group is quite small and is tilted more towards the surface normal. This indicates that the increase in the SFG signal for chaotropes (Figure 3.4f) might have arisen due to an increase in the population of free OH groups at the interfacial region. The right axis of figure 3.6a represents the ion-specific evaporation rates at the air/aqueous interface, which are found to follow an inverse correlation with the observed trend of free OH tilt angle in the presence of ions. Moreover, figure 3.6b provides a linear and direct correlation between the sessile droplet's evaporation rates (Figure 3.1b) against the relative oscillator strength acquired from SFG spectra (Figure 3.3e). Combining the observations from figure 3.6, we can conclude that the presence of kosmotropes (HPO $_4^{2-}$, SO $_4^{2-}$, and CO $_3^{2-}$) brings more strongly H-bonded water moieties at the air/aqueous interface, with free OH oscillators significantly tilted away from the surface normal. This, in turn, lowers the evaporation rates compared to the pristine air/water interface. However, with chaotropes (NO $_3^{-}$ and I $_2^{-}$), we find a more weakly H-bonded environment with a little reorientation of free OH oscillators towards the surface normal, resulting in a higher evaporation rate.

The impact of the strength of the H-bonding environment and orientation of the free OH oscillator on the evaporation process can be understood as follows: A water molecule possesses 9-degrees of freedom; 3-translational, 3-rotational, and 3-vibrational. 277-278,280 When a water molecule binds to other molecules, it loses degrees of freedom resulting in a reduction in its average/free energy. In addition, the orientation of water OH oscillator plays an essential role in the formation of H-bonds 199,255,295 and hence, in turn, determines the average/free energy of surface water molecules. This is consistent with the reported molecular dynamics study, where Musolino et al. described that the water molecule with the dipole vector oriented more towards the surface normal loses its H-bonds with nearest neighbors and carries high average/free energies at the air/water interface. In addition, the average energy difference between tetrahedral and monomer configuration of interfacial water molecules is found to be comparable with the enthalpy of vaporization, which is

11.5kcal/mol.²⁸⁰ We have shown the variation in free energy of water molecule as a function of the number of H-bonds it donates and/or accepts with its neighbors (Figure 3.7).²⁸⁰ It is evident from the plot that the water molecule possesses minimum free energy for the tetrahedral configuration. A rise in the energy value is observed for those water molecules where it breaks its H-bonds with the surrounding water molecules. This indicates that

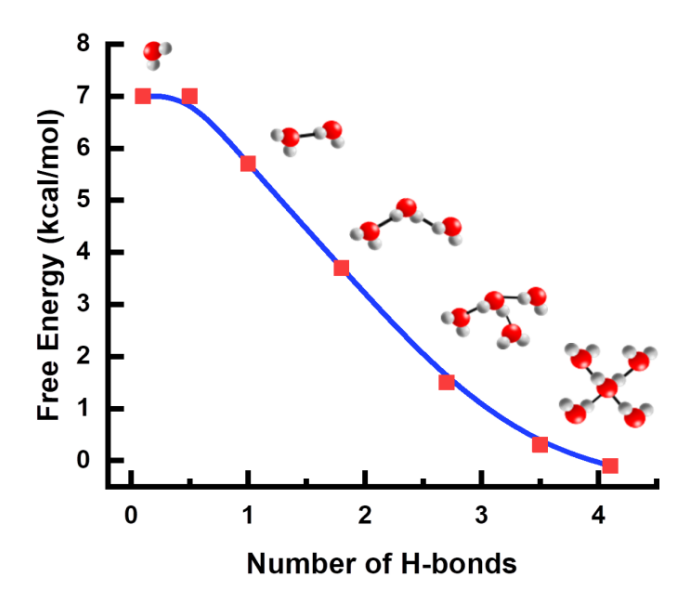


Figure 3.7 Variation in free energy of water molecule as a function of number of H-bonds it makes with the surrounding water molecules.⁶⁵ The data has been extracted from Musolino et al.²⁸⁰

Table 3.1 Binding Energy values for aqueous ionic clusters. 154-155

Sr.	Aqueous	Binding		
No.	Cluster	Energy		
		(kcal/mol)		
1.	$SO_4^{2-}(H_2O)_9$	-178.77		
2.	$Cl^{-}(H_{2}O)_{9}$	-91.06		
3.	$I^{-}(H_{2}O)_{9}$	-74.70		
4.	$(H_2 0)_{10}$	-82.42		

the strongly H-bonded species and the conformation of top layer water molecules with free OH groups tilted away from the surface normal, as observed in the presence of kosmotropes belong to the configuration of low energy. Therefore, the anticipated lower energy configuration of the water molecules in the presence of kosmotropes must be responsible for slowing down the evaporation process. In distinction, the decrease in the H-bonding strength of interfacial water molecules with the possible enhanced population of free OH oscillators in the presence of chaotropes leads to the configuration of high energy. Hence, the occurrence of higher energy configuration of the water molecules may have been responsible for accelerating the evaporation process for

chaotropes. The present argument of lower/higher energy configuration of water molecules in the presence of Hofmeister ions is further supported by the computational studies by Heindel et al.¹⁵⁴ and Herman et al.¹⁵⁵, where the kosmotropic and chaotropic anions are involved in enhancing and reducing the binding energies of the aqueous clusters (Table 3.1).

3.4 Conclusions

In summary, we have used surface-specific SFG vibrational spectroscopy and time-resolved interferometry to establish an intriguing correlation between the interfacial water structure (H-bonding and orientation of free OH oscillators) and the evaporation process. Structure making and breaking Hofmeister ions provided a platform to visualize the conformation of water molecules characteristic of slow/fast evaporation at the air/aqueous interface (figure 3.8). The presence of kosmotropes (HPO_4^{2-} , SO_4^{2-} , and CO_3^{2-}) foster strongly H-bonded water molecules with an increase in the tilt angle of the free OH oscillators at the interface, slows down the evaporation. However, for the case of chaotropes (NO_3^{-} and I^{-}), we find a more weakly H-bonded environment with little impact on the orientation of free OH oscillators, with possible enhanced population of free OH oscillators resulting in higher evaporation rate. These findings reveal a deeper fundamental insight into the prevailing concerns on evaporation. The outcomes of this work would help in designing interfacial water structures to manipulate the evaporation processes for future needs.

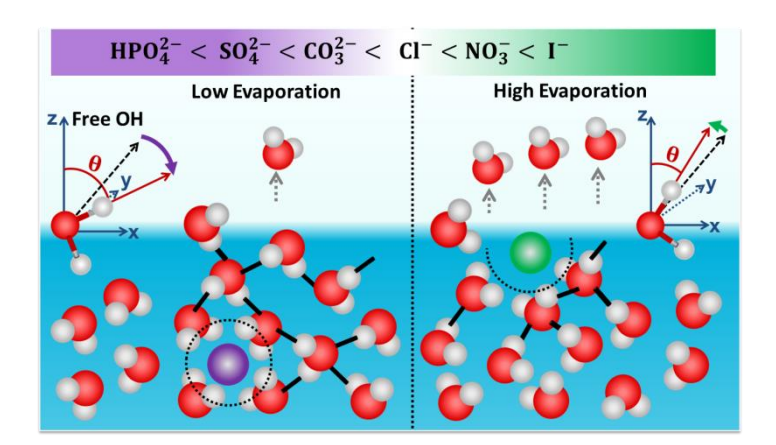


Figure 3.8 Ion-specific H-bonding environment and orientation of free OH oscillator control the water evaporation at air/water interface.

CHAPTER 4

LASER-INDUCED LIQUID MICROJETS AT AIR/AQUEOUS INTERFACE

In this chapter, we have discussed our work submitted for publication in Applied Physical Letters (APL) as: Bhawna Rana, Manoranjan Mishra, and Kailash C. Jena. Impact of Ion-Specific Interactions on Laser-Induced Liquid Microjets. *Appl. Phys. Lett.* 2023 (under review).

Jet velocity and jet power are the crucial parameters that govern the release profile of drugs/vaccines in needle-free injection systems. Salts are the essential constituents of drugs/vaccines as adjuvants; therefore, here we have explored the influence of ions on liquid jet velocity in rhodamine 6G (Rh6G) dye solution. From our experimental findings, it is observed that the presence of ions significantly affects the jet velocity that obeys the Hofmeister series: $SO_4^{2-} > I^- > SCN^-$. This, in turn, governs the ion-specific penetration depths of liquid jets as simulated for the model soft tissue. The observed Hofmeister trend is in accordance with the variation in optical absorbance at the excitation laser wavelength in the aqueous solution owing to the presence of ion-specific interactions between anions and Rh6G. Our experimental findings on ion-specific jet velocity and power could be beneficial in designing needle-free drug delivery systems with controlled penetration depths.

4.1 Introduction

For more than two centuries, needles have been a common drug delivery and vaccination practice. However, it imposes serious health issues due to contaminated waste and needle stick accidents. According to a report, millions of toxic blood injections are administered every year around the world. In order to mitigate the risk of disease spread and pain associated with needles, and the challenges faced during the Covid-pandemic, the research on needle-free injection systems has grabbed the attention in the direction of safe and better delivery tools for drugs and vaccination. 210-215 In the process of operation for the case of needle-free injections, fast liquid jets, owing to their large kinetic energy, penetrate the skin or soft tissues to deliver the drug molecules. An efficient drug delivery system requires precise and reproducible liquid jets with controlled velocity and desired penetration depth. 210,212,214 The conventional needle-free injection systems based on pressure-induced jets consist of compressed gas, spring, or piezo-electric transducer used to generate diffusive shape jets. 223-226 Park et al. demonstrated that the dispersed jets could lead to shallow injections within the skin, leading to higher pain and bruising owing to the collateral damage to tissues. ²¹⁴ In contrast, laser-induced fast liquid jets with fine diameters are less invasive than the conventional 23 G hypodermic needles of diameter $\sim 640~\mu m$. ^{211-213, 216-218} Reducing the jet diameter to a value of 100 µm shows the advantage in drug delivery with minimal damage to the tissue.²¹³ In this novel approach, continuous wave (CW)/pulsed lasers are used to generate vapor bubbles inside a capillary, and the produced vapor bubbles help in emitting the pressure waves which deform the air/liquid boundary to generate highly focused, fine diameter, and fast liquid jets inside the capillary. 211-212, 216-217 It is recognized that the retention time of the drug in the skin and the pharmacological effects are controlled by the diffusion dynamics; hence worth depends on the drug-penetration depth. 210 Recent experimental findings have demonstrated the potential application of laser-induced liquid jets in needle-free injection systems. 212, 215, 218 Hydrogel skin models, rat skin, and artificial human skin have been utilized to investigate the crucial role of jet velocity and jet power in achieving desired penetration depths. Majorly the impact of variable laser energy and the capillary diameter are investigated to achieve the control on jet velocity and penetration depths. 212,215,218 The detailed discussion on laser-induced liquid microjet formation and its parameter dependence is provided in

section 2.2 of chapter 2. We have used the idea of ion-specific variable optical absorption in the present laser-induced liquid jet experiments to study the formation of the liquid jet and its control over regulating the jet velocity and power.

In general, drugs/vaccines consist of various components, one of which is the presence of salts. ¹²³⁻¹²⁵ In the present work, we have employed a series of Hofmeister sodium salts; the selected anions are as follows:

$$SO_4^{2-} > I^- > SCN^-$$
 (4.1)

Here, SO₄²-is the kosmotropic anion whereas I⁻ and SCN⁻ are known as the most chaotropic anions.^{5,35-39} The Hofmeister series salts find considerable applications in the medical industry and are being utilized to improve the bioavailability and solubility of drugs/vaccines in the field of drug delivery.^{122,124-130} Protein-based vaccines such as hepatitis B, human papillomavirus, malaria, tuberculosis, and HIV and/or AIDS consist of aluminum salts (Alum) as adjuvants to induce a protective and long-lasting immune response.¹²³⁻¹²⁴ Since ions are known to significantly perturb the optical properties of aqueous solutions,^{39,49,98} the absorbance of laser pulse energy can be considered an imperative parameter that would govern the jet formation. Therefore, it could be crucial to investigate the influence of ions on the production of liquid microjets for their applications in needle-free injection systems, which has not been explored yet.

To achieve the targeted objectives, we have developed an in-house experimental setup, which uses 532 nm laser beam for the generation of liquid microjets, discussed in detail in section 2.2 in chapter 2. In the present chapter, we have investigated the formation of liquid microjets of an optical dye solution of rhodamine 6G (Rh6G). In medical industry, Rh6G is profoundly being utilized as a model system to investigate the release profile of drugs delivered in skin tissues. To investigate the specific ion effects, we have carried out the jet experiments in Rh6G in the presence of Hofmeister series sodium salts (equation 4.1). From our experimental analysis, it is found that the presence of sodium iodide and sodium thiocyanate significantly reduces the jet velocity of the Rh6G dye solution. In contrast, a liquid jet is formed with maximum velocity for the case of dye solution with the presence of sodium sulphate. This in turn implicates ion-specific penetration depths of liquid microjets simulated for soft tissue models. The outcome is attributed to the variation in the optical absorbance of laser pulses inside the microcapillary solution owing to the presence of the ion-specific interaction with the Rh6G molecules. Our research findings showcase the perfect inference of the role of ion-specific interactions on the generation and control over the laser-induced liquid microjets.

4.2 Experimental Section

4.2.1 Materials and Sample Preparation

Rh6G a reddish-purple dye is utilized in the present set of studies since the molecule possesses significant absorbance for the excitation wavelength (λ_{exc}) of 532 nm; the molecular structure is presented in figure 4.1. The inorganic sodium salts: sodium sulphate (Na₂SO₄), sodium iodide (NaI), and sodium thiocyanate (NaSCN) to perform an ion-specific investigation in the generation of liquid microjets are purchased from Sigma Aldrich in powdered form and are used without any further purification. All the aqueous samples are prepared in deionized water (Merck Millipore Direct-Q3, 18 M Ω .cm). Chemical Weighing is performed with an analytical balance from Mettler Toledo (XS105) with a resolution of 0.01mg.

$$H_3C$$
 $CI^ CH_3$
 H_3C
 CH_3
 CH_3
 CH_3

Figure 4.1 Molecular structure of Rh6G.

4.2.2 Laser-Induced Liquid Microjets

We have developed an in-house experimental setup for laser-induced liquid microjets; the schematic layout is provided in figure 2.5a. The instrumental details are provided in section 2.2.3 in chapter 2. Here, we used a 532 nm laser beam which is focused inside the liquid carried in a \sim 400 μ m glass capillary to generate the liquid jets. The results of jet formation we have showcased here are recorded using a high-speed camera FastCAM MINI AX from Photron at 10k fps (frames per second). A long-distance microscope with a maximum magnification of 12x (Navitar) is connected to the camera in order to capture the side view of the jet formation. The field of view can be adjusted by varying the magnification of the Navitar lens. In order to capture good contrast images, illumination is provided by a white light source (GSVITEC MultiLED). The Images are analyzed with the help of photron software (PFV4).

The velocity (v_i) and power (P_i) of the laser-induced liquid microjets are calculated as follows: 212,219

$$v_{j} = \Delta l_{j} / \Delta t \tag{4.2}$$

$$P_{j} = \frac{1}{8} \rho \pi D_{J}^{2} v_{J}^{3} \tag{4.3}$$

Penetration depth of liquid jets in soft tissues is simulated by using jet power as follows:²¹²

Penetration Depth
$$\propto \sqrt[3]{P_j}$$
 (4.4)

Here, Δl_j is the change in jet length in time interval Δt . ρ is the density of the liquid solution filled in the microcapillary ($\sim 1 g/ml$) whereas D_J is the diameter of the liquid jet which is approximated as 1/10 the of the capillary diameter.

4.2.3 UV-Visible Absorbance Studies

The absorbance studies of aqueous dye samples are carried out with UV-Visible spectrometer Lamda 950 (from Perkin Elmer) by using Quartz cuvettes of path length 1mm. The absorbance of light passing through the sample cell obeys Beer's Lambert Law as follows: ²⁶⁰⁻²⁶²

$$A = \varepsilon CL' = -\log\left(\frac{I_T}{I_0}\right) \tag{4.5}$$

Here, ε and C are the molar extinction coefficient and concentration of the aqueous sample, respectively. L' represents the optical path length, i.e., the distance traveled by the light through the sample. I_0 is the intensity of light incident on the sample and I_T is the intensity of light transmitted through the sample.

4.3 Results and Discussion

In the phenomenon of laser-induced liquid microjets, the absorption of laser pulse energy causes abrupt vaporization of a small mass of the liquid, followed by the formation of a bubble inside the capillary. The subsequent emission of the pressure wave deforms the air/liquid boundary to form microjets. ^{211-212, 216-217} The detailed discussion on laser-induced liquid microjet formation is provided in section 2.2 of chapter 2. The magnitude of this pressure impulse on the air/liquid interface decides the velocity of the liquid microjet, which is governed by the absorbed laser pulse energy in the liquid medium. ²¹⁷ The conceptual understanding is provided in parameter dependence section 2.2.2 of chapter 2. The experimental evidence of the impact of laser absorbance on microjet formation is showcased in figure 4.2. Here, we have compared the velocity and power of microjets generated in water and Rh6G dye solution, where both the samples carry different absorbance for 532 nm.

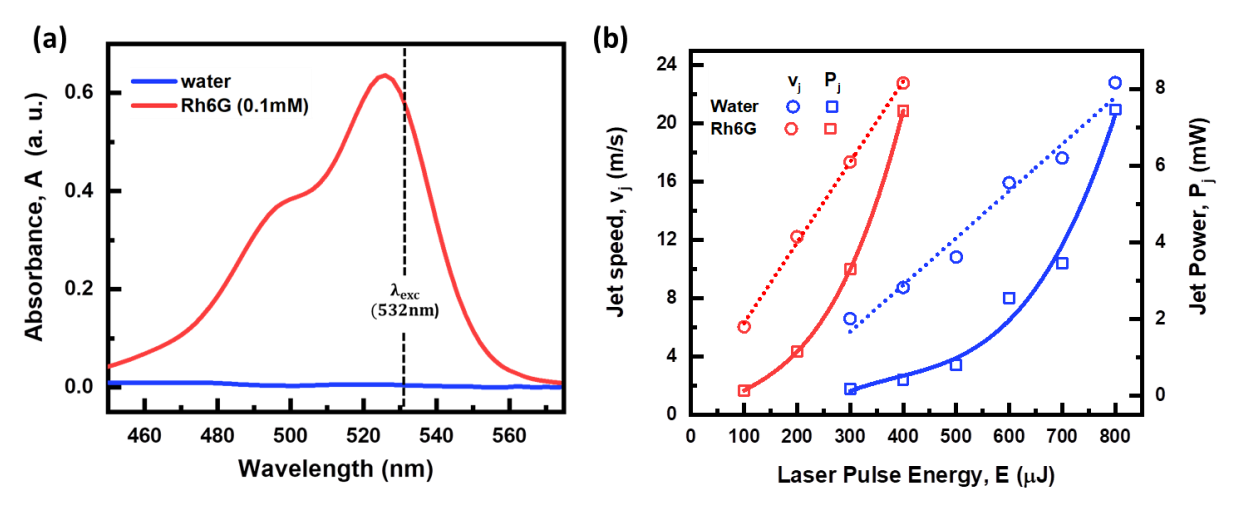


Figure 4.2 (a) UV-Visible absorbance spectra of water (reference) and Rh6G dye (0.1mM) solution. (b) The observed jet velocity (v_j) and jet power (P_j) for the aqueous samples of neat water and Rh6G (0.1 mM) with various input excitation energies of the pump laser beam at 532 nm.

Figure 4.2a represents the UV-visible absorbance spectra of neat water and Rh6G dye solution of a concentration of 0.1 mM. Neat water carries minimal absorbance at the excitation wavelength (λ_{exc}) of 532 nm in contrast to the Rh6G, which possesses a significant absorbance at 532 nm. The observed UV-Vis absorbance spectrum (red curve) is the characteristic signature of Rh6G.²⁹⁹ The spectrum consists of two bands: one at 528 nm is called the monomer band and the other at 500 nm corresponds to the dimer band owing to the self-aggregation of Rh6G dye monomers. The observed significant contrast in optical absorbance A of water and Rh6G (0.1 mM) at the λ_{exc} 532 nm is reflected in the generation of liquid microjets from the capillary tube (Figure 4.2b). It presents a variation in jet velocity and power as a function of laser pulse energy for water and Rh6G (0.1 mM). The Jet velocity (v_j) and power (P_j) are calculated by using equations 4.2 and 4.3 as given in the experimental section. It is evident from the plot (figure 4.2b) that the laser pulse energy for the production of liquid jets in Rh6G dye

solution is different from that required for neat water. For example, with the capillary of diameter 400 μ m, we observed the jet formation in Rh6G solution for a minimum energy value of 100 μ J, whereas for the case of pristine water, the jet formation starts only at 300 μ J. The variation in threshold energy for the jet formation in Rh6G solution and water is attributed to the difference in optical absorbance at the excitation pump wavelength (532 nm) for the two samples. We have further studied the jet formation at different laser pulse energies. The observed v_j is found to be a linear function of the input pump energy (E) (observed fitting parameters: $v_j = 0.03 \cdot E - 3.96$ (for water) and $v_j = 0.06 \cdot E - 0.78$ (for Rh6G)). The trend in the case of P_j follows a cubical relation with the laser energy (cubic fit parameters: $P_j \approx 7.61 \cdot 10^{-8} \cdot E^3$ (for water) and $P_j \approx 1.42 \cdot 10^{-7} \cdot E^3$ (for Rh6G)).

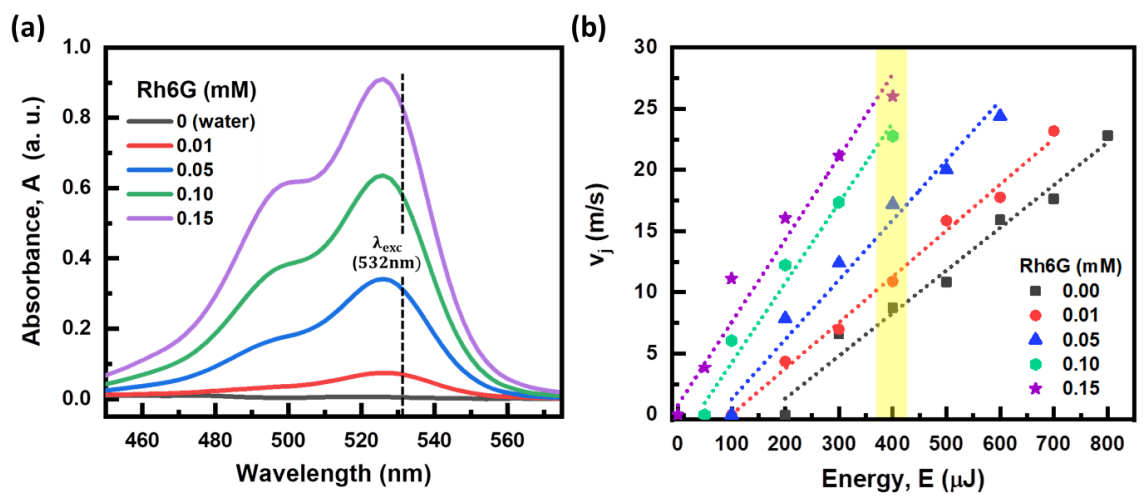


Figure 4.3 (a) Concentration-dependent UV-Visible absorbance spectra of Rh6G dye solution. (b) Variation in jet speed as a linear function of laser pulse energy, as studied for different concentrations of Rh6G. For a laser pulse of energy 400 μ J, an increment in jet velocity is observed with an increase in Rh6G concentration (yellow highlighted region).

We noticed a maximum jet velocity of $\sim 25\pm 2$ m/s in the case of Rh6G solution at an input pump energy of 400 μJ, whereas the similar pump energy generates a jet of velocity ~ 8±2 m/s for the pristine water. A similar distinction in jet power is also observed for the two samples at equal pulse energies. The current results emphasize that for a given laser pulse energy E, the jet velocity and jet power values strongly depending on the absorbance of the liquid sample in the microcapillary. 217 Our experimental observation indicates direct dependence of jet formation on the optical absorbance. This is further confirmed; when we performed the jet studies with different concentration samples of Rh6G dye solutions. Rh6G possesses concentration-dependent variation in optical absorbance, especially at 532 nm (figure 4.3a). It is interesting to observe in figure 4.3b that the values of threshold energy for the jet formation are varying consistently with the absorbance of the Rh6G solution for 532 nm. For different concentrations of Rh6G i.e., 0.15, 0.10, 0.05, and 0.00 (mM), the jet formation starts at 50, 100, 200, and 300 µJ of 532 nm. The results confirm our inference of optical absorbance-dependent jet formation as derived from figure 4.2. Consequently, for a given energy E of laser pulse, we have observed an increment in jet velocity with an increase in the optical absorbance of the liquid sample (by varying the concentration of Rh6G) as highlighted for a pulse energy of 400 µJ in figure 4.3b. The observed linear correlation between jet velocity and absorbance remained consistent even when we performed the experiments with different laser pulse energies (figure 4.3b).

After optimizing the production of liquid jets in Rh6G at different laser pulse energies (figure 4.2b, 4.3b), we have investigated the influence of Hofmeister ions on the liquid jets phenomenon in Rh6G (0.1 mM) dye solution (figure 4.4). It is observed that the presence of ions has significantly affected the jet formation for Rh6G solutions. Here, we witnessed a maximum jet length for the presence of kosmotropic sulphate anion (SO_4^{2-}). However, the presence of chaotropes iodide (I^-) and thiocyanate (SCN^-) has significantly reduced the jet lengths of Rh6G. This observation of the impact of ions in perturbing the liquid jet lengths of Rh6G dye solution obeys the Hofmeister order:

$$SO_4^{2-} \approx Rh6G > I^- > SCN^- \tag{4.6}$$

and is found to be consistently followed, when we performed the experiments with different energies of the laser pulse at 200 μ J, 300 μ J, and 400 μ J (figure 4.4).

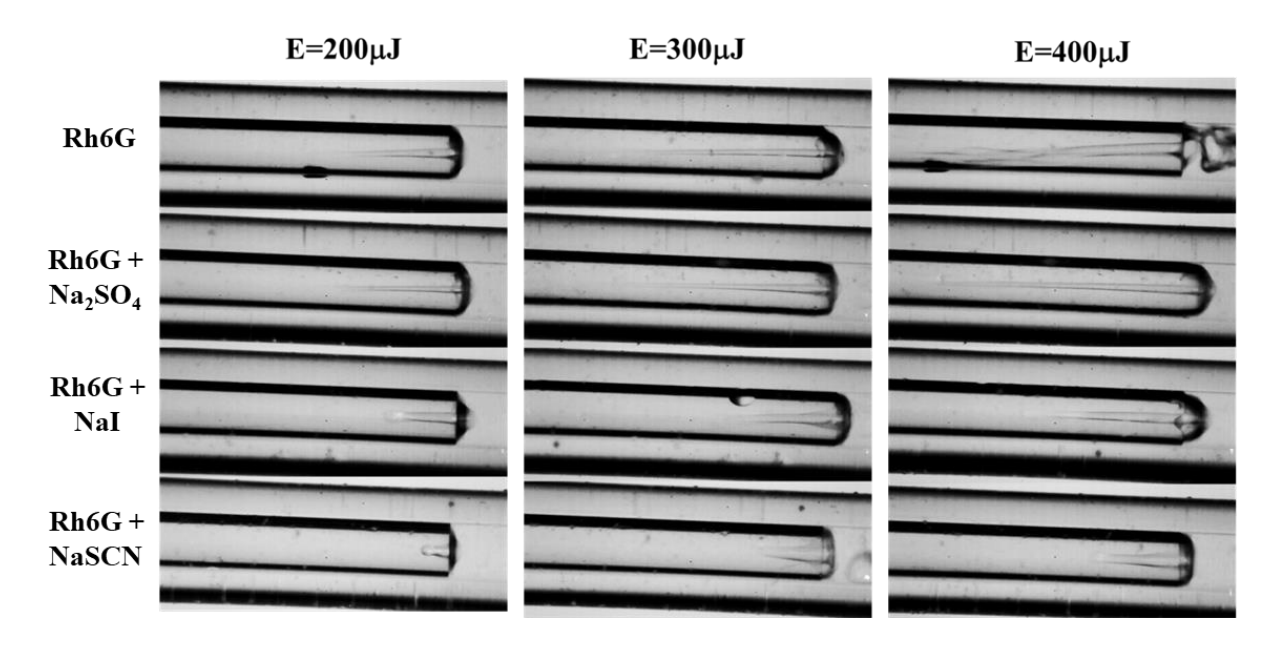


Figure 4.4 Snapshots of laser-induced liquid microjets for the pristine Rh6G dye solution (0.1 mM) and in the presence of 50 mM sodium salts; Na_2SO_4 , NaI, and NaSCN. Ion-specific variation in Jet length is recorded for three different pulse energies of 200 μJ , 300 μJ , and 400 μJ . The camera snapshots of liquid microjets are captured at 100 μs after the laser pulse of known energy is made to impinge on the capillary.

The optical absorbance of liquid solution inside the capillary governs the generation of liquid jets and therefore, in order to probe the cause of ion-specific jet lengths of Rh6G, we performed the UV-Visible absorbance studies in the presence of different sodium salts (Na₂SO₄, NaI, and NaSCN). Interestingly, it is noticed from figure 4.5a that the optical absorbance of Rh6G in the presence of ions follows the Hofmeister order as well:

$$SO_4^{2-} \approx Rh6G > I^- > SCN^- \tag{4.7}$$

We observed a maximum absorbance at 532 nm (which we have utilized for the generation of liquid jets) in the pristine Rh6G dye solution, and a nearly similar absorbance is observed in the presence of kosmotropic SO₄²-anion. However, in contrast, the presence of chaotropes (I⁻and SCN⁻) has significantly affected the absorption spectrum of the solution, resulting in a decrease in the values of absorbance at 532 nm.

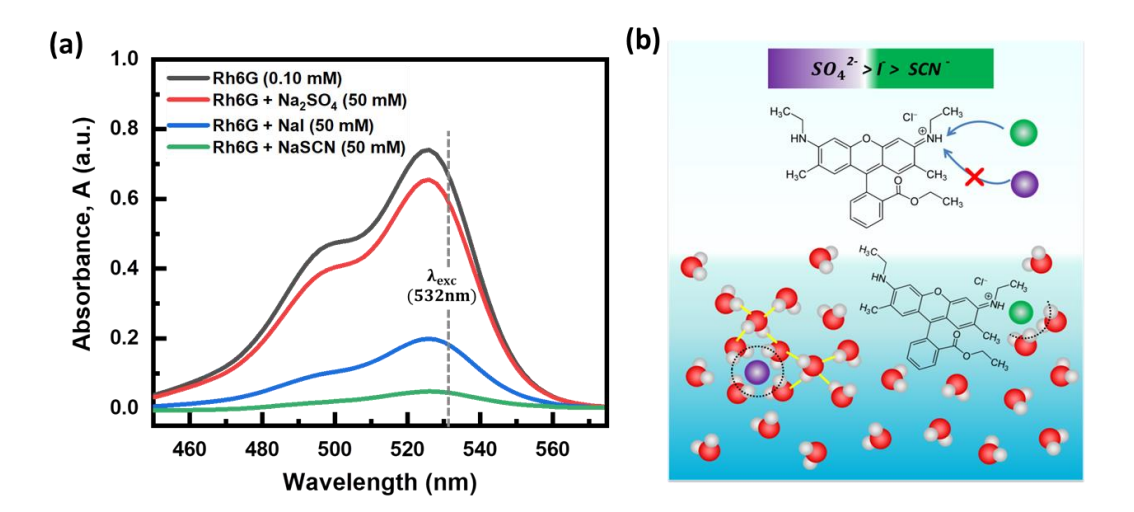


Figure 4.5 (a) UV-visible absorbance spectra of Rh6G dye solution (0.1 mM) in the presence of 50 mM sodium salts: Na₂SO₄, NaI, and NaSCN. (b) Schematic illustration of the proposed interactions between Hofmeister anions and Rh6G in an aqueous solution governing the ion-specific optical absorbance (figure 4.5a).

The observed Hofmeister trend in the absorbance characteristics of Rh6G dye solution can be ascribed to the relative tendency of the ions to adsorb towards Rh6G. 39,49,65,300 We have provided a molecular level scheme, as shown in figure 4.5b to illustrate the fundamental insights into the intermolecular interactions governing the ion-specific optical absorbance. The hydrophilic kosmotropic anion SO_4^{2-} is known to form strong hydrogen (H-) bonds with the solvent water molecules, for which it would prefer to stay away from interacting with the dye molecules in the solution. 39,49,65,300 As a consequence, the presence of the kosmotropic anion (SO_4^{2-}) has minimal impact on the absorbance of Rh6G dye solution (figure 4.5a). However, in contrast, the hydrophobic chaotropes (I^- and SCN^-) are prone to bind towards the NH- and neighboring methylene moieties

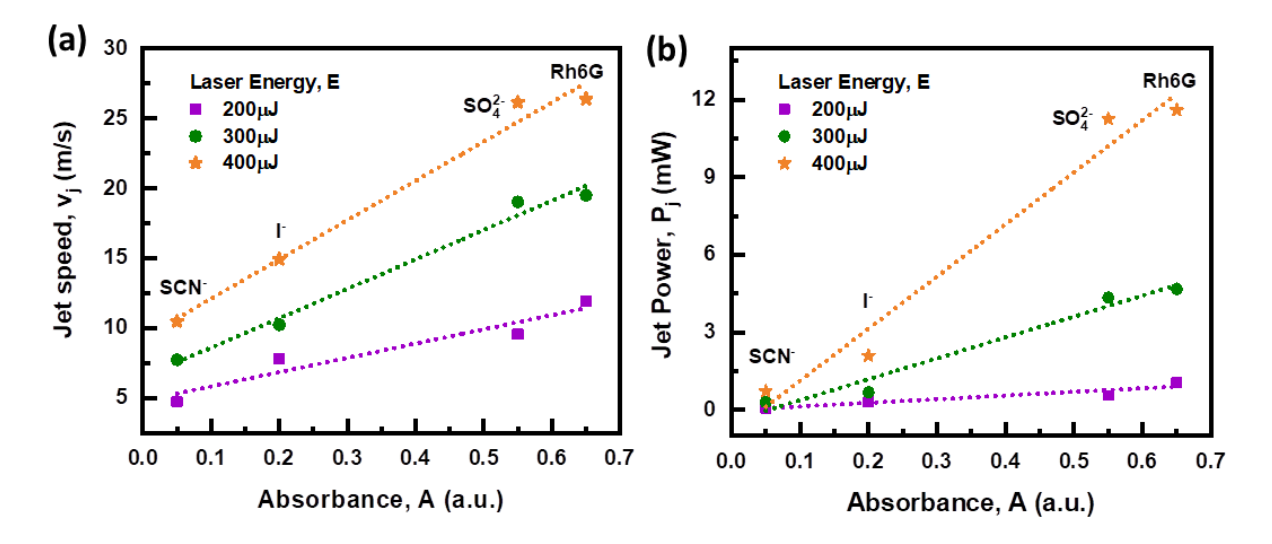


Figure 4.6 Ion-specific variation of (a) jet velocity and (b) jet power as a function of absorbance, studied for different pulse energies of 532 nm at 200 μ J, 300 μ J, and 400 μ J. The data points for calculating velocity and power are taken from ion-specific jet lengths (figure 4.4). The ion-specific absorbance values at λ_{exc} 532 nm are extracted from UV-Visible spectra of Rh6G (0.1 mM) in the presence of Hofmeister sodium salts (figure 4.5a).

of Rh6G.^{39,49,65,300} The possible interaction between the dye molecules and the ion might have contributed towards the observed variation in the optical absorption profile of the dye solution in the presence of salts (figure 4.5a), particularly the value of optical absorbance at the excitation wavelength 532 nm. The ion-specific interaction in the Rh6G dye solution (figure 4.5b), which governs the Hofmeister trend in the optical absorbance (A) of the solution (figure 4.5a) finds a linear correlation with the ion-specific jet lengths and hence the jet velocity and jet power as evidenced in figure 4.6.

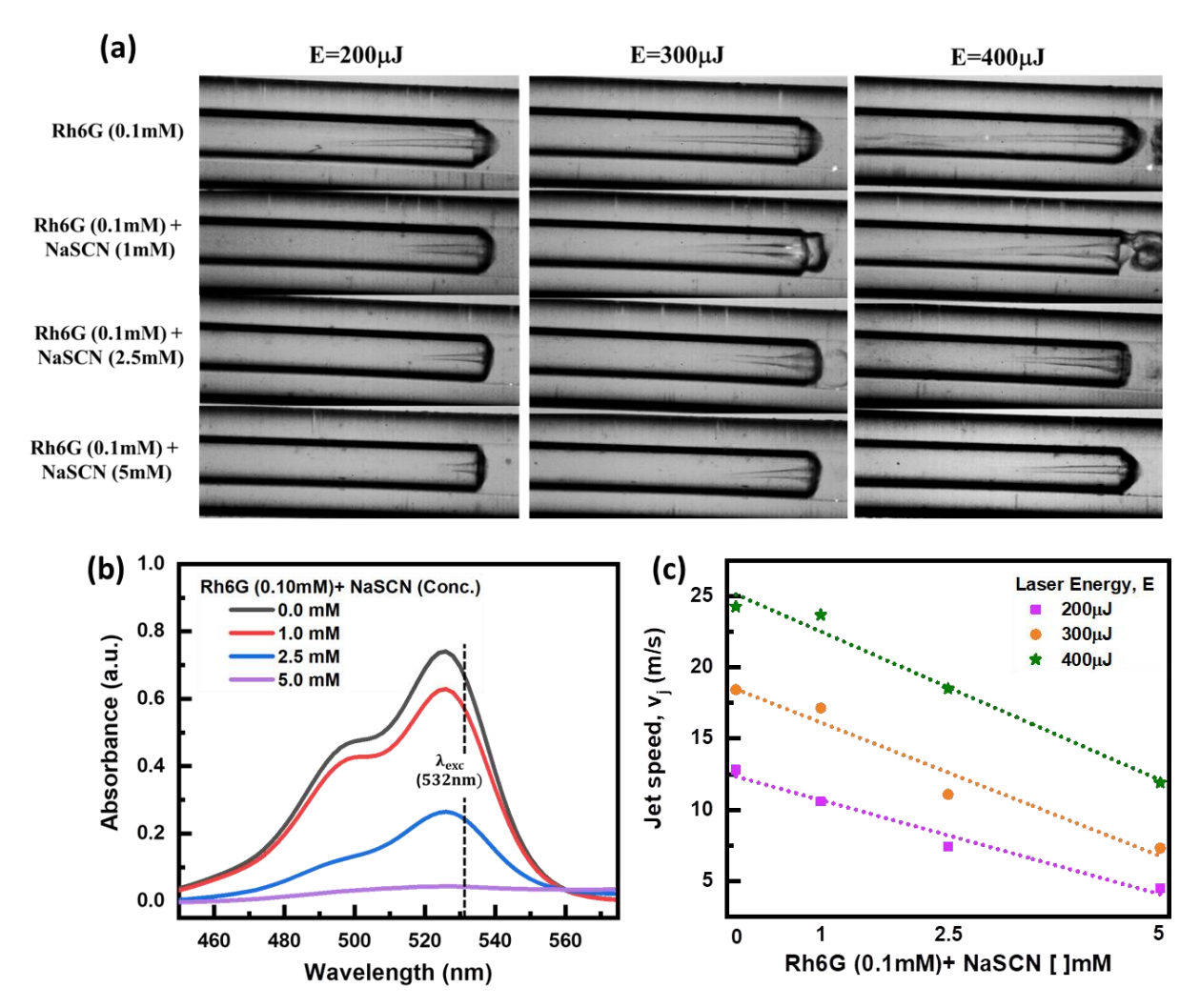


Figure 4.7 (a) Snapshots of laser-induced liquid microjets in Rh6G dye solution (0.1 mM) and that in the presence of NaSCN (1.0 mM, 2.5 mM, 5.0 mM). Concentration-dependent variation in Jet length is recorded for three different pulse energies of 200 μJ, 300 μJ, and 400 μJ. The jet snapshots are captured at 100 μs after a laser pulse of known energy is made to impinge on the capillary. (b) UV-visible absorbance spectra of Rh6G dye solution (0.1 mM) and that in the presence of NaSCN (1.0 mM, 2.5 mM, 5.0 mM), showing concentration (NaSCN) dependent variation in optical absorbance of Rh6G. (c) Jet velocity is a linear function of the concentration of NaSCN in the solution, which is verified for three different pulse energies (200 μJ, 300 μJ, and 400 μJ).

We have utilized the data of ion-specific jet lengths of Rh6G (figure 4.4) to evaluate jet velocity using equation 4.2. In figure 4.6a, we have plotted the liquid jet velocities of Rh6G as a function of ion-specific absorbance of the aqueous solutions at λ_{exc} 532 nm (data extracted from figure 4.5a). It is witnessed that the ion-specific jet velocity finds a linear relation with the optical absorbance. It is evident from the plot that the high jet velocities

are observed for the solution of Rh6G with and without kosmotropic SO_4^{2-} anion. In contrast, lower jet velocities are observed in the presence of chaotropic anions i.e., I⁻and SCN⁻. The current linear relation between ion-specific jet velocities of Rh6G and the optical absorbance of the aqueous media remained consistent for different laser pulse energies of 200 μ J, 300 μ J, and 400 μ J. A similar Hofmeister trend is also witnessed for jet power as a linear function of optical absorbance A (figure 4.6b).

The influence of ion-specific interaction in Rh6G in governing the optical absorbance and consequently the jet characteristics is further confirmed when we performed the concentration-dependent studies of SCN⁻ in the generation of liquid microjets. It is observed that the increment in anion concentration has shown decrement in the optical absorbance of Rh6G owing to the possible interactions between the chaotropic SCN⁻ ion and Rh6G. The resultant ion-concentration induced variation in optical absorbance of Rh6G dye solution found linear correlation with the jet length and jet velocities as shown in figure 4.7.

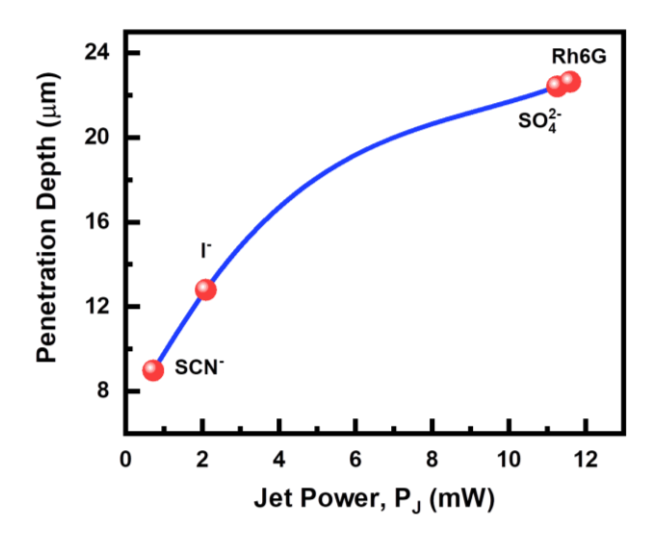


Figure 4.8 Ion-specific penetration depths of liquid jets of Rh6G (0.1 mM) solution for the model soft tissue materials. The data points are simulated by cube root dependence of penetration depth on jet power, i.e., $\sqrt[3]{P_J}$. The values of jet powers for different salt solutions have been evaluated from the measured jet velocity in Rh6G for the laser pulse energy of 400 μJ (figure 4.6).

Since jet velocity/power governs the penetration depth and hence the drug release profile in the needle-free injection systems; 212,215,218 therefore, we have showcased the impact of ions in deciding the penetration depths of laser-induced liquid jets in model soft tissues. Figure 4.8 presents the variation in penetration depths of liquid jets as a function of ion-specific jet powers. It is shown that for a given laser pulse of energy 400 μ J, the presence of SO_4^2 -brings maximum penetration depth, whereas in the case of chaotropes (I⁻and SCN⁻) shows a decrease in trend in the value of penetration depths of the liquid jets in soft tissues as simulated by cube root dependence on jet power. Evidently, using the idea of the Hofmeister series salts, we can tune the penetration depth from a value of $\sim 25 \mu m$ for the case of SO_4^2 - ion to a value of $\sim 8 \mu m$ for the case of SCN⁻ion. This gives us the upper hand in tuning the laser jet characteristics to achieve desired penetration depths of various drugs/vaccines containing different salts. Here, we showed that the absorbance of laser energy E is a crucial parameter in the generation of focused microjets with controlled velocities and penetration depths. This is demonstrated with the help of Hofmeister ions, which significantly tune the 532 nm absorbance and result in ion-specific jet velocities of Rh6G dye solution.

4.4 Conclusions

In summary, we have investigated the influence of Hofmeister anions $(SO_4^{2-}, I^-, \text{and SCN}^-)$ in the production of laser-induced liquid microjets in Rh6G dye solutions. It has been found that the presence of chaotropes $(I^-, \text{and SCN}^-)$ significantly reduced the jet velocities, whereas the presence of kosmotrope (SO_4^{2-}) shows minimal impact on the liquid jet velocities in Rh6G dye solution. The observed variation in jet velocity is attributed to the variation in laser absorbance of the aqueous dye solution, owing to the presence of ion-specific interactions with Rh6G (figure 4.9). The present results of the Hofmeister effect in laser-induced liquid microjets could find potential application in developing needle-free injection systems to achieve desired penetration depths into inner body organ tissues, blood vessels, all skin layers, or tumors in the medical industry.

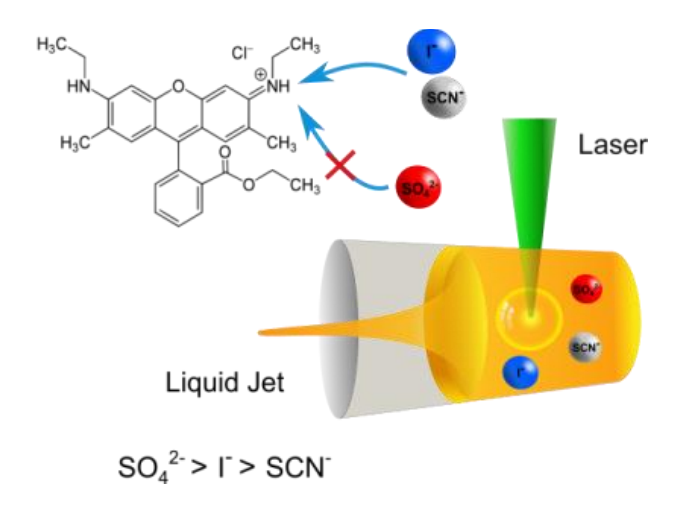


Figure 4.9 Ion-specific interactions with Rh6G govern the characteristics of laser-induced liquid microjets at the air/Rh6G dye solution interface.

CHAPTER 5

HOFMEISTER EFFECT AT AIR/POLYVINYLPYRROLIDONE AQUEOUS INTERFACE

In this chapter, we have discussed our work accepted for publication in the Journal of The American Chemical Society as: Bhawna Rana, David J. Fairhurst, and Kailash C. Jena. Ion-specific Water-Macromolecule Interactions at Air/Aqueous Interface: An Insight into the Hofmeister Effect. *J. Am. Chem. Soc.* 2023 (Accepted).

The specificity of ions in inducing order/disorder in macromolecules is introduced as Hofmeister series; however, the detailed underlying mechanism is still not comprehensible yet. We utilized surface-specific sum frequency generation (SFG) vibrational spectroscopy to explore the Hofmeister effect at air/polyvinylpyrrolidone (PVP)-water interface. The spectral signature observed from the ssp polarization scheme reveals ion-specific ordering of water molecules following the Hofmeister series. The observed trend in the OH-stretch region is attributed to the ion-macromolecule interactions similar to that reported previously by Chen et al. (J. Am. Chem. Soc. 2007, 129, 12272). However, the presence of ions does not reflect any significant influence on the structure of the PVP macromolecule in ssp polarization scheme. In contrast, the ppp-SFG spectra in the CH-stretch region reveal the impact of ions on the orientation angle of vinyl chain CH2-groups which follows the Hofmeister series: $SO_4^{2-} > Cl^- > NO_3^- > Br^- > ClO_4^- > SCN^-$. The minimal orientation angle of CH_2 -groups indicates the significant reordering in PVP vinyl chains in the presence of chaotropic anions ClO₄, and SCN⁻. The observation is attributed to the ion-specific water-macromolecule interactions at the air/aqueous interface. It is compelling to observe the signature of spectral blue shifts in the OH-stretch region in ppp configuration in the presence of chaotropic anions. The origin of the spectral blue shifts has been ascribed to the existence of weaker interactions between the interfacial water molecules and the backbone CH-, CH₂-moieties of the PVP macromolecules. The ion-specific modulation in water-macromolecule interactions is endorsed to the relative propensity of anion's adsorption towards the air/aqueous interface. The experimental findings highlight the existence and cooperative participation of ion-specific water-macromolecule interactions into the mechanism of the Hofmeister effect, along with the illustrious ion-water and ion-macromolecule interactions.

5.1 Introduction

In 1888, Franz Hofmeister proposed a series of anions ranked as per their potency to salt out (precipitate) proteins from their aqueous solutions known as Hofmeister or lyotropic series as follows:⁵

$$SO_4^{2-} > Cl^- > NO_3^- > Br^- > ClO_4^- > SCN^-$$
 (5.1)

Apart from its significance towards protein solubility, the series is known to govern various fundamental processes (section 1.2 of chapter 1) such as controlling surface tension of electrolyte solutions, enzymatic activity, stability of colloids and micro-emulsions, phase separation, depletion of the ozone layer and many more. Despite its diverse applicability, the understanding of the conceptual framework of the Hofmeister effect has still eluded the researchers to date. Two hypotheses have been put forward to comprehend the underlying mechanism. The first explains the Hofmeister effect in terms of ion-water interactions, i.e., the ability of ions to make or break hydrogen (H-) bonds in water. The ions on the left of the series (5.1) are called kosmotropes (structure makers) which are known to become highly hydrated and salt out proteins from their

aqueous solution and bring order to the native protein structure. In contrast, the right-aligned ions are called chaotropes (structure breakers) which are weakly hydrated and salt-in protein molecules in their aqueous solution, thus causing disorder in the proteins. 35,37,39,149 Though this approach successfully explains the surface tension of the vapor-electrolyte interface, 64 the range over which ion's impact on water structure persists is still under debate. 142-147 Second hypothesis involves the role of dispersion forces between ions and the macromolecule towards the Hofmeister effect. This is realised from the current understanding in terms of relative propensity of ion's adsorption towards the hydrophobic macromolecule surface. 41,35-39,67-68,76,192,301-302 However, the existing mechanism based on ion-water and ion-macromolecule interactions lacks water-macromolecule interactions, which play an imperative role in deciding the structural stability and functionality of the macromolecules. 303-304 In a recent theoretical study, Willow et al. considered the significant contribution of ion-specific watermacromolecule interactions in explaining the salt-in effect. In addition, Lakshamanan et al. and Song et al. 40 performed dilational rheology of bovine serum albumin (BSA) and translational diffusivity of water molecules near the lipid surfaces, respectively. Their experimental results indirectly suggest that the presence of ions significantly modulates the strength of the bonding environment of water molecules near the macromolecule surfaces. However, spectroscopic evidence of ion-specific water macromolecule interactions and a detailed molecular level insight into the underlying mechanism is still lacking. Therefore, it is essential to probe the ionspecific water structure near the macromolecule and the associated conformational changes in the macromolecule at the air/aqueous interface.

Sum frequency generation (SFG) vibrational spectroscopy is a robust tool that has been profoundly utilized to study the structure of water and macromolecules at the interfacial region. Previously, Cremer and co-workers have performed SFG spectroscopy in the ssp-polarization scheme to investigate the Hofmeister effect at various aqueous interfaces carrying charged monolayer, neutral polymer, and charged mineral interfaces. ^{68,76} Their observations established that the Hofmeister effect can be explained in terms of ion-macromolecule interactions. Despite observing a convincing correlation between OH-intensity and the anion Hofmeister series, the following concerns remain unprobed: (a) Do ions affect the strength of water-macromolecule interactions? If yes, then (b) what is the underlying mechanism? (c) Do these ion-specific water-macromolecule interactions contribute to the structural order/disorder of the macromolecule at the air/aqueous interface?

To answer these questions, we have investigated the Hofmeister effect at the air/water interface carrying a neutral polymer polyvinylpyrrolidone (PVP) (molecular structure is given in figure 5.1a) using ssp and ppp-polarization schemes of SFG vibrational spectroscopy (schematic is given in figure 5.1b). It is well accepted that the SFG spectroscopic investigations in different polarization schemes, i.e., ssp and ppp are necessary to probe the vibrational signatures of surface moieties involved in various intermolecular interactions present at the air/aqueous interface. For example, Tyrode et al. investigated the hydration state of non-ionic surfactants at the air/aqueous interface and reported a new OH-feature at ~3580 cm⁻¹. The observed feature was absent in ssp-SFG spectra but significantly appeared in ppp-OH spectral configuration. The feature was then attributed to the asymmetric vibrations of water molecules involved in non-hydrogen bond type weak interactions at the air/aqueous interface. Wei et al. performed SFG investigations of pristine air/water interface in different polarization schemes to report the OH-feature at ~ 3550 cm⁻¹, which appears distinctively in the ppp-scheme compared to the ssp- SFG spectra. Later, Gan et al. attributed this OH-feature to singly H-bonded water at the air/water interface. The past findings motivated us to utilize SFG spectroscopy in different

polarization schemes to perform a thorough molecular level investigation of the Hofmeister effect at the air/aqueous interface.

The ssp-SFG spectra at the air/PVP aqueous interface showed that the ion-specific variation in OH-region intensity follows the Hofmeister series, whereas the CH-peak intensities remained nearly superimposed. In contrast, ppp-SFG spectra highlighted significant variation in CH-peak intensities in the presence of Hofmeister ions. Here, we have performed a detailed analysis to quantify the CH₂-group orientation angle to probe the impact of ions on the polymer chain ordering at the air/aqueous interface, which follows the Hofmeister series. In comparison to kosmotropes, the chaotropes bring significant reordering in the polymer backbone chains, which intriguingly is correlated with the ion-specific variation in the water structure at the air/PVP aqueous interface. We demonstrate that compared to kosmotropes, the chaotropes induce weaker intermolecular interactions between the interfacial water molecules and the hydrophobic surface moieties (-CH, -CH₂ of polymer backbone), which in turn disrupts the PVP structure at the air/aqueous interface.

5.2 Experimental Section

5.2.1 Materials

Polyvinylpyrrolidone (PVP) of Molecular weight Mw = 40000 and all the six inorganic sodium salts (sodium sulphate, sodium chloride, sodium bromide, sodium nitrate, sodium perchlorate and sodium thiocyanate) were purchased from Sigma Aldrich and used without any further purification. In order to avoid the interference of OH-region intensity with the CH-region peaks, we have also carried out some SFG experiments in high purity heavy water (D_2O) with 99.9 atom % D was purchased from Sigma Aldrich.

5.2.2 Sum Frequency Generation (SFG) Vibrational Spectroscopy

We have used surface-specific SFG vibrational spectroscopy to investigate the bonding environment and orientation of molecules present at the air/aqueous interface. The theory and instrumental set up are discussed in section 2.3 of chapter 2. All the SFG spectra are collected in different polarization schemes (ssp and ppp) in the OH stretching region from 3000 to 3800 cm⁻¹ at a step size of 2 cm⁻¹ and acquisition per step of 200 and are fitted with Lorentzian line shape function (equation 5.2). The fitting parameters are provided in appendix B.

$$\chi^{(2),\text{eff}} = \chi_{NR}^{(2)} + \sum_{\nu} \frac{A_{\nu}}{(\omega_{\nu} - \omega_2 - i\Gamma_{\nu})}$$
 (5.2)

All the aqueous samples for SFG measurements are prepared in deionized water. We used a Teflon sample cell (diameter \sim 5cm) to carry the aqueous sample for SFG measurements. The sample cell is cleaned every time before the experiment using a piranha solution (3:1 v/v of concentrated sulphuric acid to 30% hydrogen peroxide solution) and then rinsed thoroughly with deionized water. All the experiments are conducted in the lab temperature of 21.5 \pm 0.5°C.

5.3 Results and Discussion

The SFG spectra in the CH-stretch region for the air/PVP-water interface in ssp- and ppp-polarization configurations are presented in figure 5.1(c) and (d), respectively. The spectral features positioned at 2863 cm⁻¹, 2903 cm⁻¹, 2924 cm⁻¹, 2956 cm⁻¹, and 2984 cm⁻¹ are the characteristic signature of tertiary C-H, symmetric

stretching modes of ring-CH₂, and vinyl chain CH₂ groups, and asymmetric stretching modes of ring-CH₂, and vinyl chain CH₂ groups of PVP polymer.²⁵⁷ It is evident that the SFG peaks for symmetric CH-stretch modes are more intense in ssp-spectra (figure 5.1c), whereas those of asymmetric CH-stretch modes contribute significantly in ppp-spectra (figure 5.1d). The observation is in agreement with the symmetry and polarization selection rules of the SFG vibrational spectroscopy.^{173,256} Absence of SFG signatures in the CH-stretch region for the air/water interface (grey curve) marks the pristine nature of the water sample utilized to perform the SFG experiments (figure 5.1 c and d).

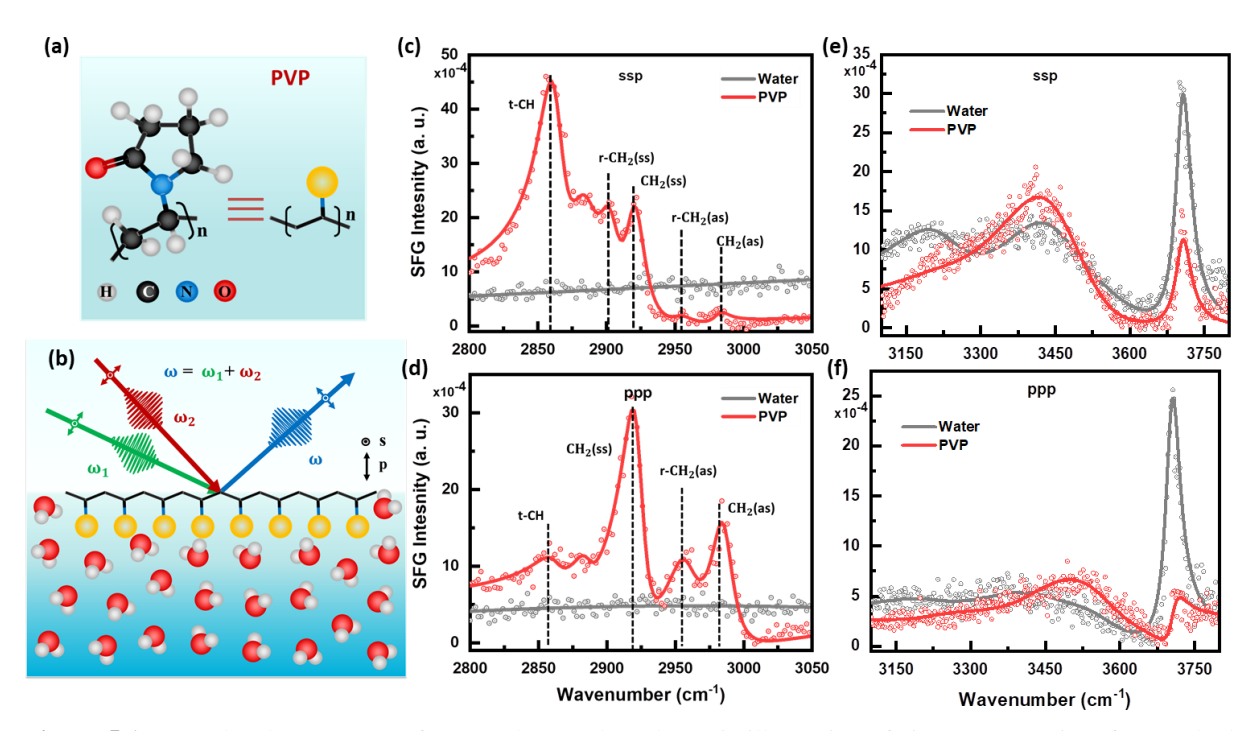


Figure 5.1 (a) Molecular structure of PVP polymer. (b) Schematic illustration of air/PVP-water interface probed by SFG spectroscopy with the scope to perform polarization-dependent studies such as in ssp and ppp, polarization configuration. Here, the three letters indicate the states of polarization of the fields in the sequence of SFG, visible and infrared beams, respectively. The letters "s" and "p" stand for the beam polarization perpendicular and parallel to the plane of incidence. SFG spectra at the air/PVP-water interface in the CH-stretch region (panel c in ssp and d in ppp) and OH-stretch region (panel e in ssp and f in ppp). The scattered points in the plots (panel c-f) represent experimental data, while the solid line is the Lorentzian fit to the spectra. The details of fitting parameters are given in tables B1 and B2 of Appendix B.

The signatures of interfacial water structure in pristine conditions at the air/water interface and in the presence of PVP at the air/PVP-water interface are also recorded in ssp and ppp-SFG schemes which are illustrated in figure 5.1e and 5.1f, respectively. The ssp-SFG spectrum at pristine air/water interface consists of a broad region from 3100-3600 cm⁻¹ attributed to the bonded water OH-oscillators, while the sharp peak positioned at ~ 3704 cm⁻¹ corresponds to the free-OH-oscillator which is protruding out of the interface. The assignment of peaks in the bonded OH-region is less straightforward and continues to be ambiguous. ^{160,171,176,178,181,193,272,283-290} However, more often, the lower frequency peak located at ~ 3240 cm⁻¹ is assigned to strongly H-bonded, while the higher frequency peak ~3440 cm⁻¹ corresponds to weakly H-bonded water species. The relative intensity of both peaks qualitatively provides insights into the H-bonding strength of water molecules residing in the interfacial

region. 65,160,288-289 Similar to ssp-SFG spectrum, the ppp-spectrum at the pristine air/water interface (figure 5.1f) consists of an intense free OH feature at ~3704 cm⁻¹. In contrast to ssp-spectrum, the water structure in ppp configuration has no significant SFG intensity in the bonded OH-stretch region except a weak feature at ~ 3540 cm⁻¹ characteristic of weakly H-bonded water species. 253-254,282 Interestingly, water spectral profile in the presence of PVP polymer at the air/PVP-water interface has displayed minor enhancement in intensity at ~3440 cm⁻¹ and ~3540 cm⁻¹ in ssp (figure 5.1e) and ppp-SFG spectra (Figure 5.1f) respectively. This can be attributed to the increment in weakly hydrogen-bonded water species owing to the presence of PVP polymer at the air/aqueous interface. The feature at ~ 3540 cm⁻¹ in ppp-SFG spectrum at the air/PVP-water interface (Figure 5.1f) is assigned to the water OH-oscillators involved in weak H-bonding interactions with the carbonyl groups of the pyrrolidone ring of PVP. ³⁰⁷ In addition, the observed substantial decrement in the free OH intensity strongly indicates the disruption in the free OH oscillator population owing to the surface coverage by the PVP moieties at the interface.

In order to extract the molecular level insight into anion-induced changes in the interfacial arrangement of polymer and water molecules, we have carried out the SFG experiments at the air/PVP-water interface. Figure 5.2a represents the OH-stretch region of SFG spectra in ssp configuration at air/PVP-water interface in the presence of various sodium salts at 1M concentration. From the spectral features, it is observed that the SFG intensity in the OH-stretch region reflects the characteristic signature of anions present in the solution. We have observed significant ion-specific variation in the overall SFG intensity. For the case of kosmotropic ion SO₄²⁻, the changes in SFG intensity are minimal and comparable to that of the air/PVP-water interface. In contrast, a significantly enhanced SFG intensity is observed for the presence of weakly hydrated and most chaotropic ClO₄²⁻, and SCN⁻ions at the air/aqueous interface. The variation in SFG intensity of the overall OH-stretch region can be ascribed towards the induced ordering of water molecules in the presence of surface field originating due to the presence of ions at the air/PVP-water interface.

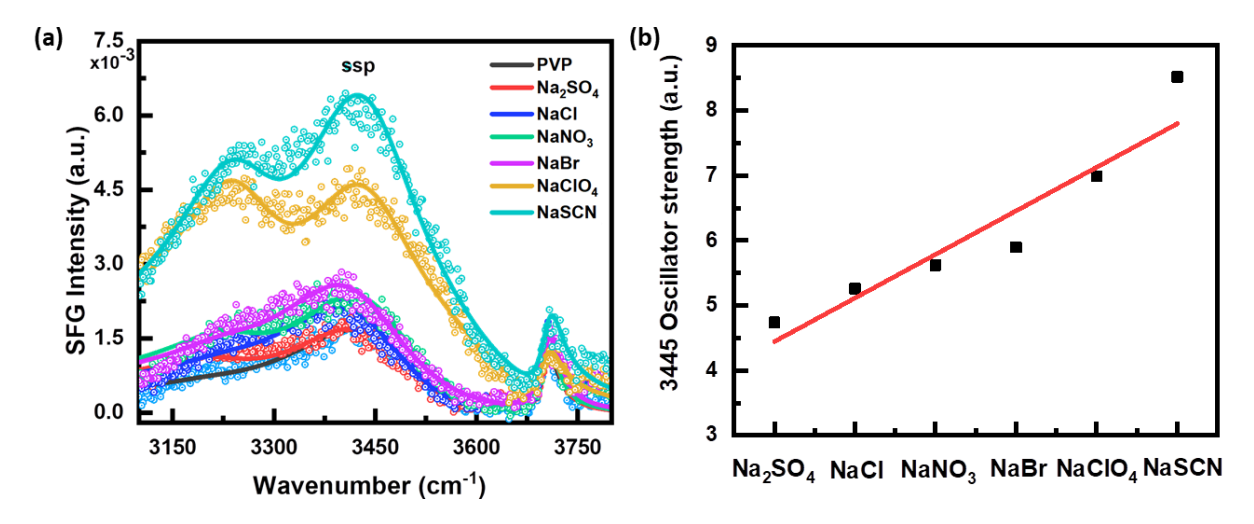


Figure 5.2 (a) ssp-SFG spectra at air/PVP-water interface with 1M sodium salts in the aqueous subphase, showing anion-specific variation in the OH-region intensity. (b) Anion-specific variation in 3440 cm⁻¹ OH-oscillator's strength shows a monotonic increment and follows the Hofmeister series. The data points are Lorentzian fit amplitudes at 3440 cm⁻¹ peak of SFG spectra as provided in panel (a). See table B3 of Appendix B for fitting parameters.

In figure 5.2b, we have shown the variation in the amplitude of 3440 cm⁻¹ peak taken from the SFG spectra (figure 5.2a) in the presence of various sodium salts. The observed monotonic increase in the SFG intensity at 3440 cm⁻¹ in the presence of various ions implies that the ion's impact on water structure follows a Hofmeister trend (equation 5.3) at the air/PVP-water interface.⁶⁸

$$SO_4^{2-} < Cl^- < NO_3^- < Br^- < ClO_4^- < SCN^-$$
 (5.3)

The observed trend based on ion-specific variation in SFG intensity in the OH-stretch region can be explained in terms of the relative propensity of anion's adsorption towards the hydrophobic air/PVP-water interface, which is known to follow the Hofmeister series. $^{41,35,39,67-68,76,192,301-302}$ The hydrophobic moieties (-CH, -CH₂) of the polymer backbone are more prone to provide binding sites to the larger chaotropic and weakly hydrated anions, to get adsorbed at the air/aqueous interface. 41,39

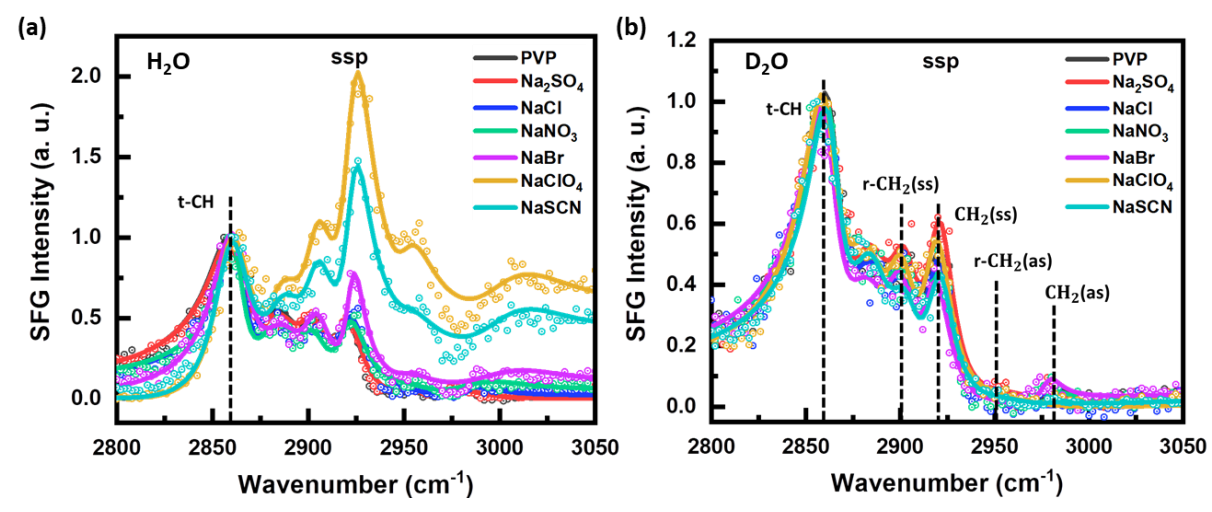


Figure 5.3 ssp-SFG spectra in CH-stretch region at (a) air/PVP-water interface and (b) air/PVP-D₂O interface in the presence of 1 M sodium salts (Na₂SO₄, NaCl, NaNO₃, NaBr, NaClO₄, and NaSCN). All the spectra are normalized with respect to the t-CH peak (2862 cm⁻¹). The details of fitting parameters are given in tables B4 and B5 of Appendix B.

Further, in the quest to find any impact of the anion-induced ordering of water structure (figure 5.2) on the structural arrangement of the polymer chains, we have carried out ssp-SFG experiments in the CH-stretch region (2800-3050) cm⁻¹ at the air/PVP-water interface (Figure 5.3a). We have observed a dramatic variation in CH-peak intensities, especially from 2900-3050 cm⁻¹ in the presence of most chaotropic ClO₄, and SCN⁻ions at the air/PVP-water interface. The relative variation in the CH-peaks intensities indicates towards the ability of ions to perturb the ordering of polymer chains at the air/aqueous interface. However, on close inspection of the combined SFG spectral signatures in CH-stretch region (Figure 5.3a) and OH-stretch (Figure 5.2a) region at the air/PVP-water interface, it appears that the significant SFG intensity in OH-stretch region for ClO₄, and SCN⁻ might have interfered constructively with the CH-signature to mislead the overall appearance of the SFG spectral profile from 2900-3050 cm⁻¹ (figure 5.3a).

It is therefore necessary to isolate the SFG signature originating from the OH-stretch region to obtain a deconvoluted spectral profile in the CH-stretch region that is free from these interference effects. To achieve this, we performed the SFG experiments at the air/PVP-D₂O interface in the presence of 1M sodium salts (figure

5.3b).⁶⁸ Now from the SFG spectral signature, it is quite clear that the previously observed ion-induced variations in SFG peak intensities in the CH-stretch region (2900-3050 cm⁻¹) at the air/PVP- water interface (Figure 5.3a) is absent at the air/PVP-D₂O interface. The following observation with the D₂O solution confirms that the variation in CH-peak intensities in the water solution cannot be correlated directly with the conformational changes in the polymer structure. In addition, we have observed that the CH-peak intensities are nearly superimposed within the experimental errors (figure 5.3b), indicating no impact of sodium salts on the polymer (PVP) chain conformations at the aqueous interface.

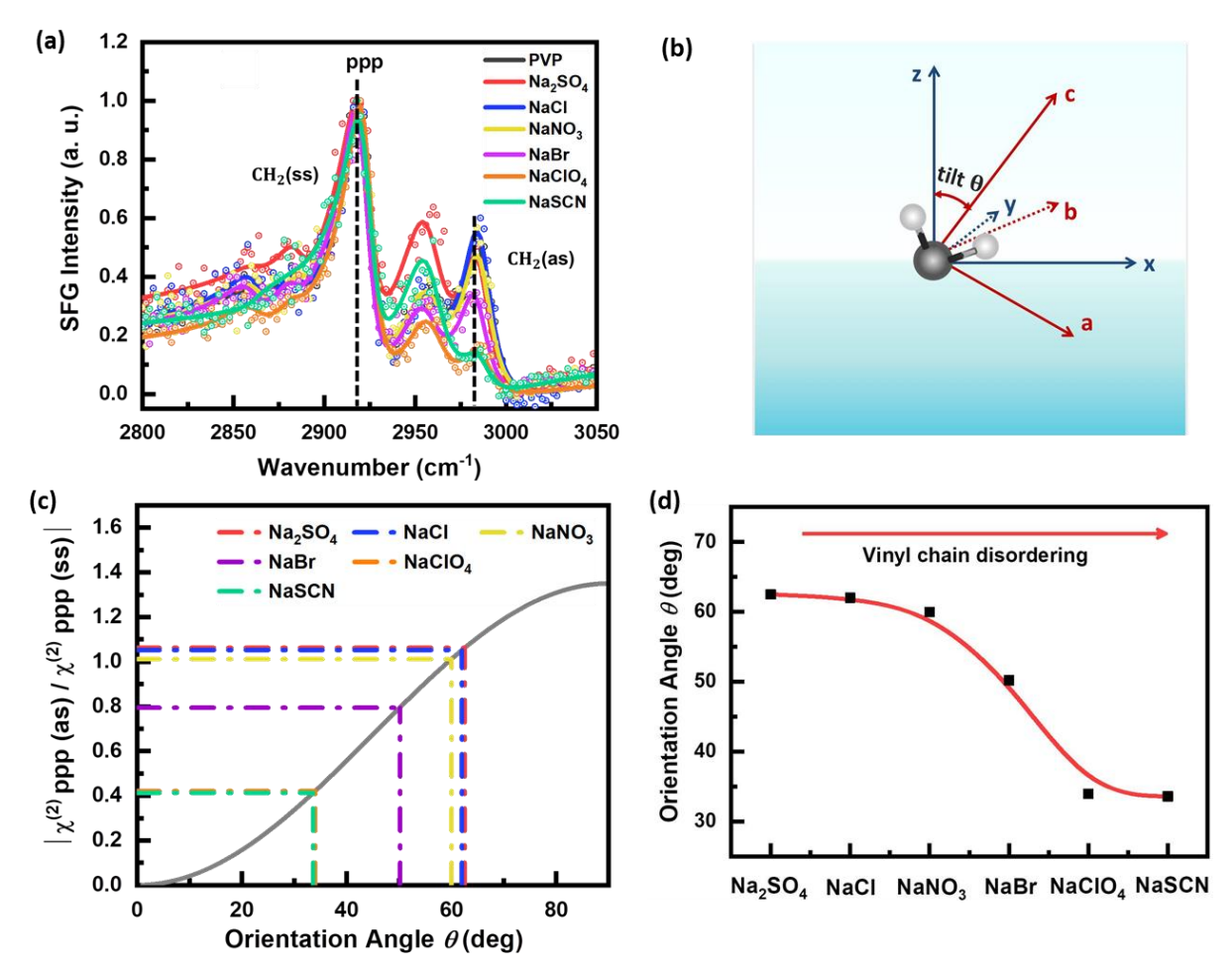


Figure 5.4 (a) ppp-SFG spectra in the CH-stretch region at air/PVP-D₂O interface in the presence of various sodium salts at 1 M concentration. All the SFG spectra are normalized with respect to the max intense CH₂ (ss) peak (2924 cm⁻¹). The scattered points represent experimental data, while the solid line is the Lorentzian fit to the spectra. The details of fitting parameters are given in table B6 of Appendix B. (b) Representation of orientation angle θ formed by CH₂-group with the surface normal. (c) Theoretical orientation curve plotted by using delta function, showing variation of $|\chi_{ppp}^{(2),eff}(as)/\chi_{ppp}^{(2),eff}(ss)|$ (equation 5.3) with θ for CH₂-group of C_{2v} symmetry at the air/PVP-D₂O interface. The horizontal dashed lines are the experimental values of $|\chi_{ppp}^{(2),eff}(as)/\chi_{ppp}^{(2),eff}(ss)|$ and the respective projection on x-axis gives the tilt angle values. The observed trend in the tilt angle values as a function of anions is shown in (panel d), which follows the Hofmeister series.

On examining the air/PVP aqueous interface in ssp-SFG scheme, we have concluded that ions have negligible impact on the conformational changes in the polymer chains at the air/aqueous interface. However, an ion-induced ordering of water structure has been observed, which is attributed to the ion-macromolecule interactions

at the air/aqueous interface.⁶⁸ Along with this, the ssp-SFG spectral profiles in figure 5.2 did not showcase any peak shift in the OH-oscillator frequency in the presence of ions at the air/aqueous interface. This indicates that the investigation of the Hofmeister effect at the air/PVP-water interface solely using the ssp-mode of SFG spectroscopy is insufficient to address the concerns raised by Willow et al.³⁰⁵, Lakshamanan et al.³⁰⁶ and Song et al.⁴⁰ regarding the impact of ions on the strength of water-macromolecule interactions and their contribution in the Hofmeister effect at the air/aqueous interface.

Therefore, in order to perform a detailed investigation on the intermolecular interactions participating in the Hofmeister effect, we continued SFG investigations at the air/PVP aqueous interface in ppp-polarization configuration. Figure 5.4a presents the CH-stretch region of SFG spectra at the air/PVP-D₂O interface in ppppolarization scheme. It is quite evident from the spectral features that the presence of ions bring significant changes in the relative SFG peak intensities of 2924 cm⁻¹(CH₂ (ss)), and 2984 cm⁻¹ (CH₂ (as)), characteristic of symmetric and asymmetric CH-vibrational modes of vinyl chain methylene groups of PVP polymer. For better clarity, we have normalized all the SFG spectra with respect to the intensity of CH₂ (ss) mode, peak position located at around 2924cm⁻¹. The relative intensity variations for the peak positions 2924 cm⁻¹(CH₂ (ss)), and 2984 cm⁻¹ (CH₂ (as)) are minimum with the presence of sulphate, chloride and nitrate ions whereas prominent effects are observed with perchlorate and thiocyanate anions. This indicates that the presence of ClO₄, and SCN⁻has significantly perturbed the interfacial ordering of polymer vinyl chains. To estimate the ioninduced conformational changes in the polymer structure, we have implemented a detailed theoretical analysis to calculate the orientation angle of CH₂-groups (figure 5.4b) of polymer vinyl chain at the air/PVP-D₂O interface. It is a well-established fact that the orientation angle of alkyl groups at the air/aqueous interface indicates the structural changes in the polymer chains. 233,308 The orientation angle is estimated by the amplitude ratios of as and ss- peaks of methylene groups in the ppp-SFG spectra as depicted by left hand side term of equation 5.3. Figure 5.4c presents the theoretical orientation curve in accordance to the right hand term of equation 5.3. The details of the mathematical formulation are given in section 2.3.4-2.3.6 of chapter 2.

$$\left| \frac{\chi_{\text{ppp}}^{(2),\text{eff}}(as)}{\chi_{\text{ppp}}^{(2),\text{eff}}(ss)} \right| = \left| \frac{5.89(\langle \cos \theta \rangle - \langle \cos^3 \theta \rangle)}{\langle \cos \theta \rangle} \right|$$
 (5.3)

where the ensemble average $\langle \cos \theta \rangle$ and $\langle \cos^3 \theta \rangle$ are evaluated by using the delta distribution function $f(\theta)$ with $\sigma = 0$ as follows: $^{65,233,238-239,254}$

$$f(\theta) = \frac{1}{\sigma\sqrt{2\pi}} e^{-(\theta - \theta_0)^2/2\sigma^2}$$
 (5.4)

$$\langle \cos \theta \rangle = \int_0^{\pi} f(\theta) \sin \theta \cos \theta d\theta \tag{5.5}$$

$$\langle \cos^3 \theta \rangle = \int_0^{\pi} f(\theta) \sin\theta \cos^3 \theta d\theta \tag{5.6}$$

The horizontal dotted lines shown in figure 5.4c are the experimental values of $|\chi_{ppp}^{(2),eff}(as)/\chi_{ppp}^{(2),eff}(ss)|$ which are computed from the Lorentzian fitted amplitudes of the SFG spectra presented in figures 5.4a. The fitting parameters are provided in table B6 of Appendix B. The intersection points of the same with the orientation

theoretical curve provide the information of the influence of ions on the orientation angles of CH₂ groups of the PVP polymer. The obtained tilt angle values of vinyl chain methylene groups are plotted in figure 5.4d as a function of various Hofmeister ions (table B7). The ion-specific orientation angles of CH₂ groups follow a monotonic trend in accordance to the rank of anions in the Hofmeister series (equation 5.1).

$$SO_4^{2-} > Cl^- > NO_3^- > Br^- > ClO_4^- > SCN^-$$

The maximum value of orientation angle 62.5° is obtained in the presence of SO_4^{2-} , while the minimum value of 33.6° is obtained for SCN⁻. The lower tilt angle values for CH₂-groups (figure 5.4d) are observed with ClO_4^- , and SCN⁻imply that the presence of the most chaotropic ions significantly reorders the PVP vinyl chain at the interface. The present finding of ion-specific structural changes in the polymer chains at the air/aqueous interface as probed in ppp-SFG spectra remained unearthed in ssp-polarization scheme.

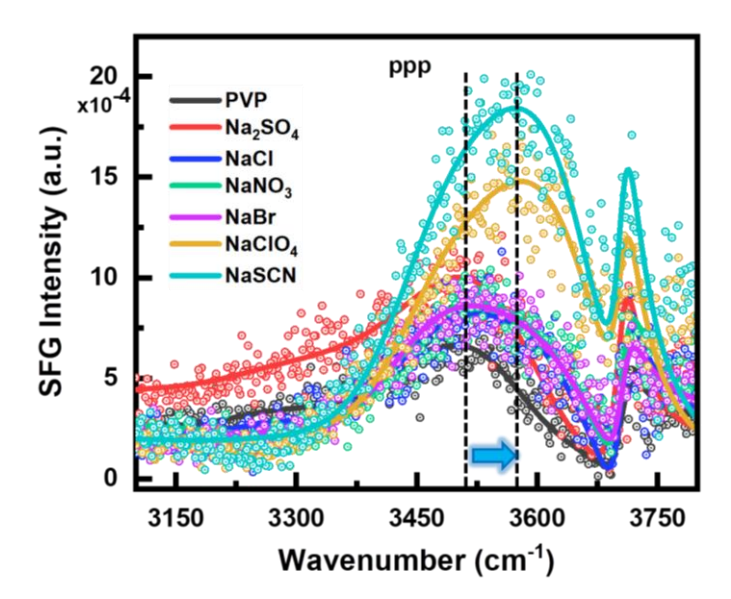


Figure 5.5 ppp-SFG spectra in OH-stretch region at air/PVP-water interface in presence of 1 M Na₂SO₄, NaCl, NaNO₃, NaBr, NaClO₄, and NaSCN. The scattered points represent experimental data, while the solid line is the Lorentzian fit to the spectra. The details of fitting parameters are given in table B8 of Appendix B.

Further, in order to investigate the possible correlation between the observed ion-induced changes in the polymer chain conformation and the interfacial water structure, we have probed the OH-stretch region at the air/PVP-water interface in ppp-polarization configuration. The SFG spectral features as shown in Figure 5.5 reveal significant impact of ions on the ppp-water structure at the air/aqueous interface. The presence of SO_4^{2-} ions bring an overall enhancement in the OH-region SFG intensity. In contrast, in the presence of CI^- , CI^- , C

and C=O groups of the polymer.³⁰⁷ For the air/PVP-water interface in presence of ClO₄ and SCN⁻, we have attributed the OH-band at 3580 cm⁻¹ to the non-hydrogen bonded water molecules which are involved in weak interactions with the hydrophobic moieties at the air/PVP-water interface. ²⁸² Since the 3580 cm⁻¹ band appears in the presence of chaotropic anions, it could have been interpreted as originated from the OH-feature of weakly bonded water molecules surrounding the anions in spite of water molecules in weak interactions with the macromolecule. In order to justify the peak assignment, we have showcased the ppp-SFG spectra at the air/water interface carrying chaotropic anions in figure 5.6 (in absence of PVP). The ppp-water structure for ClO₄ is very similar to the water structure of pristine air/water interface. However, we did observe an enhancement at ~ 3540 cm⁻¹ for the presence of SCN⁻. This OH-feature corresponds to the water molecules involved in weak interactions with thiocyanate anions at the interface. Evidently, the absence of OH-band ~ 3580 cm⁻¹ at the air/salt-water interface justifies our interpretation of ion-specific weaker water-macromolecule interactions at the air/PVP-water interface. The origin of this weak interactions between water and the macromolecule can be understand as follows: The weakly hydrated chaotropic anions are more prone to get adsorbed at the hydrophobic -CH, and -CH₂ moieties of PVP backbone, 41,39 therefore providing the binding sites to their surrounding water molecules to undergo weak interactions with the backbone -CH, and -CH2 moieties of PVP at the air/PVP-water interface, as evidenced through appearance of blue shifted OH-feature at 3580 cm⁻¹(figure 5.5).

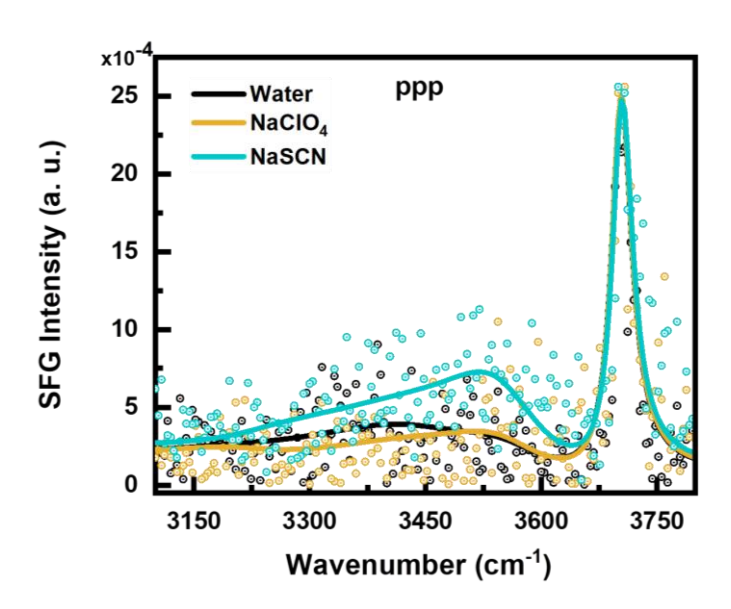


Figure 5.6 ppp-SFG spectra in OH-stretch region at air/water interface in presence of 1 M NaClO₄, and NaSCN. The scattered points represent experimental data, while the solid line is the Lorentzian fit to the spectra. The details of fitting parameters are given in table B9 of Appendix B.

Interestingly, the anion induced variation in the water-macromolecule interactions (figure 5.5) are directly correlated with the changes in the macromolecule structure (figure 5.4) at the air/PVP aqueous interface. This enables us to comprehend the molecular level mechanism of Hofmeister effect as follows (figure 5.7): the weakly hydrated chaotropic anions (ClO₄, and SCN⁻) which are prone for adsorption towards the hydrophobic surface (-CH, -CH₂ of polymer backbone), offer binding sites to the surrounding water molecules to form weak interactions with the hydrophobic moieties of the macromolecule, and in turn perturb the macromolecule structure at the interface. The current results provide experimental evidence to the recent Born-Oppenheimer

molecular dynamic simulation study by Willow et al.³⁰⁵ which emphasizes on incorporating the water-macromolecule interactions towards the explanation of salt-in effect. Along with this, the present experimental work offers a comprehensive mechanism to understand the ion induced variation in the strength of water-macromolecule interactions indirectly indicated by experiments of Lakshamanan et al.³⁰⁶ and Song et al.⁴⁰

5.4 Conclusions

In summary, we have used SFG vibrational spectroscopy in ssp and ppp-polarization schemes to investigate the molecular level mechanism of the Hofmeister effect at the air/PVP aqueous interface. The detailed quantitative analysis of the orientation angle of CH₂-group of vinyl chains at the air/aqueous interface demonstrates the impact of ions towards the conformational changes in the macromolecule structure that obeys the Hofmeister series. Large orientation angles of the CH₂-group in the presence of kosmotrope (SO₄²⁻), while small angle values with the presence of chaotropes (ClO₄ and SCN⁻) indicate the ability of kosmotropic/chaotropic anions to bring reordering in the polymer backbone chains, respectively. We have monitored the intensity and frequency of the OH-stretching modes, which is the characteristic of water structure at the air/aqueous interface in the presence of various salts. The blue shift in OH-band provides experimental evidence of the ion-induced variation in the strength of water-macromolecule interactions at the air/aqueous interface, which plays an important role in governing the Hofmeister effect. It has been demonstrated that the weakly hydrated anions (ClO₄ and SCN⁻) drive weak interactions between water and the hydrophobic surface moieties to offer vital contributions in bringing conformational changes in the macromolecule structure. The current work presents the mechanism of ion-induced modulation in water-macromolecule interactions and their participation in the Hofmeister effect alongside the known ion-water and ion-macromolecule interactions. We believe that the present experimental findings could be helpful in building a better understanding of the ion-specific and/or Hofmeister phenomenon, which profoundly prevailed in diverse physical systems.

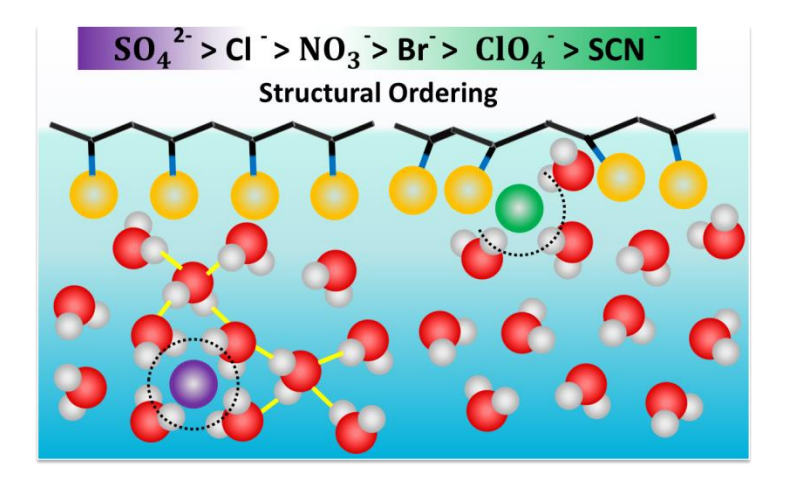


Figure 5.7 Ion-specific water-macromolecule interactions cooperatively participate with the ion-water and ion-macromolecule interactions to govern the order/disorder in the macromolecule structure at the air/aqueous interface.

CHAPTER 6

SUMMARY AND CONCLUSIONS

The systematic research work presented in this thesis provides molecular level insights into specific ion effects on the water evaporation process, laser-induced liquid microjets, and ordering/disordering of macromolecule structure at the air/aqueous interface. Hofmeister series appear to recur in all the studies. It is demonstrated that the impact of ions on the strength of the interfacial bonding environment and the orientation of surface molecules govern the specific ion phenomena at the air/aqueous interface. Chapter 1 of the introduction is devoted to a critical literature review of specific ion effects highlighting the historical background, the ubiquity of the phenomenon, and the molecular level insights into the intermolecular interactions provided by the surfacespecific SFG vibrational spectroscopy. The chapter also highlights the research gaps which motivated the present thesis work. In order to achieve the targeted research objectives, in the experimental scheme, we have developed experimental setups in our lab: 1) Time-resolved Newton's ring interferometry to investigate the evaporation dynamics of sessile aqueous droplets. 2) Laser-induced microjets to study radiation-induced deformation of air/aqueous interface. We have utilized a state-of-the-art surface-specific SFG vibrational spectroscopic tool to investigate the intermolecular interactions, bonding environment, and conformations of molecules at the air/aqueous interface. The detailed theoretical and instrumental aspects of the experimental techniques have been provided in Chapter 2. The research work carried out in this thesis has provided the following potential contributions:

In chapter 3, we investigated specific ion effects in the water evaporation process at the air/water interface. Using surface-specific SFG vibrational spectroscopy and time-resolved Newton's ring interferometry, we have provided molecular level insights into the significant contribution of the H-bonding environment and orientation of Free OH oscillators in governing the fate of the evaporation process. When employing time-resolved interferometry on sessile aqueous droplets, it is found that the kosmotropes (HPO $_4^{2-}$, SO $_4^{2-}$, and CO $_3^{2-}$) reduce evaporation, whereas chaotropes (NO₃ and I⁻) accelerate the evaporation process that follows the Hofmeister series: $HPO_4^{2-} < SO_4^{2-} < CO_3^{2-} < Cl^- \approx water < NO_3^- < I^-$. To extract deeper molecular level insights into the observed Hofmeister trend in the evaporation rates, we have employed surface-specific SFG vibrational spectroscopy to investigate the air/water interface in the presence of Hofmeister ions. The SFG spectra reveal that the presence of ions significantly impacts the strength of the H-bonding environment and the orientation of free OH oscillators from ~ 36.2° to 48.4° at the air/water interface that follows the Hofmeister series and, in turn, govern the evaporation process. It is established that the slow evaporating water molecules experience a strong H-bonding environment with free OH oscillators tilted away from the surface normal in the presence of kosmotropes (HPO $_4^{2-}$, SO $_4^{2-}$, and CO $_3^{2-}$). In contrast, the fast evaporating water molecules experience a weak Hbonding environment with free OH oscillators tilted towards the surface normal in the presence of chaotropes (NO_3^-) and I^- , at the air/water interface. The outcomes of this work would be helpful in designing interfacial water structures to manipulate the evaporation processes for future needs.

The second important finding resulted from the examination of the impact of salts on laser-induced liquid microjets at the air/Rh6G dye solution interface (chapter 4). The laser-induced liquid microjets are the potential candidates for the development of needle-free injection systems. It is showcased that the impact of ions on jet velocity and jet power obeys the Hofmeister order as: $SO_4^{2-} \approx Rh6G > I^- > SCN^-$. The observed ion-specific liquid jet velocity finds a linear correlation with the ion-induced variation in the optical absorbance of Rh6G that

also follows the Hofmeister series. It is suggested that the hydrophilic kosmotropic anion (SO_4^{2-}) prefers to bind to the water molecules, whereas the hydrophobic chaotropic anions (I^- , and SCN^-) are prone to bind the NH-and hydrophobic CH- moieties of Rh6G. This relative adsorption of ions towards Rh6G determines the ion-induced variation in the optical absorbance and, thus, the liquid jet velocities. We have also showcased ion-specific penetration depths of liquid jets as simulated for model soft tissues. The maximum penetration depth is observed with SO_4^{2-} , however, a three-fold reduction in penetration depth is reported for I^- and SCN^- . The present research demonstrates the contribution of ion-specific interactions in governing the jet velocity and jet power that is crucial in developing needle-free drug delivery systems with controlled penetration depths.

The third potential contribution of the present thesis is to provide the molecular level insights into the mechanism of Hofmeister phenomenon. Here, we have used a novel SFG vibrational spectroscopy in ssp and ppp- polarization schemes to investigate the impact of ions in ordering/disordering the macromolecule structure at the air/PVP aqueous interface. It is showcased that the orientation angle of vinyl chain CH2-groups of PVP changes from 62.5° to 33.6° in the presence of ions that follows the Hofmeister series: $SO_4^{2-} > Cl^- > NO_3^- > Cl^- > NO_3^-$ $Br^- > ClO_4^- > SCN^-$. The minimal orientation angle of CH_2 -groups in the presence of chaotropic anions ClO₄, and SCN⁻ indicates the ion-induced significant reordering in the PVP vinyl chains. The observed Hofmeister trend in the structural changes of PVP macromolecule finds an intriguing correlation with the ionspecific changes in the strength of water-macromolecule interactions as evidenced by a blue shift of ~ 40 cm⁻¹ in the OH-stretch band at ~ 3540 cm⁻¹in the ppp-SFG spectra. This enables us to comprehend the molecular level mechanism of Hofmeister effect as follows: the weakly hydrated chaotropic anions (ClO₄-, and SCN-) which are prone to adsorb towards the hydrophobic surface (-CH, -CH₂ of polymer backbone), offer binding sites to the surrounding water molecules to form weak interactions with the hydrophobic moieties of the macromolecule, and, in turn, perturb the macromolecule structure at the interface. Our current experimental findings provide the spectroscopic evidence and importance of ion-specific water-macromolecule interactions that cooperatively participate in the Hofmeister effect along with the well-known ion-water and ion-macromolecule interactions.

The molecular level approach developed in this thesis could potentially motivate new experiments and theoretical studies to comprehend the fundamentals of specific ion phenomena that widely prevail in various scientific and technological applications.

Future outlook

The work presented in this thesis inspires several new avenues of further exploration. Some of the speculative ideas are as follows:

- [1]. We have performed evaporation studies at the air/water interface in the presence of sodium salts of Hofmeister anions which increase the surface tension of water. In contrast, monoprotic halogen acids reduce the surface tension of water; therefore, it would be interesting to see how their presence would influence the evaporation process.
- [2]. One can investigate the fundamentals of specific cation effects on the water evaporation process at the air/aqueous interface.
- [3]. Evaporation of biological droplets carries utmost importance in the medical industry in disease diagnosis, especially during the Covid-endemic era to investigate the lifetime of contaminant aqueous droplets in the environment, avoiding the risk of spreading infection. We have observed exciting evaporation dynamics

- of protein droplets with the variation in pH and ions under the influence of a magnetic field that can be carried forward.
- [4]. The orientation angle of the free OH oscillator at the air/water interface has grabbed attention recently. Some interesting reports have utilized various orientation distribution functions like Dirac delta, step function, Gaussian, and exponential function to interpret the free OH angle. It interests us to work out in this direction to develop a unified picture of the orientation angle distribution of this free OH moiety with $C_{\infty v}$ symmetry at the air/water interface.
- [5]. In the area of laser-induced liquid microjets, it would be interesting to work with actual drugs/vaccines to compare their liquid jet characteristics, i.e., jet velocity/power and penetration depths for developing needle-free injection systems.

REFERENCES

- 1. Poiseuille, J. L. M. Ann. Chim. Phys. **1847**, 21, 76–109.
- 2. Adamson, A. W. A Textbook of Physical Chemistry, 2nd ed. Academic Press, New York, 1979.
- 3. Kunz, W.; Henle, J.; Ninham, B. W. 'Zur Lehre Von Der Wirkung Der Salze' (About the Science of the Effect of Salts): Franz Hofmeister's Historical Papers. Curr. Opin. Colloid Interface Sci. **2004**, 9, 19–37.
- 4. Hofmeister, F. Zur Lehre Von Der Wirkung Der Salze. NaunynSchmiedeberg's Arch. Pharmacol. **1888**, 24, 247–260.
- 5. Hofmeister, F. Zur Lehre Von Der Wirkung Der Salze. NaunynSchmiedeberg's Arch. Pharmacol. **1888**, 25, 1–30.
- 6. Robertson, T. B. Contributions to the theory of the mode of action of inorganic salts upon proteins in solution. J. Biol. Chem.**1911**, 9(3), 303-326.
- 7. Loeb, J. The proteins and colloid chemistry. Science **1920**, 52(1350), 449-456.
- 8. Gustavson, K. H. Specific ion effects in the behaviour of tanning agents toward collagen treated with neutral salts. In Colloid Symposium Monograph; Weiser, H. B., Ed.; The Chemical Catalog Company Inc.: New York, 1926.
- 9. Green, A. A. Studies in the physical chemistry of the proteins: X. The solubility of hemoglobin in solutions of chlorides and sulfates of varying concentration. J. Biol. Chem. **1932**, 95(1), 47-66.
- 10. Jones, G.; Dole, M. The transference number of barium chloride as a function of the concentration. J. Am. Chem. Soc. **1929**, 51(4), 1073-1091.
- 11. Cox, W. M.; Wolfenden, J. H. The viscosity of strong electrolytes measured by a differential method. Proc. R. Soc. Lond. A **1934**, 145(855), 475-488.
- 12. Frank, H. S.; Evans, M. W. Free volume and entropy in condensed systems III. Entropy in binary liquid mixtures; partial molal entropy in dilute solutions; structure and thermodynamics in aqueous electrolytes. J. Chem. Phys. **1945**, 13(11), 507-532.
- 13. Voet, A. Quantative Lyotropy. Chem. Rev. **1937**, 20(2), 169-179.
- Eckfeldt, E. L.; Lucasse, W. W. Lyotropic Order and the Effects of Sodium Salts on the Miscibility of Cyclohexane and Methyl Alcohol. J. Phys. Chem. 1943, 47(2), 183-189.
- 15. Pearson, R. G. Hard and soft acids and bases. J. Am. Chem. Soc. **1963**, 85(22), 3533-3539.
- 16. Gurney. R. W. Ionic Processes In Solution, McGraw-Hill, 1953.
- 17. Meyer, K. H.; Klemm, O. La solubilité de l'anhydride du glycocolle. Helv. Chim. Acta **1940**, 23(1), 25-27.

- 18. Bello, J.; Bello, H. R.; Vinograd, J. R. The functional groups in the gelation of gelatin. Biochim. Biophys. Acta 1962, 57(1), 222-229.
- 19. Robinson, D. R.; Jencks, W. P. The effect of concentrated salt solutions on the activity coefficient of acetyltetraglycine ethyl ester. J. Am. Chem. Soc. **1965**, 87(11), 2470-2479.
- 20. Schrier, E. E.; Schrier, E. B. The salting-out behavior of amides and its relation to the denaturation of proteins by salts. J. Phys. Chem. **1967**, 71(6), 1851-1860.
- 21. Nandi, P. K.; Robinson, D. R. Effects of salts on the free energy of the peptide group. J. Am. Chem. Soc. 1972, 94(4), 1299-1308.
- 22. Von Hippel, P. H.; Peticolas, V.; Schack, L.; Karlson, L. Model studies on the effects of neutral salts on the conformational stability of biological macromolecules. I. Ion binding to polyacrylamide and polystyrene columns. Biochemistry **1973**, 12(7), 1256-1264.
- 23. Arakawa, T.; Timasheff, S. N. Preferential interactions of proteins with salts in concentrated solutions. Biochemistry, **1982**, 21(25), 6545-6552.
- 24. Marcus, Y. The structuredness of solvents. J. Solution Chem. 1992, 21(12), 1217-1230.
- 25. Marcus, Y. The structuredness of solvents. 2. Data for ambient conditions. J. Solution Chem. **1996**, 25(5), 455-469.
- 26. Marcus, Y. The structuredness of water at elevated temperatures along the saturation line. J. Mol. liq. **1999**, 79(2), 151-165.
- 27. Marcus, Y. Effect of ions on the structure of water: structure making and breaking. Chem. Rev. **2009**, 109(3), 1346-1370.
- 28. Collins, K. D.; Washabaugh, M. W. The Hofmeister effect and the behaviour of water at interfaces. Q Rev. Biophys. **1985**, 18(4), 323-422.
- 29. Collins, K. D. Ions from the Hofmeister series and osmolytes: effects on proteins in solution and in the crystallization process. Methods **2004**, 34(3), 300-311.
- 30. Jungwirth, P.; Winter, B. Ions at aqueous interfaces: From water surface to hydrated proteins. Annu. Rev. Phys. Chem. **2008**, 59(1), 343-366.
- 31. Baldwin, R. L. How Hofmeister Ion Interactions Affect Protein Stability. Biophys. J. **1996**, 71, 2056–2063
- 32. Cacace, M. G.; Landau, E. M.; Ramsden, J. J. The Hofmeister Series: Salt and Solvent Effects on Interfacial Phenomena. Q. Rev. Biophys. **1997**, 30, 241–277.
- 33. Record, M. T.; Zhang, W. T.; Anderson, C. F. Analysis of Effects of Salts and Uncharged Solutes on Protein and Nucleic Acid Equilibria and Processes: A Practical Guide to Recognizing and Interpreting Polyelectrolyte Effects, Hofmeister Effects, and Osmotic Effects of Salts. Adv. Protein Chem. 1998, 51, 281–353.

- 34. Pegram, L. M.; Record, M. T. Thermodynamic Origin of Hofmeister Ion Effects. J. Phys. Chem. B **2008**, 112, 9428–9436.
- 35. Kunz, W.; Neueder, R. An attempt of a general overview. Specific Ion Effects. 2010, 3-54.
- 36. Lo Nostro, P.; Ninham, B. W. Hofmeister phenomena: an update on ion specificity in biology. Chem. Rev.**2012**, 112(4), 2286-2322.
- 37. Salis, A.; Ninham, B. W. Models and mechanisms of Hofmeister effects in electrolyte solutions, and colloid and protein systems revisited. Chem. Soc. Rev. **2014**, 43(21), 7358-7377.
- 38. Schwierz, N.; Horinek, D.; Sivan, U.; Netz, R. R. Reversed Hofmeister Series "The Rule Rather Than the Exception". Curr. Opin. Colloid Interface Sci. **2016**, 23, 10–18
- 39. Okur, H. I.; Hladílková, J.; Rembert, K. B.; Cho, Y.; Heyda, J.; Dzubiella, J.; Cremer, P. S.; Jungwirth, P. Beyond the Hofmeister series: Ion-specific effects on proteins and their biological functions. J Phys. Chem. B **2017**, 121(9), 1997-2014.
- 40. Song, J.; Franck, J.; Pincus, P.; Kim, M. W.; Han, S. Specific ions modulate diffusion dynamics of hydration water on lipid membrane surfaces. J. Am. Chem. Soc. **2014**, 136(6), 2642-2649.
- 41. Rembert, K. B.; Okur, H. I.; Hilty, C.; Cremer, P. S. An NH moiety is not required for anion binding to amides in aqueous solution. Langmuir **2015**, 31(11), 3459-3464.
- 42. Neal, J. F.; Saha, A.; Zerkle, M. M.; Zhao, W.; Rogers, M. M.; Flood, A. H.; Allen, H. C. Molecular Recognition and Hydration Energy Mismatch Combine To Inform Ion Binding Selectivity at Aqueous Interfaces. J. Phys. Chem. A **2020**, 124(49), 10171-10180.
- 43. Guggenheim, E. A. The Specific Thermodynamic Properties of Aqueous Solutions of Strong Electrolytes. London, Edinburgh, Dublin Philos. Mag. J. Sci. **1935**, 19, 588–643.
- 44. Guggenheim, E. A.; Turgeon, J. C. Specific Interaction of Ions. Trans. Faraday Soc. **1955**, 51, 747–761.
- 45. Moghaddam, S. Z.; Thormann, E. Hofmeister Effect of Salt Mixtures on Thermo-Responsive Poly(propylene oxide). Phys. Chem. Chem. Phys. **2015**, 17, 6359–6366.
- 46. Ottosson, N.; Heyda, J.; Wernersson, E.; Pokapanich, W.; Svensson, S.; Winter, B.; Öhrwall, G.; Jungwirth, P.; Björneholm, O. The Influence of Concentration on the Molecular Surface Structure of Simple and Mixed Aqueous Electrolytes. Phys. Chem. Chem. Phys. 2010, 12, 10693–10700.
- 47. Bruce, E. E.; Bui, P. T.; Rogers, B. A.; Cremer, P. S.; Van Der Vegt, N. F. Nonadditive ion effects drive both collapse and swelling of thermoresponsive polymers in water. J. Am. Chem. Soc. **2019**, 141(16), 6609-6616.
- 48. Medda, L.; Monduzzi, M.; Salis, A. The molecular motion of bovine serum albumin under physiological conditions is ion specific. Chem. Commun. **2015**, 51(30), 6663-6666.
- 49. Qiu, M.; Long, S.; Li, B.; Yan, L.; Xie, W.; Niu, Y.; Wang, X.; Guo, Q.; Xia, A. Toward an understanding of how the optical property of water-soluble cationic polythiophene derivative is altered by the addition of salts: The Hofmeister effect. J. Phys. Chem. C **2013**, 117(42), 21870-21878.

- 50. Kielland, J. Individual activity coefficients of ions in aqueous solutions. J. Am. Chem. Soc. **1937**, 59(9), 1675-1678.
- 51. Stokes, R. H.; Robinson, R. A. Ionic hydration and activity in electrolyte solutions. J. Am. Chem. Soc. 1948, 70(5), 1870-1878.
- 52. Hamer, W. J.; Wu, Y. C. Osmotic coefficients and mean activity coefficients of uni-univalent electrolytes in water at 25° C. J. Phys. Chem. Ref. Data **1972**, 1(4), 1047-1100.
- 53. Salis, A.; Cristina Pinna, M.; Bilanic ova, D.; Monduzzi, M.; Nostro, P. L.; Ninham, B. W. Specific anion effects on glass electrode pH measurements of buffer solutions: bulk and surface phenomena. J. Phys. Chem. B **2006**, 110(6), 2949-2956.
- 54. Parsons, D. F.; Carucci, C.; and Salis, A. Buffer-specific effects arise from ionic dispersion forces. Phys. Chem. Chem. Phys. **2022**, 24(11), 6544-6551.
- 55. Jin, S. A.; Khan, S. A.; Spontak, R. J.; and Rojas, O. J. Anion-Specific Water Interactions with Nanochitin: Donnan and Osmotic Pressure Effects as Revealed by Quartz Microgravimetry. Langmuir, **2021**, 37(38), 11242-11250.
- Voinescu, A. E.; Bauduin, P.; Pinna, M. C.; Touraud, D.; Ninham, B. W.; and Kunz, W. Similarity of salt influences on the pH of buffers, polyelectrolytes, and proteins. J. Phys. Chem. B 2006, 110(17), 8870-8876.
- 57. Rossi, S.; Lo Nostro, P.; Lagi, M.; Ninham, B. W.; and Baglioni, P. Specific anion effects on the optical rotation of α-amino acids. J. Phys. Chem. B **2007**, 111(35), 10510-10519.
- 58. Nostro, P. L.; Ninham, B. W.; Milani, S.; Fratoni, L.; Baglioni, P. Specific anion effects on the optical rotation of glucoseand serine. Biopolymers **2006**, 81(2), 136-148.
- 59. Ashraf, H.; Guo, Y.; Wang, N.; Pang, S.; Zhang, Y. H. Hygroscopicity of Hofmeister salts and glycine aerosols–salt specific interactions. J. Phys. Chem. A **2021**, 125(7), 1589-1597.
- 60. Yu, W.; Du, N.; Gu, Y.; Yan, J.; Hou, W. Specific ion effects on the colloidal stability of layered double hydroxide single-layer nanosheets. Langmuir **2020**, 36(23), 6557-6568.
- 61. Thareja, S.; Kumar, A. "Water-in-salt" electrolyte-based high-voltage (2.7 V) sustainable symmetric supercapacitor with superb electrochemical performance—an analysis of the role of electrolytic ions in extending the cell voltage. ACS Sustain. Chem. Eng. **2021**, 9(5), 2338-2347.
- 62. Wu, Y.; Mu, Y.; Luo, Y.; Menon, C.; Zhou, Z.; Chu, P. K.; Feng, S. P. Hofmeister Effect and Electrostatic Interaction Enhanced Ionic Conductive Organohydrogels for Electronic Applications. Adv. Funct. Mater. **2022**, 32(15), 2110859.
- 63. Wu, Y.; Qu, J.; Zhang, X.; Ao, K.; Zhou, Z.; Zheng, Z.; Mu, Y.; Wu, X.; Luo, Y.; Feng, S. P. Biomechanical energy harvesters based on ionic conductive organohydrogels via the hofmeister effect and electrostatic interaction. ACS Nano **2021**, 15(8), 13427-13435.

- 64. Levin, Y.; Dos Santos, A. P.; Diehl, A. Ions at the air-water interface: an end to a hundred-year-old mystery? Phys. Rev. Lett. **2009**, 103(25), 257802.
- 65. Rana, B.; Fairhurst, D. J.; Jena, K. C. Investigation of water evaporation process at air/water interface using Hofmeister ions. J. Am. Chem. Soc. 2022, 144(39), 17832-17840.
- 66. dos Santos, A. P.; Diehl, A.; Levin, Y. Surface tensions, surface potentials, and the hofmeister series of electrolyte solutions. Langmuir **2010**, 26 (13), 10778–83.
- 67. Gurau, M. C.; Lim, S. M.; Castellana, E. T.; Albertorio, F.; Kataoka, S.; Cremer, P. S. On the mechanism of the Hofmeister effect. J. Am. Chem. Soc. **2004**, 126(34), 10522-10523.
- 68. Chen, X.; Yang, T.; Kataoka, S.; Cremer, P. S. Specific ion effects on interfacial water structure near macromolecules. J. Am. Chem. Soc. **2007**, 129(40), 12272-12279.
- 69. Foster, K. L.; Plastridge, R. A.; Bottenheim, J. W.; Shepson, P. B.; Finlayson-Pitts, B. J.; Spicer, C. W. The role of Br2 and BrCl in surface ozone destruction at polar sunrise. Science **2001**, 291(5503), 471-474.
- Cuevas, C. A.; Fernandez, R. P.; Kinnison, D. E.; Li, Q.; Lamarque, J. F.; Trabelsi, T.; Francisco J. S.;
 Solomon S.; Saiz-Lopez, A. The influence of iodine on the Antarctic stratospheric ozone hole. Proc.
 Natl. Acad. Sci. 2022, 119(7), e2110864119.
- Huang, D. D.; Zhang, Q.; Cheung, H. H.; Yu, L.; Zhou, S.; Anastasio, C.; Smith, J. D.; Chan, C. K. Formation and evolution of aqSOA from aqueous-phase reactions of phenolic carbonyls: Comparison between ammonium sulfate and ammonium nitrate solutions. Environ. Sci. Technol. 2018, 52(16), 9215-9224.
- 72. Craig, V. S. J.; Ninham, B. W.; Pashley, R. M.; The effect of electrolytes on bubble coalescence in water. J. Phys. Chem. **1993**, 97,10192–10197
- 73. Craig, V. S. J.; Ninham, B. W.; Pashley, R. M. Effect of electrolytes on bubble coalescence. Nature 1993, 364(6435), 317-319.
- 74. Amani, P.; Karakashev, S. I.; Grozev, N. A.; Simeonova, S. S.; Miller, R.; Rudolph, V.; Firouzi, M. Effect of selected monovalent salts on surfactant stabilized foams. Adv. Colloid Interface Sci. **2021**, 295, 102490.
- 75. Murgia, S.; Portesani, F.; Ninham, B. W.; Monduzzi, M. Interaction of sodium ions with cationic surfactant interfaces. Euro. J. Chem. **2006**, 12(30), 7889-7898.
- 76. Chen, X.; Flores, S. C.; Lim, S. M.; Zhang, Y.; Yang, T.; Kherb, J.; Cremer, P. S. Specific anion effects on water structure adjacent to protein monolayers. Langmuir **2010**, 26(21), 16447-16454
- Neves, C. M.; Dinis, T. B.; Carvalho, P. J.; Schröder, B.; Santos, L. M.; Freire, M. G.; Coutinho, J. A. Binary Mixtures of Ionic Liquids in Aqueous Solution: Towards an Understanding of Their Salting-In/Salting-Out Phenomena. J. Solution Chem. 2019, 48(7), 983-991.

- 78. Shukla, S. K.; Mikkola, J. P. Use of ionic liquids in protein and DNA chemistry. Front. Chem. **2020**, 8, 598662.
- 79. Sun, P.; Huang, K.; Liu, H. The nature of salt effect in enhancing the extraction of rare earths by non-functional ionic liquids: Synergism of salt anion complexation and Hofmeister bias. J. Colloid Interface Sci. **2019**, 539, 214-222.
- 80. Shang, Y.; Wu, C.; Hang, C.; Lu, H.; Wang, Q. Hofmeister-Effect-Guided Ionohydrogel Design as Printable Bioelectronic Devices. Adv. Mater. **2020**, *32*(30), 2000189.
- 81. Zhu, R.; Baraniak, M. K; Jäkle, F.; Liu, G. Anion Specificity in Dimethyl Sulfoxide–Water Mixtures Exemplified by a Thermosensitive Polymer. J. Phys. Chem. B **2018**, 122(34), 8293-8300.
- 82. Zhang, Y.; Furyk, S.; Bergbreiter, D. E.; Cremer, P. S. Specific ion effects on the water solubility of macromolecules: PNIPAM and the Hofmeister series. J. Am. Chem. Soc. **2005**, 127(41), 14505-14510.
- 83. Wojciechowski, K.; Bitner, A.; Warszyński, P.; Żubrowska, M. The Hofmeister effect in zeta potentials of CTAB-stabilised toluene-in-water emulsions. Colloids Surf, A Physicochem. Eng. Asp. **2011**, 376(1-3), 122-126.
- 84. Aleid, S.; Wu, M.; Li, R.; Wang, W.; Zhang, C.; Zhang, L.; Wang, P. Salting-in effect of zwitterionic polymer hydrogel facilitates atmospheric water harvesting. ACS Mater. Lett. **2022**, 4(3), 511-520.
- 85. Lyu, T.; Wang, Z.; Liu, R.; Chen, K.; Liu, H.; Tian, Y. Macroporous Hydrogel for High-Performance Atmospheric Water Harvesting. ACS Appl. Mater. Interfaces **2022**, 14(28), 32433-32443.
- 86. Warren, J. C.; Cheatum, S. G. Effect of neutral salts on enzyme activity and structure. Biochemistry **1966**, 5(5), 1702-1707.
- 87. Hayashi, M.; Unemoto, T.; Hayashi, M. pH-and anion-dependent salt modifications of alkaline phosphatase from a slightly halophilic Vibrio alginolyticus. Biochim. Biophys. Acta, Enzymol. **1973**, 315(1), 83-93.
- 88. Cacace, M. G.; Landau, E. M.; Ramsden, J. J. The Hofmeister series: salt and solvent effects on interfacial phenomena. Q. Rev. Biophys. **1997**, 30(3), 241-277.
- 89. Bilanicová, D.; Salis, A.; Ninham, B. W.; Monduzzi, M. Specific anion effects on enzymatic activity in nonaqueous media. J. Phys. Chem. B **2008**, 112(38), 12066-12072.
- 90. Zhang, Y.; Cremer, P. S. The inverse and direct Hofmeister series for lysozyme. Proc. Natl. Acad. Sci. **2009**, 106(36), 15249-15253.
- 91. Garajová, K.; Balogová, A.; Dušeková, E.; Sedláková, D.; Sedlák, E.; Varhač, R. Correlation of lysozyme activity and stability in the presence of Hofmeister series anions. Biochim. Biophys. Acta, Proteins Proteomics **2017**, 1865(3), 281-288.
- 92. Collu, M.; Carucci, C.; Salis, A. Specific anion effects on lipase adsorption and enzymatic synthesis of biodiesel in nonaqueous media. Langmuir **2020**, 36(32), 9465-9471.

- 93. Salis, A.; Bhattacharyya, M. S; Monduzzi, M. Specific ion effects on adsorption of lysozyme on functionalized SBA-15 mesoporous silica. J. Phys. Chem. B **2010**, 114(23), 7996-8001.
- 94. Grigsby, J. J.; Blanch, H. W.; Prausnitz, J. M. Cloud-point temperatures for lysozyme in electrolyte solutions: effect of salt type, salt concentration and pH. Biophys. Chem. **2001**, 91(3), 231-243.
- 95. Lo Nostro, P.; Peruzzi, N.; Severi, M.; Ninham, B. W.; Baglioni, P. Asymmetric partitioning of anions in lysozyme dispersions. J. Am. Chem. Soc. **2010**, 132(18), 6571-6577.
- Zhang, Y.; Cremer, P. S. Chemistry of Hofmeister anions and osmolytes. Annu. Rev. Phys. Chem. 2010, 61(1), 63-83.
- 97. Medda, L.; Barse, B.; Cugia, F.; Bostrom, M. Parsons, D. F.; Ninham, B. W.; Monduzzi, M.; Salis, A. Hofmeister challenges: ion binding and charge of the BSA protein as explicit examples. Langmuir **2012**, 28(47), 16355-16363.
- 98. Ghosh, R.; Chatterjee, D. P.; Das, S.; Mukhopadhyay, T. K.; Datta, A.; Nandi, A. K. Influence of Hofmeister I–on Tuning Optoelectronic Properties of Ampholytic Polythiophene by Varying pH and Conjugating with RNA. Langmuir **2017**, 33(44), 12739-12749.
- 99. Zdrali, E.; Okur, H. I.; Roke, S. Specific ion effects at the interface of nanometer-sized droplets in water: structure and stability. J. Phys. Chem. C **2019**, 123(27), 16621-16630.
- 100. Zdrali, E.; Chen, Y.; Okur, H. I.; Wilkins, D. M.; Roke, S. The molecular mechanism of nanodroplet stability. ACS Nano **2017**, 11(12), 12111-12120.
- 101. Schwidetzky, R.; Lukas, M.; YazdanYar, A.; Kunert, A. T.; Pöschl, U.; Domke, K. F.; Frohlich-Nowoisky, J.; Bonn, M.; Koop, T.; Nagata, Y.; Meister, K. Specific Ion–Protein Interactions Influence Bacterial Ice Nucleation. Euro. J. Chem. 2021, 27(26), 7402-7407.
- 102. Worthy, S. E.; Kumar, A.; Xi, Y.; Yun, J.; Chen, J.; Xu, C.; Irish, V. E.; Amato, P.; Bertram, A. K. The effect of (NH₄)₂SO₄ on the freezing properties of non-mineral dust ice-nucleating substances of atmospheric relevance. Atmospheric Chem. Phys. **2021**, 21(19), 14631-14648.
- 103. Gokarn, Y. R.; Fesinmeyer, R. M.; Saluja, A.; Razinkov, V.; Chase, S. F.; Laue, T. M.; Brems, D. N. Effective charge measurements reveal selective and preferential accumulation of anions, but not cations, at the protein surface in dilute salt solutions. Protein Sci. 2011, 20(3), 580-587.
- 104. López-León, T.; Jódar-Reyes, A. B.; Bastos-González, D.; Ortega-Vinuesa, J. L. Hofmeister effects in the stability and electrophoretic mobility of polystyrene latex particles. J. Phys. Chem. B 2003, 107(24), 5696-5708.
- 105. Salis, A.; Cugia, F.; Parsons, D. F.; Ninham, B. W.; Monduzzi, M. Hofmeister series reversal for lysozyme by change in pH and salt concentration: insights from electrophoretic mobility measurements. Phys. Chem. Chem. Phys. 2012, 14(13), 4343-4346.
- 106. Holm, G. E.; Sherman, J. M. Salt effects in bacterial growth. J. Bacterial. 1921, 6(6), 511-519.

- 107. Nostro, P. L.; Ninham, B. W.; Nostro, A. L.; Pesavento, G.; Fratoni, L.; Baglioni, P. Specific ion effects on the growth rates of Staphylococcus aureus and Pseudomonas aeruginosa. Phys. Biol. **2005**, 2(1), 1.
- 108. Gong, L.; Zhang, J.; Wang, W.; Xiang, L.; Pan, M.; Yang, W.; Han, L.; Wang, J.; Yan, B.; Zeng, H. Ion-specific effect on self-cleaning performances of polyelectrolyte-functionalized membranes and the underlying nanomechanical mechanism. J. Membr. Sci. 2021, 634, 119408.
- 109. Chen, Y.; Luo, S. C. Synergistic effects of ions and surface potentials on antifouling poly (3, 4-ethylenedioxythiophene): Comparison of oligo (ethylene glycol) and phosphorylcholine. Langmuir **2018**, 35(5), 1199-1210.
- 110. Higaki, Y.; Inutsuka, Y.; Ono, H.; Yamada, N. L.; Ikemoto, Y.; Takahara, A. Counteranion-specific hydration states of cationic polyelectrolyte brushes. Ind. Eng. Chem. Res. **2018**, 57(15), 5268-5275.
- 111. Hamley, I. W. Peptide nanotubes. Angew. Chem. Int. Ed. 2014, 53(27), 6866-6881.
- 112. Gobeaux, F.; Fay, N.; Tarabout, C.; Mériadec, C.; Meneau, F.; Ligeti, M.; Buisson, D. A.; Cintrat, J. C.; Nguyen, K. M. H.; Perrin, L.; Valery, C.; Artzner, F.; Paternostre, M. Structural role of counterions adsorbed on self-assembled peptide nanotubes. J. Am. Chem. Soc. 2012, 134(1), 723-733.
- 113. Loh, W. W.; Lin, Q.; Lim, C. C.; Guo, L.; Tang, Y. K.; Loh, X. J.; Lim, J. Y. C. Hofmeister effects of anions on self-assembled thermogels. Mater. Today Chem. **2022**, 23, 100674.
- Iscen, A.; Schatz, G. C. Hofmeister effects on peptide amphiphile nanofiber self-assembly. J. Phys. Chem. B 2019, 123(32), 7006-7013.
- 115. Assaf, K. I.; Nau, W. M. The chaotropic effect as an assembly motif in chemistry. Angew. Chem. Int. Ed. 2018, 57(43), 13968-13981.
- 116. Zou, H.; Meng, X.; Zhao, X.; Qiu, J. Hofmeister Effect-Enhanced Hydration Chemistry of Hydrogel for High-Efficiency Solar-Driven Interfacial Desalination. Adv. Mater. **2022**, 2207262.
- 117. Wilson, H. M.; Lim, H. W.; Lee, S. J. Highly Efficient and Salt-Rejecting Poly (vinyl alcohol) Hydrogels with Excellent Mechanical Strength for Solar Desalination. ACS Appl. Mater. Interfaces 2022, 14(42), 47800-47809.
- 118. Borthakur, P.; Aryafard, M.; Zara, Z.; David, Ř.; Minofar, B.; Das, M. R.; Vithanage, M. Computational and experimental assessment of pH and specific ions on the solute solvent interactions of clay-biochar composites towards tetracycline adsorption: implications on wastewater treatment. J. Environ. Manage. 2021, 283, 111989.
- 119. Zuo, Y.; Long, X.; Zheng, Y.; Zhang, J.; Wang, L.; Hu, J.; Jiao, F. Gelatin-tannic acid coating for high flux oil-water separation. J. Environ. Chem. Eng. **2022**, 107992.
- 120. Huang, X.; Wu, S.; Ke, X.; Li, X.; Du, X. Phosphonated pillar [5] arene-valved mesoporous silica drug delivery systems. ACS Appl. Mater. Interfaces **2017**, 9(23), 19638-19645.

- 121. Russo, J.; Fiegel, J.; Brogden, N. K. Effect of Salt Form on Gelation and Drug Delivery Properties of Diclofenac-Loaded Poloxamer Gels for Delivery to Impaired Skin. Pharm. Res. 2022, 39(10), 2515-2527.
- 122. Guo, Y.; Li, S.; Li, W.; Moosa, B.; Khashab, N. M. The Hofmeister effect on nanodiamonds: how addition of ions provides superior drug loading platforms. Biomater. Sci. **2014**, 2, 84-88.
- Peek, L.J.; Middaugh, C.R.; Berkland, C. Nanotechnology in vaccine delivery. Adv. Drug Deliv. Rev. 2008, 60, 915-928.
- 124. Reed, S.G.; Bertholet, S.; Coler, R.N.; Friede, M. New horizons in adjuvants for vaccine development. Trends Iimmunol. **2009**, 30, 23-32.
- 125. Wiedmann, T. S.; Naqwi, A. Pharmaceutical salts: Theory, use in solid dosage forms and in situ preparation in an aerosol. Asian J. Pharm. Sci. **2016**, 11, 722-734.
- Hoog, T. G.; Pawlak, M. R.; Aufdembrink, L. M.; Bachan, B. R.; Galles, M. B.; Bense, N. B.; Adamala K. P.; Engelhart, A. E. Switchable DNA-Based Peroxidases Controlled by a Chaotropic Ion. ChemBioChem. 2022, e202200090.
- 127. Holm, R.; Schönbeck, C.; Somprasirt, P.; Westh, P.; Mu, H. A study of salt effects on the complexation between β-cyclodextrins and bile salts based on the Hofmeister series. J. Incl. Phenom. Macrocycl. Chem. **2014**, 80, 243-251.
- 128. Paladino, A.; Balasco, N.; Graziano, G.; Vitagliano, L. A Protein Data Bank survey of multimodal binding of thiocyanate to proteins: Evidence for thiocyanate promiscuity. Int. J. Biol. Macromol. **2022**, 208, 29-36.
- 129. Chandler, J. D.; Day, B. J. Thiocyanate: a potentially useful therapeutic agent with host defense and antioxidant properties. Biochem. Pharmacol. **2012**, 84, 1381-1387.
- 130. Hirt, S.; Jones, O. G. Effects of chloride, thiocyanate and sulphate salts on β-lactoglobulin–pectin associative complexes. Int. J. Food Sci. Technol. **2014**, 49, 2391-2398.
- 131. Taratuta, V. G.; Holschbach, A.; Thurston, G. M.; Blankschtein, D.; Benedek, G. B. Liquid-liquid phase separation of aqueous lysozyme solutions: effects of pH and salt identity. J. Phys. Chem. **1990**, 94(5), 2140-2144.
- 132. Fetahaj, Z.; Ostermeier, L.; Cinar, H.; Oliva, R.; Winter, R. Biomolecular condensates under extreme martian salt conditions. J. Am. Chem. Soc. **2021**, 143(13), 5247-5259.
- 133. Yuan, Y.; Yang, J.; Liu, Z.; Tan, R.; Chuai, M.; Sun, J.; Xu, Y.; Zheng, X.; Wang, M.; Ahmad, T.; Chen, N.; Zhu, Z.; Li, K.; Chen, W. A Proton-Barrier Separator Induced via Hofmeister Effect for High-Performance Electrolytic MnO2–Zn Batteries. Adv. Energy Mater. 2022, 12(16), 2103705.
- 134. Yuan, G.; Kienzle, P. A.; Satija, S. K. Salting Up and Salting Down of Bovine Serum Albumin Layers at the Air–Water Interface. Langmuir **2020**, 36(50), 15240-15246.

- 135. Li, Y.; Shrestha, M.; Luo, M.; Sit, I.; Song, M.; Grassian, V. H.; Xiong, W. Salting up of proteins at the air/water interface. Langmuir **2019**, 35(43), 13815-13820.
- 136. Sedlák, E.; Sedláková, D.; Marek, J.; Hančár, J.; Garajová, K.; Žoldák, G. Ion-specific protein/water interface determines the Hofmeister effect on the kinetic stability of glucose oxidase. J. Phys. Chem. B 2019, 123(38), 7965-7973.
- 137. Kang, B.; Tang, H.; Zhao, Z.; Song, S. Hofmeister series: Insights of ion specificity from amphiphilic assembly and interface property. ACS Omega **2020**, 5(12), 6229-6239.
- Moghaddam, S. Z.; Thormann, E. The Hofmeister series: Specific ion effects in aqueous polymer solutions. J. Colloid Interface Sci. 2019, 555, 615-635.
- 139. Gregory, K. P.; Elliott, G. R.; Robertson, H.; Kumar, A.; Wanless, E. J.; Webber, G. B.; Craig, V. S. J.; Andersson, G. G.; Page, A. J. Understanding specific ion effects and the Hofmeister series. Phys. Chem. Chem. Phys. **2022**, 24(21), 12682-12718.
- 140. Israelachvili, J. N. Intermolecular and surface forces. Academic press, 2011.
- 141. Butt, H. J.; Kappl, M. Surface and interfacial forces. John Wiley & Sons, 2018.
- 142. Omta, A. W.; Kropman, M. F.; Woutersen, S.; Bakker, H. J. Negligible Effect of Ions on the Hydrogen-Bond Structure in Liquid Water. Science **2003**, 301, 347-349.
- 143. Batchelor, J. D.; Olteanu, A.; Tripathy, A.; Pielak, G. J. Impact of protein denaturants and stabilizers on water structure. J. Am. Chem. Soc. **2004**, 126(7), 1958-1961.
- 144. Funkner, S.; Niehues, G.; Schmidt, D. A.; Heyden, M.; Schwaab, G.; Callahan, K. M.; Tobias, D. J.; Havenith, M. Watching the LowFrequency Motions in Aqueous Salt Solutions: The Terahertz Vibrational Signatures of Hydrated Ions. J. Am. Chem. Soc. 2012,134, 1030-1035.
- 145. Stirnemann, G.; Wernersson, E.; Jungwirth, P.; Laage, D. Mechanisms of Acceleration and Retardation of Water Dynamics by Ions. J. Am. Chem. Soc. **2013**, 135, 11824-11831.
- O'Brien, J. T.; Prell, J. S.; Bush, M. F.; Williams, E. R. Sulfate ion patterns water at long distance. J. Am. Chem. Soc. 2010, 132(24), 8248-8249.
- Paschek, D.; Ludwig, R. Specific ion effects on water structure and dynamics beyond the first hydration shell. Angew. Chem. Int. Ed. 2011, 50(2), 352-353.
- 148. Nucci, N. V.; Vanderkooi, J. M. Effects of salts of the Hofmeister series on the hydrogen bond network of water. J. Mol. Liq. **2008**, 143(2-3), 160-170.
- 149. Thomas, A. S.; Elcock, A. H. Molecular dynamics simulations of hydrophobic associations in aqueous salt solutions indicate a connection between water hydrogen bonding and the Hofmeister effect. J. Am. Chem. Soc. **2007**, 129(48), 14887-14898.
- 150. Pauling, L. The structure and entropy of ice and of other crystals with some randomness of atomic arrangement. J. Am. Chem. Soc. **1935**, 57(12), 2680-2684.

- 151. Martin, T. W.; Zygmunt S. D. "The name is bond—H bond." Nat. Struct. Boil. 1999, 6(5), 403-406.
- 152. Isaacs, E. D.; Shukla, A.; Platzman, P. M.; Hamann, D. R.; Barbiellini, B.; Tulk, C. A. Covalency of the hydrogen bond in ice: A direct X-ray measurement. Phys. Rev. Lett. **1999**, 82(3), 600.
- 153. Heindel, J. P.; Xantheas, S. S. The many-body expansion for aqueous systems revisited: I. Water–water interactions. J. Chem. Theory Comput. **2020**, 16(11), 6843-6855.
- 154. Heindel, J. P.; Xantheas, S. S. The many-body expansion for aqueous systems revisited: II. Alkali metal and halide ion—water interactions. J. Chem. Theory Comput. **2021**, 17(4), 2200-2216.
- 155. Herman, K. M.; Heindel, J. P.; Xantheas, S. S. The many-body expansion for aqueous systems revisited: III. Hofmeister ion—water interactions. Phys. Chem. Chem. Phys. **2021**, 23(19), 11196-11210.
- 156. Herman, K. M.; Stone, A. J.; Xantheas, S. S. A classical model for three-body interactions in aqueous ionic systems. J. Chem. Phys. **2022**, 157(2), 024101.
- 157. Jungwirth, P. Water's wafer-thin surface. Nature 2011, 474(7350), 168-169.
- 158. Jungwirth, P.; Finlayson-Pitts, B. J.; Tobias, D. J. Introduction: Structure and chemistry at aqueous interfaces. Chem. Rev. **2006**, 106(4), 1137-1139.
- 159. Shen, Y. R.; Ostroverkhov, V. Sum-frequency vibrational spectroscopy on water interfaces: polar orientation of water molecules at interfaces. Chem. Rev. **2006**, 106(4), 1140-1154.
- 160. Smolentsev, N.; Smit, W. J.; Bakker, H. J.; Roke, S. The interfacial structure of water droplets in a hydrophobic liquid. Nat. Commun. **2017**, 8(1), 1-6.
- 161. Chandler, D. Interfaces and the driving force of hydrophobic assembly. Nature **2005**, 437(7059), 640-647.
- 162. Dhopatkar, N.; Defante, A. P.; Dhinojwala, A. Ice-like water supports hydration forces and eases sliding friction. Sci. Adv. **2016**, 2(8), e1600763.
- 163. Davis, J. G.; Rankin, B. M.; Gierszal, K. P.; Ben-Amotz, D. On the cooperative formation of non-hydrogen-bonded water at molecular hydrophobic interfaces. Nat. Chem. **2013**, 5(9), 796-802.
- 164. Jungwirth, P.; Tobias, D. J. Specific ion effects at the air/water interface. Chem. Rev. **2006**, 106(4), 1259-1281.
- 165. Finlayson-Pitts, B. J.; Pitts, J. N., Jr. Chemistry of the Upper and Lower Atmosphere: Theory, Experiments and Applications; Academic Press: San Diego, CA, 2000.
- 166. Knipping, E. M.; Lakin, M. J.; Foster, K. L.; Jungwirth, P.; Tobias, D. J.; Gerber, R. B.; Dabdub, D.; Finlayson-Pitts, B. J. Experiments and simulations of ion-enhanced interfacial chemistry on aqueous NaCl aerosols. Science 2000, 288(5464), 301-306.
- 167. Levin, Y. Polarizable ions at interfaces. Phys. Rev. Lett. 2009, 102(14), 147803.
- 168. Vrbka, L.; Mucha, M.; Minofar, B.; Jungwirth, P.; Brown, E. C.; Tobias, D. J. Propensity of soft ions for the air/water interface. Curr. Opin. Colloid Interface Sci. **2004**, 9(1-2), 67-73.

- 169. Padmanabhan, V.; Daillant, J.; Belloni, L.; Mora, S.; Alba, M.; Konovalov, O. Specific ion adsorption and short-range interactions at the air aqueous solution interface. Phys. Rev. Lett. **2007**, 99(8), 086105.
- 170. Jubb, A. M.; Hua, W.; Allen, H. C. Organization of water and atmospherically relevant ions and solutes: vibrational sum frequency spectroscopy at the vapor/liquid and liquid/solid interfaces. Acc. Chem. Res. **2012**, 45(1), 110-119.
- 171. Jubb, A. M.; Hua, W.; Allen, H. C. Environmental chemistry at vapor/water interfaces: insights from vibrational sum frequency generation spectroscopy. Annu. Rev. Phys. Chem. **2012**, 63(1), 107-130.
- 172. Lund, M.; Jungwirth, P.; Woodward, C. E. Ion specific protein assembly and hydrophobic surface forces. Phys. Rev. Lett. **2008**, 100(25), 258105.
- 173. Wang, H. F.; Gan, W.; Lu, R.; Rao, Y.; Wu, B. H. Quantitative spectral and orientational analysis in surface sum frequency generation vibrational spectroscopy (SFG-VS). Int. Rev. Phys. Chem. **2005**, 24(2), 191-256.
- 174. Perakis, F.; De Marco, L.; Shalit, A.; Tang, F.; Kann, Z. R.; Kühne, T. D.; Torre, R.; Bonn, M.; Nagata, Y. Vibrational spectroscopy and dynamics of water. Chem. Rev. **2016**, 116(13), 7590-7607.
- 175. Bloembergen, N.; Pershan, P. S. Light waves at the boundary of nonlinear media. Physical review **1962**, 128(2), 606.
- 176. Du, Q.; Superfine, R.; Freysz, E.; Shen, Y. R. Vibrational spectroscopy of water at the vapor/water interface. Phys. Rev. Lett. **1993**, 70(15), 2313.
- 177. Eisenthal, K. B. Liquid interfaces probed by second-harmonic and sum-frequency spectroscopy. Chem. Rev. **1996**, 96(4), 1343-1360.
- 178. Moore, F. G.; Richmond, G. L. Integration or segregation: how do molecules behave at oil/water interfaces?. Acc. Chem. Res. **2008**, 41(6), 739-748.
- 179. Gopalakrishnan, S.; Liu, D.; Allen, H. C.; Kuo, M.; Shultz, M. J. Vibrational spectroscopic studies of aqueous interfaces: salts, acids, bases, and nanodrops. Chem. Rev. **2006**, 106(4), 1155-1175.
- 180. Tian, C. S.; Shen, Y. R. Recent progress on sum-frequency spectroscopy. Surface Science Reports **2014**, 69(2-3), 105-131.
- 181. Morita, A. Theory of sum frequency generation spectroscopy (Vol. 97). Singapore: Springer, 2018.
- 182. Nihonyanagi, S.; Mondal, J. A.; Yamaguchi, S.; Tahara, T. Structure and dynamics of interfacial water studied by heterodyne-detected vibrational sum-frequency generation. Annu. Rev. Phys. Chem. 2013, 64, 579-603.
- 183. Heydweiller, A. On physical properties of solutions in their context. II. Surface tension and electrical conductivity of aqueous salt solutions. Ann. Phys. **1910**, 338 (11), 145-185.
- 184. Jarvis, N. L.; Scheiman, M. A. Surface potentials of aqueous electrolyte solutions. J. Phys. Chem. 1968, 72(1), 74-78.

- 185. Weissenborn, P. K.; Pugh, R. J. Surface tension of aqueous solutions of electrolytes: relationship with ion hydration, oxygen solubility, and bubble coalescence. J. Colloid Interface Sci. **1996**, 184(2), 550-563.
- 186. Pegram, L. M.; Record, M. T. Hofmeister salt effects on surface tension arise from partitioning of anions and cations between bulk water and the air—water interface. J. Phys. Chem. B **2007**, 111(19), 5411-5417.
- 187. Onsager, L.; Samaras, N. N. The surface tension of Debye-Hückel electrolytes. J. Chem. Phys. **1934**, 2(8), 528-536.
- 188. Tobias, D. J.; Hemminger, J. C. Getting specific about specific ion effects. Science **2008**, 319(5867), 1197-1198.
- 189. Jungwirth, P.; Tobias, D. J. Molecular structure of salt solutions: A new view of the interface with implications for heterogeneous atmospheric chemistry. J. Phys. Chem. B **2001**, 105(43), 10468-10472.
- 190. Liu, D.; Ma, G.; Levering, L. M.; Allen, H. C. Vibrational spectroscopy of aqueous sodium halide solutions and air-liquid interfaces: Observation of increased interfacial depth. J. Phys. Chem. B **2004**, 108(7), 2252-2260.
- 191. Raymond, E. A.; Richmond, G. L. Probing the molecular structure and bonding of the surface of aqueous salt solutions. J. Phys. Chem. B **2004**, 108(16), 5051-5059.
- 192. Tian, C.; Byrnes, S. J.; Han, H. L.; Shen, Y. R. Surface propensities of atmospherically relevant ions in salt solutions revealed by phase-sensitive sum frequency vibrational spectroscopy. J. Phys. Chem. Lett. **2011**, 2(15), 1946-1949.
- 193. Piatkowski, L.; Zhang, Z.; Backus, E. H.; Bakker, H. J.; Bonn, M. Extreme surface propensity of halide ions in water. Nat. Commun. **2014**, 5(1), 1-7.
- 194. Hua, W.; Verreault, D. Allen, H. C. Surface prevalence of perchlorate anions at the air/aqueous interface. J. Phys. Chem. Lett. **2013**, 4(24), 4231-4236.
- 195. Viswanath, P.; Motschmann, H. Oriented thiocyanate anions at the air— electrolyte interface and its implications on interfacial water-a vibrational sum frequency spectroscopy study. J. Phys. Chem. C **2007**, 111(12), 4484-4486.
- 196. Viswanath, P., Motschmann, H. Effect of interfacial presence of oriented thiocyanate on water structure. J. Phys. Chem. C **2008**, 112(6), 2099-2103.
- 197. Miller, Y.; Thomas, J. L.; Kemp, D. D.; Finlayson-Pitts, B. J.; Gordon, M. S.; Tobias, D. J.; Gerber, R. B. Structure of large nitrate— water clusters at ambient temperatures: simulations with effective fragment potentials and force fields with implications for atmospheric chemistry. J. Phys. Chem. A 2009, 113(46), 12805-12814.
- 198. Dang, L. X.; Chang, T. M.; Roeselova, M.; Garrett, B. C.; Tobias, D. J. On NO₃-H₂ O interactions in aqueous solutions and at interfaces. J. Chem. Phys. **2006**, 124(6), 066101.

- 199. Feng, R. R.; Guo, Y.; Wang, H. F. Reorientation of the "free OH" group in the top-most layer of air/water interface of sodium fluoride aqueous solution probed with sum-frequency generation vibrational spectroscopy. J. Chem. Phys. **2014**, 141(18), 18C507.
- 200. Imamura, T.; Mizukoshi, Y.; Ishiyama, T.; Morita, A. Surface structures of NaF and Na2SO4 aqueous solutions: Specific effects of hard ions on surface vibrational spectra. J. Phys. Chem. C 2012, 116(20), 11082-11090.
- 201. Roy, S.; Mondal, J. A. Kosmotropic Electrolyte (Na₂CO₃, NaF) Perturbs the Air/Water Interface through Anion Hydration Shell without Forming a Well-Defined Electric Double Layer. J. Phys. Chem. B 2021, 125(16), 3977-3985.
- 202. Hua, W.; Jubb, A. M.; Allen, H. C. Electric field reversal of Na₂SO₄,(NH₄) ₂SO₄, and Na₂CO₃ relative to CaCl₂ and NaCl at the air/aqueous interface revealed by heterodyne detected phase-sensitive sum frequency. J. Phys. Chem. Lett. **2011**, 2(20), 2515-2520.
- 203. Tarbuck, T. L.; Richmond, G. L. Adsorption and Reaction of CO2 and SO2 at a Water Surface. J. Am. Chem. Soc. **2006**, 128(10), 3256-3267.
- 204. Deiseroth, M.; Bonn, M.; Backus, E. H. G. Electrolytes Change the Interfacial Water Structure but Not the Vibrational Dynamics. J. Phys. Chem. B **2019**, 123, 8610–8616.
- 205. Nihonyanagi, S.; Yamaguchi, S.; Tahara, T. Counterion effect on interfacial water at charged interfaces and its relevance to the Hofmeister series. J. Am. Chem. Soc. **2014**, 136(17), 6155-6158.
- 206. Sung, W.; Avazbaeva, Z.; Kim, D. Salt promotes protonation of amine groups at air/water interface. J. Phys. Chem. Lett. **2017**, 8(15), 3601-3606.
- 207. Lovering, K.; Nayak, S.; Bu, W.; Uysal, A. The Role of Specific Ion Effects in Ion Transport: The Case of Nitrate and Thiocyanate. J. Phys. Chem. C **2020**, 124(1), 573-581.
- 208. Verma, G.; Singh, K. P. Time-resolved interference unveils nanoscale surface dynamics in evaporating sessile droplet. Appl. Phys. Lett. **2014**, 104(24), 244106.
- Verma, G.; Singh, K. P. Universal long-range nanometric bending of water by light. Phys. Rev. Lett.
 2015, 115(14), 143902.
- 210. Inoue, N.; Todo, H.; Iidaka, D.; Tokudome, Y.; Hashimoto, F.; Kishino, T.; Sugibayashi, K. Possibility and effectiveness of drug delivery to skin by needle-free injector. Int. J. Pharm. **2010**, 391, 65-72.
- 211. Berrospe-Rodriguez, Visser, C.W.; Schlautmann, S.; Ramos-Garcia, R.; Fernandez Rivas, D. Continuous-wave laser generated jets for needle free applications. Biomicrofluidics **2016**, 10, 014104.
- 212. Krizek, J.; Delrot, P.; Moser, C. Repetitive regime of highly focused liquid microjets for needle-free injection. Sci. Rep. **2020**, 10,1-9.
- 213. Park, M.A.; Jang, H.J.; Sirotkin, F.V.; Yoh, J.J. Er: YAG laser pulse for small-dose splashback-free microjet transdermal drug delivery. Opt. Lett. **2012**, 37, 3894-3896.

- 214. Park, G.; Modak, A.; Hogan, N.C.; Hunter, I.W. The effect of jet shape on jet injection. In 2015 37th Annual International Conference of the IEEE Engineering in Medicine and Biology Society (EMBC) 2015, 7350-7353.
- 215. Kiyama, A.; Endo, N.; Kawamoto, S.; Katsuta, C.; Oida, K.; Tanaka, A.; Tagawa, Y. Visualization of penetration of a high-speed focused microjet into gel and animal skin. J. Vis. **2019**, 22, 449-457.
- 216. Tagawa, Y.; Oudalov, N.; Visser, C.W.; Peters, I.R.; van der Meer, D.; Sun, C.; Prosperetti, A.; Lohse, D. Highly focused supersonic microjets. Phys. Rev. X 2012, 2, 031002.
- 217. Peters, I.R.; Tagawa, Y.; Oudalov, N.; Sun, C.; Prosperetti, A.; Lohse, D.; van der Meer, D. Highly focused supersonic microjets: numerical simulations. J. Fluid Mech. 2013, 719, 587-605.
- 218. Krizek, J.; Lavickova, B.; Moser, C. Degradation study on molecules released from laser-based jet injector. Int. J. Pharm. **2021**, 602,120664.
- Schramm-Baxter, J.; Mitragotri, S. Needle-free jet injections: dependence of jet penetration and dispersion in the skin on jet power. J. Controlled Rel. 2004, 97, 527–535.
- Schoppink, J.; Rivas, D. F. Jet injectors: Perspectives for small volume delivery with lasers. Adv. Drug Deliv. Rev. 2022, 114109.
- 221. McKeage, J. W.; Ruddy, B. P.; Nielsen, P. M.; Taberner, A. J. The effect of jet speed on large volume jet injection. J. Control. Release **2018**, 280, 51-57.
- Moradiafrapoli, M.; Marston, J. O. High-speed video investigation of jet dynamics from narrow orifices for needle-free injection. Chem. Eng. Res. Des. 2017, 117, 110-121.
- 223. Arora, A.; Hakim, I.; Baxter, J.; Rathnasingham, R.; Srinivasan, R.; Fletcher, D. A.; Mitragotri, S. Needle-free delivery of macromolecules across the skin by nanoliter-volume pulsed microjets. Proc. Natl. Acad. Sci. 2007, 104, 4255-4260.
- 224. Stachowiak, J. C.; von Muhlen, M. G.; Li, T. H.; Jalilian, L.; Parekh, S. H.; Fletcher, D. A. Piezoelectric control of needle-free transdermal drug delivery. J. Control. Release **2007**, 124, 88-97.
- 225. Cu, K.; Bansal, R.; Mitragotri, S.; Fernandez Rivas, D. Delivery strategies for skin: comparison of nanoliter jets, needles and topical solutions. Ann. Biomed. Eng. **2020**, 48, 2028-2039.
- 226. Miyazaki, H.; Atobe, S.; Suzuki, T.; Iga, H.; Terai, K.Development of pyro-drive jet injector with controllable jet pressure. J. Pharma. Sci. **2019**, 108, 2415-2420.
- 227. Boyd, R. W. Nonlinear optics; Academic press, 2020.
- 228. Shen, Y. R. Fundamentals of sum-frequency spectroscopy; Cambridge University Press, 2016.
- 229. Lambert, A. G.; Davies, P. B.; Neivandt, D. J. Implementing the theory of sum frequency generation vibrational spectroscopy: a tutorial review. Appl. Spectrosc. Rev. **2005**, 40(2), 103-145.

- 230. Hirose, C.; Akamatsu, N.; Domen, K. Formulas for the analysis of surface sum-frequency generation spectrum by CH stretching modes of methyl and methylene groups. J. Chem. Phys. **1992**, 96(2), 997-1004.
- 231. Bain, C. D. Sum-frequency vibrational spectroscopy of the solid/liquid interface. J. Chem. Soc., Faraday Trans. 1995, 91(9), 1281-1296.
- 232. Backus, E. H.; Schaefer, J.; Bonn, M. Probing the mineral-water interface with nonlinear optical spectroscopy. Angew. Chem. Int. Ed. **2021**, 60(19), 10482-10501.
- 233. Lu, X.; Zhang, C.; Ulrich, N.; Xiao, M.; Ma, Y. H.; Chen, Z. Studying polymer surfaces and interfaces with sum frequency generation vibrational spectroscopy. Anal. Chem. **2017**, 89(1), 466-489.
- 234. Jena, K. C.; Hore, D. K. Variation of ionic strength reveals the interfacial water structure at a charged mineral surface. J. Phys. Chem. C **2009**, 113(34), 15364-15372.
- 235. Scheu, R.; Rankin, B. M.; Chen, Y.; Jena, K. C.; Ben-Amotz, D.; Roke, S. Charge asymmetry at aqueous hydrophobic interfaces and hydration shells. Angew. Chem. **2014**, 126(36), 9714-9717.
- 236. Jena, K. C.; Covert, P. A.; Hore, D. K. The effect of salt on the water structure at a charged solid surface: Differentiating second-and third-order nonlinear contributions. J. Phys. Chem. Lett. **2011**, 2(9), 1056-1061.
- 237. Jena, K. C.; Hung, K. K.; Schwantje, T. R.; Hore, D. K. Methyl groups at dielectric and metal surfaces studied by sum-frequency generation in co-and counter-propagating configurations. J. Chem. Phys. **2011**, 135(4), 044704.
- 238. Kaur, H.; Tomar, D.; Kaur, H.; Rana, B.; Chaudhary, S.; Jena, K. C. Sum-frequency generation vibrational spectroscopy: A nonlinear optical tool to probe the polymer interfaces. *In Advances in Spectroscopy: Molecules to Materials*; Springer, Singapore, 2019; pp. 39-55.
- 239. Tomar, D.; Rana, B.; Jena, K. C. The structure of water–DMF binary mixtures probed by linear and nonlinear vibrational spectroscopy. J. Chem. Phys. **2020**, 152(11), 114707.
- 240. Chaudhary, S.; Kaur, H.; Kaur, H.; Rana, B.; Tomar, D.; Jena, K. C. Probing the Bovine Hemoglobin Adsorption Process and its Influence on Interfacial Water Structure at the Air–Water Interface. Appl. Spectrosc. **2021**, 75(12), 1497-1509.
- 241. Kaur, H.; Verma, M.; Kaur, S.; Rana, B.; Singh, N.; Jena, K. C. Elucidating the Molecular Structure of Hydrophobically Modified Polyethylenimine Nanoparticles and Its Potential Implications for DNA Binding. Langmuir **2022**, 38(44), 13456-13468.
- 242. Zhuang, X.; Miranda, P. B.; Kim, D.; Shen, Y. R. Mapping molecular orientation and conformation at interfaces by surface nonlinear optics. Phys. Rev. B **1999**, 59(19), 12632.
- 243. Backus, E. H.; Garcia-Araez, N.; Bonn, M.; Bakker, H. J. On the role of Fresnel factors in sum-frequency generation spectroscopy of metal-water and metal-oxide-water interfaces. J. Phys. Chem. C **2012**, 116(44), 23351-23361.

- 244. Humbert, C.; Noblet, T.; Dalstein, L.; Busson, B.; Barbillon, G. Sum-frequency generation spectroscopy of plasmonic nanomaterials: A review. Materials **2019**, 12(5), 836.
- Fu, L.; Wang, Z.; Yan, E. C. Chiral vibrational structures of proteins at interfaces probed by sum frequency generation spectroscopy. Int. J. Mol. Sci. 2011, 12(12), 9404-9425.
- 246. Hsieh, C. S.; Okuno, M.; Hunger, J.; Backus, E. H.; Nagata, Y.; Bonn, M. Aqueous Heterogeneity at the Air/Water Interface Revealed by 2D-HD-SFG Spectroscopy. Angew. Chem. Int. Ed. 2014, 53(31), 8146-8149.
- 247. Hosseinpour, S.; Roeters, S. J.; Bonn, M.; Peukert, W.; Woutersen, S.; Weidner, T. Structure and dynamics of interfacial peptides and proteins from vibrational sum-frequency generation spectroscopy. Chem. Rev. 2020, 120(7), 3420-3465.
- 248. Azam, M. S.; Cai, C.; Gibbs, J. M.; Tyrode, E.; Hore, D. K. Silica surface charge enhancement at elevated temperatures revealed by interfacial water signals. J. Am. Chem. Soc. **2020**, 142(2), 669-673.
- 249. Ahmed, M.; Nihonyanagi, S.; Tahara, T. Ultrafast vibrational dynamics of the free OD at the air/water interface: Negligible isotopic dilution effect but large isotope substitution effect. J. Chem. Phys. **2022**.
- 250. Dutta, C.; Benderskii, A. V. On the assignment of the vibrational spectrum of the water bend at the air/water interface. J. Phys. Chem. Lett. 2017, 8(4), 801-804.
- 251. Sun, S.; Tang, F.; Imoto, S.; Moberg, D. R.; Ohto, T.; Paesani, F.; Bonn. M.; Backus, E. H. G.; Nagata, Y. Orientational distribution of free OH groups of interfacial water is exponential. Phys. Rev. Lett. 2018, 121(24), 246101.
- 252. Downing, H. D.; Williams, D. Optical constants of water in the infrared. J. Geophys. Res. **1975**, 80(12), 1656-1661.
- Wei, X.; Shen, Y. R. Motional effect in surface sum-frequency vibrational spectroscopy. Phys. Rev. Lett. 2001, 86(21), 4799.
- 254. Gan, W.; Wu, D.; Zhang, Z.; Feng, R. R.; Wang, H. F. Polarization and experimental configuration analyses of sum frequency generation vibrational spectra, structure, and orientational motion of the air/water interface. J. Chem. Phys. 2006, 124(11), 114705.
- 255. Boily, J. F.; Fu, L.; Tuladhar, A.; Lu, Z.; Legg, B. A.; Wang, Z. M.; Wang, H. Hydrogen bonding and molecular orientations across thin water films on sapphire. J. Colloid Interface Sci. 2019, 555, 810-817.
- 256. Lu, R.; Gan, W.; Wu, B. H.; Chen, H.; Wang, H. F. Vibrational polarization spectroscopy of CH stretching modes of the methylene group at the vapor/liquid interfaces with sum frequency generation. J. Phys. Chem. B 2004, 108(22), 7297-7306.
- 257. Borodko, Y; Habas, S. E.; Koebel, M.; Yang, P.; Frei, H.; Somorjai, G. A. Probing the Interaction of Poly (vinylpyrrolidone) with Platinum Nanocrystals by UV- Raman and FTIR. J. Phys. Chem. B **2006**, 110(46), 23052-23059.

- 258. Bertie, J. E.; Ahmed, M. K.; Eysel, H. H. Infrared intensities of liquids. 5. Optical and dielectric constants, integrated intensities, and dipole moment derivatives of water and water-d2 at 22. degree. C. J. Phys. Chem. 1989, 93(6), 2210-2218.
- 259. Barrow, R. E.; Hills, B. A. A critical assessment of the Wilhelmy method in studying lung surfactants. J. Physiol. **1979**, 295(1), 217-227.
- 260. Tomar, D.; Kaur, H.; Kaur, H.; Rana, B.; Talegaonkar, K.; Maharana, V.; Jena, K.C. ATR-FTIR Spectroscopy and Its Relevance to Probe the Molecular level Interactions Between Amino Acids and Metal-Oxide Nanoparticles at Solid/Aqueous Interface. *In Advances in Spectroscopy: Molecules to Materials*; Springer, Singapore, 2019; pp 3-21.
- 261. Kaur, H.; Rana, B.; Tomar, D.; Kaur, S.; Jena, K.C. Fundamentals of ATR-FTIR Spectroscopy and Its Role for Probing In-Situ Molecular level Interactions. *In Modern Techniques of Spectroscopy*; Springer, Singapore, 221; pp 3-37.
- 262. M. Milosevic. Internal reflection and ATR spectroscopy, Vol. 262; John Wiley and Sons, USA, 2012.
- 263. Li, Y.; Diddens, C.; Segers, T.; Wijshoff, H.; Versluis, M.; Lohse, D. Evaporating droplets on oil-wetted surfaces: Suppression of the coffee-stain effect. Proc. Natl. Acad. Sci. 2020, 117 (29), 16756-16763.
- 264. Jing, J.; Reed, J.; Huang, J.; Hu, X.; Clarke, V.; Edington, J.; Housman, D.; Anantharaman, T. S.; Huff, E. J.; Porter, B.; Shenker, A.; Wolfson, E.; Hiort, C.; Kantor, R.; Aston, C.; Schwartz, D. C. Automated high resolution optical mapping using arrayed, fluid-fixed DNA molecules. Proc. Natl. Acad. Sci. 1998, 95(14), 8046-8051.
- 265. Squyres, S. W., Grotzinger, J. P., Arvidson, R. E., Bell III, J. F., Calvin, W., Christensen, P. R.; Clark, B. C.; Crisp, J. A.; Farrand, W. H.; Herkenhoff, K. E.; Johnson, J. R.; Klingelho fer, G.; Knoll, A. H.; Mclennan, S. M.; Mcsween Jr., H. Y.; Morris, R. V.; Rice Jr., J. W.; Rieder, R.; Soderblom, L. A. In situ evidence for an ancient aqueous environment at Meridiani Planum, Mars. Science 2004, 306 (5702), 1709-1714.
- 266. Wang, X.; Zhang, M.; Schubert, D. W.; Liu, X. Oil-Water Separation Polypropylene Foam with Advanced Solvent-Evaporation Induced Coexistence of Microspheres and Microporous Structure. Macromol. Rapid Commun. 2022, 2200177.
- 267. Tao, P.; Ni, G.; Song, C.; Shang, W.; Wu, J.; Zhu, J.; Chen. G.; Deng, T. Solar-driven interfacial evaporation. Nat. Energy **2018**, 3(12), 1031-1041.
- 268. Brutin, D.; Sobac, B.; Loquet, B.; Sampol, J. Pattern formation in drying drops of blood. J. of fluid Mech. 2011, 667, 85-95.
- 269. Rosenfeld, D.; Lohmann, U.; Raga, G. B.; O'Dowd, C. D.; Kulmala, M.; Fuzzi, S.; Reissell, A.; Andreae, M. O. Flood or drought: how do aerosols affect precipitation?. Science, **2008**, 321(5894), 1309-1313.

- 270. Rosenfeld, D. Suppression of rain and snow by urban and industrial air pollution. Science **2000**, 287(5459), 1793-1796.
- Clement, A. C.; Burgman, R.; Norris, J. R. Observational and model evidence for positive low-level cloud feedback. Science 2009, 325(5939), 460-464.
- 272. Ji, N.; Ostroverkhov, V.; Tian, C. S.; Shen, Y. R. Characterization of vibrational resonances of water-vapor interfaces by phase-sensitive sum-frequency spectroscopy. Phys. Rev. Lett. 2008, 100(9), 096102.
- 273. Pahlavan, A. A.; Yang, L.; Bain, C. D.; Stone, H. A. Evaporation of Binary-Mixture Liquid Droplets: The Formation of Picoliter Pancakelike Shapes. Phys. Rev. Lett. **2021**, 127(2), 024501.
- 274. Li, Y.; Diddens, C.; Lv, P.; Wijshoff, H.; Versluis, M.; Lohse, D. Gravitational effect in evaporating binary microdroplets. Phys. Rev. Lett. **2019**, 122(11), 114501.
- 275. Jaiswal, V.; Dwivedi, R. K.; Harikrishnan, A. R.; Dhar, P. Magnetohydrodynamics-and magnetosolutal-transport-mediated evaporation dynamics in paramagnetic pendant droplets under field stimulus. Phys. Rev. E **2018**, 98(1), 013109.
- 276. Edwards, A. M. J.; Atkinson, P. S.; Cheung, C. S.; Liang, H.; Fairhurst, D. J.; Ouali, F. F. Density-driven flows in evaporating binary liquid droplets. Phys. Rev. Lett. **2018**, 121(18), 184501.
- 277. Varilly, P.; Chandler, D. Water evaporation: A transition path sampling study. J. Phys. Chem. B **2013**, 117(5), 1419-1428.
- 278. Mason, P. E. Molecular dynamics study on the microscopic details of the evaporation of water. J. Phys. Chem. A **2011**, 115(23), 6054-6058.
- 279. Nagata, Y.; Usui, K.; Bonn, M. Molecular mechanism of water evaporation. Phys. Rev. Lett. 2015, 115(23), 236102.
- 280. Musolino, N.; Trout, B. L. Insight into the molecular mechanism of water evaporation via the finite temperature string method. J. Chem. Phys. **2013**, 138(13), 134707.
- 281. Mondal, J. A.; Nihonyanagi, S.; Yamaguchi, S.; Tahara, T. Three distinct water structures at a zwitterionic lipid/water interface revealed by heterodyne-detected vibrational sum frequency generation. J. Am. Chem. Soc. **2012**, 134(18), 7842-7850.
- 282. Tyrode, E.; Johnson, C. M.; Kumpulainen, A.; Rutland, M. W.; Claesson, P. M. Hydration state of nonionic surfactant monolayers at the liquid/vapor interface: Structure determination by vibrational sum frequency spectroscopy. J. Am. Chem. Soc. **2005**, 127(48), 16848-16859.
- 283. Walker, D. S.; Hore, D. K.; Richmond, G. L. Understanding the population, coordination, and orientation of water species contributing to the nonlinear optical spectroscopy of the vapor—water interface through molecular dynamics simulations. J. of Phys. Chem. B **2006**, 110(41), 20451-20459.

- 284. Sovago, M.; Campen, R. K.; Wurpel, G. W.; Müller, M.; Bakker, H. J.; Bonn, M. Vibrational response of hydrogen-bonded interfacial water is dominated by intramolecular coupling. Phys. Rev. Lett. **2008**, 100(17), 173901.
- 285. Mondal, J. A.; Nihonyanagi, S.; Yamaguchi, S.; Tahara, T. Structure and orientation of water at charged lipid monolayer/water interfaces probed by heterodyne-detected vibrational sum frequency generation spectroscopy. J. Am. Chem. Soc. **2010**, 132(31), 10656-10657.
- 286. Schaefer, J.; Backus, E. H.; Nagata, Y.; Bonn, M. Both inter-and intramolecular coupling of O–H groups determine the vibrational response of the water/air interface. J. Phys. Chem. Lett. **2016**, 7(22), 4591-4595.
- 287. Suzuki, Y.; Nojima, Y.; Yamaguchi, S. Vibrational coupling at the topmost surface of water revealed by heterodyne-detected sum frequency generation spectroscopy. J. Phys. Chem. Lett. **2017**, 8(7), 1396-1401.
- 288. Rogers, M. M.; Neal, J. F.; Saha, A.; Algarni, A. S.; Hill, T. C., Allen, H. C. The Ocean's Elevator: Evolution of the Air–Seawater Interface during a Small-Scale Algal Bloom. ACS Earth Space Chem. **2020**, 4(12), 2347-2357.
- 289. Strazdaite, S.; Versluis, J.; Backus, E. H.; Bakker, H. J. Enhanced ordering of water at hydrophobic surfaces. J. Chem. Phys. **2014**, 140(5), 054711.
- 290. Dalchand, N.; Dogangun, M.; Ohno, P. E.; Ma, E.; Martinson, A. B.; Geiger, F. M. Perturbation of hydrogen-bonding networks over supported lipid bilayers by poly (allylamine hydrochloride). J. Phys. Chem. B 2019, 123(19), 4251-4257.
- 291. Ishiyama, T.; Morita, A. Nuclear quantum effect on the χ (2) band shape of vibrational sum frequency generation spectra of normal and deuterated water surfaces. J. Phys. Chem. Lett. **2019**, 10(17), 5070-5075.
- 292. Parsons, D. F.; Boström, M.; Nostro, P. L.; Ninham, B. W. Hofmeister effects: interplay of hydration, nonelectrostatic potentials, and ion size. Phys. Chem. Chem. Phys. **2011**, 13(27), 12352-12367.
- 293. Gan, W.; Feng, R. R.; Wang, H. F. Comment on "Orientational Distribution of Free O- H Groups of Interfacial Water is Exponential". Phys. Rev. Lett. **2019**, 123(9), 099601.
- Sun, S.; Tang, F.; Imoto, S.; Moberg, D. R.; Ohto, T.; Paesani, F.; Bonn, M.; Backus, E. H. G.; Nagata,
 Y. Sun et al. Reply. Phys. Rev. Lett. 2019, 123(9), 099602.
- 295. Luzar, A.; Chandler, D. Hydrogen-bond kinetics in liquid water. Nature 1996, 379(6560), 55-57.
- 296. Liu, G.; Xu, S.; Liu, Y.; Gao, Y.; Tong, T.; Qi, Y.; Zhang, C. Flexible drug release device powered by triboelectric nanogenerator. Adv. Funct. Mater. **2020**, 30(12), 1909886.
- 297. Chen, W. H.; Liao, W. C.; Sohn, Y. S.; Fadeev, M.; Cecconello, A.; Nechushtai, R.; Willner, I. Stimuli-responsive nucleic acid-based polyacrylamide hydrogel-coated metal—organic framework nanoparticles for controlled drug release. Adv. Funct. Mater. 2018, 28(8), 1705137.

- 298. Mishra, V.; Jung, S. H.; Park, J. M.; Jeong, H. M.; Lee, H. I. Triazole-containing hydrogels for time-dependent sustained drug release. Macromol. Rapid Commun. **2014**, 35(4), 442-446.
- 299. Moreno-Villoslada, I.; Fuenzalida, J. P.; Tripailaf, G.; Araya-Hermosilla, R.; Pizarro, G. D. C.; Marambio, O. G.; Nishide, H. Comparative Study of the Self-Aggregation of Rhodamine 6G in the Presence of Poly (sodium 4-styrenesulfonate), Poly (N-phenylmaleimide-co-acrylic acid), Poly (styrene-alt-maleic acid), and Poly (sodium acrylate). J. Phys. Chem. B 2010, 114, 11983-11992.
- 300. Rembert, K. B.; Paterová, J.; Heyda, J.; Hilty, C.; Jungwirth, P.; Cremer, P. S. Molecular mechanisms of ion-specific effects on proteins. J. Am. Chem. Soc. **2012**, 134(24), 10039-10046.
- Boström, M.; Williams, D. R. M.; Ninham, B. W. Specific ion effects: why DLVO theory fails for biology and colloid systems. Phys. Rev. Lett. 2001, 87(16), 168103.
- 302. Dos Santos, A. P.; Levin, Y. Ion specificity and the theory of stability of colloidal suspensions. Phys. Rev. Lett. **2011**, 106(16), 167801.
- 303. Fernández, A.; Scheraga, H. A. Insufficiently dehydrated hydrogen bonds as determinants of protein interactions. Proc. Natl. Acad. Sci. **2003**, 100(1), 113-118.
- 304. Brovchenko, I.; Oleinikova, A. Which properties of a spanning network of hydration water enable biological functions?. ChemPhysChem **2008**, 9(18), 2695-2702.
- 305. Willow, S. Y.; Xantheas, S. S. Molecular level insight of the effect of Hofmeister anions on the interfacial surface tension of a model protein. J. Phys. Chem. Lett. **2017**, 8(7), 1574-1577.
- 306. Lakshmanan, M.; Dhathathreyan, A.; Miller, R. Synergy between Hofmeister effect and coupled water in proteins: unusual dilational moduli of BSA at air/solution interface. Colloids Surf. A: Physicochem. Eng. Asp. 2008, 324(1-3), 194-201.
- 307. Tyrode, E.; Corkery, R. Charging of carboxylic acid monolayers with monovalent ions at low ionic strengths: molecular insight revealed by vibrational sum frequency spectroscopy. J. Phys. Chem. C **2018**, 122(50), 28775-28786.
- 308. Jang, J. H.; Jacob, J.; Santos, G.; Lee, T. R.; Baldelli, S. Image contrast in sum frequency generation microscopy based on monolayer order and coverage. J. Phys. Chem. C **2013**, 117(29), 15192-15202.

APPENDIX A

SUPPORTING INFORMATION FOR CHAPTER 3

Table A1 Fitting parameters of SFG spectra at air/aqueous interface carrying 1M salt solutions as recorded in OH-stretch region (3000 cm⁻¹-3800 cm⁻¹) in ssp-polarization scheme (figure 3.3 (b-d)).

Sr.	System	$\left \chi_{NR}^{(2)}\right $	ω_v	$ A_v $	$\Gamma_{\!\scriptscriptstyle \mathcal{V}}$
No.		(a. u.)	(cm ⁻¹)	(a. u.)	(cm ⁻¹)
1.	Water	0.01	3230	0.60	95
			3445	2.83	120
			3555	0.06	90
			3704	0.96	20
2.	Na ₂ HPO ₄	0.01	3185	0.70	95
			3445	0.85	120
			3555	0.76	90
			3704	0.79	20
3.	Na ₂ SO ₄	0.02	3230	0.64	95
			3445	2.02	120
			3555	0.94	90
			3704	0.91	20
4.	Na ₂ CO ₃	0.02	3230	0.68	95
			3445	1.65	120
			3555	1.04	90
			3704	0.98	20
5.	NaCl	0.01	3230	0.37	95
			3440	2.36	120
			3555	0.31	90

			3704	0.96	20
6.	NaNO ₃	0.01	3230	0.20	90
			3440	2.70	120
			3555	0.10	90
			3704	1.03	20
7.	NaI	0.01	3230	0.20	90
			3440	3.55	120
			3555	0.11	90
			3705	1.10	20

Table A2 Fitting parameters of SFG spectra at air/aqueous interface carrying 1M sodium salt solutions as recorded in Free OH-region (3660-3750) cm⁻¹in ssp-and ppp-polarization scheme (figure 3.4).

$$\Gamma_v = 17 \pm 3 \text{ cm}^{-1}, \, \omega_v = 3704 \text{ cm}^{-1}$$

Sr. No.	System	S	sp	p	рр
		$ \chi_{\mathrm{NR}}^{(2)} $	$ A_{\rm v}/\Gamma_{ m v} $	$\left \chi_{\mathrm{NR}}^{(2)}\right $	$ A_v/\Gamma_v $
1.	Water	0.05	1	0.05	0.84
2.	Na ₂ HPO ₄	0.05	1	0.02	0.43
3.	Na ₂ SO ₄	0.05	1	0.09	0.75
4.	Na ₂ CO ₃	0.05	1	0.05	0.81
5.	NaCl	0.05	1	0.09	0.86
6.	NaNO ₃	0.05	1	0.09	0.86
7.	NaI	0.05	1	0.05	0.89

Table A3 Free OH peak (3704 cm⁻¹) ratio, $\left|\chi_{ssp}^{(2),eff}/\chi_{ppp}^{(2),eff}\right|$ as estimated from fitted $|A_v/\Gamma_v|$, table A2 for ssp and ppp SFG spectra for 1M sodium salt solutions at the air/aqueous interface (figure 3.4) and the resultant ion-specific orientation angle (θ).

Sr. No.	System	$\left \chi_{ssp}^{(2),eff}\right $	$\left \chi_{ppp}^{(2),eff}\right $	$\left \chi_{ssp}^{(2),eff}/\chi_{ppp}^{(2),eff}\right $	Orientation Angles θ (°)
1.	Water	1	0.84	1.19	37.6
2.	Na ₂ HPO ₄	1	0.43	2.33	48.4
3.	Na ₂ SO ₄	1	0.75	1.33	39.8
4.	Na ₂ CO ₃	1	0.81	1.23	38.3
5.	NaCl	1	0.86	1.17	37.3
6.	NaNO ₃	1	0.86	1.16	37.1
7.	NaI	1	0.89	1.13	36.2

APPENDIX B

SUPPORTING INFORMATION FOR CHAPTER 5

Table B1 Fitting parameters of CH-region SFG spectra at air/PVP-water interface as probed in ssp and ppp-polarization schemes (figure 5.1 c and d).

PVP (0.05wt %)		$ \chi_{NR} $ (a.u.)	ω_v (cm ⁻¹)	t-CH 2863±1	r- CH ₂ (ss) 2886±2	r- CH ₂ (ss) 2903±1	CH ₂ (ss) 2924±2	r- CH ₂ (as) 2956±2	CH ₂ (as) 2984±2
ssp	$ A_v $ (a.u.) (Γ_v) (cm ⁻¹)	0.02		0.42 (11)	0.38 (14)	0.27 (10)	0.32 (9)	0.24 (20)	0.01 (7)
ppp		0.02		0.06 (11)	0.04 (8)	0.03 (14)	0.34 (9)	0.25 (14)	0.34 (10)

Table B2 Fitting parameters of OH-region SFG spectra at air/water and air/PVP-water interface as probed in ssp and ppp-polarization schemes (figure 5.1 e and f).

	System	$ \chi_{NR} $ (a. u.)	$\omega_V \text{ (cm}^{-1})$ $\Gamma_V \text{ (cm}^{-1})$	3240±5 96	3440±5 120	3540±10 90	3705±3 19
ssp	water	0.02		0.89	3.22	0.71	1.12
	PVP	0.01		0.23	5.06	0.79	0.54
A _V (a. u.)							
	water	0.02		0.33	1.19	1.17	0.92
ppp	PVP	0.02		0.32	0.79	1.07	0.19

Table B3 Fitting parameters of OH-region ssp-SFG spectra at air/PVP- H_2O interface in the presence of series of 1M sodium salts (figure 5.2a).

ssp	System	$ \chi_{NR} $ (a.u.)	$\omega_V \text{ (cm}^{-1})$ $\Gamma_V \text{ (cm}^{-1})$	3240±10 96	3440±10 120	3540±10 90	3705±3 19
	0.05 wt% PVP	0.01		0.23	5.06	0.79	0.54
	Na_2SO_4	0.01		0.85	4.74	0.52	0.59
A _V (a. u.)	NaCl	0.01		0.29	5.26	0.34	0.62
(a. u.)	NaNO ₃	0.01		0.95	5.62	0.52	0.55
	NaBr	0.01		0.46	5.89	0.11	0.59
	NaClO ₄	0.01		3.46	6.69	0.82	0.29
	NaSCN	0.01		3.01	8.52	0.41	0.42

Table B4 Fitting parameters of CH-region ssp-SFG spectra at air/PVP-water interface in the presence of series of 1M sodium salts (figure 5.3a).

ssp	System	$ \chi_{NR} $ (a.u.)	ω_V (cm ⁻¹)	t-CH 2862±2	r-CH ₂ (ss) 2886±2	r-CH ₂ (ss) 2903±1	CH ₂ (ss) 2924±2	r-CH ₂ (as) 2956±2	CH ₂ (as) 2984±4
			Γ_V (cm ⁻¹)	11	14	10	9	12	14
	0.05 wt% PVP	0.21		7.47	6.11	3.59	4.21	0.99	2.17
	Na ₂ SO ₄	0.21		7.26	5.67	3.80	4.38	1.50	2.07
A _V (a. u.)	NaCl	0.21		5.61	6.27	3.39	4.71	0.53	3.98
(u. u.)	NaNO ₃	0.07		9.60	5.27	4.09	3.33	1.16	8.00
	NaBr	0.26		4.85	6.47	3.63	4.69	2.70	6.00
	NaClO ₄	0.48		10.00	6.44	5.06	7.49	2.32	8.00
	NaSCN	0.39		10.00	6.12	4.32	5.29	1.15	8.00

Table B5 Fitting parameters of CH-region ssp-SFG spectra at the air/PVP- D_2O interface in the presence of series of 1M sodium salts (figure 5.3b).

		$ \chi_{NR} $	ω_V	t-CH	r-	r-	CH ₂ (ss)	r-	CH ₂ (as)
ssp	System	(a.u.)	(cm ⁻¹)	2863 ± 1	$CH_2(ss)$	$CH_2(ss)$	2924 ± 2	CH ₂ (as)	2984 ± 2
			$\Gamma_{\!V}$	11	2886 ± 2	2903±1	9	2956 ± 2	7
			(cm ⁻¹)		14	10		20	
	0.05 wt%	0.29		5.89	5.27	3.43	4.89	1.61	2.04
	PVP								
	Na_2SO_4	0.29		5.57	5.36	3.68	5.33	2.36	2.07
$ A_V $	NaCl	0.29		5.64	5.15	3.17	4.80	1.12	0.10
(a. u.)									
	NaNO ₃	0.29		5.72	5.41	3.51	4.38	1.59	1.80
		0.00		. = 0	4.50	2.52	4.0.5	0.45	2.27
	NaBr	0.29		6.70	4.52	3.72	4.26	0.47	2.25
	NaClO ₄	0.21		6.70	5.94	3.79	4.80	1.13	0.01
	1,40104	0.21		0.70	5.7 1	3.77		1.10	0.01
	NaSCN	0.25		5.74	6.00	2.93	4.35	1.57	1.23

Table B6 Fitting parameters of CH-region ppp-SFG spectra at air/PVP- D_2O interface in the presence of series of 1M sodium salts (figure 5.4a).

ppp	System	$ \chi_{NR} $ (a.u.)	ω_V (cm ⁻¹) Γ_V (cm ⁻¹)	t-CH 2863±1 11	r-CH ₂ (ss) 2886±2 8	r-CH ₂ (ss) 2903±1 14	CH ₂ (ss) 2924±2 9	r-CH ₂ (as) 2956±2 14	CH ₂ (as) 2984±2 10
	0.05 wt% PVP	0.39		0.55	0.68	0.58	6.03	3.79	6.09
	Na ₂ SO ₄	0.46		0.36	0.65	0.56	4.89	6.17	5.20
A _V (a. u.)	NaCl	0.37		1.22	0.72	0.13	6.09	4.08	6.40
(a. u.)	NaNO ₃	0.37		0.97	0.40	0.30	6.02	4.54	5.76
	NaBr	0.36		1.02	0.42	0.45	5.93	4.68	4.71
	NaClO ₄	0.32		0.82	0.35	0.26	6.74	4.91	2.84
	NaSCN	0.4		0.31	0.07	0.02	5.23	6.76	2.16

Table B7 Variation in orientation angle of vinyl chain CH_2 groups at the air/PVP-D₂O interface in the presence of series of 1M sodium salts (figure 5.4c and d) $\left|\chi_{ppp}^{(2),eff}(as)/\chi_{ppp}^{(2),eff}(ss)\right|$ is estimated by $|A_V|$ values provided in table B6.

Sr. No.	PVP (0.05 wt%) + 1M()	$\left \chi_{ppp}^{(2),eff}(ss)\right $ 2924 cm ⁻¹	$\left \chi_{ppp}^{(2),eff}(as)\right $ 2984 cm^{-1}	$\left \chi_{ppp}^{(2),eff}(as)/\chi_{ppp}^{(2),eff}(ss)\right $	Orientation Angle θ (°)
1.	Na ₂ SO ₄	4.90	5.20	1.06	62.5
2.	NaCl	6.09	6.40	1.05	62.0
3.	NaNO ₃	6.02	5.76	0.96	60.0
4.	NaBr	5.94	4.71	0.79	50.2
5.	NaClO ₄	6.74	2.84	0.42	34.0
6.	NaSCN	5.23	2.16	0.41	33.6

Table B8 Fitting parameters of OH-region ppp-SFG spectra at the air/PVP-water interface in the presence of series of 1M sodium salts (figure 5.5).

ppp	System	$ \chi_{NR} $ (a.u.)	$\omega_V \text{ (cm}^{-1})$ $\Gamma_V \text{ (cm}^{-1})$	3240±5 96	3440±5 120	3540±10 90	3705±3 19
	0.05 wt% PVP	0.02		0.32	0.79	1.07	0.19
	Na_2SO_4	0.02		0.51	0.77	1.13	0.18
A _V (a. u.)	NaCl	0.02		0.01	1.67	1.34	0.30
, ,	NaNO ₃	0.02		0.06	1.94	0.91 (3550±10)	0.20
	NaBr	0.02		0.01	1.85	1.08	0.20
						(3550 ± 10)	
	NaClO ₄	0.01		0.06	2.01	5.15	1.18
						(3580 ± 10)	
	NaSCN	0.01		0.05	2.61	5.69 (3580±10)	1.30

Table B9 Fitting parameters of OH-region ppp-SFG spectra at the air/water interface in the presence of 1M sodium salts (figure 5.6).

ppp	System	$ \chi_{NR} $ (a.u.)	$\omega_V \text{ (cm}^{-1})$ $\Gamma_V \text{ (cm}^{-1})$	3240±10 90	3440±10 120	3540±10 90	3705±2 16
A _V (a. u.)	water	0.01		0.14	1.11	1.14	0.88
	NaClO ₄	0.01		0.20	0.50	1.40	0.88
	NaSCN	0.01		0.16	0.50	1.97	0.89

LIST OF RESEARCH VISITS/ CONFERENCES/ COURSES/ SYMPOSIUMS

Newton-Bhabha Fellowship

[1]. 4-month research visit to Dr. David J. Fairhurst, SOFT Group, School of Physics and Mathematics, Nottingham Trent University, Clifton Campus, Nottingham, United Kingdom, Nov. 2020- Feb. 2021.

Oral Presentations

[1]. Rana, B. and Jena, K.C., Probing Water Molecules in Vicinity of Ions at Air/Water Interface using Sum Frequency Generation (SFG) Vibrational Spectroscopy, *National Conference on Advances in Spectroscopy: Molecules to Materials (NCASMM-2018)*, IITRAM, Ahmedabad, Gujarat, India, Oct. 4-6 (2018).

(Appreciation for Oral Presentation)

Poster Presentations

- [1]. Rana, B., Fairhurst, D. J. and Jena, K.C., Evaporation Process at Air/Aqueous Interface: A Molecular Level Insight, National Technology Day 2022, Indian Institute of Technology Ropar, Rupnagar, Punjab, India, May 12 (2022).
- [2]. Rana, B. and Jena, K.C., Producing Liquid Microjets Using Picosecond Laser Pulse Excitation, 30th DAE-BRNS, National Laser Symposium (NLS-30), RRCAT, Indore, Madhya Pradesh, India, Jan. 19-22 (2022). Online Mode.
- [3]. Rana, B. and Jena, K.C., Studying the Evaporation Process at Air/Aqueous Interface using Interferometry and Nonlinear Vibrational Spectroscopy, 11th International Conference on Advanced Vibrational Spectroscopy (ICAVS), Krakow, Poland, August 23-26 (2021). Online Mode
- [4]. Rana, B. and Jena, K.C., Specific Ion Effects on Polymer and Water structure at Air/Water Interface: A Study by Nonlinear Optical Vibrational Spectroscopy, 8th International Conference on Perspectives in Vibrational Spectroscopy (ICOPVS-2020), JNCASR, Jakkur, Bengaluru, India, Feb. 24-29 (2020).
- [5]. Rana, B. and Jena, K.C., Specific Ion Induced Impacts on Molecular Structure of Air/Polymer Aqueous Interface: Probed by Nonlinear Optical Vibrational Spectroscopy, *National Symposium on Light-Matter Interactions (NSLIMI-2019)*, IIT Madras, Chennai, India, Dec. 26 (2019).
- [6]. Rana, B. and Jena, K.C., Water Molecules in Vicinity of Polyvinylpyrrolidone at Air/Water Interface: Structure and Orientation Determination by Non Linear Optical Vibrational Spectroscopy, *Research Conclave-2*, Indian Institute of Technology Ropar, Rupnagar, Punjab, India, May 14-15 (2019).
 - (Institute Appreciation for research performance during year 2018-2019)
- [7]. Rana, B. and Jena, K.C., Water Molecules in Vicinity of Polyvinylpyrrolidone at Air/Water Interface: Structure and Orientation Determination by Non Linear Optical Vibrational Spectroscopy, 4th Physics Day, Department of Physics, Indian Institute of Technology Ropar, Rupnagar, Punjab, India, August 10 (2019).

(Best poster presentation award)

[8]. Rana, B. and Jena, K.C., Probing the Conformation and Orientation of Water Molecules at Air/Water Interface in Presence of Polyvinylpyrrolidone using Non Linear Optical Vibrational Spectroscopy, *National Laser Symposium-27*, RRCAT, Indore, Madhya Pradesh, India, Dec. 3-6 (2018).

(Best poster presentation award)

[9]. Rana, B. and Jena, K.C., Structural and Orientational Investigations of Polyvinylpyrrolidone (PVP) polymer at Air/Water Interface by Sum Frequency Generation Vibrational Spectroscopy, 7th International Conference on Perspectives in Vibrational Spectroscopy (ICOPVS-2018), BARC Mumbai, India, Nov. 25-29 (2018).

(Best Poster presentation award)

[10]. Rana, B. and Jena, K.C., Physics of Interfacial Water Molecules in Presence of Hofmeister Salts at Air/Water Interface by using Nonlinear Vibrational Spectroscopy, 26th DAE-BRNS, National Laser Symposium, BARC Mumbai, India, Dec. 20-23 (2017).

Courses/Lectures/Workshops

- [1]. GIAN (Global Initiative of Academic Networks) course on "Theory of Surface Nonlinear Spectroscopy", Department of Physics, Indian Institute of Technology Ropar, Rupnagar, Punjab, India, Sep. 26 30 (2022).
- [2]. Web Workshop "Introduction to COMSOL Multiphysics" involving geometry modelling concept, meshing, solvers, two phase flow and turbulence models, fluid structure interactions, COMSOL India, June 01-05 (2020) Online Mode.
- [3]. Webinar on "Finding needles in a haystack: Liquid biopsy for nucleic acid and protein molecular biomarkers for disease diagnosis" The national academy of sciences India (NASI)-Delhi chapter June 02 (2020) Online Mode.
- [4]. Atmanirbhar Bharat Webinar Series "Engineering Solutions for Point-of-Care & Early Diagnostics" The National Academy of Sciences, India (NASI) Delhi Chapter, IEEE Electron Device Society (EDS) Delhi Chapter, May 30 (2020) Online Mode.
- [5]. Research Methodology Workshop-II, Indian Institute of Technology Ropar, Rupnagar, Punjab, India, May 23 (2020) Online Mode.
- [6]. 1st National Webinar on "Strengthening Research capabilities remotely: Empowering Indian researchers on COVID-19", Department of Biotechnology (DBT), India, and Elsevier, May 22 (2020) Online Mode.
- [7]. Virtual Symposium on "Emerging areas of photonics to celebrate international day of light", The national academy of sciences India (NASI)-Delhi chapter and The Optical Society of India, May 16 (2020).
- [8]. Virtual lectures on "Happy 60th Birthday Laser" Tata Institute of Fundamental Research (TIFR), Mumbai, India, May 16 (2020).
- [9]. Research Methodology Workshop-I, Indian Institute of Technology Ropar, Rupnagar, Punjab, India, April 29 (2020) Online Mode.

- [10]. IIT Ropar British Council Researcher Connect Workshop, Career Development and Corporate Relations Centre, Indian Institute of Technology Ropar, Rupnagar, Punjab, India, March 29– April 01 (2019).
- [11]. GIAN (Global Initiative of Academic Networks) course on "Motor Proteins and Molecular Motors" Department of Mathematics, Indian Institute of Technology Ropar, Rupnagar, Punjab, India, Feb. 04–08 (2019).

BIO-DATA OF AUTHOR

Name: Bhawna Rana

Gender: Female

Nationality: Indian

E-mail: <u>bhawnaraizada@gmail.com</u> / <u>bhawna.rana@iitrpr.ac.in</u>

Residential Address: 107, Venus Hostel, Indian Institute of Technology (IIT) Ropar, Nangal Road,

Rupnagar, Pinjab-140001, INDIA

Permanent Address: c/o Shakti Singh, Near Delhi Enclave Society, Chattara (Village), UNA-174306,

Himachal Pradesh, INDIA

Research Interests:

- Nonlinear Optics
- Sum Frequency Generation Vibrational Spectroscopy
- Interfacial Molecular Structure (Air/water interface, Air/polymer-water Interface and Air/biomoleculewater interface)
- Specific Ion Effects
- Evaporation of biological Droplets
- Radiation Pressure Induced Surface deformations (air/liquid Interface and liquid/liquid interface)
- Laser-Induced Liquid Microjets (Needle-free Drug Injections)

Technical Skills:

- Sum Frequency Generation Vibrational Spectroscopy
- Attenuated Total Reflectance (ATR)- Fourier Transform Infrared (FTIR) vibrational spectroscopy
- Langmuir Blodgett for monolayer formation and Whilhelmy Plate method for surface tensión studies
- UV-Visible Absorbance Spectroscopy
- Dynamimc light scattering (DLS) and Zetasizer
- Time-resolved Newton's ring interferometry for evaporation dynamics of sessile aqueous droplets
- Radiation pressure induced Surface deformation
- Pendant drop method for the evaporaton dynamics and surface tensión studies of aqueous droplets
- Laser-induced liquid microjet using ps-and ns-LASERs

Software Skills:

• Python, Matlab, C++, Origin, Image J, Tracker, LabVIEW, Photron, OPUS, Inkscape, MS-Office

Teaching Experience:

• Assistant Professor, 2014 (July) – 2016 (June)

Department of Physics, S.D. (P.G.) College, Panipat, Haryana, India

(Teaching Experience in Subjects: Mathematical Physics, Classical Mechanics, Quantum Mechanics, Electronic Devices and Circuits, Solid State Physics, Statistical Mechanics, Electrodynamics and Plasma Physics, Atomic and Molecular Physics for M.Sc. Physics Course).

• Teaching Assistant for the following courses @ IIT Ropar

PH101: Physics for Engineers, B. Tech Course—(January to June) 2017, 2018, 2019, 2020

PHL511: Modern Optics, M. Sc. Course—(July to December) 2017

PHP510: Physics Laboratory-II Optics, M. Sc. Course—(July to December) 2016, 2017, 2018, 2019

Professional Experience:

- PhD representative, Department of Physics, Indian Institute of Technology Ropar (2019-2021)
- Organiser, 4th Physics Day, Department of Physics, Indian Institute of Technology Ropar (August 10, 2019).